

Study on Hybrid Control Design based on Fuzzy Logic for Photovoltaic Solar Systems

太陽光発電システムのためのファジー論理
に基づくハイブリッド制御設計に関する研究

July 2015

Gia Minh Thao NGUYEN

グエン ザー ミン タオ

Study on Hybrid Control Design based on Fuzzy Logic for Photovoltaic Solar Systems

太陽光発電システムのためのファジー論理
に基づくハイブリッド制御設計に関する研究

July 2015

Waseda University

Graduate School of Advanced Science and Engineering

Department of Electrical Engineering and Bioscience,
Research on Intelligent Control

Gia Minh Thao NGUYEN

グエン ザー ミン タオ

Department of Electrical Engineering and Bioscience
Graduate School of Advanced Science and Engineering
Waseda University

APPROVAL OF DOCTORAL THESIS

Theme of Doctoral Thesis:

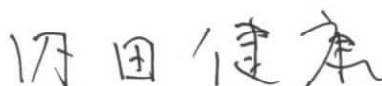
Study on Hybrid Control Design based on Fuzzy Logic for Photovoltaic Solar Systems

Full name of Doctoral student: Gia Minh Thao NGUYEN

This Thesis has been approved by the undersigned Members of the Examining Committee.

Department's Examining Committee:

Chairman and Thesis Supervisor:



Professor Dr. Kenko UCHIDA
Graduate School of Advanced Science and Engineering,
Waseda University.

Committee Member:



Professor Dr. Noboru MURATA
Graduate School of Advanced Science and Engineering,
Waseda University.

Committee Member:



Professor Dr. Shinji WAKAO
Graduate School of Advanced Science and Engineering,
Waseda University.

Committee Member:



Professor Dr. Ryo WATANABE
Graduate School of Advanced Science and Engineering,
Waseda University.

Date of Approval: June 25, 2015

Acknowledgements

Firstly, I would like to express the most sincere and deepest thanks to my supervisor in Doctoral program, Prof. Kenko UCHIDA, for his greatly enthusiastic and efficient guide during the study time and doing the Doctoral thesis at Waseda University.

Moreover, I thank so much AUN/SEED-Net JICA scholarship foundation for the fully financial support for my Doctoral program in Waseda University in three years. Wherein, I am especially grateful Ms. Junko OKURA, Ms. Makiko HAGIWARA and other officers in JICA Tokyo International Center for all their good assistances on my life in Japan.

Furthermore, I really thank Prof. Ryo WATANABE, Department of Electrical Engineering and Bioscience, Waseda University, for his helpful comments and contributions on my study at regular seminars in semesters. Besides, I would like to thank sincerely all the review committee members for my Doctoral thesis: Prof. Noboru MURATA, Prof. Shinji WAKAO, Prof. Ryo WATANABE, and Prof. Kenko UCHIDA for their useful reviews and valuable suggestions.

As one thing more should be mentioned, that is I would like to thank all members, especially Mr. Yusuke OKAJIMA, in Kenko Uchida Laboratory, Dr. Nam NGUYEN-QUANG, a senior lecturer at Ho Chi Minh City University of Technology in Vietnam, and my other close friends, who often help me a lot during the study process.

Besides, I thank my parents, family and lover in Vietnam, who are always the source of great encouragement and solid mental support of mine.

Finally, this Doctoral thesis is also partially supported by JST-CREST.

Tokyo, Japan, July 2015

Gia Minh Thao NGUYEN

Contents

Acknowledgements.....	i
Chapter 1	1
Introduction.....	1
1.1. Problem statement.....	1
1.2. Brief literature reviews.....	3
1.3. Main objectives of thesis.....	4
1.4. Organization of thesis	7
Chapter 2	13
Basic Theory of Fuzzy Logic and Brief Introduction of Fuzzy Logic Toolbox in MATLAB...	13
2.1. Introduction of chapter	13
2.2. Basics of Fuzzy logic system	14
2.2.1. Definition of fuzzy set and related concepts.....	14
2.2.2. Composition proposition, Fuzzy association rule and inference	17
2.2.3. Structure and design of fuzzy logic controller.....	25
2.2.4. Some notes about fuzzy logic control.....	26
2.2.5. Discussion about the combination of fuzzy logic and artificial neural network	27
2.3. Brief introduction of using Fuzzy Logic Toolbox in MATLAB	28
Chapter 3	34
Enhanced Fuzzy-based Incremental Conductance - Maximum Power Point Tracking Algorithm.....	34
3.1. Introduction of chapter	34
3.2. Demonstrative PV system	36
3.2.1. Demonstrative PV system description	36
3.2.2. PV panel model.....	37
3.3. Proposed Fuzzy-based INC-MPPT algorithm	39
3.3.1. The first sub-controller	41
3.3.2. The second sub-controller.....	47
3.4. Simulation results.....	47

3.4.1.	<i>Simulation 1: Start-up response in tracking the MPP at the standard test condition</i>	48
3.4.2.	<i>Simulation 2: Effects of solar radiation changes</i>	50
3.4.3.	<i>Simulation 3: Impacts of temperature variations</i>	52
3.5.	Experimental results.....	53
3.5.1.	<i>Experiment 1: Start-up response in tracking MPP.....</i>	54
3.5.2.	<i>Experiment 2: When the partial shadow happens.....</i>	55
3.5.3.	<i>Experiment 3: When the partial shadow ends.....</i>	55
3.6.	Discussion about effects of partially shaded condition and related solutions.....	56
3.6.1.	In the case of relatively small-scale PV array	56
3.6.2.	In the case of large-scale PV array	57
3.7.	Sample program in C and evaluation of program capacity and computation time.....	61
3.7.1.	Sample program in C language to implement the proposed FLC	61
3.7.2.	Evaluation of the used memory capacity and estimated computation time for FLC....	65
3.8.	Summary of chapter	68
Chapter 4	69	
Fuzzy-based Control of Active and Reactive Powers with Feedback Linearization for Grid-Connected PV Inverters	69	
4.1.	Introduction of chapter	70
4.2.	Modeling of the three-phase grid-connected PV inverter	72
4.2.1.	Demonstrative PV inverter description	72
4.2.2.	Demonstrative PV inverter modeling	72
4.3.	The two FBL-based control schemes	75
4.3.1.	The direct FBL control approach.....	77
4.3.2.	The proposed FBL-FL hybrid control technique	78
4.4.	Simulation settings in MATLAB	92
4.5.	Simulation results and discussions.....	94
4.5.1.	<i>Case 1: Simulation without the parametric uncertainties and the unbalanced grid voltage sag</i>	94
4.5.2.	<i>Case 2: Simulation within parametric uncertainties and without unbalanced grid voltage sag</i>	98
4.5.3.	<i>Case 3: Simulation within parametric uncertainties and the unbalanced grid voltage sag</i>	102
4.5.4.	<i>Case 4: Simulation within parametric uncertainties and the reference values change in ramp functions</i>	105

4.6. Summary of chapter	109
Chapter 5	110
Fuzzy-based Control Strategy with Supporting the Regulation of Grid Frequency for Large-scale PV Farm	110
5.1. Introduction of chapter	110
5.2. Design grid-connected large-scale PV farm with multi-string PV array topology.....	112
5.2.1. Description of the grid-connected large-scale solar farm.....	112
5.2.2. PV panel model.....	113
5.3. The proposed Fuzzy-based control strategy.....	115
5.3.1. The Prediction Module in each Local Controller	116
5.3.2. Process steps in the Central Coordinating Controller.....	118
5.3.3. Determine the operations for PV arrays and battery bank in each Local Controller..	119
5.3.4. Design of the proposed FLC for Frequency Regulation Module in Central Controller... ..	122
5.4. Simulation results and discussion	125
5.4.1. Case 1: Effects of solar radiation and AC-system load.....	126
5.4.2. Case 2: Effects of air temperature and AC-system load.....	129
5.5. Summary of chapter	132
Chapter 6	134
Conclusion	134
6.1. Completed contents and results in thesis	134
6.2. Several optionally complementary suggestions for the three study parts of thesis	135
6.3. Direction of future development for thesis	136
List of Research Achievements.....	138
Bibliography	140

Chapter 1

Introduction

1.1. Problem statement

In recent years, because the fossil-fuel resources, such as coal, natural gas and oil, are likely going to be exhausted, and the environmental preservation is an important problem; the use of renewable-energy sources is currently a salient advance and also becomes more popular in many countries. Referring in [1],[2], the very common renewable-energy sources are the photovoltaic (PV) solar, wind, ocean and fuel-cell. Wherein, PV solar energy systems, which have outstanding features such as an unlimited power and environmentally friendly resource, are playing an ever-increasingly significant role in supplying electricity. For example, PV energy systems are applied in the automatic irrigation system in agriculture, household uses especially in remote areas, street signaling and lighting systems in public services, electricity generation stations, space satellites in universe engineering and so forth.

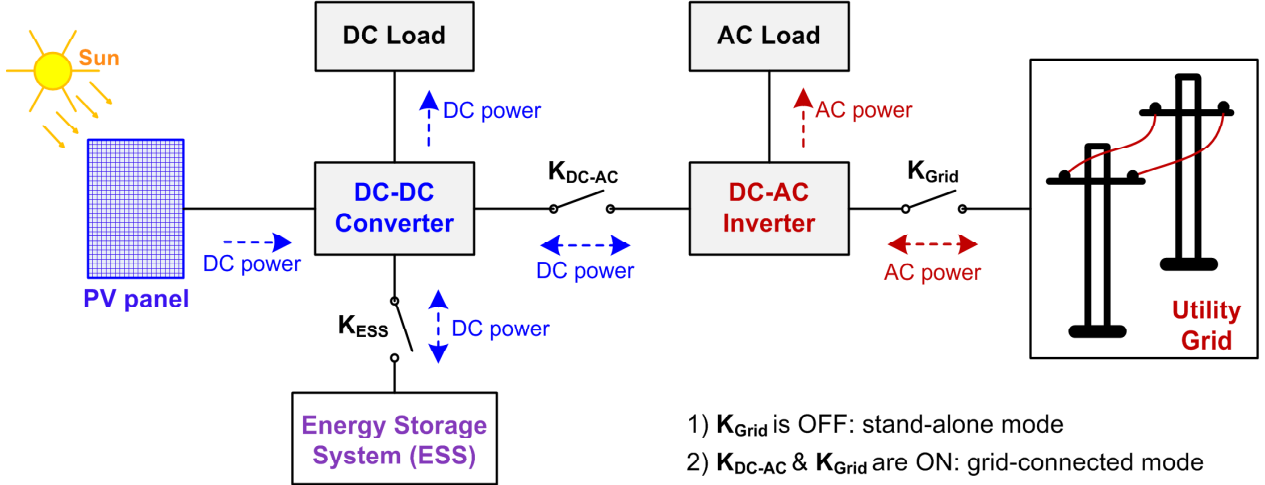


Figure 1.1: A typical structure of photovoltaic (PV) solar energy system.

According to [2],[3] and as shown in Figure 1.1, PV systems commonly have two modes in operation; that is the stand-alone PV system and the grid-connected PV system. In detail, the stand-alone PV system uses the energy obtained from solar panels to supply for the load and/or the energy storage system (ESS), and its operation is independent of the electric grid. The stand-alone PV system is very useful in remote areas or islands where a utility grid is not available or is really difficult to set up. So one of the most important control objective in this PV system is how to obtain

optimally the DC power from PV arrays in varying weather conditions. Whereas, the grid-connected PV system is normally used in distributed generation systems to deliver the active and/or reactive AC power(s) to the utility grid. Therefore, in grid-connected PV systems, beside the aim to obtain optimally the DC power from PV arrays, there is another main control goal as how to deliver effectively the active and/or reactive output AC power(s) of the DC-AC inverter to the utility grid [4]-[6].

Furthermore, to have a mega-watt or giga-watt amount of active power for injecting into the utility grid, the grid-connected large-scale PV solar farm, where many local grid-connected PV power agents and ESS are integrated, has been broadly utilized [7]-[9]. Nevertheless, if the total active output power from the large-scale solar farm is not controlled well, it may cause the frequency deviation of an electric grid to exceed much over the tolerable range of ± 0.2 Hz. Therefore, the grid-frequency regulation problem in an electric grid, containing grid-connected large-scale PV farms with battery banks for storing energy, also should be examined and resolved thoroughly. As well, to ensure the durability of battery banks, a control method for regulating the state-of-charge (SOC) of battery banks should be implemented appropriately. Besides, in the poor solar radiation condition which usually happens in the rainy or winter seasons, the issue about smoothing effect of fluctuation of the output power from grid-connected large-scale PV farms also should be considered and studied carefully [10]. According to [11], as a potential and safe solution, a large-scale high-power storage system utilized the recycled electric-vehicles (EV) batteries has been installed in trial to help resolve the above issue efficiently.

As introduced in [12],[13], to achieve a good efficacy for a PV energy system, two key effect factors should be examined thoroughly. Namely, the first one is impacts of weather parameters. Another is effects of the power-electronic converters, controllers, ESS and loads utilized in the designed PV system. Obviously, the weather condition is out of the user's control and usually alters continually, so control methods used in PV energy systems should be researched and developed thoroughly to achieve the best possible efficacy. Moreover, since characteristics of PV array are highly affected by weather parameters, and the power-electronic converters, loads and electric grid are the nonlinear and complex objects, fuzzy logic, an intelligent control algorithm based on heuristics from experts' experiences, is suitable for developing the novel hybrid controllers to improve significantly the overall effectiveness of PV systems. As well, due to the significant development of commercially modern microcontroller (MCU) and digital signal processor (DSP), the implementation of fuzzy logic controllers in real PV solar systems is relatively simple and easy.

In this thesis, literature reviews about the conventional control methods and existing fuzzy-based hybrid controllers used in PV systems and their drawbacks will be briefly presented in the

next section of this chapter, and then will be continually described more detail in the introduction sections of Chapter 3, Chapter 4 and Chapter 5. Besides, the two last sections in this chapter show the main objectives and organization of the remainder of the dissertation, respectively.

1.2. Brief literature reviews

Regarding the issue how to obtain optimally the DC power from PV array, according to [2],[12], the well-known maximum power point tracking (MPPT) algorithms have been introduced such as Perturb and Observe (P&O), Fractional Open-Circuit Voltage and Incremental Conductance - Maximum Power Point Tracking (INC-MPPT) algorithm. Wherein, the conventional INC-MPPT algorithm, which uses the ratio-value between the slope of P-V curve and PV panel's voltage, $C_p = (\Delta P_p / \Delta V_p) / V_p = I_p / V_p + \Delta I_p / \Delta V_p$ as described in Figure 1.2, to seek the maximum power point (MPP), is also widely used due to its high accuracy in tracing the MPP. Furthermore, this method is fairly simple and easy to implement. However, in the technique, the step-size is a fixed value; and is often adjusted to being small enough to capture the MPP accurately and reduce the oscillation around the MPP. Therefore, the response time of this method is relatively long, especially when the weather condition changes suddenly. On the other hand, the fuzzy logic controller (FLC) has been proposed to the performances of the conventional MPPT methods [12]-[15]. According to [12],[14], in most of the existing fuzzy-based INC-MPPT techniques, the ratio-value, $C_p = I_p / V_p + \Delta I_p / \Delta V_p$, and its change are used to search the MPP. However, in those methods, because the change of the step-size is fully disregarded, the operating point of PV panel may move away far from the MPP when the weather condition varies abruptly. In addition, the authors in [15] presented a FLC in which the change of power and the PV array voltage variation are two inputs; and the FLC's output is the new voltage variation. This algorithm ameliorates the response time in reaching the MPP under variations of the solar radiation and temperature. Nevertheless, the performance of the method has not yet been examined with experimental PV systems.

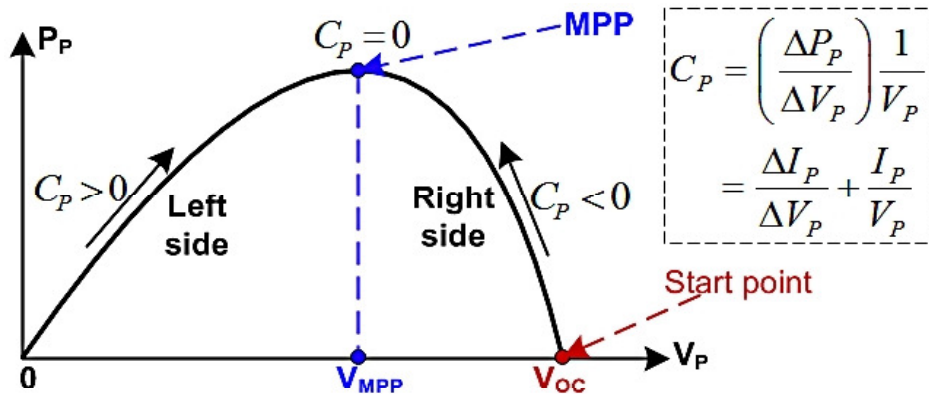


Figure 1.2: Power-voltage (P-V) curve of PV array with the conventional INC-MPPT algorithm.

Regarding the issue how to inject effectively the active and reactive output powers of the PV DC-AC inverter into the utility grid, according to [16], the output powers can be indirectly controlled by regulating the relevant currents, hence the name *current-controlled* technique. Wherein, the most popular control method, the traditional proportional-integral (PI) control, is often utilized to regulate the currents. The main advantage of those PI controllers is the simplicity in implementation. However, traditional PI controllers suffer from the slow response and large overshoot especially when the reference values are changed suddenly. Furthermore, as proposed in [17], the backstepping approach was adopted to control the active and reactive output powers. The approach can regulate independently the active and reactive output powers, and its response is better than the traditional PI control method. Nonetheless, this study did not propose any efficient method to reduce oscillations in the output powers. Additionally, in the previous study of mine [18], the author proposed a proportional-integral-derivative (PID)-Fuzzy hybrid controller for single-phase grid-connected PV inverters. In which, fuzzy logic controllers (FLCs) were designed to tune automatically three coefficients (K_P, K_I, K_D) of the PID controller. The suggested PID-Fuzzy controller actually has better performances than the traditional PID controller in both transient dynamics and steady state, but the proposed modeling technique in this research might be optimized only for the single-phase grid-connected inverters.

Regarding the issue how to control the total active output power of grid-connected large-scale PV farm with supporting the grid-frequency regulation, according to [7],[19], a coordinated-control technique based on fuzzy logic for PV-diesel hybrid systems without battery banks has been presented to regulate grid frequency. This technique utilized two 49-rule FLCs to define the desired value for active power needed to supply to the grid. Moreover, in [8],[20], grid-connected PV systems with battery banks for storing energy have been used to control grid frequency. Even so, the common disadvantage of most these studies is that state-of-charge (SOC) values of the battery banks have not yet been stabilized in the safe ratio range of [0.2 0.8] in order to ensure durability of the battery banks. As introduced in [9], a double-layer capacitor and a proportional controller for grid-connected PV system have been utilized to regulate grid frequency. The control technique has not only the fairly simple structure but also good performances. However, effects of AC-system loads in the grid have not yet been examined in this research.

1.3. Main objectives of thesis

The main objective of this Doctoral thesis is to develop the efficient hybrid controllers based on fuzzy logic for PV solar systems. Wherein, fuzzy logic is combined appropriately with the related

conventional control methods for enhancing noticeably performance and adaptability of the newly proposed hybrid controllers to diminish efficiently nonlinear effects of weather parameters, power-electronic converters and grid in PV systems. In detail, this thesis has three key study parts as follows.

1) To propose an improved Incremental Conductance - Maximum Power Point Tracking (INC-MPPT) algorithm based on fuzzy logic for PV systems to seek quickly and efficiently the MPP of the solar array in varying weather conditions.

As presented in the previous section, in the conventional INC-MPPT algorithm, the step-size is a fixed positive value, and is often adjusted to being small enough to track the MPP accurately and to decrease the oscillation around the MPP. Therefore, the response time of this method is fairly long, especially when the weather condition alters abruptly. To resolve this drawback thoroughly, in the proposed INC-MPPT algorithm, a novel FLC is designed to adjust suitably the step-size of the INC-MPPT algorithm for making the step-size to become a changeable non-negative value, instead of a fixed positive value in the conventional INC-MPPT method. Obviously, this is to determine rapidly and accurately the optimal voltage where the PV array operates at the MPP, that helps improve the response time in seeking the MPP and to eliminate steady-state oscillations around the MPP. So the suggested algorithm can fulfill well all the goals listed above even if the solar radiation and temperature change suddenly. Furthermore, in simulation results, as compared with the conventional INC-MPPT and an existing fuzzy-based INC-MPPT, the advantages of the proposed algorithm in terms of response speed, accuracy and steady-state oscillation in seeking the MPP are demonstrated. Besides, the feasibility and effectiveness of the suggested algorithm, including the consideration on effects of the partial shadow condition, are also verified by experiments.

2) To propose a hybrid control technique based on the feedback linearization and fuzzy logic (FBL-FL) to regulate independently the active and reactive output AC powers of three-phase grid-connected PV inverters to the reference values even within the parametric uncertainties and the unbalanced grid voltage condition.

As described in the previous section, the traditional PI controller can regulate the active and reactive output AC powers of three-phase grid-connected PV inverters with small steady-state fluctuations in the output powers, and also has relatively small total harmonic distortion (THD) of grid current. However, the traditional PI controller has the bad transient-response such as slow response speed and large overshoot, especially when the reference values of the output powers

change suddenly. Furthermore, the traditional PI controller likely cannot regulate well the output powers under the unbalanced grid voltage condition. Whereas, as presented in [21] and then checked in this thesis, the direct feedback linearization (FBL) approach may regulate the active and reactive output powers of three-phase grid-connected PV inverters with the quick response speed and high robustness, even when the reference values of output powers unexpectedly alter and when the unbalance of grid voltages happens. Nonetheless, due to undesired errors in system modelling and parametric uncertainties, the direct FBL, a model-based control approach, often includes big steady-state fluctuations and fairly large overshoot in transient responses.

In the proposed FBL-FL hybrid technique, fuzzy logic is used to enhance effectiveness of the direct FBL approach in order to inherit the main advantages of both the direct FBL approach (as the quick response speed and high robustness) and the traditional PI controller (as the small steady-state fluctuation and acceptable THD), and also to reduce as efficiently as possible the aforementioned drawbacks of the direct FBL approach (as the big steady-state fluctuation and fairly large overshoot in the transient state). In detail, a unique FLC, consisting of 25 association rules, is newly designed to improve efficacy of the linear PI control method used in the direct FBL approach as follows:

- i. The FLC fine-tunes automatically and properly for the gain factors of integral modules in the linear method. This helped enhance considerably the transient response (response time, overshoot) of the output powers, especially when the reference values are varied noticeably and abruptly.
- ii. Additionally, the FLC also adjusts suitably the final virtual-control signals to reduce efficiently the steady-state fluctuations in the output powers, especially in the parametric uncertainty condition.

Based on the two above functions of the FLC, the proposed FBL-FL technique can regulate independently the active and reactive output AC powers to the reference values in both the step and ramp functions, even within the parametric uncertainties and the unbalanced grid voltage condition. Moreover, comparisons of simulation results with the traditional PI controller and the direct FBL approach are performed to show the efficacy of the proposed FBL-FL technique. Besides, the stability for the proposed FBL-FL hybrid method is also analyzed and proved.

3) To introduce a novel coordinated-control strategy based on fuzzy logic to inject efficiently the total active power from a grid-connected large-scale PV farm, consisting of many local solar power agents and the battery bank to store energy at each agent, into an electric grid with supporting the regulation of grid frequency. Moreover, the proposed strategy should also fulfill

well the key objective in regulating the grid-frequency even when the AC-system load and the weather condition abruptly alter.

In most the previous studies related to the large-scale grid-connected solar farm, the common disadvantage is that state-of-charge (SOC) values of the battery banks have not yet been stabilized in the safe ratio range of [0.2 0.8] in order to ensure durability of the battery banks. Besides, in some other studies, effects of AC-system loads in the grid have not yet been examined. To resolve thoroughly these issues, in this study part, the fuzzy-based coordinated-control strategy is proposed with three major objectives as follows:

- a) The total output active power from the PV farm supplied to the grid is tuned suitably to ensure the grid frequency in acceptable ranges. Two tolerable ranges used for frequency deviation are ± 0.2 Hz in transient states and ± 0.05 Hz at steady states, where the nominal grid frequency is 60 Hz.
- b) At each local PV power agent, state-of-charge (SOC) of the battery bank is governed in the safe ratio range of [0.2 0.8] to improve durability of the battery bank. Also, steady-state SOC of the battery bank is regulated closely to a desired ratio value of 0.5 if the frequency deviation is in the so small range of ± 0.05 Hz.
- c) The two above objectives listed in a) and b) of the suggested fuzzy-based strategy have to be validated well even if the AC-system load, solar radiation and temperature unexpectedly change. Moreover, the efficacy in regulating grid frequency of the suggested fuzzy-based strategy is also compared with the conventional control strategy which uses the full MPPT mode.

In summary, as the overall goal, this thesis is to perform a pretty comprehensive study in designing the efficient hybrid controllers for PV systems. Wherein, the first two proposed control methods, that are the fuzzy-based INC-MPPT algorithm and the FBL-FL hybrid technique, are applied respectively for the DC-DC converter connected with PV arrays and the three-phase DC-AC inverter installed in a solar power agent; and the last proposed method, that is the fuzzy-based coordinated-control strategy, is applied for a grid-connected large-scale solar farm, consisting of many local solar power agents and the battery bank to store energy at each agent.

1.4. Organization of thesis

The remainder of this Doctoral thesis is organized as follows.

The basic theory of fuzzy logic and the brief introduction of Fuzzy Logic Toolbox in MATLAB are shown in Chapter 2. Wherein, the basics of fuzzy logic such as the fuzzy set, fuzzification, membership function, composition proposition, association rule, inference method and defuzzification are presented. The main characteristics, fields of application and drawbacks of fuzzy logic are also given. As well, some simple illustrative examples are included for easier to understand. Then, the standard structure and the design steps for a FLC are shown in this chapter. Finally, the detailed design process for a FLC with Fuzzy Inference System (FIS) Editor of Fuzzy Logic Toolbox in MATLAB is illustrated graphically.

Chapter 3 is the first key study part of this thesis, that is to present a newly improved INC-MPPT method based on fuzzy logic for stand-alone PV systems as shown in Figure 1.3(a). In detail, firstly, the basic contents of some common MPPT methods, including the conventional INC-MPPT, and drawbacks of the previously existing fuzzy-based INC-MPPT algorithms are analyzed. The equivalent circuits and mathematical models of the non-inverting DC-DC buck-boost converter and PV array used in the demonstrative stand-alone PV system are described briefly. Then, the unique scheme of the proposed fuzzy-based INC-MPPT algorithm is presented in detail. Wherein, a novel FLC is designed to boost the effectiveness of the conventional INC-MPPT, especially in improving the response speed and reducing fluctuations around the MPP. From the absolute value of a modified ratio-value or the absolute value of PV current's change, and the previous step-size, the proposed FLC, comprising 25 fuzzy association rules, adjusts suitably the step-size to determine speedily and exactly the optimal voltage $V_{MPP}^{ref}(k)$ where the PV array operates at the MPP as shown in Figure 1.3(b). Simulation results in MATLAB, including the consideration on impacts of the solar radiation and temperature, are provided to demonstrate the advantages of the proposed algorithm in terms of fast response speed, accuracy, and small oscillation around the MPP. As well, comparisons between the proposed fuzzy-based INC-MPPT and the conventional INC-MPPT and a existing fuzzy-based INC-MPPT algorithm are also performed in the result section. Finally, the efficacy of the suggested algorithm is also validated with the experimental 320W stand-alone PV system as shown in Figure 1.3(c).

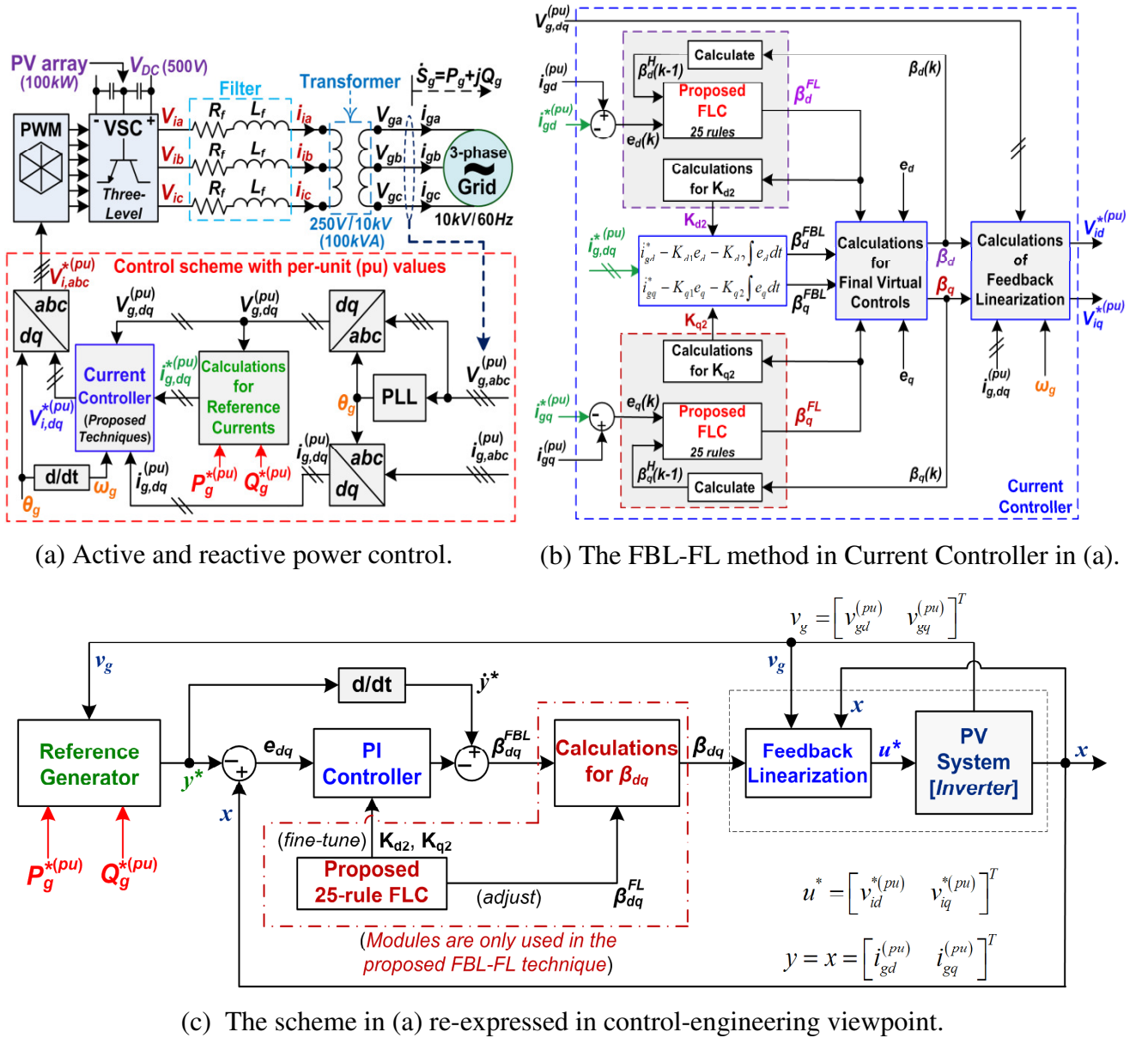


Figure 1.4: Active and reactive powers control for three-phase PV inverter studied in Chapter 4.

As shown in Figure 1.4(b), a unique FLC, consisting of 25 association rules, is proposed to enhance effectiveness of the linear PI method used in the direct FBL approach for generating the newly compatible final-virtual-control signals (β_d, β_q) . The first FLC's input ($e_d(k)$ or $e_q(k)$) is the error between the measured value of grid current and its reference; and the second input ($\beta_d^H(k-1)$ or $\beta_q^H(k-1)$) is the subtraction between the previous final-virtual-control signal ($\beta_d(k-1)$ or $\beta_q(k-1)$) and its mean value at the fundamental frequency of grid voltage ($\beta_d^M(k-1)$ or $\beta_q^M(k-1)$). As illustrated in Figure 1.4(b)-(c), the FLC's output is an additional value, $\beta_d^{FL}(k)$ or $\beta_q^{FL}(k)$, utilized for two separate functions as follows: [i] to fine-tune automatically the gain factors of integral modules in the linear PI method (K_{d2}, K_{q2}) for enhancing considerably the transient responses (response time, overshoot) of the output powers (P_g, Q_g),

[ii] to adjust suitably the final virtual-control signals (β_d, β_q) to reduce efficiently the steady-state fluctuations in the output powers. Furthermore, the stability for the proposed FBL-FL hybrid method is analyzed and proved according to the theory “Affine Parameter-Dependent Lyapunov Functions” applied for the second-order systems. Finally, in the result section, numerical simulations in MATLAB, including considerations on the parametric uncertainties and the unbalanced grid voltage condition, are performed to illustrate the efficacy in regulating independently the active and reactive output powers of the two FBL-based structures. As well, comparisons of simulation results, obtained from the traditional PI controller and the two FBL-based structures, also are analyzed to show advantages of the proposed FBL-FL hybrid technique in terms of fast response, small overshoot, acceptable steady-state fluctuation and robustness.

As a combination and development from the first two study parts in Chapter 3 and Chapter 4 which are applied for a local solar energy agent, Chapter 5 introduces a novel coordinated-control strategy based on fuzzy logic to inject efficiently the total active power from a grid-connected large-scale PV farm, consisting of many local solar energy agents and the battery bank to store energy at each agent, into an electric grid with supporting the regulation of grid frequency. This chapter is the last key study part of the thesis and contains the following sections.

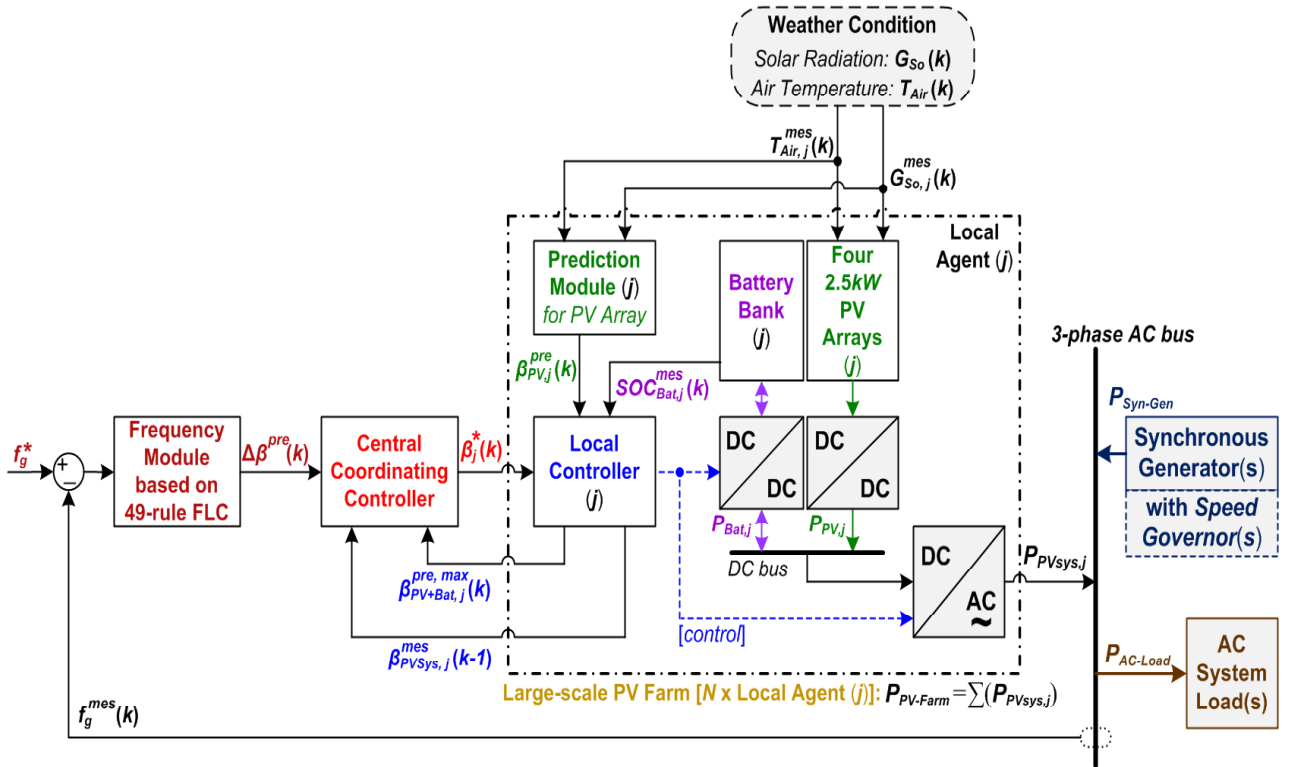


Figure 1.5: The proposed fuzzy-based control strategy for large-scale PV farm studied in Chapter 5.

Firstly, literature reviews about the existing control methods for grid-connected large-scale PV farms and their drawbacks are presented. Then the detailed design structure of the proposed strategy is shown as follows. It is designed according to the two-level control structure, consists of a central coordinating controller and local controllers at PV power agents as shown in Figure 1.5. Wherein, the central controller uses a frequency regulation module based on a newly designed 49-rule FLC, which two inputs are the frequency deviation and its derivative value, to determine the adjustable value $\Delta\beta^{pre}(k)$ for updating the reference value of total active power needed from the solar farm; and then appropriately coordinates the individual reference value $\beta_j^*(k)$ for the local controller at each PV agent. As well, each local controller drives the power-electronic DC-DC converters connected with PV arrays, bidirectional DC-DC battery charger and three-phase DC-AC inverter installed at the PV agent to deliver the active power to the grid accurately according to the reference value $\beta_j^*(k)$ obtained from the central controller. Besides, in each local controller, a prediction module based on simulation with the mathematical model of PV panel is utilized to forecast the maximum power from PV arrays $\beta_{PV,j}^{pre}(k)$; and a control method, used for regulating SOC of the battery bank $SOC_{Bat,j}^{mes}(k)$ in the safe ratio range of [0.2 0.8] and especially close to the desired ratio value of 0.5 at the steady state to ensure durability of the battery bank, is also implemented. In the result section, simulations in MATLAB demonstrate that the proposed fuzzy-based strategy has good performance in injecting the output active power from the PV farm into the grid with regulating the grid frequency in tolerable ranges of [-0.2Hz 0.2Hz] in the transient state and [-0.05Hz 0.05Hz] in the steady state even if the AC-system load, solar radiation and air temperature suddenly vary. Moreover, the efficacy in regulating grid frequency of the suggested fuzzy-based strategy is also compared with the conventional control strategy which uses the full MPPT mode.

Finally, the conclusion and future development sections of this thesis are given in Chapter 6. In the conclusion section, the completed contents and achieved results in the thesis are summarized again. Moreover, several optionally complementary suggestions to continue to improve the three main study parts of the thesis are also provided. Besides, in the future developments of this thesis, notable issues about coordinated-control strategy, balance of supply and demand of power and power quality in the large-scale electric network, where many distributed PV solar and wind energy agents are integrated, will be examined and researched.

Chapter 2

Basic Theory of Fuzzy Logic and Brief Introduction of Fuzzy Logic Toolbox in MATLAB

This chapter presents the basic theory of fuzzy logic [22],[23], and then introduces briefly the use of Fuzzy Logic Toolbox in MATLAB simulation software [35].

2.1. Introduction of chapter

Fuzzy logic was first introduced by Professor L.A. Zadeh at University of Berkeley, California, the United States, in 1965. Since then, fuzzy logic has been developed much and widely applied in many fields of control and automation engineering. Some early notable examples about applications of fuzzy logic are recorded as follows. In early 1970s, in Queen Mary University, the United Kingdom, E. Mamdani used fuzzy logic to control a steam engine which could be not controlled well by classical control methods. Then, in 1977, H.J. Zimmermann utilized fuzzy logic to design an expert system for loan evaluation in Germany. In Japan, fuzzy logic was applied to the water-treatment plant of Fuji Electric company in 1984, and the subway system developed by Hitachi company in 1985 and then has operated commercially since 1987. In the United States, in 1985, the first fuzzy chip was designed and developed by M. Togai and H.Watanabe at Bell Labs. Fuzzy logic was first presented in the United States, had the first control application in the United Kingdom and was implemented into industrial applications in Japan; and nowadays, it has been applied broadly in the world.

As compared with the classical control methods, the salient advantage of fuzzy logic control is able to synthesize the controller without knowing in advance correctly characteristics of the object. This is really useful for controlling the complex and nonlinear objects which transfer functions cannot be obtained exactly or are much affected by many external uncertainty variables. Furthermore, as the second major advantage in fields of application, fuzzy logic control also is often utilized for circumstances where a ‘nearly true’ solution with quick design but can fulfill pretty well the control goals.

Fuzzy logic control processes the ‘unclear’ or ‘incomplete’ information from the object, and its accuracy is only found among interactive relationships of the obtained information and can only be described by linguistic variables for real parameters of the object; but it still can make a suitable control decision for the object. Fuzzy logic, also known as a heuristic intelligent control based on

information processing and control of humans, is the beginning of the application of artificial intelligence in the fields of control engineering.

Besides, fuzzy logic also has other notable benefits as follows [24],[25]:

- Fuzzy logic mainly uses linguistic variables, which are expressed in the natural language, to encode directly the expert knowledge and experiences. Moreover, mathematic concepts and inference mechanism used in fuzzy systems are pretty simple and possible to understand.
- The designer/user with knowledge and experiences can modify and tune some contents and/or parameters in a previously designed FLC to become a novel efficient FLC for a newly controlled object without mandatory re-develop a fully new FLC from the beginning. It means that fuzzy logic system is fairly flexible in design, upgradation and improvement.
- In applications with complex objects, instead of replacing entirely for related conventional control algorithms, fuzzy logic can be utilized to combine aptly with the conventional control methods in order to enhance effectiveness and adaptability for control system.
- Besides, most of the previously introduced fuzzy logic controllers, which can fulfill pretty well objectives of PV energy systems in typical applications, are usually designed with two or three input variables. Obviously, this is not too complicated to design and implement.

According to the salient advantages as observed above, in this thesis, fuzzy logic is suitable for researching and developing the efficient hybrid controllers to enhance noticeably the overall performance of PV systems, where characteristics of PV array are highly affected by weather condition (which is uncontrollable and often changes suddenly), and power-electronic converters, integrated loads and electric grid are complex and nonlinear objects.

2.2. Basics of Fuzzy logic system [22],[23],[26],[27]

In general, fuzzy logic system is a set of association rules in the form “**If ...Then...**” to simulate the behaviours of human and then to integrate into the structure of the control system.

2.2.1. Definition of fuzzy set and related concepts

2.2.1.1. Definition of fuzzy set:

The fuzzy set F defined on a classical set A is a set in which its every element is a pair of values $(x, \mu_F(x))$ where $x \in X$ and μ_F is the mapping $\mu_F : X \rightarrow [0,1]$. Wherein, the mapping μ_F is called the membership function of the fuzzy set F . And the classical set X is called the universe (base set) of the fuzzy set F .

2.2.1.2. Membership function:

- With a set A , the mapping $\mu_A : A \rightarrow R$ is defined as follows:

$$\mu_A = \begin{cases} 1, x \in A \\ 0, x \notin A \end{cases} \quad (2.1)$$

, is called the membership function of A .

- The classical set X , which always has $\mu_X(x) = 1$ with every element x , is called the universe (base set). So, according to the above concept, the membership function μ_A of the set A that has the universe X will be the mapping $\mu_A : X \rightarrow \{0,1\}$.

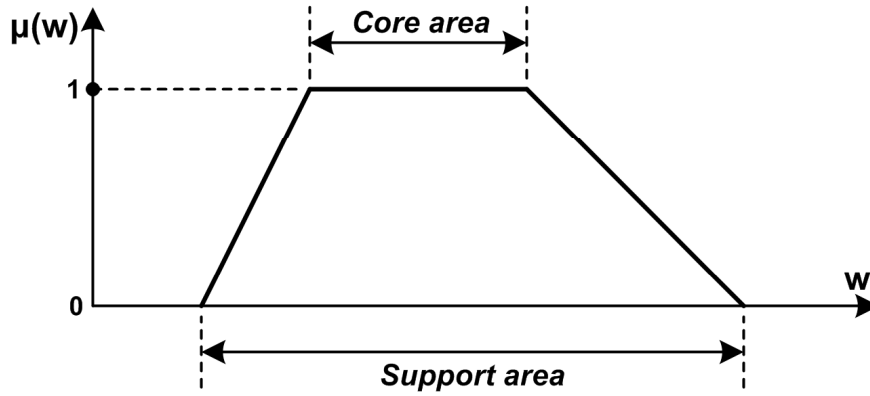


Figure 2.1: Membership function of a fuzzy set with the *core area* and *support area*.

- *Support area*: The support area of the fuzzy set F (defined on the universe X) is denoted by a subset S which satisfies: $S = \{x \in X \mid \mu_F(x) > 0\}$.
- *Core area*: The core area of the fuzzy set F (defined on the universe X) is denoted by a subset T which satisfies: $T = \{x \in X \mid \mu_F(x) = 1\}$.

Example 2.1:

In this example, Figure 2.2 describes a membership function of the fuzzy set W . With each individual value of variable w such as w_1, w_2 and w_3 , we have the mapping values (fuzzy reading) respectively as follows: $\mu(w_1) = 0.5$; $\mu(w_2) = 1$; $\mu(w_3) = 0.75$.

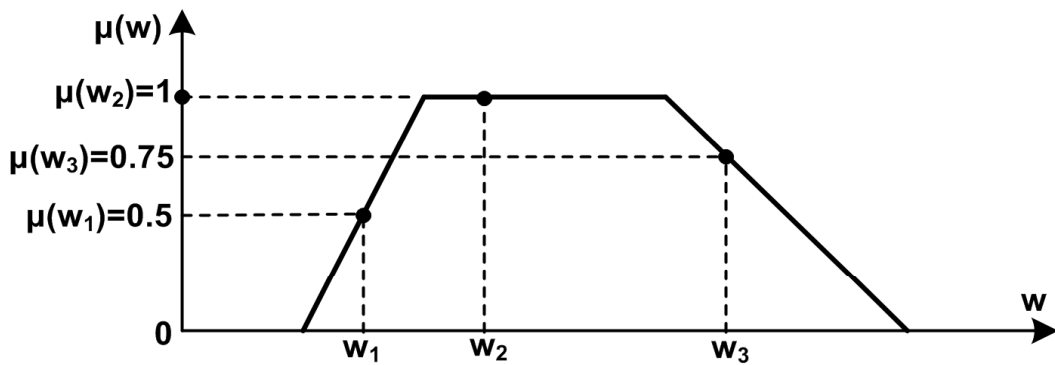


Figure 2.2: An example about fuzzy reading with a membership function.

2.2.1.3. Linguistic variable

Linguistic variable is a key element within the system using fuzzy logic. Wherein, linguistic components in a same circumstance are combined together. Each linguistic value of a variable is determined by a fuzzy set defined on the universe (base set) that includes real numbers to indicate the physical value of the variable.

Example 2.2:

In measuring the temperature in a room, it often is divided into five levels such as very cold temperature, cold temperature, normal temperature, hot temperature and very hot temperature. According to the common experience of human, threshold values for the five above levels can be chosen as follows: very cold temperature is 10°C , cold temperature is 18°C , normal temperature is 25°C , hot temperature is 32°C , and very hot temperature is 36°C . In the fuzzification process of a FLC designed to control the room temperature, firstly, we choose the measured value of temperature T_{Room} as the input of the FLC, which consists of five linguistic variables as follows:

$$T_{Room} = \{\text{Very Cold, Cold, Normal, Hot, Very Hot}\} = \{\text{VC, CO, NO, HO, VH}\} \quad (2.2)$$

The value range for T_{Room} is in $[10^{\circ}\text{C } 36^{\circ}\text{C}]$, and then the fuzzy membership function is chosen according to the triangle function as shown in Figure 2.3.

In summary, T_{Room} is an input of the designed FLC, and this input has five linguistic variables as given in (2.2) and has the value range in $[10^{\circ}\text{C } 36^{\circ}\text{C}]$; finally, T_{Room} has the triangle-based membership function as presented in Figure 2.3.

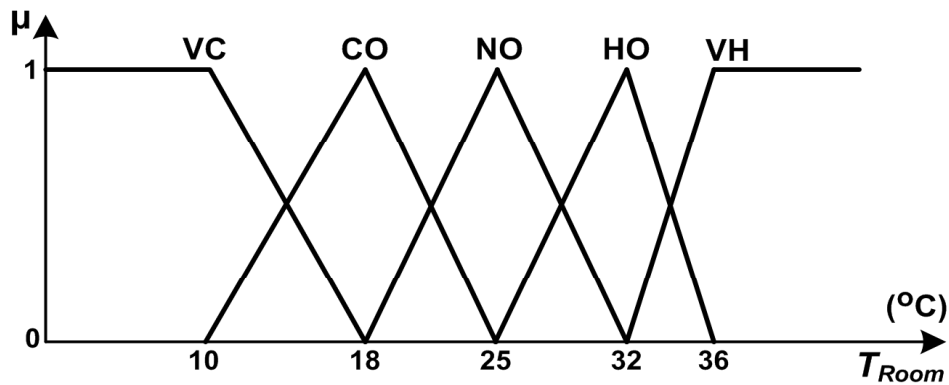


Figure 2.3: Membership functions for the linguistic variable T_{Room} of temperature in room.

2.2.1.4. Operations of Fuzzy set

The common operations of fuzzy set are *Intersection*, *Union* and *Complement*, which are expressed in (2.3), (2.4) and (2.5), respectively.

- *Intersection* operation:

$$\mu_{A \cap B} = \mu_A(x) \cdot \mu_B(x) = \text{Min}\{\mu_A(x), \mu_B(x)\} \quad (2.3)$$

- *Union* operation:

$$\mu_{A \cup B} = \mu_A(x) + \mu_B(x) - \mu_A(x) \cdot \mu_B(x) = \text{Max}\{\mu_A(x), \mu_B(x)\} \quad (2.4)$$

- *Complement* operation:

$$\mu_{\bar{A}}(x) = 1 - \mu_A(x) \quad (2.5)$$

2.2.2. Composition proposition, Fuzzy association rule and inference

2.2.2.1. Composition Proposition:

The composition proposition, corresponding to a control rule, is often expressed in the form as follows:

IF *<condition proposition>* **THEN** *<consequence proposition>*

According to [22], there are three popular deductive technique used for fuzzy inference as follows: (i) the Mamdani system, (ii) the Sugeno model, and (iii) the Tsukamoto model. Wherein, the Mamdani system is the most widely applied method. The meaning of the principle of Mamdani system is expressed as follows: “The membership value of the consequence must be not larger the membership value of the condition”. This principle is usually used to describe the fuzzy proposition in a fuzzy logic controller.

In the case where the designed fuzzy system has multiple inputs and multiple outputs, the general proposition is expressed as follows:

IF $G = g$ and $H = h$ and $K = k \dots$ **THEN** $M = m$ and $N = n \dots$

The three common rules for the fuzzy composition proposition are given as below:

- *Max* composition rule: The fuzzy composition proposition $A \Rightarrow B$ has the value as a fuzzy set B' (defined on the universe Y of the fuzzy set B), and it has the membership function as $\mu_{B'}(y) = \text{Max}\{\mu_A, \mu_B(y)\}$.
- *Min* composition rule: The fuzzy composition proposition $A \Rightarrow B$ has the value as a fuzzy set B' (defined on the universe Y of the fuzzy set B), and it has the membership function as $\mu_{B'}(y) = \text{Min}\{\mu_A, \mu_B(y)\}$.

- *Product* composition rule: The fuzzy composition proposition $A \Rightarrow B$ has the value as a fuzzy set B' (defined on the universe Y of the fuzzy set B), and it has the membership function as $\mu_{B'}(y) = \mu_A \bullet \mu_B(y)$.

2.2.2.2. Fuzzy association rule

Fuzzy association rule is a set of one or many composition proposition(s) as presented in the subsection 2.2.2.1.

If the fuzzy association rule has only one composition proposition, it is called the single association rule. On the other hand, if the fuzzy association rule has many composition propositions, it is called the multiple association rule. For more detail, *Example 2.3* shows fuzzy association rules developed for a FLC.

Example 2.3:

A simple controller for the room temperature T_{Room} (described in *Example 2.2*) that use a bidirectional air conditioner, including both the cooling and heating functions, can be developed with five fuzzy association rules as follows.

- *Rule 1: IF T_{Room} is very hot (VH) THEN the bidirectional air conditioner is controlled to operate in cooling mode with high power.*
- *Rule 2: IF T_{Room} is hot (HO) THEN the bidirectional air conditioner is controlled to operate in cooling mode with medium power.*
- *Rule 3: IF T_{Room} is normal (NO) THEN the bidirectional air conditioner is operated in rest mode.*
- *Rule 4: IF T_{Room} is cold (CO) THEN the bidirectional air conditioner is controlled to operate in heating mode with medium power.*
- *Rule 5: IF T_{Room} is very cold (VC) THEN the bidirectional air conditioner is controlled to operate in heating mode with high power.*

2.2.2.3. Composition operations (inference methods) for fuzzy system

The common composition operations (inference methods) for fuzzy system are:

- *Max–Min* composition operation: the *Intersection* (\wedge) is according to the *Min* composition rule, while the *Union* (\vee) is according to the *Max* composition rule.

$$C = A \circ B \leftrightarrow \mu_C(x, v) = \vee \{ \mu_A(x, y) \wedge \mu_B(y, v) \} = \text{Max} \{ \text{Min} \{ \mu_A(x, y), \mu_B(y, v) \} \} \quad (2.6)$$

- *Max–Product* composition operation: the *Intersection* (\wedge) is according to the *Product* composition rule, while the *Union* (\vee) is according to the *Max* composition rule

$$C = A \circ B \leftrightarrow \mu_C(x, v) = \vee \{ \mu_A(x, y) \bullet \mu_B(y, v) \} = \text{Max} \{ \mu_A(x, y) \bullet \mu_B(y, v) \} \quad (2.7)$$

- *Sum–Min* composition operation: the *Intersection* (\wedge) is according to the *Min* composition rule, while the *Union* (\vee) is according to the *Lukasiewicz* [23] composition rule

$$\mu_{A \cup B}(x) = \text{Min} \{ 1, \mu_A(x) + \mu_B(x) \}.$$

- *Sum–Product* composition operation: the *Intersection* (\wedge) is according to the *Product* composition rule, while the *Union* (\vee) is according to the *Lukasiewicz* composition rule

$$\mu_{A \cup B}(x) = \text{Min} \{ 1, \mu_A(x) + \mu_B(x) \}.$$

Besides, some other composition operations (inference methods) can be found in [22]. In this Doctoral thesis, the *Max–Min* composition operation is used for inference operation of all the proposed FLCs in Chapters 3, 4 and 5. For more detail, *Example 2.4* shows a numerical sample of the *Max–Min* inference operation.

Example 2.4:

Two fuzzy realtions expressed in two matrixs A and B has the result as shown in matrix C .

$$A = \begin{matrix} & & v_1 & v_2 \\ \begin{matrix} x_1 \\ x_2 \end{matrix} & \begin{bmatrix} 0 & 1 & 1 \\ 1 & 0 & 1 \end{bmatrix} \end{matrix} ; B = \begin{matrix} & v_1 & v_2 \\ \begin{bmatrix} 1 & 0 \\ 0 & 1 \\ 0 & 0 \end{bmatrix} \end{matrix}.$$

$$\mu_C(x_1, v_1) = \text{Max} [\text{Min}(0, 1), \text{Min}(1, 0), \text{Min}(1, 0)] = \text{Max} [0, 0, 0] = 0 ;$$

$$\mu_C(x_1, v_2) = \text{Max} [\text{Min}(0, 0), \text{Min}(1, 1), \text{Min}(1, 0)] = \text{Max} [0, 1, 0] = 1 ;$$

$$\mu_C(x_2, v_1) = \text{Max} [\text{Min}(1, 1), \text{Min}(0, 0), \text{Min}(1, 1)] = \text{Max} [1, 0, 1] = 1 ;$$

$$\mu_C(x_2, v_2) = \text{Max} [\text{Min}(1, 0), \text{Min}(0, 1), \text{Min}(1, 0)] = \text{Max} [0, 0, 0] = 0 .$$

Finally, the result is expressed as follows.

$$C = A \circ B = \begin{bmatrix} 0 & 1 \\ 1 & 0 \end{bmatrix}.$$

2.2.2.4. Defuzzification

Defuzzification is a process to define clearly the real output from the membership functions of fuzzy sets. Some popular methods used in this process are as follows:

- *Maximum membership principle*: also called as the *height method*, is only used for the kinds of fuzzy set with sharp peak, and is given by (2.8).

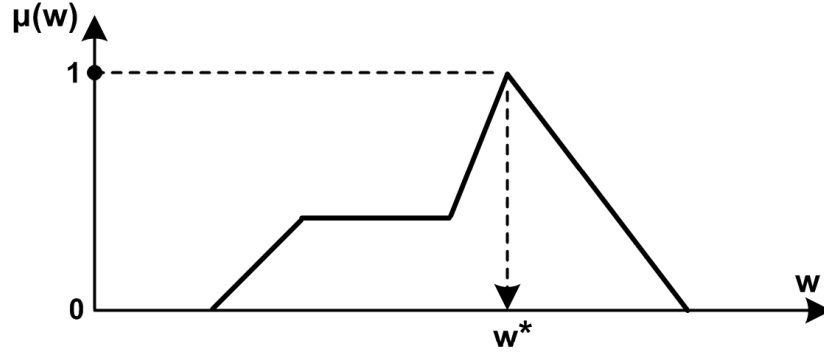


Figure 2.4: *Maximum membership principle*.

$$\mu(w^*) \geq \mu(w), \forall w \in W \quad (2.8)$$

In the case where the fuzzy set has multiple sharp peaks or the maximum value is not only a single point, the following methods are used for defuzzification.

- *Centroid method* (CoG: *Center of Gravity*, or CoA: *Center of Area*): is very widely used in applications, and is expressed in Figure 2.5 and (2.9). For more detail, *Example 2.5* shows a numerical sample of the *centroid* defuzzification method.

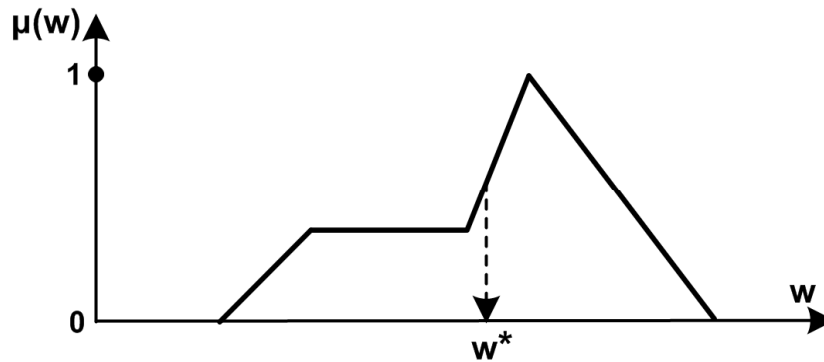


Figure 2.5: *Centroid method*.

$$w^* = \frac{\int \mu(w) \cdot w dw}{\int \mu(w) dw} \quad (2.9)$$

Example 2.5:

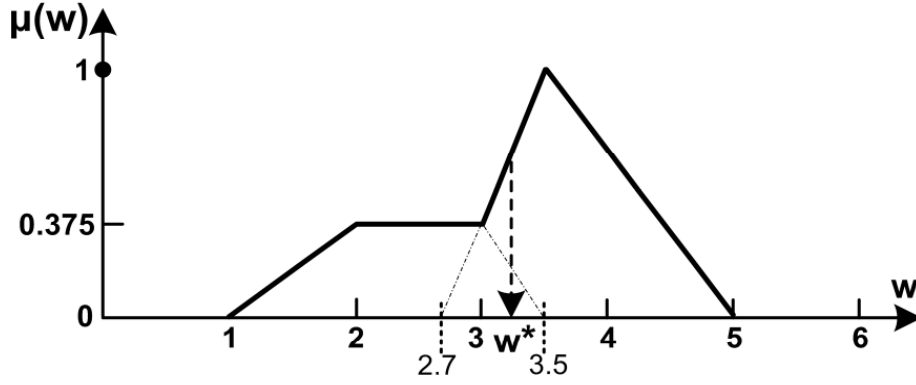


Figure 2.6: A numerical example for the defuzzification process using the *centroid* method.

According to the *centroid* method for defuzzification expressed in (2.9), the real output value w^* of the fuzzy set W described in Figure 2.8 is calculated as follows.

$$\begin{aligned}
 w^* &= \frac{\int \mu(w).w dw}{\int \mu(w) dw} \\
 &= \frac{\left[\int_1^2 (0.375(w-1)) w dw + \int_2^3 (0.375) w dw + \int_3^{3.5} \left(\frac{w-2.7}{0.8} \right) w dw + \int_{3.5}^5 \left(\frac{5-w}{1.5} \right) w dw \right]}{\left[\int_1^2 (0.375(w-1)) dw + \int_2^3 (0.375) dw + \int_3^{3.5} \left(\frac{w-2.7}{0.8} \right) dw + \int_{3.5}^5 \left(\frac{5-w}{1.5} \right) dw \right]} \\
 &= \frac{\left[\frac{5}{16} + \frac{15}{16} + \frac{217}{192} + 3 \right]}{\left[\frac{3}{16} + \frac{3}{8} + \frac{11}{32} + \frac{3}{4} \right]} = 3.2484
 \end{aligned}$$

- *Center of Sums method* (CoS): is a variant of the *centroid* method, where the integral formula is replaced by the sigma formula to simplify computation as expressed in (2.10). This method is often utilized to implement in real experimental applications. For more detail, *Example 2.6* shows a numerical sample of the *center of sums* defuzzification method.

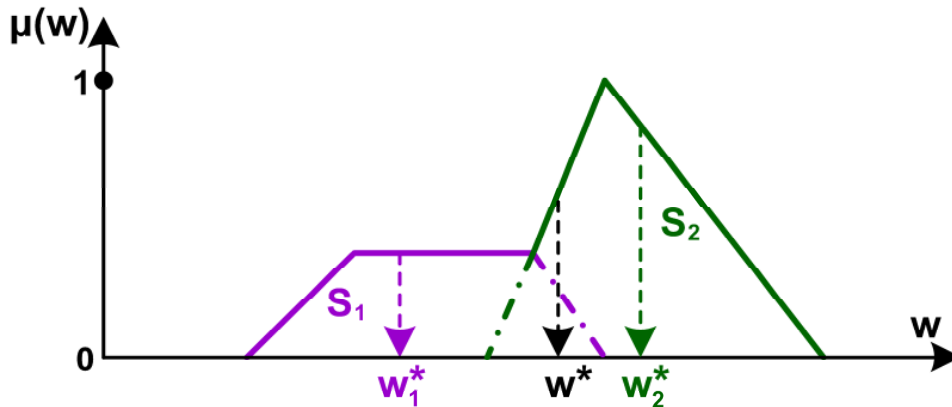


Figure 2.7: *Center of sums* method.

$$w^* = \frac{\sum_{k=1}^N (w_k^* \cdot S_k)}{\sum_{k=1}^N S_k} \quad (2.10)$$

Where w_k^* and S_k are the individual centroid position and acreage of each the k th output fuzzy set, respectively.

According to [26], the centroid position of a trapezoidal fuzzy set with four peaks on the horizontal axis (p_a, p_b, p_c, p_d) can be determined as follows:

$$centroid_position = \frac{1}{3} \left[p_a + p_b + p_c + p_d - \frac{p_c p_d - p_a p_b}{(p_c + p_d) - (p_a + p_b)} \right] \quad (2.11)$$

In the case of a triangular fuzzy set, where $p_b = p_c$, equation (2.11) can be rewritten as (2.12).

$$centroid_position = \frac{p_a + p_b + p_d}{3} \quad (2.12)$$

Example 2.6:

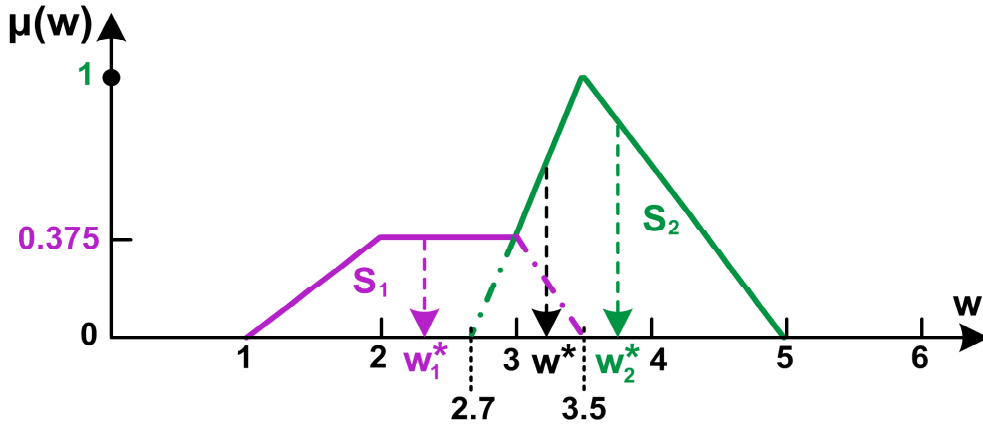


Figure 2.8: A numerical example for defuzzification process using the *center of sums* method.

Based on (2.10)-(2.12), we perform steps of the defuzzification process as follows:

- Calculate the individual centroid and acreage (w_1^*, S_1) of the first fuzzy set in Figure 2.8.

$$w_1^* = \frac{1}{3} \left[p_a + p_b + p_c + p_d - \frac{p_c p_d - p_a p_b}{(p_c + p_d) - (p_a + p_b)} \right] = \frac{1}{3} \left[1 + 2 + 3 + 3.5 - \frac{(3 \times 3.5) - (1 \times 2)}{(3 + 3.5) - (1 + 2)} \right] = 2.3571$$

$$S_1 = 0.5 \times 0.375 \times [(3.5 - 1) + (3 - 2)] = 0.6563$$

- Compute the individual centroid and acreage (w_2^*, S_2) of the second fuzzy set in Figure 2.8.

$$w_2^* = \frac{p_a + p_b + p_d}{3} = \frac{2.7 + 3.5 + 5}{3} = 3.7333$$

$$S_2 = 0.5 \times 1 \times (5 - 2.7) = 1.15$$

- Finally, use (2.10) to determine the output value (w^*) of the defuzzification process.

$$w^* = \frac{(w_1^* \cdot S_1) + (w_2^* \cdot S_2)}{S_1 + S_2} = \frac{(2.3571 \times 0.6563) + (3.7333 \times 1.15)}{0.6563 + 1.15} = 3.2333$$

With the same conditions of fuzzy sets, as compared with the result using the *centroid* method in *Example 2.5* ($w^* = 3.2484$), the result using the *center of sums* method in *Example 2.6* ($w^* = 3.2333$) is nearly equivalent.

- *Weighted Average method* (CoM: *Center of Maximum*): is a variant of the *centroid* method in which the integral formula is now replaced by the sigma formula in order to simplify the calculation. This method is normally used for the symmetric fuzzy membership functions as shown in Figure 2.9, and is usually applied for small-scale control applications.

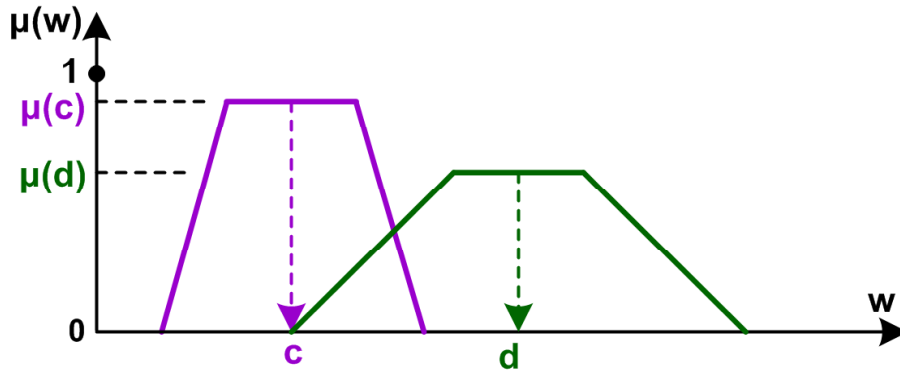


Figure 2.9: *Weighted average method*.

- Where the output fuzzy set in the *singleton* form [23]:

$$w^* = \frac{\sum_{k=1}^N [\mu_k(w) \cdot w_k]}{\sum_{k=1}^N \mu_k(w)} \quad (2.13)$$

- Where the output fuzzy set without the sharp peak, but with symmetrical shape:

$$w^* = \frac{\sum_{k=1}^N [\mu_k(\bar{w}) \cdot \bar{w}_k]}{\sum_{k=1}^N \mu_k(\bar{w})} \quad (2.14)$$

For example, according to (2.14), where the membership function is shown in Figure 2.9, we have the output result using the *weighted average* method for defuzzification as follows:

$$w^* = \frac{[\mu(c).c] + [\mu(d).d]}{\mu(c) + \mu(d)} \quad (2.15)$$

- *Average of Maxima method (MoM)*:

$$w^* = \frac{\sum_{k=1}^N \bar{w}_k}{N} \quad (2.16)$$

For example, according to (2.16), where the membership function is shown in Figure 2.9, we have the output result using the *average of maxima* method for defuzzification as follows:

$$w^* = \frac{c + d}{2} \quad (2.17)$$

- *Center of Largest Area method*: is based on the *weighted average* method, but it only uses the largest area of the fuzzy set to calculate as described in Figure 2.10.

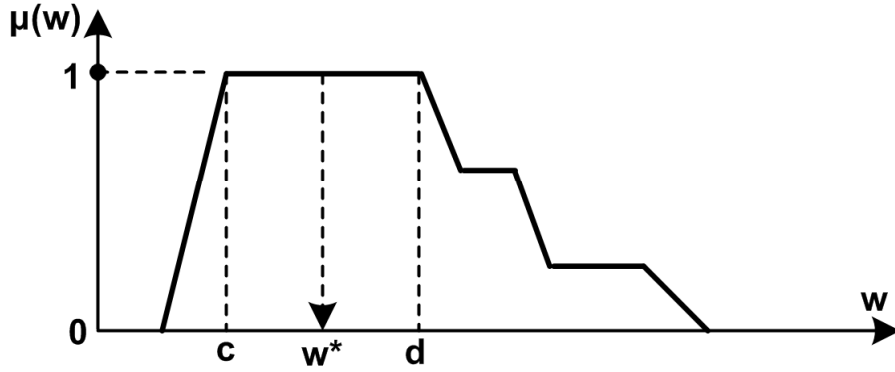


Figure 2.10: *Center of largest area method.*

In fact, the *centroid* (CoA), the *center of sums* (CoS), the *weighted average* (CoM) and the *average of maxima* (MoM) methods are most widely used. Wherein, the *centroid*, or the *center of sums*, or the *weighted average* method gives a result with compromise of all the output fuzzy sets, and is often used in control applications. As compared with the *centroid* method, the *center of sums* method offers a nearly equivalent result in defuzzification, but it is much simpler in computation, especially within cases of the trapezoidal and/or triangular fuzzy sets (as given in *Example 2.6*). So the *center of sums* defuzzification method is often chosen to implement in real applications. While the *average of maxima* method is usually utilized in identification and classification applications.

2.2.3. Structure and design of fuzzy logic controller

2.2.3.1. Structure of fuzzy logic controller

A fuzzy logic controller (FLC) often consists of three main components as follows:

- Fuzzification
- Fuzzy association rules and inference
- Defuzzification

As illustrated in Figure 2.11, the typical design structure of a FLC commonly includes:

- *Input interface*: includes the fuzzification (and other optionally editing modules).
- *Fuzzy inference system*: is the implementation of fuzzy association rules and the fuzzy inference process.
- *Output interface*: includes the defuzzification (and other optional components connected directly to the control object).

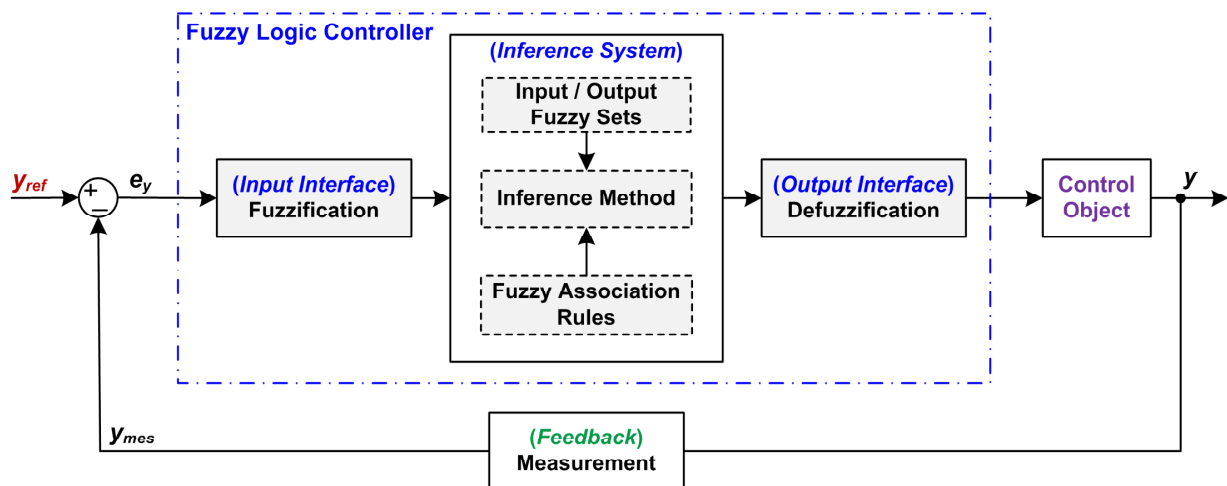


Figure 2.11: The typical design structure of a FLC.

2.2.3.2. Design of fuzzy logic controller

The order usually used to design a FLC is listed as follows:

- Step 1: Define all the input and output linguistic variables.
- Step 2: (Fuzzification) Determine the fuzzy set for each the input/output linguistic variable, including:
 - + The physical value ranges of the linguistic variables,
 - + The number of the input and output fuzzy sets,
 - + The membership functions of the input and output fuzzy sets,
 - + Discretize the input and output fuzzy sets.
- Step 3: Develop the fuzzy association rules.

- Step 4: Select the composition operation (such as: *Max-Min* operation, *Max-Product* operation, so forth) and the inference model (such as: the Madami system, Sugeno model, Tsukamoto model) for fuzzy association rules.
- Step 5: Defuzzification, and then optimizing the four previous steps (if necessary) to achieve the best possible control result.

Besides, a basic sample program in C language of mine to implement a 25-rule FLC (proposed in this thesis) with microcontroller will be presented for reference in subsection 3.7.1 of Chapter 3.

2.2.4. Some notes about fuzzy logic control

Although fuzzy logic has been developed much and applied very broadly, but until now, there are not any standard general guidelines for the design of a FLC; and we also cannot examine in detail the stability, robustness and quality of a designed FLC based on theoretical principles. In fact, the design of a FLC is heavily dependent on knowledge and experiences of the expert on each particular object wanted to control. Besides, the most popular technique used to develop and tune a FLC is the ‘trial-error and then revise’ process. The quality and stability of the designed FLC are evaluated mainly according to the results obtained in simulations and/or experiments.

According to [25],[27], based on linguistic variables, fuzzy logic can encode fairly easily the expert knowledge on controlled object, and the behavior of a fuzzy logic controller is interpretable and explainable (as the ‘gray box’). However, it often takes pretty much time to choose and fine-tune manually the optimal fuzzy membership functions and association rules for linguistic variables, especially in complicated large-scale systems. Besides, because an ordinary fuzzy system does not integrate any self-learning or self-tuning mechanism; hence, additional changes (adding, removing, adjusting) for membership functions and rules need to be performed manually by the designer.

Moreover, applications of ordinary fuzzy logic systems are often limited within the relatively little number of input variables, where the related knowledge and experiences on controlled object can be obtained and applied appropriately. For example, most of the introduced fuzzy logic controllers for PV energy systems in typical applications are usually designed with only two or three input variables. Meanwhile, in the case with very complicated large-scale object, characteristics of the object are often dependent on a lot of different parametric variables; thus, the fuzzy logic controller must be designed with many input variables and accompanied membership functions to ensure generate the appropriate control signal. Nonetheless, this obviously boosts significantly complexity and computation time, which leads to reduce quality of the designed FLC.

Therefore, in controlling the complex and nonlinear objects, fuzzy logic is usually combined suitably with conventional control methods, that have relevance and are normally applied to the objects, in order to design the hybrid controllers which have the much better performance and also ensure the stability. On the other hand, in some special real-time applications, fuzzy system also can be equipped with an additional adaptive algorithm for adjusting automatically its parameters (membership functions, association rules) to achieve the best control efficacy under the complexity of object and/or large changes of load.

2.2.5. Discussion about the combination of fuzzy logic and artificial neural network

Referring in [27], artificial neural networks based on mathematical models, which simulate the brain system of human, can perform the parallel computation and processing. Artificial neural systems are developed and trained by the numerical database obtained from real objects to do tasks as controller, system modeling, predictor, estimator and pattern recognizer. Neural networks have the learning algorithms (such as back-propagation algorithm) for tuning automatically the weights used in their structure layers to maximize their performance fitting to the optimal benefit functions chosen beforehand. Normally, with more real data used for training and layers in structure, the behavior of neural network becomes really better. Moreover, neural networks have other helpful functions as adaptation capacity in varying operation conditions and generalization capacity. Thus, neural networks are especially useful to apply for complicated large-scale systems, which are heavily affected by many input parametric variables and are pretty difficult to perform with the heuristics control methods such as fuzzy logic. In fact, similarly with fuzzy logic control, artificial neural network has been pretty broadly applying in PV solar systems as another possibility [28].

However, the learning process in neural network often takes a fairly much time to complete the desired optimization. Furthermore, the learning process is affected by the quantity of data collected from real objects and the initial parameters chosen randomly in the beginning. A neural network, which uses many layers and neurons in design structure, usually has a better performance, but it has the longer training time and the more complexity in real-time implementation. Besides, it is difficult and non-transparent to analyze the training process in neural networks. So neural network can be considered according to the ‘black box’ technique. Detailed comparisons in theoretical mechanism between fuzzy logic system and artificial neural network can be found in [27]-[29].

Motivated by the observations as shown in this subsection and the previous subsection 2.2.4, neural network and fuzzy logic have been combined together to develop the hybrid control system, which can inherit the prominent advantages of both and can reduce their individual drawbacks. The

hybrid control system can be called as neural-fuzzy or neuro-fuzzy system [29],[30]. Wherein, the neural network is often utilized to perform major functions as follows:

- To fine-tune automatically the membership functions of the fuzzy logic controller.
- Additionally, to generate and optimize the fuzzy association rules from realistic numerical data of the controlled objects.
- The above adjustments of neural network for parameters (membership functions, rules) of the fuzzy logic controller can be performed in offline or in real-time online.

Typical applications in complicated large-scale energy systems of neuron-fuzzy control are: maximum power point tracking in PV solar and wind hybrid systems in varying weather conditions [31], forecasting electricity demands and optimizing economic benefits in energy markets [32], predicting and managing flows of active and reactive powers in the electric grid to help regulate grid frequency and voltage [33], analyzing the transient stability of three-phase power grid in cases of short circuit faults and unbalanced grid voltages [34]. In general, the neuron-fuzzy system is chosen to utilize only for specific objects, which are very complicated, include many uncertainty parameters, and cannot be controlled well by the ordinary fuzzy logic system or neural network.

2.3. Brief introduction of using Fuzzy Logic Toolbox in MATLAB

To design and implement a FLC in MATLAB, the Fuzzy Logic Toolbox package [35] needs to be installed in advance. After the installment is completed, the Fuzzy Logic Toolbox will be available in the Simulink library. In this section, the design of a FLC is shown graphically according to the step-by-step process with figures. In detail:

- **Step 1:** Open the Fuzzy Inference System (FIS) Editor interface in MATLAB

In the workspace of MATLAB, write the command `>> fuzzy` to call the FIS Editor interface. Then, the interface of FIS Editor will be opened as shown in Figure 2.12.

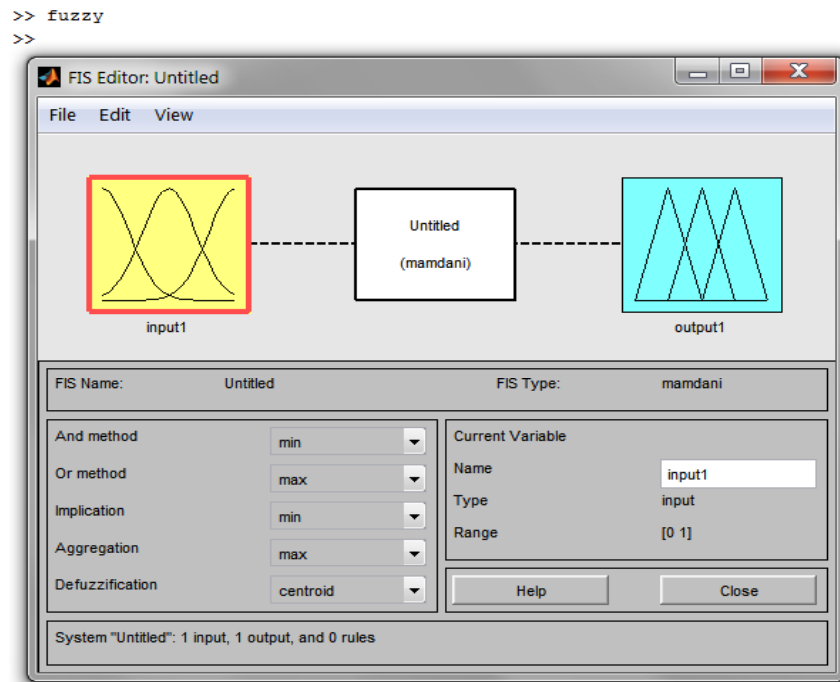


Figure 2.12: The interface of FIS Editor in MATLAB [35].

- **Step 2:** Design the inputs and outputs of FLC and membership functions

To choose the number of inputs and outputs of FLC, on the interface of FIS Editor, click the menu *Edit/ Add Variable... / Input* (or *Output*). For example, in the left part of Figure 2.13, the FLC is designed with two inputs and one output.

To design the linguistic variables, value ranges and membership functions for the inputs and output, click the corresponding icon of the input/output (or click the menu *Edit/ Membership Functions...(Ctrl+2)*), then the interface of Membership Function Editor will be opened as illustrated in the right part of Figure 2.13.

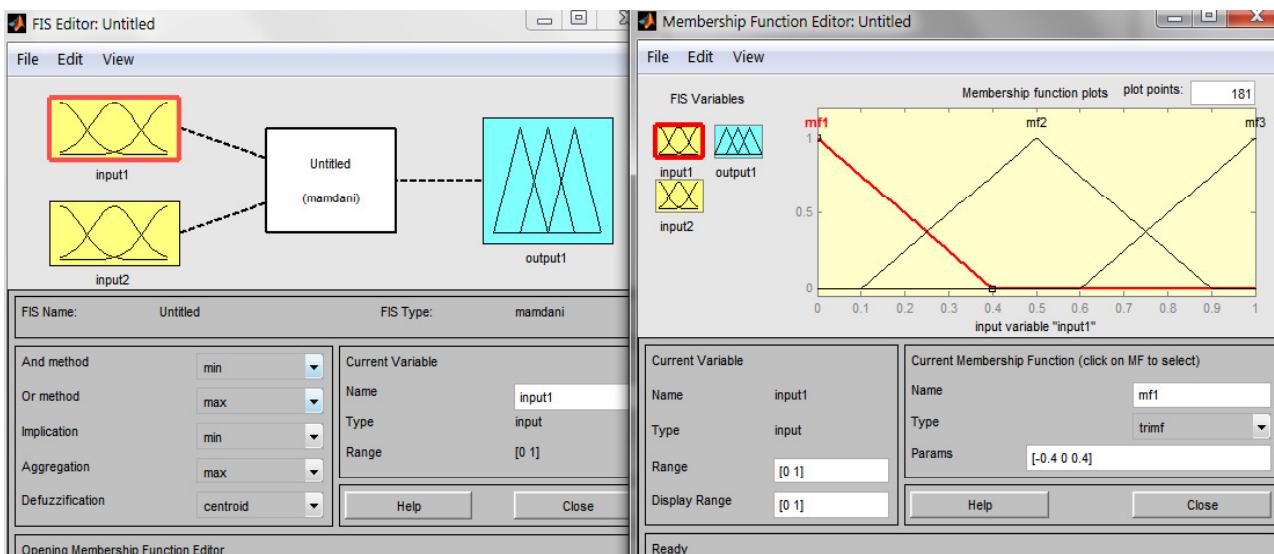


Figure 2.13: The design interface for input and output variables of a FLC with FIS Editor.

To add or remove the membership functions, click the menu *Edit/ Add MFs...* (or *Remove Selected MF*)

- **Step 3:** Design the fuzzy association rules

To develop the fuzzy association rules, in the interface of Membership Function Editor, click the menu *Edit/ Rules...* as described in the left part of Figure 2.14, then the interface of Rule Editor will be opened as presented in the right part of Figure 2.14. On this interface, use the three buttons “Delete rule”, “Add rule” and “Change rule” to delete, add and change the selected association rule, respectively.

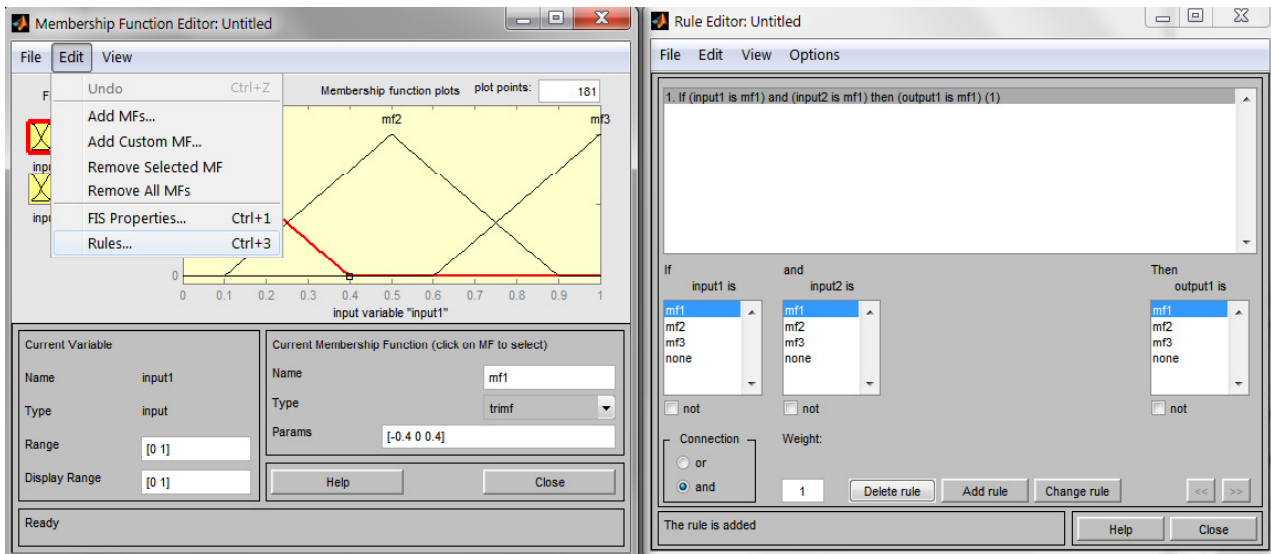


Figure 2.14: The design interface for fuzzy association rules of a FLC with FIS Editor in MATLAB.

- **Step 4:** Choose the inference method and defuzzification method.

With the interface of FIS Editor as shown in Figure 2.12, we can define the inference method such as *Max-Min* operation, and the defuzzification method such as *centroid*.

For example, Figure 2.15 illustrates a completely designed FLC to use in Chapter 5 of this thesis. Wherein, the FLC has two inputs such as $Ef(k)$ and $d-Ef(k)$ and one output $d-Beta(k)$ as given in the left part of Figure 2.15. Besides, the inference and defuzzification methods are chosen as the *Max-Min* operation and *centroid*, respectively. The right part of this figure shows the detailed membership functions of the first input $Ef(k)$.

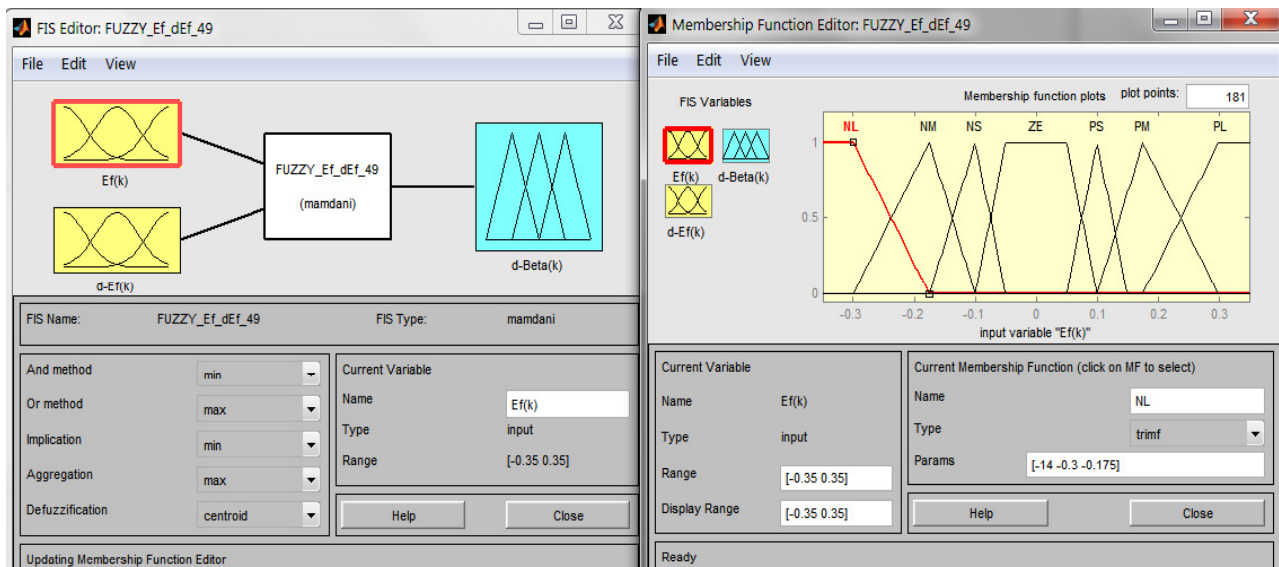


Figure 2.15: An detailed example about input, output variables and membership functions of the 49-rule FLC in FIS Editor.

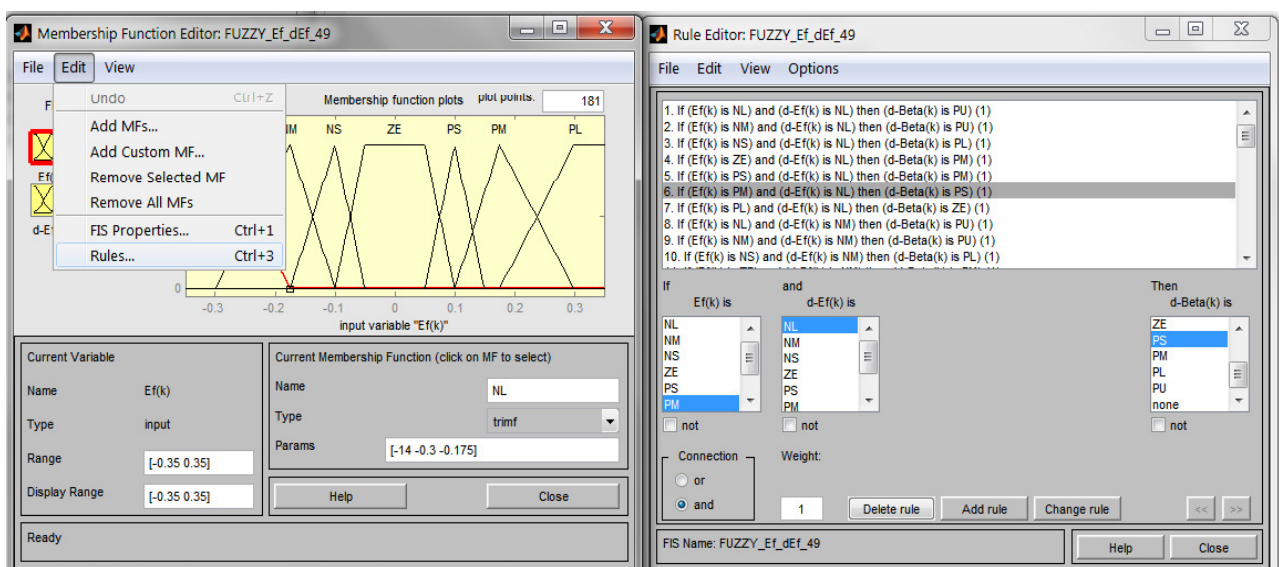


Figure 2.16: An detailed example about fuzzy association rules of the 49-rule FLC in FIS Editor.

On the other hand, the left part of Figure 2.16 shows how to open the interface of Rule Editor from the interface of Membership Function Editor; and the right part of Figure 2.16 illustrates the 49 association rules of the designed FLC.

- **Step 5:** Export the designed FLC to a file for saving or to workspace for using in simulation.

To export the designed FLC to a file, in the interface of FIS Editor, click the menu *File/Export/ To File...(Ctrl+S)* for save. For example, with the designed 49-rule FLC in Figure 2.15 and the lower part of Figure 2.17, it is saved with the name *FUZZY_Ef_dEf_49.fis*. This name of the designed FLC will be linked for using in the Simulink model.

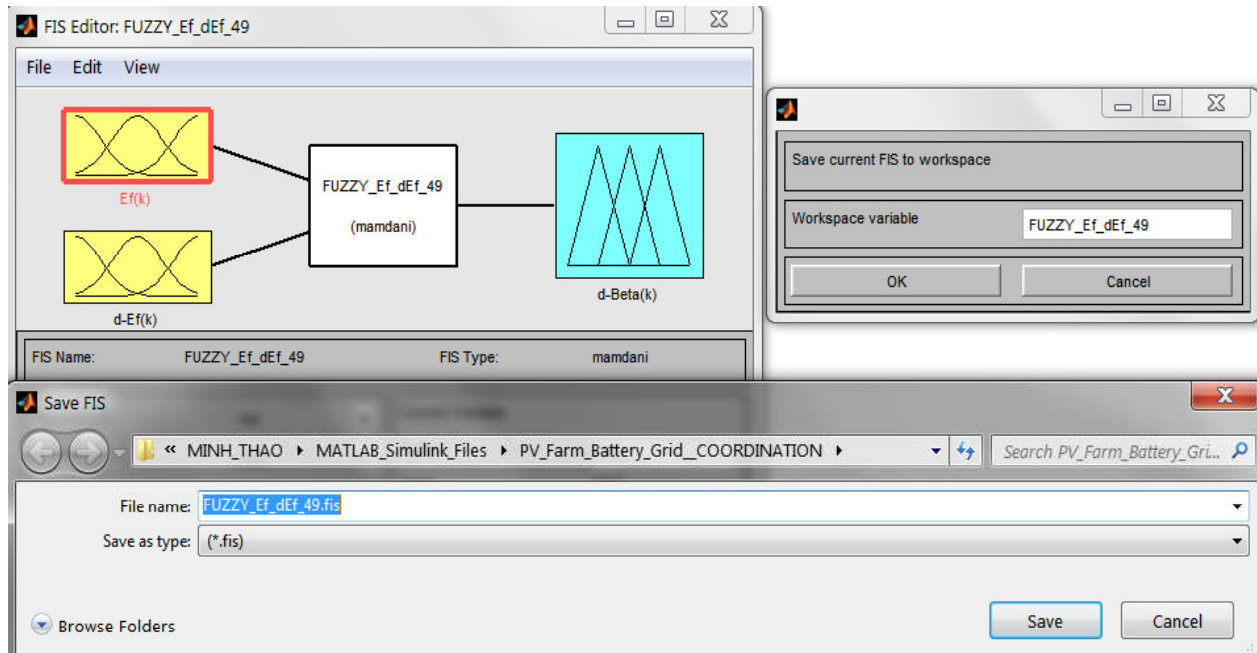


Figure 2.17: The way to export the designed FLC into a file for save and then export it to workspace of MATLAB.

Then, to export the design FLC to workspace of MATLAB, click the menu *File/ Export/ To Workspace...(Ctrl+T)*. For example, with the designed 49-rule FLC in Figure 2.15 and the upper right part of Figure 2.17, after exporting to workspace, there will be a new variable named *FUZZY_Ef_dEf_49* in the workspace of MATLAB.

- **Step 6:** Design the block of FLC in a Simulink model

Firstly, as shown in the upper-left part of Figure 2.18, from the interface of Simulink Library Browser, click the icon of Fuzzy Logic Toolbox; and then choose and bring the block Fuzzy Logic Controller into the simulation model as described in the middle part of Figure 2.18. In the next step, double-click the block Fuzzy Logic Controller in the simulation model, and then on the interface of Function Block Parameters as shown in the lower-right part of Figure 2.18, fill the name of the designed FLC in the parameter box labeled as “FIS file or structure:”; for example, to use the 49-rule FLC already designed in Figure 2.15 and 2.16, fill the name *FUZZY_Ef_dEf_49* in this parameter box. Finally, click the button “Apply” on the interface of Function Block Parameters to finish.

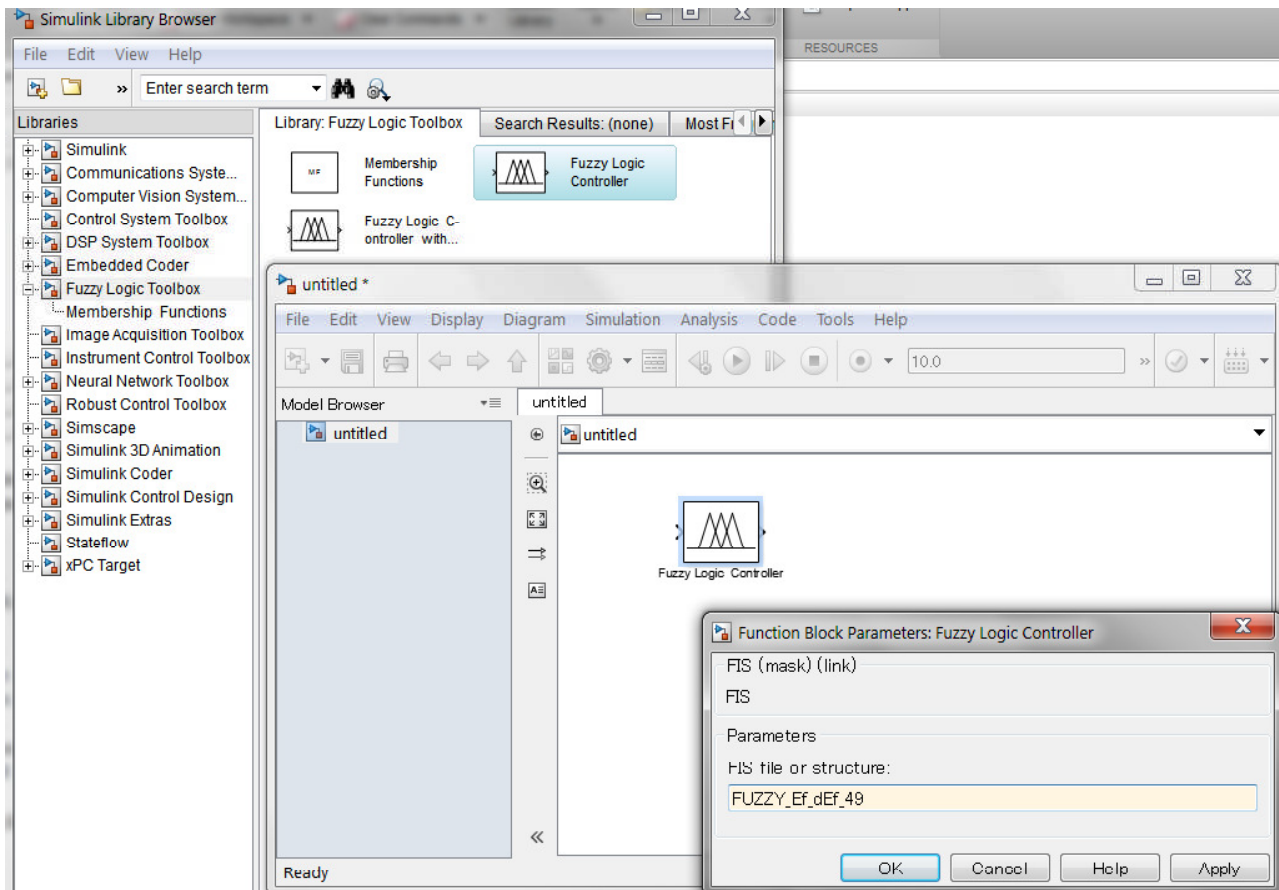


Figure 2.18: Implementation of a FLC model in MATLAB/Simulink with Fuzzy Logic Toolbox.

Chapter 3

Enhanced Fuzzy-based Incremental Conductance - Maximum Power Point Tracking Algorithm

This chapter is the first key study part of the thesis, which presents an enhanced INC-MPPT algorithm based on fuzzy logic for solar systems to obtain optimally the DC power from PV arrays in varying weather conditions.

3.1. Introduction of chapter

Referring in [12]-[13], in a PV system, to obtain the power from PV panels efficiently, two key factors should be examined thoroughly. Namely, the first one is impacts of the weather parameters. Another is effects of power-electronic converters, controllers and loads utilized in the designed PV system. Obviously, the weather condition is out of the user's control. Thus, the converters in use must be controlled effectively to maximize the output power. According to [12], there are many MPPT algorithms have been introduced with varying the complexity, response speed, accuracy, adaptability, and cost.

Wherein, Perturb and Observe (P&O) is known as the most popular algorithm used in commercial products [2],[12]. In detail, they use the slope value of the power-voltage (P-V) curve, $(\Delta P_p / \Delta V_p)$, to track the MPP. However, they make large fluctuations around the MPP, and fail to determine the new MPP of the PV panel when weather parameters drastically change [2]. Another common MPPT method is the Fractional Open-Circuit Voltage. This algorithm assigns the ratio of the optimal voltage V_{MPP} to the open-circuit voltage V_{OC} as a constant K_{MPP} , ($V_{MPP} = K_{MPP} \times V_{OC}$; Figure 3.6). Referring in [12], the constant K_{MPP} often has value in the interval (0.71 0.78). Nevertheless, it is too difficult to choose exactly the optimal value for K_{MPP} , since characteristics of PV panel are highly nonlinear and affected by changes of weather parameters.

According to [3],[12] and Figure 3.6, the INC-MPPT algorithm uses the ratio-value between the slope value of P-V curve and the PV panel's voltage, $C_p = (\Delta P_p / \Delta V_p) / V_p = I_p / V_p + \Delta I_p / \Delta V_p$, to seek the MPP. In detail, the ratio-value is zero at the MPP, negative on the right side and positive on the left side of the MPP. The INC-MPPT algorithm also is widely used owing to its high accuracy in tracing the MPP. Furthermore, this method is relatively simple and pretty easy to implement in experiments. However, in the technique, the step-size $\Delta V(k)$ is a fixed value; and is often adjusted to being small enough to capture the MPP accurately and reduce the oscillation

around the MPP. Thus, the response time of this method is relatively long, especially when the weather condition changes suddenly.

To overcome the listed major disadvantage and elevate the effectiveness of the conventional INC-MPPT method, many techniques have been introduced in [2]-[4],[12]-[15],[36]-[43]. The main purpose of those improved INC-MPPT algorithms is to make the step-size be variable. In [3], the step-size is changed adaptively according to the absolute value of the slope of P-V curve $|\Delta P_p / \Delta V_p|$. In detail, the step-size will be tiny when $|\Delta P_p / \Delta V_p|$ becomes very small to avoid oscillating around the MPP. Hence, this method has a good steady-state response. Nevertheless, when the solar radiation drastically varies, $|\Delta P_p / \Delta V_p|$ becomes huge, and this will cause the step-size to be very large in a short transient-time [36]. Therefore, dynamic characteristics of the PV system in use may be not stable in this condition. Authors in [36] presented a modified variable step-size INC-MPPT algorithm based on the current-mode control. This method improves the response speed in seeking the MPP and reduces steady-state fluctuations. Its efficacy is highly dependent on characteristics of the proposed threshold function $C = P_p^n \times |\Delta P_p / \Delta V_p|$, where n is a manually chosen index.

On the other hand, the FLC has been proposed to the performances of the conventional MPPT methods [2],[14],[15],[36]-[43]. According to [12],[37], in most of the existing fuzzy-based INC-MPPT techniques, the ratio-value $C_p = (I_p / V_p + \Delta I_p / \Delta V_p)$ and its change ΔC_p are used to search the MPP. However, in those methods, because the change of the step-size is fully disregarded, the operating point of PV array may move away far from the MPP when the weather condition varies abruptly. In addition, the authors in [15] presented a FLC in which the change of power $\Delta P_p(k)$ and the PV array voltage variation $\Delta U(k)$ are two inputs; and the FLC's output is the new voltage variation $\Delta U(k + 1)$. This algorithm ameliorates the response time in reaching the MPP under variations of the solar radiation and temperature. Nevertheless, the performance of the method has not yet been examined with experimental PV systems. Besides, a self-organizing FLC for MPPT based on the Look-up-Table method, is described in [38]. The response of the method is pretty good, but is affected by the technique utilized to set and update values in the reference tables. Referring in [39], fuzzy cognitive networks are supplemented to elevate the speed in seeking the MPP. The response speed of this algorithm is faster than the ordinary fuzzy-based MPPT. The technique needs a specialized sensor to calculate the short-circuit current of PV panels.

In this research, an ameliorated INC-MPPT algorithm based on fuzzy logic for stand-alone PV systems is proposed. Therein, a novel FLC is designed to boost the effectiveness of the conventional INC-MPPT, especially in improving the response speed and reducing fluctuations around the MPP. In detail, from the absolute value of a modified ratio-value and the previous

step-size $\Delta V(k-1)$, the proposed FLC, comprising 25 fuzzy rules, adjusts suitably the step-size $\Delta V(k)$ to determine speedily and exactly the optimal voltage V_{MPP} (see Figures 3.7 and 3.8). Simulation and experimental results, including the consideration on impacts of the weather parameters, are shown to assess the effectiveness of the suggested algorithm. The content in this chapter is developed from my 1st published journal paper in List of Research Achievements at page 138 with newly added modifications, explanations and reviews in the subsections 3.1, 3.3, 3.6, 3.7 and 3.8.

The remainder of this chapter is organized as follows. Section 3.2 shows the description of demonstrative PV system. Design steps of the proposed fuzzy-based algorithm are presented in the next section. Simulation results of the closed-loop control system are illustrated in Section 3.4. This section also describes comparisons between the suggested algorithm, the conventional INC-MPPT in [12] and the conventional fuzzy-based INC-MPPT in [37]. Section 3.5 shows efficacy of the proposed method in experiments. Besides, detailed discussions about effects of partially shaded condition and related solutions are presented in Section 3.6. After that, Section 3.7 illustrates the evaluation of program capacity and computation time in implementing FLCs with microcontroller. Lastly, the conclusion of this chapter is given in Section 3.8.

3.2. Demonstrative PV system

3.2.1. Demonstrative PV system description

Referring in [2]-[4],[12]-[15],[36]-[43], many different kinds of DC-DC converter have been utilized in PV systems. In this study, the non-inverting buck-boost converter introduced in [44] is used for the demonstrative PV system.

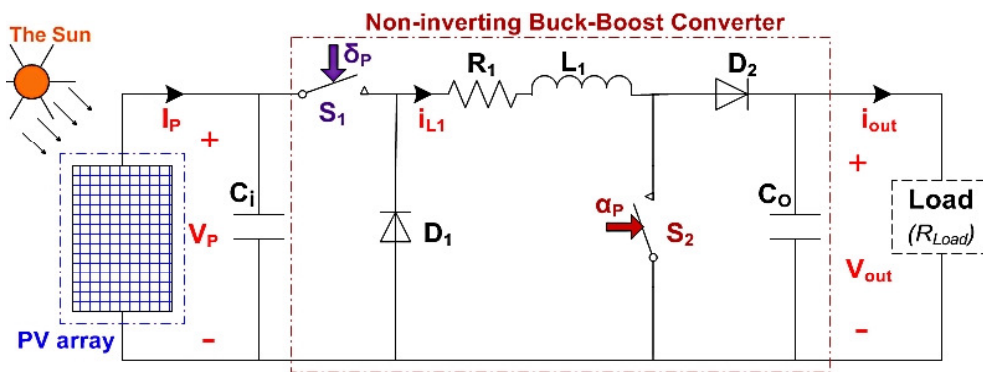


Figure 3.1: The demonstrative PV system used in this study.

As seen in Figure 3.1, the illustrative PV system consists of the PV array with a nominal power of 320W, the non-inverting buck-boost converter, and a resistive load. The electric energy is transferred from the PV array to the buck-boost converter, and then supplies for the load. Wherein, switches S_1 and S_2 are activated by the control signals δ_p and α_p respectively.

Table 3.1: Some variables of the demonstrative PV system

Variable	(see Figure 3.1)	Symbol
PV array's voltage		V_p
PV array's current		I_p
Input binary control signals of the non-inverting buck-boost converter		δ_p and α_p $\{0, 1\}$

According to [44]-[46], main advantages of the buck-boost converter in Figure 3.1 are: it has the non-inverting output and can be driven to operate in three different modes. In detail,

- *Buck-Boost* mode: In this case, the switches S_1 and S_2 are synchronously activated as follows:

$$\delta_p = \alpha_p = \begin{cases} 0 & ; S_1 \text{ and } S_2 \text{ are OFF} \\ 1 & ; S_1 \text{ and } S_2 \text{ are ON} \end{cases}$$

- *Buck* mode: The switch S_2 is always OFF ($\alpha_p = 0$); meanwhile, S_1 is activated by δ_p as follows:

$$\delta_p = \begin{cases} 0 & ; S_1 \text{ is OFF} \\ 1 & ; S_1 \text{ is ON} \end{cases}$$

- *Boost* mode: The switch S_1 is always ON ($\delta_p = 1$); meanwhile, S_2 is activated by α_p as follows:

$$\alpha_p = \begin{cases} 0 & ; S_2 \text{ is OFF} \\ 1 & ; S_2 \text{ is ON} \end{cases}$$

3.2.2. PV panel model

According to [47],[2],[36] where the number of cells in parallel of the PV panel in use is $N_p = 1$, the one-diode equivalent circuit of the PV panel now is shown in Figure 3.2 and (3.1), respectively.

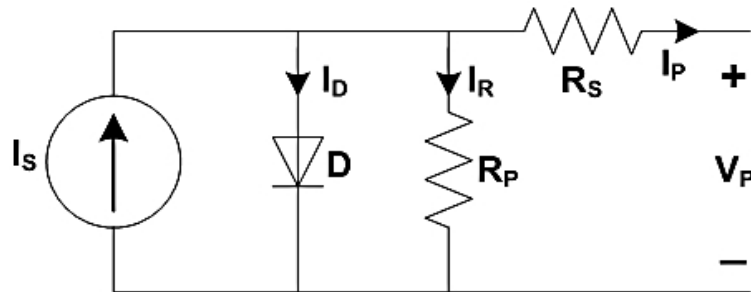


Figure 3.2: The equivalent circuit for a PV panel.

$$I_p = I_s - I_o \left[\exp \left\{ \frac{q(V_p + R_s I_p)}{N_s a k T_{cell}} \right\} - 1 \right] - \left(\frac{V_p + R_s I_p}{R_p} \right) \quad (3.1)$$

$$I_s(T_{cell}, G_{so}) = \left[I_{sc,n} + k_T(T_{cell} - T_n) \right] \frac{G_{so}}{G_n} \quad (3.2)$$

$$I_o(T_{cell}) = \left[\frac{I_{sc,n}}{\exp \left\{ \frac{q V_{OC,n}}{N_s a k T_{cell}} \right\} - 1} \right] \left(\frac{T_{cell}}{T_n} \right)^3 \exp \left\{ \frac{q E_g}{a k} \left(\frac{1}{T_n} - \frac{1}{T_{cell}} \right) \right\} \quad (3.3)$$

I_s is the photoelectric current related to the solar radiation; I_o is the saturation diode current; q is the electric charge, 1.602×10^{-19} (C); k is the Boltzmann's constant, 1.381×10^{-23} (J/K); a is the diode ideality constant and its value is in the interval [1 2], 1.6; E_g is the energy gap of the material used to make the solar cell, 1.12 (eV); k_T is the temperature coefficient, 0.075 (%/K); N_s and N_p are the number of PV cells in series and parallel respectively in the PV panel; G_{so} and $G_n = 1000$ (W/m²), are the solar irradiance at the operating condition and standard condition, respectively; T_{cell} and $T_n = 298$ (K), are the absolute temperatures (in Kelvin degree) of the PV cell at the operating condition and the standard condition, respectively; $I_{sc,n}$ and $V_{OC,n}$ are the short-circuit current and the open-circuit voltage of the PV panel at the standard condition, respectively.

In this study, the *BP-380J* 80W PV panel in [48] is used. In detail, Table 3.2 shows its characteristics at the standard test condition, where $G_{so} = G_n = 1000$ (W/m²), $T_{cell} = T_n = 298$ (K) = 25 (°C). Effects of solar irradiance and temperature to the PV panel are represented in Figures 3.3 and 3.4, respectively. As shown in Table 3.3, the PV array in Figure 3.1 comprises two parallel branches with two the *BP-380J* PV panels in series in each branch.

Table 3.2: The manufacturing characteristics of the *BP-380J* PV panel

Parameter	Symbol	Value
Maximum (peak) output power	P_p^{\max}	80 W
Voltage at the MPP	V_{MPP}	17.6 V
Current at the MPP	I_{MPP}	4.5 A
Open-circuit voltage	V_{OC}	22.1 V
Short-circuit current	I_{SC}	4.8 A
Number of PV cells in series	N_s	36
Number of PV cells in parallel	N_p	1

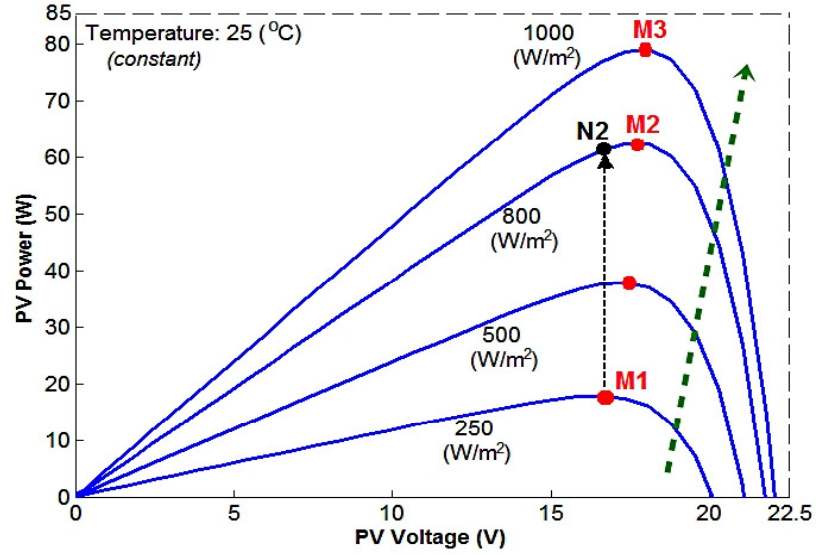


Figure 3.3: Effect of solar radiation changes to *BP-380J* PV panel.

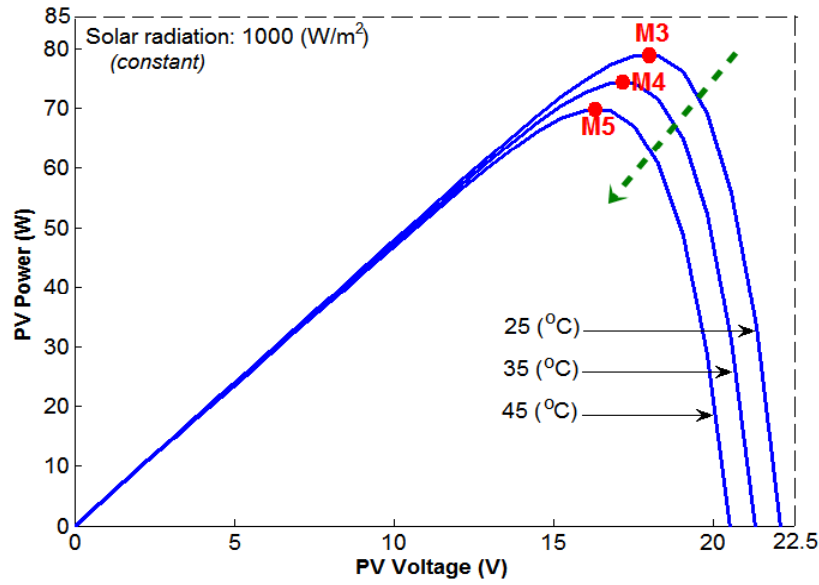


Figure 3.4: Impact of temperature variations to *BP-380J* PV panel.

Table 3.3: Values of six MPPs shown in Figure 3 and Figure 4.

a PV panel	M1	M2	M3	M4	M5
$V_{P,panel}$ (V)	16.49	17.46	17.65	16.94	16.1
$P_{P,panel}$ (W)	18.28	63.3	80	75.3	70.85
PV array	M1	M2	M3	M4	M5
V_P (V)	32.98	34.92	35.3	33.88	32.2
P_P (W)	73.12	253.2	320	301.2	283.4

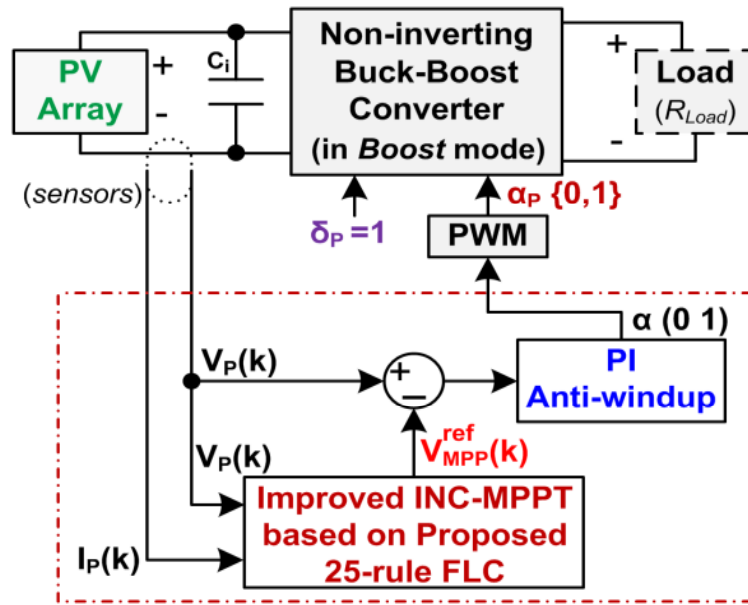
3.3. Proposed Fuzzy-based INC-MPPT algorithm

The key goal of the designed PV system is to obtain optimally electric energy from the PV array in varying weather conditions. Scheme of the proposed INC-MPPT is expressed in Figure 3.5.

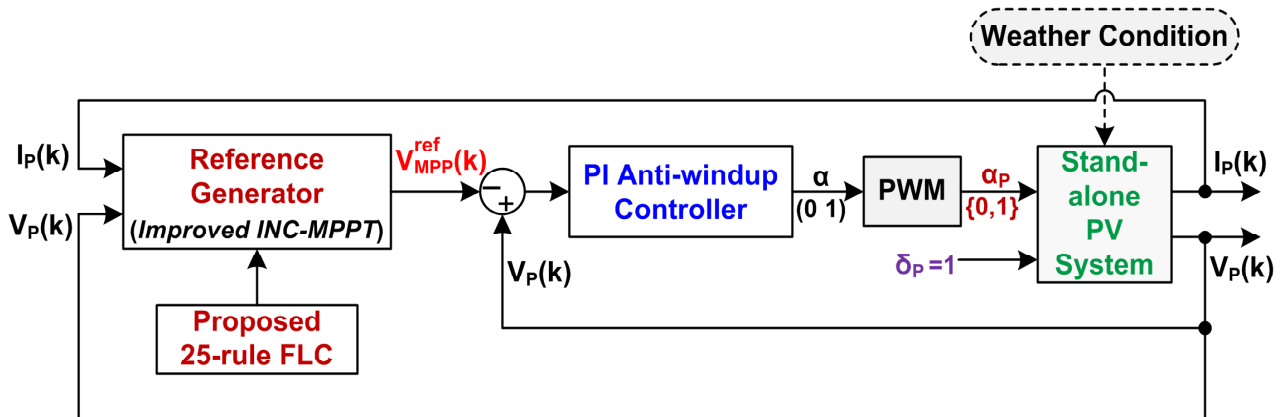
As shown in Figure 3.5(a), the proposed algorithm consists of two major sub-controllers as follows:

- The first is an ameliorated INC-MPPT method based on a novel FLC, which function is as a reference generator. From the PV array's voltage and current, it calculates the reference voltage $V_{MPP}^{ref}(k)$, where the PV array operates at the MPP (see Figure 3.6). It is noted that the proposed FLC in this sub-controller is the most important part of the suggested algorithm.
- Another is a PI controller, including an anti-windup block. It controls the converter to ensure that the PV array's voltage $V_p(k)$ must be closely equal to $V_{MPP}^{ref}(k)$, computed beforehand by the first sub-controller, which is called the reference generator as illustrated in Figure 3.5(b).

As seen in Figure 3.5(a), the designed buck-boost converter now is controlled to operate in *Boost* mode.



(a) Structure of the proposed fuzzy-based INC-MPPT expressed in design and implementation



(b) The scheme in (a) re-expressed in control-engineering viewpoint

Figure 3.5: The structure of the proposed fuzzy-based INC-MPPT algorithm.

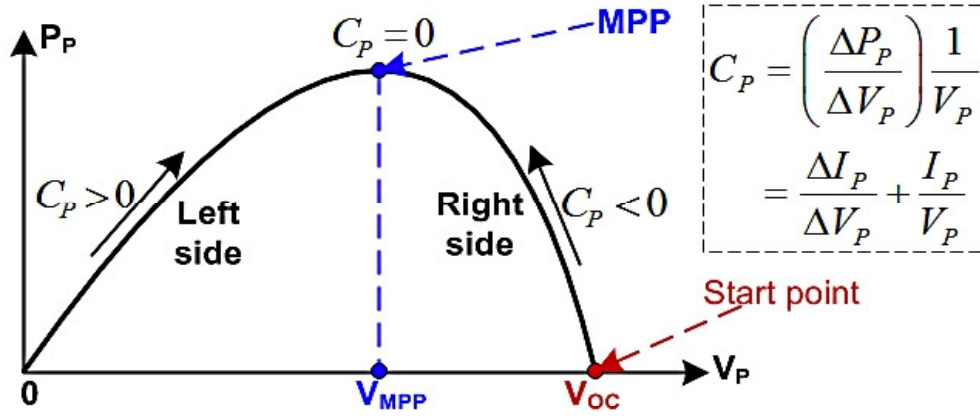


Figure 3.6: The power-voltage (P-V) curve of the PV array.

As illustrated in Figure 3.6, the output power P_p of PV array is computed from the measured voltage and current values of PV array as follows.

$$P_p(k) = V_p(k)I_p(k) \quad (3.4)$$

3.3.1. The first sub-controller

As presented in Figure 3.7, this sub-controller is a modified INC-MPPT method based on fuzzy logic. Wherein, the proposed FLC adjusts appropriately the step-size $\Delta V(k)$ for improving the response time in seeking the MPP and eliminating oscillations around the MPP. As illustrated in Figure 3.8, the FLC is designed with two inputs and one output. In detail, the first input of the FLC is the absolute value of a modified ratio-value $|A_p(k)|$, including a scaling factor f_l , where $A_p(k)$ is expressed in (3.5); or is the absolute value of PV current's change $|\Delta I_p(k)|$, where $\Delta I_p(k)$ is given by (3.7). The other input is the previous value of the step-size $\Delta V(k-1)$. The FLC's output is the additional value $V_{Add}(k)$ utilized to tune adaptively the step-size $\Delta V(k)$. Obviously, the main aim of the suggested FLC is to make the step-size $\Delta V(k)$ to be a variable value, instead of the fixed value in the conventional INC-MPPT method. Figures 3.7 and 3.8 illustrate the detailed flowchart of the proposed algorithm.

$$A_p(k) = f_l C_p(k) = f_l \left[\frac{\Delta I_p(k)}{\Delta V_p(k)} + \frac{I_p(k)}{V_p(k)} \right] \quad (3.5)$$

Where f_l is a positive value, and is utilized to enhance sensitivity of the ratio-value $C_p(k)$. This factor f_l is chosen manually based on characteristics of the designed PV system and tuning process.

$$\Delta V_p(k) = V_p(k) - V_p(k-1) \quad (3.6)$$

$$\Delta I_p(k) = I_p(k) - I_p(k-1) \quad (3.7)$$

As can be seen in Figure 3.7, in the condition “ $\Delta V_p(k) = 0$ and $\Delta I_p(k) \neq 0$ ”, the first FLC’s input is chosen as $|\Delta I_p(k)|$. Let us note that this case is only utilized in a special time-period when the weather parameters change suddenly.

For example, as shown in Figure 3.3, if the solar radiation increases abruptly from 250 W/m^2 to 800 W/m^2 , the operating point of the PV panel will move instantly from the point M1 to the point N2. Meanwhile, the PV panel’s voltage does not change in this transient time-period, and it means that $\Delta V_p(k) = 0$. Furthermore, it is clearly to see that M1 is the MPP where the solar irradiance is 250 W/m^2 , but N2 is not the MPP where the solar radiation is 800 W/m^2 . Therefore, in the moving time-period from the point M1 to the point N2, $|\Delta I_p(k)|$ is chosen as the first input of FLC. Then, when $\Delta V_p(k) \neq 0$, the first FLC’s input is switched to be $|A_p(k)|$ for forcing the operating point from the point N2 to reach the new MPP M2 (see Figures 3.3 and 3.7).

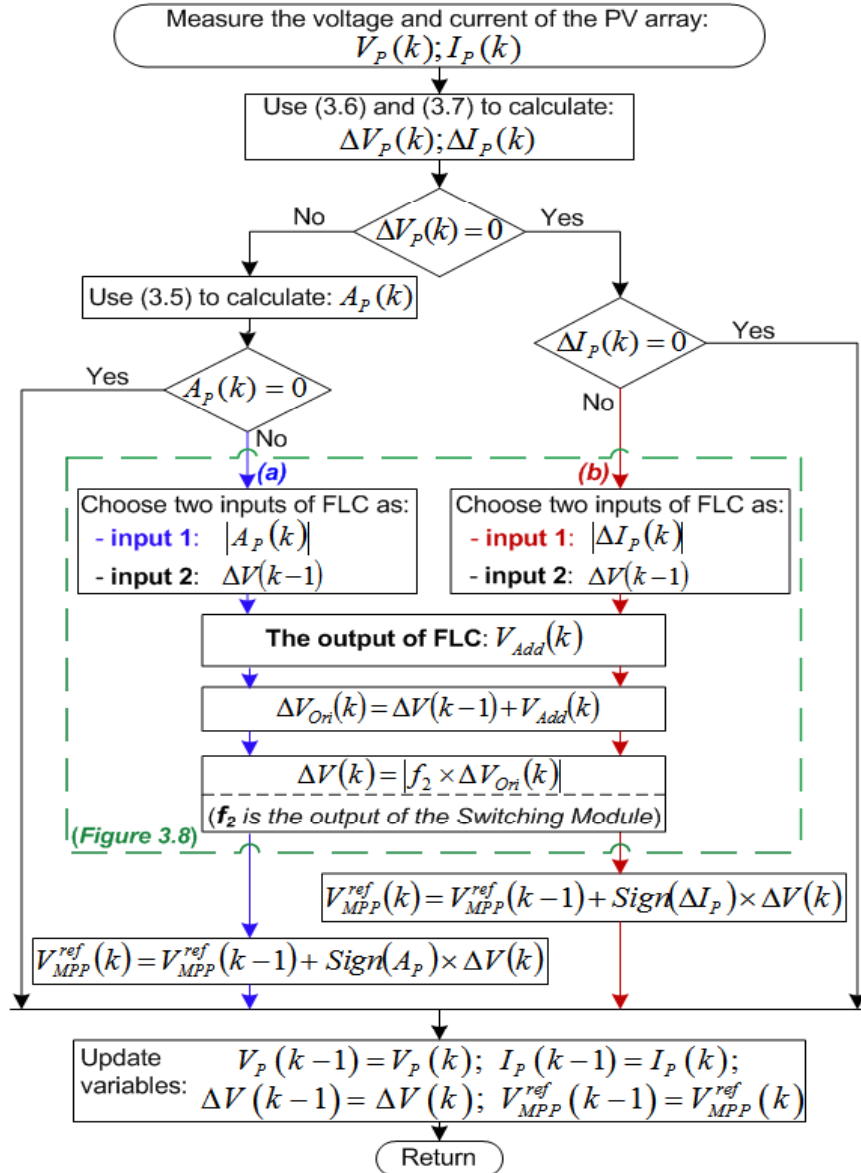


Figure 3.7: The detailed flowchart of the proposed fuzzy-based INC-MPPT algorithm.

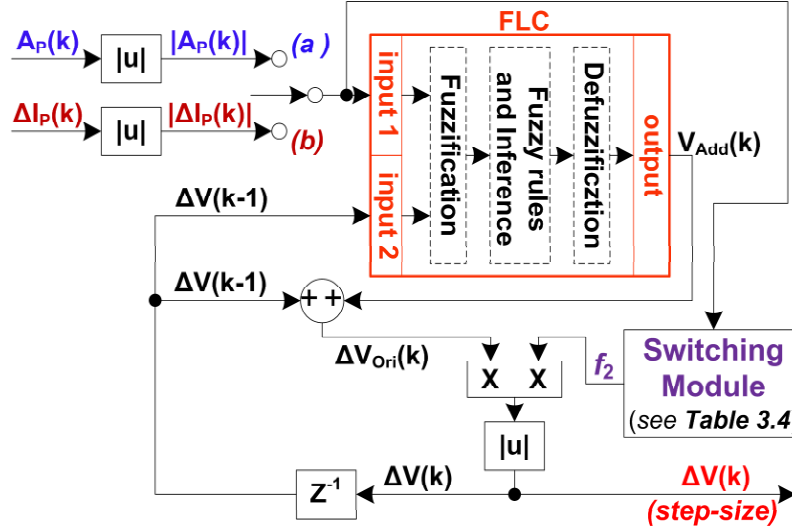


Figure 3.8: The particular scheme of the proposed FLC.

Table 3.4: Operation of the Switching Module in Figure 3.8.

(a) If the input is $ A_P(k) $	$\frac{ A_P(k) }{f_1} \geq 0.05$	$\frac{ A_P(k) }{f_1} < 0.05$
	$f_2 = 1$	$f_2 = 0.34$
(b) If the input is $ \Delta I_P(k) $	$f_2 = 1$ (where every value of $ \Delta I_P(k) $)	

In addition, unexpected big variations of the step-size may cause fluctuations in the PV output power at the steady state. Thus, a switching module is proposed to eliminate this inconvenience thoroughly as shown in Figure 3.8. Based on the value of the input, $|A_P(k)|$ or $|\Delta I_P(k)|$, the suggested module assigns a suitable value for the output scaling factor f_2 . Table 3.4 shows the operation of the switching module. Wherein, the concrete values of f_2 and the threshold value (as 0.05 in this study) can be chosen and fine-tuned manually based on characteristics of the PV system in use to fulfill priori objectives as follows: to boost response speed in tracking the MPP in the transient state, and then to help reduce steady-state oscillations around the MPP.

3.3.1.1. Fuzzification

First of all, as illustrated in Figures 3.7 and 3.8, the k th step-size $\Delta V(k)$ is always a non-negative value due to the absolute value block designed in the output side. As a result, the second input $\Delta V(k-1)$ of the proposed FLC also is non-negative value as the first FLC's input ($|A_P(k)|$ or $|\Delta I_P(k)|$). This really helps not only to simplify the design of fuzzy linguistic variables, membership function for $\Delta V(k-1)$, but also to ensure the proposed INC-MPPT algorithm to operate correctly.

Two inputs: have same five linguistic variables, membership function, and value in interval [0 1].

- $|A_p(k)|$ or $|\Delta I_p(k)| = \{\text{Almost Zero, Small, Medium, Large, Very Large}\}$
 $= \{\text{AZ, SM, ME, LA, VL}\}$
- $\Delta V(k-1) = \{\text{Almost Zero, Small, Medium, Large, Very Large}\}$
 $= \{\text{AZ, SM, ME, LA, VL}\}$

The output: has nine linguistic variables and the value in the interval [-1 1].

$$V_{Add}(k) = \{\text{Negative Large, Negative Medium, Negative Small, Negative Zero, Zero, Positive Zero, Positive Small, Positive Medium, Positive Large}\}$$

$$= \{\text{NL, NM, NS, NZ, ZE, PZ, PS, PM, PL}\}$$

Membership functions:

The membership functions for the two inputs and the output of the FLC are described in Figures 3.9 and 3.10, respectively. Wherein, the shapes of membership functions are adjusted manually by the author with the highest priority as follows: $V_{Add}(k)$ should have the large value in the case where the operating point of PV array is far away the MPP to improve significantly the response time in tracking the MPP, and then $V_{Add}(k)$ must have the very small value in the case where the operating point is close to the MPP to eliminate thoroughly the steady-state fluctuations around the MPP.

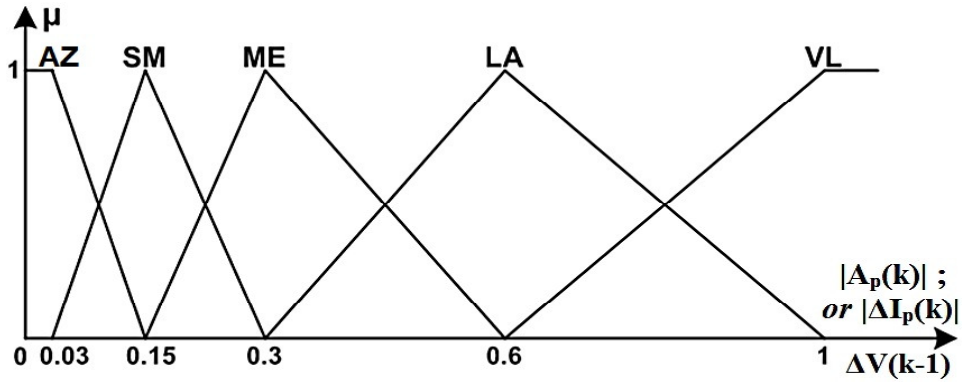


Figure 3.9: The membership function for the two inputs of FLC.

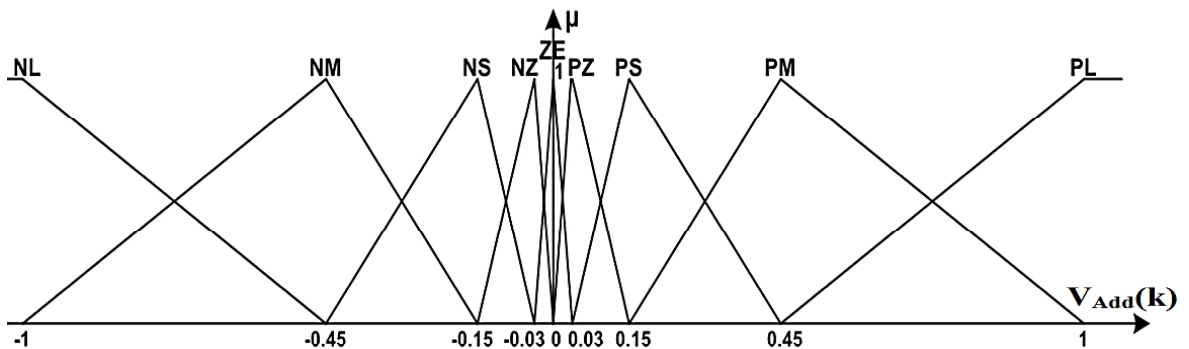


Figure 3.10: The membership function for the output of FLC.

3.3.1.2. Fuzzy association rules

The proposed fuzzy associative matrix is illustrated by Table 3.5. It is represented in the form “**if...then...**”, and totally has $5 \times 5 = 25$ rules. Wherein, a sample fuzzy rule is expressed as follows: “**if** $|A_p(k)|$ is VL and $\Delta V(k-1)$ is SM **then** $V_{Add}(k)$ is PM”.

The design technique for the fuzzy association rules is mainly based on the authors’ knowledge and real experiences in the PV system. Moreover, in this study, the designed association rules and membership functions have been already optimized by the *trial-and-error* method.

Table 3.5: The fuzzy association rules of the proposed FLC.

$V_{Add}(k)$		$ A_P(k) $ or $ \Delta I_P(k) $				
		AZ	SM	ME	LA	VL
$\Delta V(k-1)$	AZ	ZE	PZ _(ZE)	PS	PM	PL
	SM	NZ _(ZE)	ZE	PZ	PS	PM
	ME	NS	NZ	ZE	PZ	PS
	LA	NM	NS	NZ	ZE	PZ
	VL	NL	NM	NS	NZ	ZE

Interpretation for the fuzzy association rules:

According to Figures 3.7 and 3.8, if $\Delta V_p(k) \neq 0$ and $A_p(k) \neq 0$, the first FLC's input is chosen as $|A_p(k)|$, the absolute value of the modified ratio-value. As expressed in Table 3.5 and Figure 3.6, if $|A_p(k)|$ is VL (very large), it can be predicted that the operating point of PV array may be on the left side or the right side of the P-V curve, where is so far away from the top of P-V curve (the MPP). Meanwhile, as shown in Table 3.5, the second FLC’s input $\Delta V(k-1)$, the previous step-size, is a value in five following cases: AZ, SM, ME, LA and VL.

In detail, firstly, if $\Delta V(k-1)$ is AZ (almost zero), it means that the step-size must be summed with a big positive value to force the operating point of PV array to move to the MPP quickly. So the additional value for the step-size, $V_{Add}(k)$, needs to be assigned as PL (positive large). Similarly, if $\Delta V(k-1)$ is SM (small), $V_{Add}(k)$ can be chosen as PM (positive medium) to reach the MPP speedily. Besides, if $\Delta V(k-1)$ is ME (medium), it is easy to see that the step-size should be added a small positive value to achieve the MPP without the steady-state fluctuations. Therefore, $V_{Add}(k)$ should be assigned as PS (positive small). On the other hand, in the two remaining cases, if $\Delta V(k-1)$ is LA (large) or VL (very large), this means that the operating point of PV array has the tendency in

automatically reaching the MPP. Hence, to do not surpass the MPP of PV array into the other side of P-V curve as compared with the currently operating point for eliminating thoroughly fluctuations, $V_{Add}(k)$ must be PZ (positive zero) or ZE (zero), respectively.

In addition, another fuzzy rule case “**if** $|A_p(k)|$ is AZ and $\Delta V(k-1)$ is SM **then** $V_{Add}(k)$ is NZ” now is utilized to examine. Because $|A_p(k)|$ is AZ (almost zero), it can be predicted that the operating point of PV array is likely on the left side or right side surrounding the peak of P-V curve, where is presently very close to the MPP. Meanwhile, the second FLC’s input, the previous step-size $\Delta V(k-1)$ is SM (small); it means that the operating point of PV array has the tendency in not only automatically reaching the MPP, but also then probably surpassing slightly the MPP in the other side on the P-V curve as compared with its current position. Thus, to eliminate thoroughly steady-state fluctuations around the MPP, the additional value $V_{Add}(k)$ should be chosen optimally as NZ (negative zero) to reduce a little moving speed of the operating point to the MPP. The actual value for the linguistic variable NZ is defined as -0.03 as shown in Figure 3.10, and that is tiny enough to fulfill well this objective within the demonstrative PV system used in this study. Besides, in this case, the additional value $V_{Add}(k)$ also could be chosen as ZE (zero) as another pretty suitable selection as illustrated in Table 3.5. Likewise, in the rule case “**if** $|A_p(k)|$ is SM and $\Delta V(k-1)$ is AZ **then** $V_{Add}(k)$ is PZ”, the additional value $V_{Add}(k)$ should be assigned as PZ (positive zero) as an optimal choice, or it could be set as ZE (zero) as another fairly appropriate solution. In general, the similar deductive way can be used to interpret for the other fuzzy rules described in Table 3.5.

On the other hand, if the first FLC's input is defined as $A_p(k)$ or $\Delta I_p(k)$ (instead of $|A_p(k)|$ or $|\Delta I_p(k)|$, respectively), which has ten linguistic variables in both negative and positive values, the fuzzy associative matrix will have $10 \times 5 = 50$ rules. However, this 50-rule FLC has the same control cases (the same control quality) as the suggested 25-rule FLC shown in Table 3.5, where $|A_p(k)|$ or $|\Delta I_p(k)|$ is utilized as the first FLC’s input. Thus, the design technique for the 25-rule FLC helps reduce fifty percent of the quantity of fuzzy association rules (from 50 rules to 25 rules) to elevate the feasibility of the proposed INC-MPPT method. In detail, as will be presented in the subsection 3.7.2 (especially in Table 3.8) of this chapter, the memory volumes and estimated computation time for this 25-rule FLC (also listed in the fourth row of Table 3.8) are acceptable values for implementation into real PV systems, and they are noticeably smaller as compared with the 49-rule FLC listed in the last row of Table 3.8. Additionally, due to consisting of the considerably more number of fuzzy association rules, the control quality of the proposed 25-rule FLC is significantly better as compared with the 9-rule FLC and 15-rule FLC listed in Table 3.8. In summary, the proposed 25-rule FLC is chosen in this chapter because it has very good control quality as a 50-rule controller and its implementation in experiment is pretty simple and feasible.

3.3.1.3. Fuzzy rule inference and defuzzification

In this study part, the *Max-Min* composition operation and the *centroid* (CoA: center of area) method, which are presented in Chapter 2 and in [22],[23], are utilized for the fuzzy rule inference and the defuzzification process in MATLAB simulation, respectively. In detail, the design of the fuzzy rule inference and defuzzification, based on the Fuzzy Inference System (FIS) editor in MATLAB software, is described in Figure 3.11.

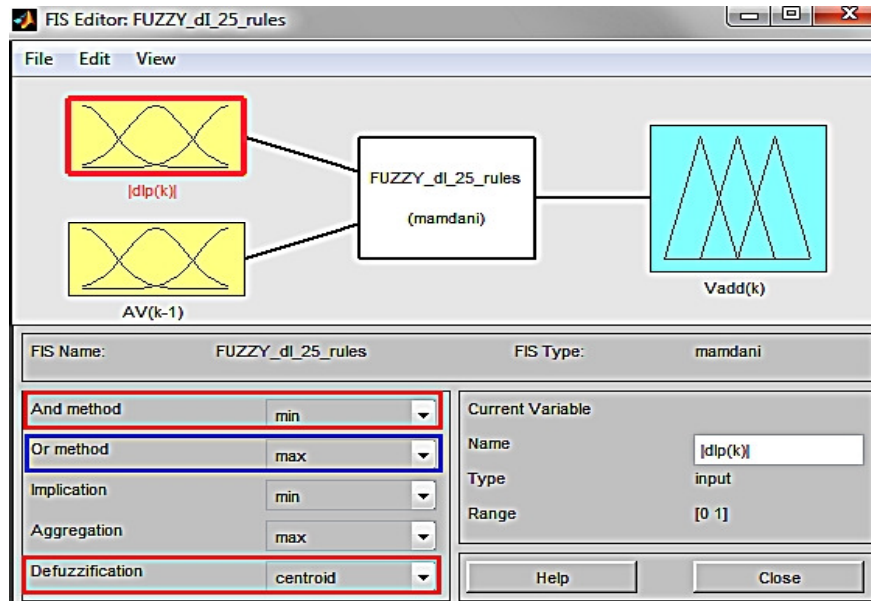


Figure 3.11: Design the proposed FLC with FIS Editor in MATLAB.

3.3.2. The second sub-controller

The second sub-controller is a PI controller, including an anti-windup block based on the back-calculation method [49],[50]. It is emphasized that the anti-windup module is used here to eliminate the large overshoot in the transient response. And its detailed scheme is represented in Figure 3.12.

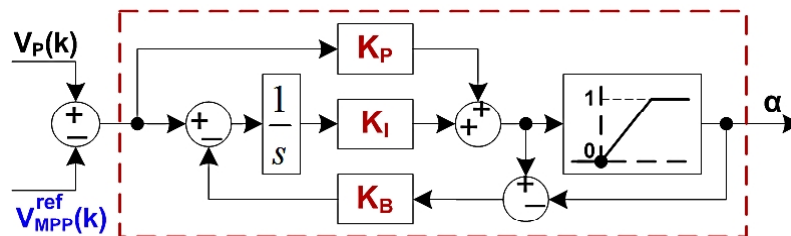


Figure 3.12: The detailed scheme of the PI anti-windup in use.

3.4. Simulation results

In MATLAB simulations, the PV panel model is based on (3.1); and the closed-loop PV system is developed with Simulink and Fuzzy Logic Toolbox [18],[35]. Design parameters of the

demonstrative PV system utilized in this study are presented in Table 3.6. Additionally, it is noted that the PV array consists of two parallel branches with two the 80W PV panels in series in each branch; and its rated total power is 320 W.

Table 3.6: Parameters of the demonstrative PV system.

Module	Parameter and Value
Non-inverting Buck-Boost DC-DC converter	$C_i = C_o = 1 \text{ mF} ; R_l = 50 \text{ m}\Omega ;$ $L_l = 1 \text{ mH} ; R_{Load} = 15 \text{ }\Omega ;$
Sub-controller	Parameter and Value
PI with Anti-windup	$K_P = 1.5 ; K_I = 15 ; K_B = 0.5$

Besides, the authors in [37] introduced two modified INC-MPPT techniques, using a conventional FLC and an adaptive FLC, respectively. In our research, for comparison purpose, the conventional fuzzy-based INC-MPPT technique in [37] is chosen to simulate. As shown in Figure 3.13, the ratio-value ($C_p = I_p / V_p + \Delta I_p / \Delta V_p$) and its change (dC_p) are two inputs of the conventional FLC in this technique. The FLC's output is the change of duty-cycle value $du(k)$, where $u(k)$ plays as the input control signal of the converter. Table 3.7 shows design values for the input and output scaling gains of the FLC in Figure 3.13. In this study, these coefficients are tuned to get a fine balance performance as possible between the fast response speed in tracking the MPP and the small steady-state fluctuation around the MPP.

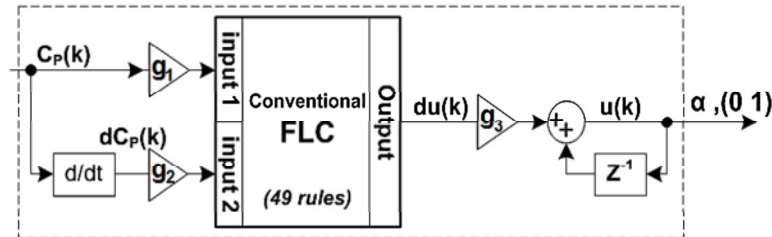


Figure 3.13: The structure of the conventional fuzzy-based INC-MPPT method presented in [37].

Table 3.7: Input-output scaling gains of the FLC in Figure 3.13

Input scaling gains	Output scaling gain
$g_1 = 3.8 ; g_2 = 4.1$	$g_3 = 4$

3.4.1. Simulation 1: Start-up response in tracking the MPP at the standard test condition

In this situation, the solar irradiance and the temperature are kept constant at 1000 W/m^2 and 25°C , in the same order. Figure 3.14 shows that the operating PV voltage V_p is equal to its desired

value $V_{MPP}^{ref}(k)$ from the time $t = 0.1$ s (with the proposed fuzzy-based method). Additionally, Figure 3.15 illustrates the comparison between the proposed fuzzy-based algorithm, the conventional INC-MPPT method in [12] and the conventional fuzzy-based INC-MPPT introduced in [37].

In detail, firstly, the conventional INC-MPPT with the fixed step-size as 0.5 V (big value) has the fast response time, but includes the large overshoot and steady-state error. Otherwise, the conventional INC-MPPT with the fixed step-size as 0.1 V (small value) has the tiny overshoot and little steady fluctuations; nevertheless, its response speed is slow. Whereas, the conventional fuzzy-based INC-MPPT in [37] can reach the MPP fairly speedily. In fact, its response is faster than the conventional INC-MPPT with fixed step-size as 0.1 V; however, variations around the MPP at the steady state have not yet been eliminated really efficiently. Lastly, the proposed method not only tracks rapidly and exactly the MPP but also significantly lowers oscillations around MPP.

Moreover, Figure 3.16 shows that the step-size $\Delta V(k)$ in the proposed technique is a variable value, and is adjusted suitably by the suggested FLC to seek the MPP efficiently. In detail, firstly, $\Delta V(k)$ has the large value as 0.7 V to reach speedily the MPP of 319.7 W. Then, its value is decreased to around 0.17 V for reducing the overshoot. Finally, it is tiny after the time $t = 0.2$ s to eliminate the steady-state error.

In two next simulations, the conventional INC-MPPT method will be utilized only with the fixed step-size as 0.1 V (small value) to reduce overshoot in the transient period and power fluctuations around the MPP at the steady state.

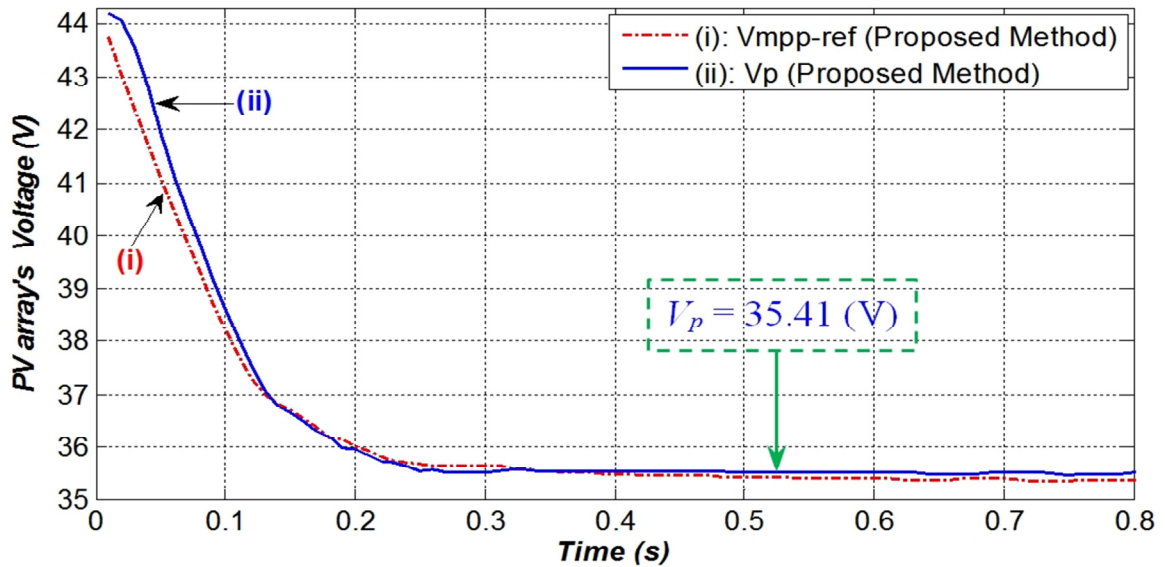


Figure 3.14: The PV array's voltage in *Simulation 1*.

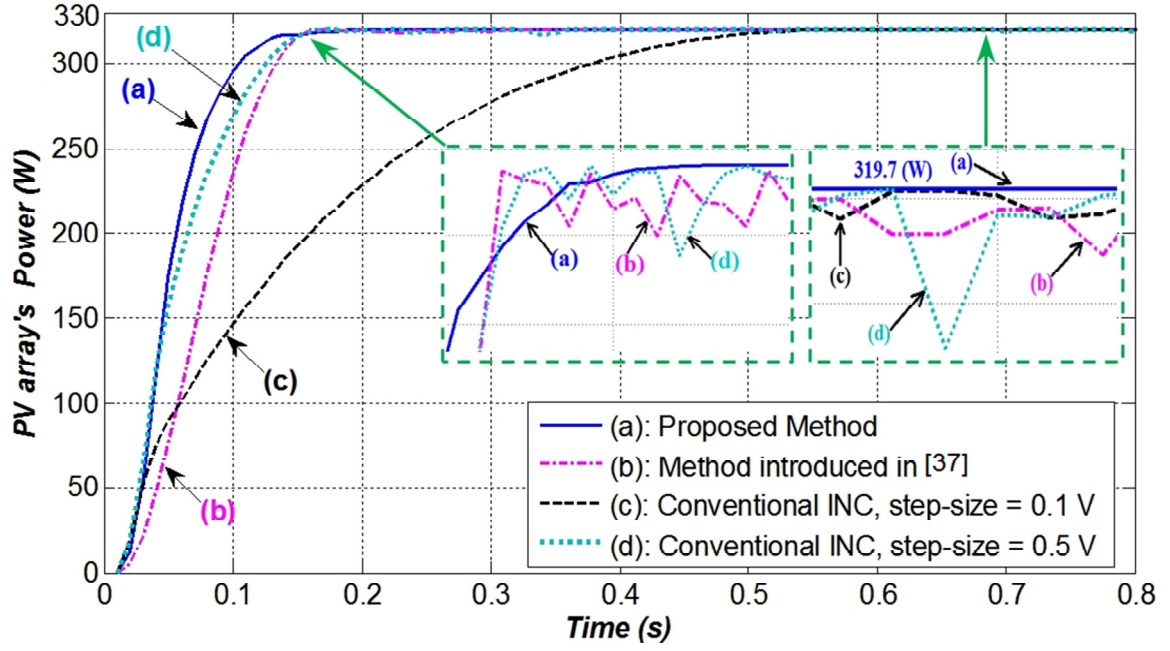


Figure 3.15: The PV array's output power in *Simulation 1*.

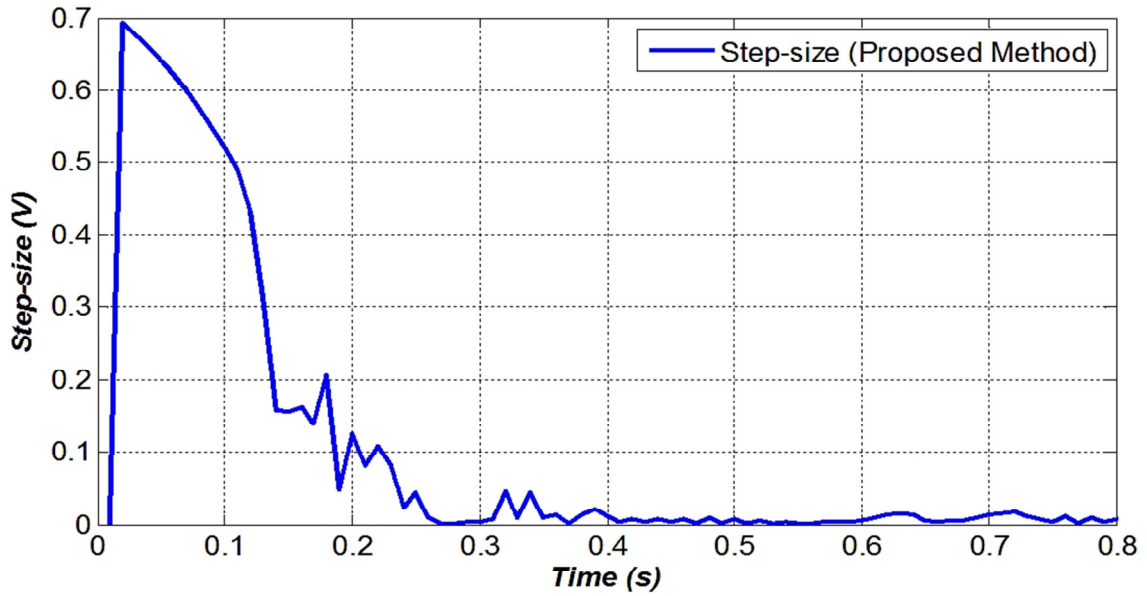


Figure 3.16: The variable step-size $\Delta V(k)$ in *Simulation 1*.

3.4.2. Simulation 2: Effects of solar radiation changes

In this condition, solar radiation changes its value as follows: 1000 W/m^2 from the time $t = 0 \text{ s}$, 250 W/m^2 from the time $t = 1 \text{ s}$, and 800 W/m^2 from the time $t = 1.75 \text{ s}$; in the meantime, the temperature is kept invariant at 25°C .

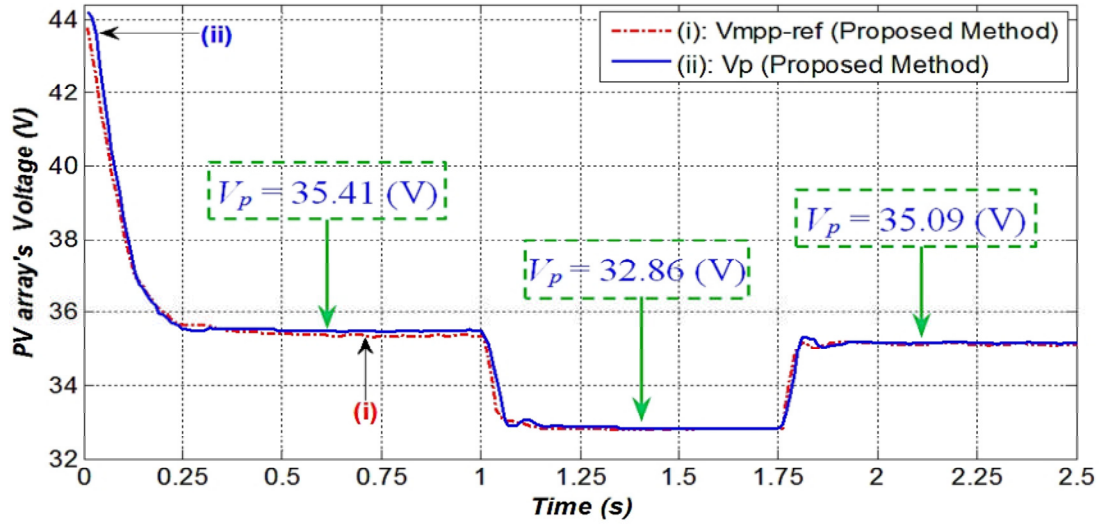


Figure 3.17: The PV array's voltage in *Simulation 2*.

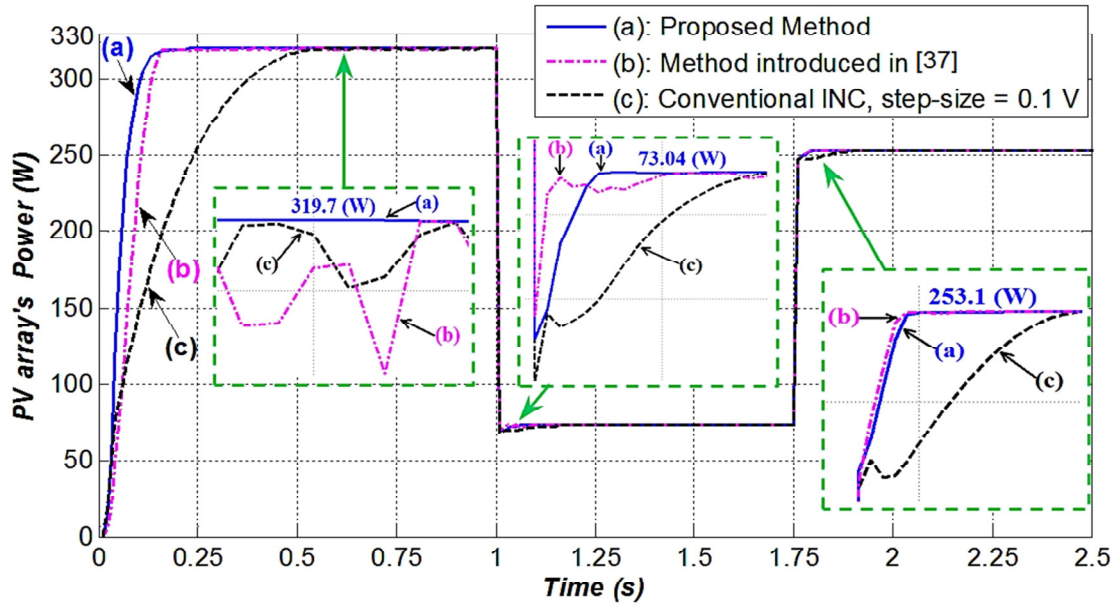


Figure 3.18: The PV array's output power in *Simulation 2*.

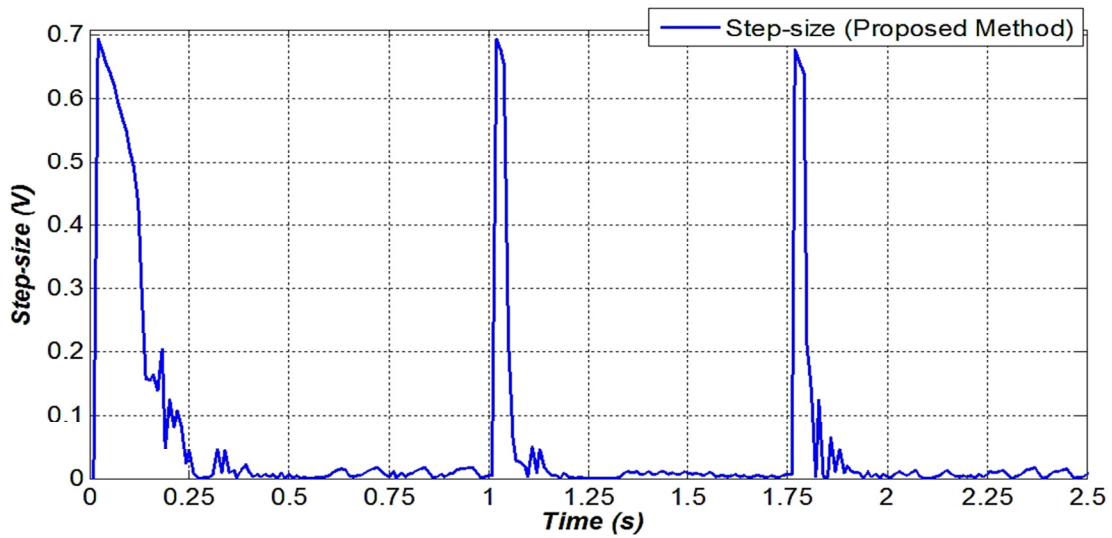


Figure 3.19: The variable step-size $\Delta V(k)$ in *Simulation 2*.

Figure 3.17 illustrates that the PV array's voltage V_p always closely tracks to its reference $V_{MPP}^{ref}(k)$ calculated by the FLC in advance. As shown in Figure 3.18, the PV power is 319.7 W, 73.04 W and 253.1 W, highly corresponding to the MPPs M3, M1 and M2 (of PV array) seen in Table 3.3, respectively.

In addition, Figure 3.19 represents that the step-size $\Delta V(k)$ is tuned adaptively to track the MPP quickly and exactly. In detail, when the solar radiation decreases suddenly from 1000 W/m^2 to 250 W/m^2 at the time $t = 1 \text{ s}$, $\Delta V(k)$ is adjusted instantly from 0 V to 0.7 V to force the operating point to reach the new MPP rapidly. After that, at about the time $t = 1.2 \text{ s}$, as the operating point is moving nearly to the MPP of 73.04 W, $\Delta V(k)$ is decreased promptly to be very small for reducing the fluctuation around the MPP. Similarly, as seen in this figure, the above process of $\Delta V(k)$ is done again when the solar irradiance increases abruptly from 250 W/m^2 to 800 W/m^2 at the time $t = 1.75 \text{ s}$.

3.4.3. Simulation 3: Impacts of temperature variations

In the cases, the temperature varies its value as follows: 25°C from the time $t = 0 \text{ s}$, 45°C from the time $t = 1 \text{ s}$, and 35°C from the time $t = 1.75 \text{ s}$; meanwhile, the solar irradiance is kept unvarying at 1000 W/m^2 . With using the suggested algorithm, Figure 3.20 and Figure 3.21 shows that the PV array operated at the points: 35.41 V / 319.7 W, 32.29 V / 283.25 W, and 33.98 V / 300.8 W in three operating time-periods, clearly matching the MPPs M3, M5 and M4 (of the PV array) represented in Table 3.3, respectively.

Besides, as described in Figure 3.22, the step-size $\Delta V(k)$ is altered appropriately to eliminate oscillations around the MPP. In detail, when the temperature changes its value at the time $t = 1 \text{ s}$ (or at $t = 1.75 \text{ s}$), $\Delta V(k)$ is tuned immediately to 0.7 V (or to 0.78 V, respectively) to seek speedily the new MPP. Then, it is decreased continually to become zero.

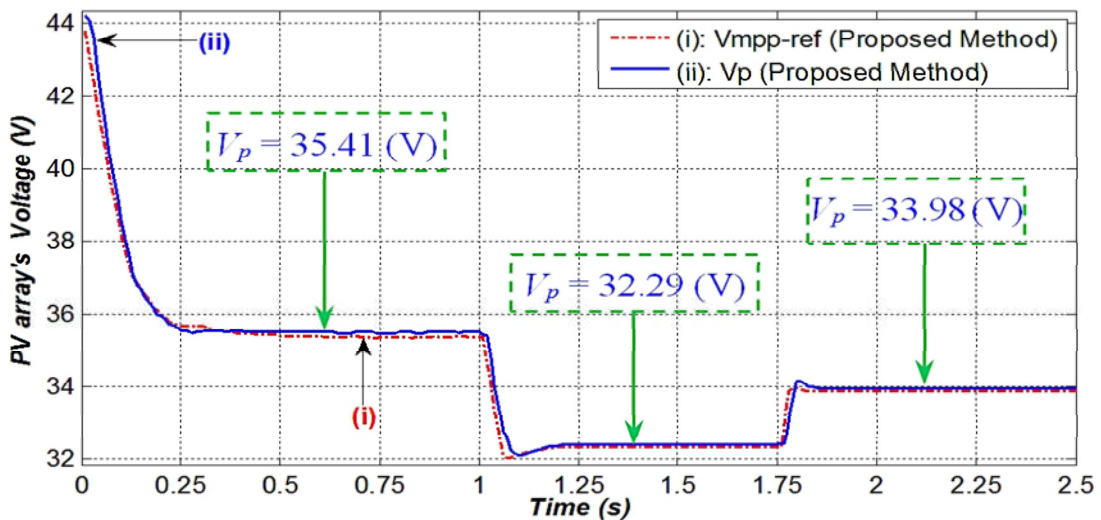


Figure 3.20: The PV array's voltage in *Simulation 3*.

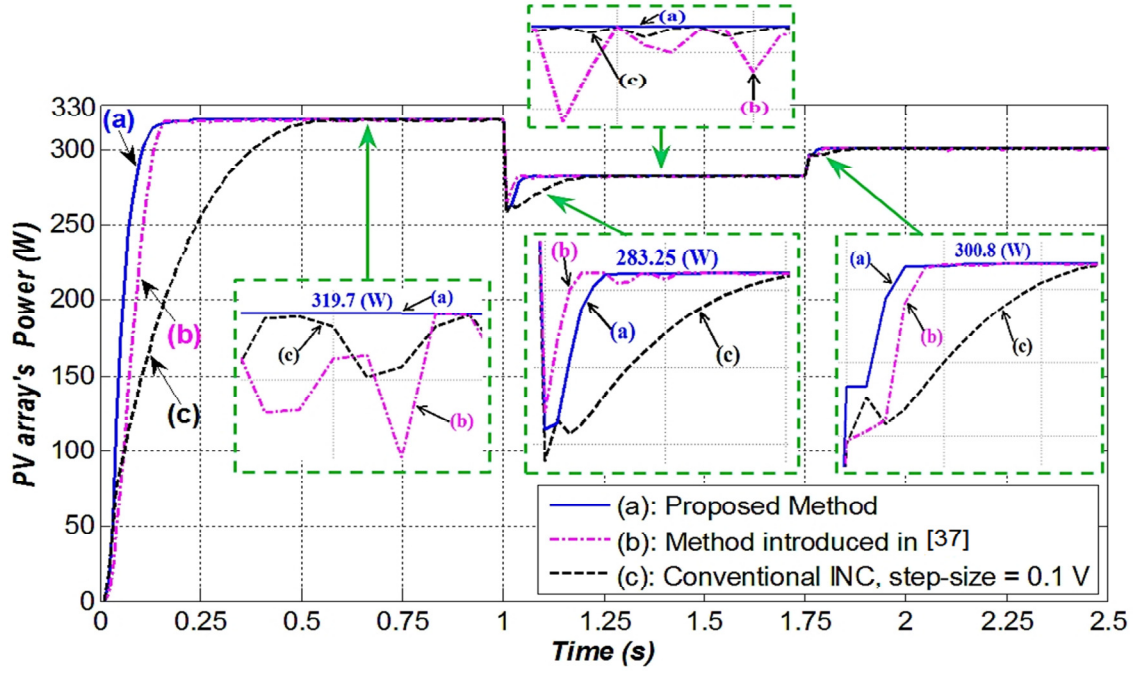


Figure 3.21: The PV array's output power in *Simulation 3*.

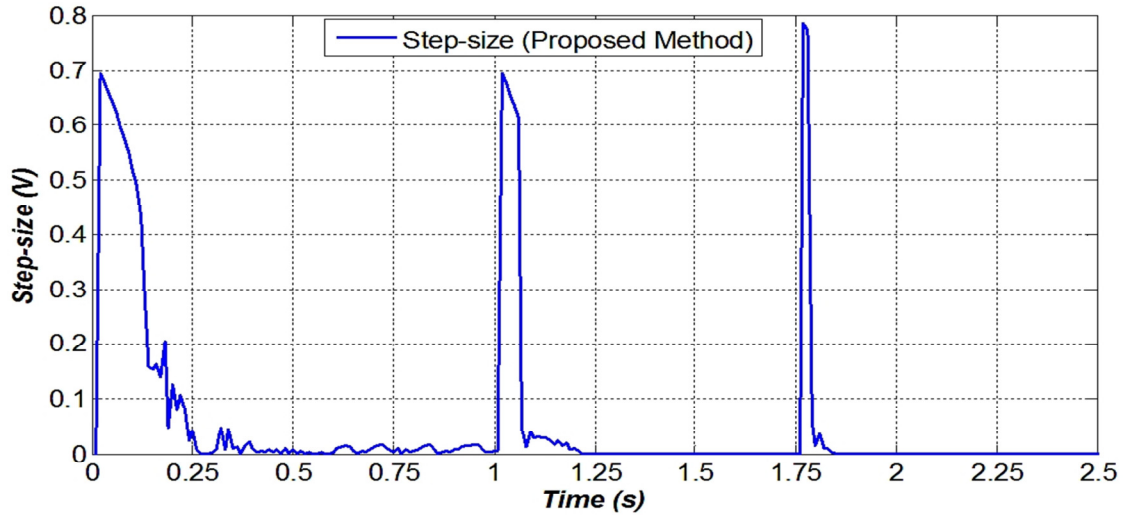


Figure 3.22: The variable step-size $\Delta V(k)$ in *Simulation 3*.

3.5. Experimental results

The experimental stand-alone PV system utilized in this study is described in Figure 3.23. Therein, the PV array with a nominal power of 320W is installed on the rooftop of the Green Power Laboratory, Ho Chi Minh City University of Technology, Vietnam. The experimental non-inverting buck-boost converter is implemented according to the parameters given by Figure 3.1 and Table 3.6. And the microcontroller board is the *Tiva C Series LaunchPad* from Texas Instrument [51]. The proposed fuzzy-based algorithm is programed in the laptop, and then embedded into the microcontroller *TM4C123G* to execute in real-time. The sample time for generating the control signal α_p is $T_s = 5 \text{ ms}$.

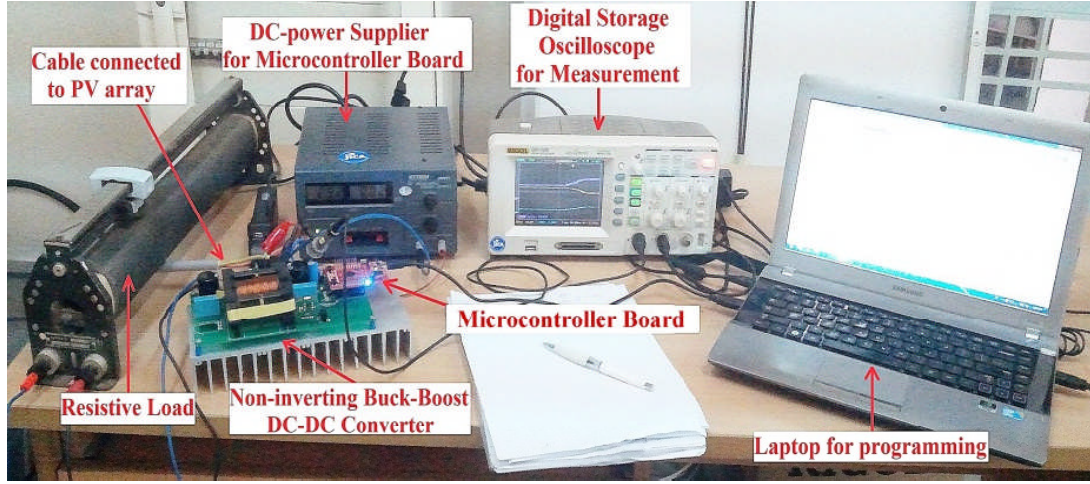
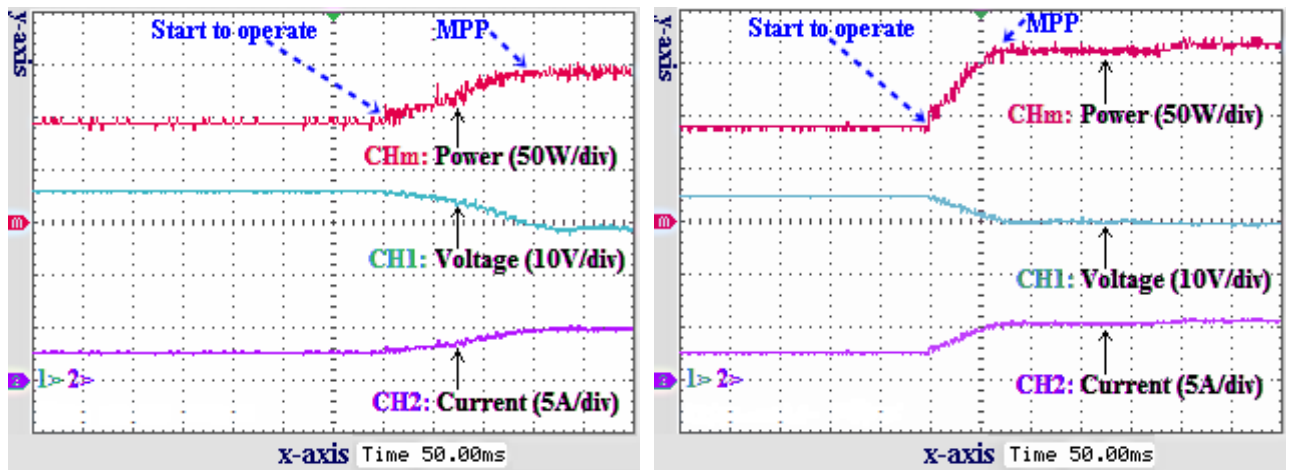


Figure 3.23: The experimental PV system used in this study.

In our experiments, the solar radiation is measured as about 650 W/m^2 and the temperature on PV array's surface is nearly 42°C . As well, the performance of the proposed fuzzy-based algorithm is compared to the conventional INC-MPPT method in [12] with the fixed step-size as 0.1V . Performances of the experimental PV system (shown in Figures 3.24 to 3.26) are observed and collected with using the digital oscilloscope. In Figures 3.24 to 3.26, the vertical axis (y-axis) is scales for the PV array's voltage (channel CH1), current (channel CH2) and output power (channel CHm); and the horizontal axis (x-axis) is the time scale.

3.5.1. Experiment 1: Start-up response in tracking MPP

This experiment is implemented to assess the response speed in seeking the MPP of the proposed method when the PV system starts to operate.



(a) Conventional INC-MPPT [x-axis: 50ms/div]

(b) The proposed method [x-axis: 50ms/div]

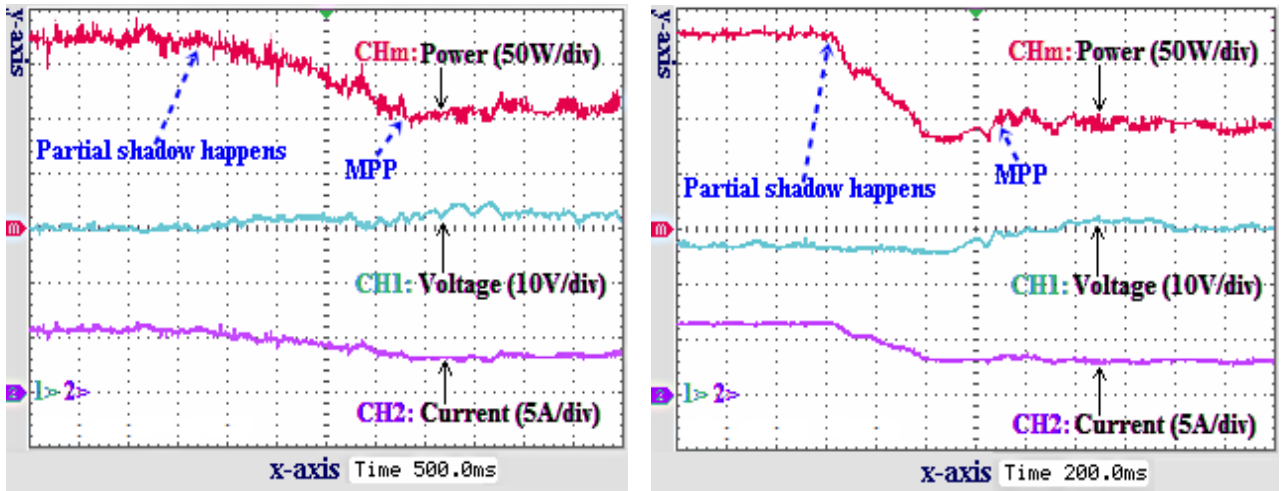
Figure 3.24: Performances of the PV system in *Experiment 1*.

According to Figure 3.24 (a), the conventional INC reaches the MPP of 150W (30V / 5A) within about 140 ms. Besides, as shown in Figure 3.24 (b), the proposed algorithm takes only 70 ms for tracking the MPP of 160W (30V / 5.33A). And the above results show that the response speed of the proposed method is considerably faster than the conventional INC-MPPT in this test.

In next two experiments, the effectiveness and adaptability of the proposed method will be evaluated when the PV array is suddenly affected by the partial shadow. In detail, *Experiment 2* and *Experiment 3* are performed when the partial shadow occurs and ends, respectively.

3.5.2. Experiment 2: When the partial shadow happens

Next the *Experiment 1*, when PV array is operating at the power point of 180W, the surface of PV array is covered suddenly within 50% of its area. This means that only 50% of the surface area of PV array is now exposed in the solar insolation. So the output power of PV array will decrease.



(a) Conventional INC-MPPT [x-axis: 500ms/div] (b) The proposed method [x-axis: 200ms/div]

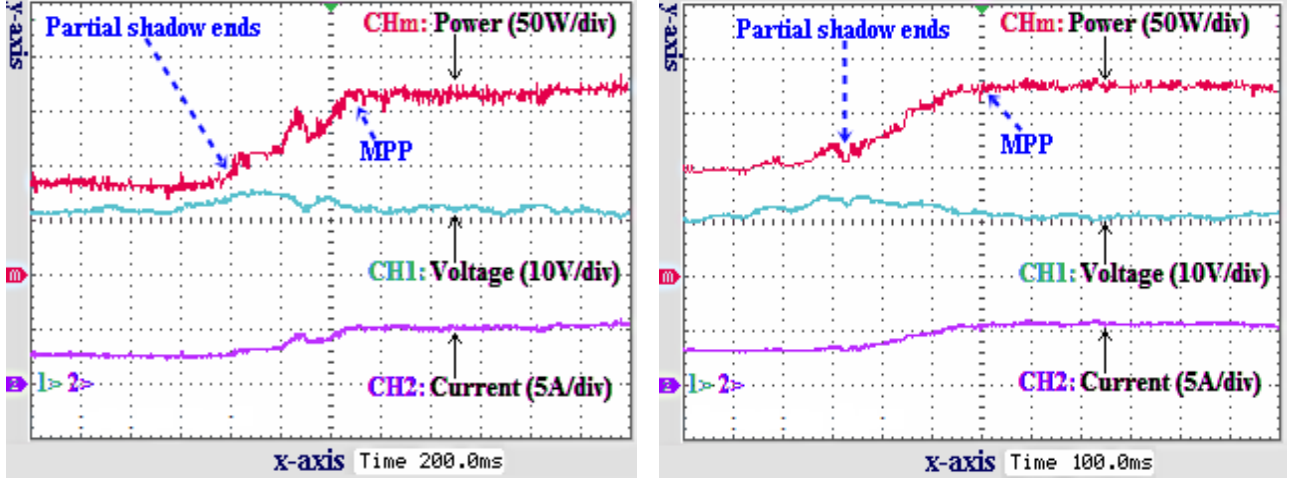
Figure 3.25: Performances of the PV system in *Experiment 2*.

As illustrated in Figure 3.25 (a), the conventional INC-MPPT takes nearly 2000 ms to search the new MPP of 100W (30V / 3.33A) from the time when the partial shadow happens. Whereas, the proposed algorithm needs only 680 ms to reach the new MPP of 100W (30V / 3.33A) as in Figure 3.25(b). Obviously, the suggested algorithm can seek exactly the new MPP, and it also has the better performance than the conventional INC-MPP in this experimental circumstance.

3.5.3. Experiment 3: When the partial shadow ends

Subsequent the *Experiment 2*, when the PV array is operating at the power point of about 100W, the covered surface area of it is now entirely uncovered. This means that 100% of the surface area of PV array is now exposed in the solar irradiance. Thus, the PV output power will increase.

In detail, as expressed in Figure 3.26 (a), the conventional INC-MPPT method needs nearly 500 ms to trace the new MPP of 170W (32V / 5.31A) after the partial shadow ends. While it takes 260 ms for the proposed algorithm to reach the new MPP of 175W (32V / 5.47A) as seen in Figure 3.26 (b). This continually demonstrates that the response speed of the suggested algorithm is always significantly quicker than the conventional INC-MPPT. And all results obtained in *Experiments 2-3* show clearly the fine adaptability of the proposed method under influences of the partial shadow.



(a) Conventional INC-MPPT [x-axis: 200ms/div] (b) The proposed method [x-axis: 100ms/div]

Figure 3.26: Performances of the PV system in *Experiment 3*.

Additionally, we can also see that fluctuations in the PV output powers with using the proposed algorithm, as shown in parts (b) of Figures 3.24, 3.25 and 3.26, are pretty much smaller than the other ones with using the conventional INC-MPPT as expressed in parts (a) of Figures 3.24, 3.25 and 3.26, respectively.

3.6. Discussion about effects of partially shaded condition and related solutions

3.6.1. In the case of relatively small-scale PV array

In this case, a relatively small-scale PV array often consists of several PV panels such as the 320W PV array used to study in this chapter. As illustrated in Figure 3.27, in the normal condition, the MPP of PV array is point A. Then, when the partial shadow occurs, the new P-V curve has one local MPP (point B) and one global MPP (point C). So the objective of the MPPT algorithm in use is to reach exactly the new global MPP C instead of to be trapped at the local MPP B.

Within the proposed fuzzy-based INC-MPPT algorithm in this chapter, in the time from the previous MPP A to point B (the line *l* in Figure 3.27), because $\Delta V_p(k) = 0$, the first input of FLC is now chosen as $|\Delta I_p(k)|$. Besides, the power value of point B is smaller than the power value of point A, so $\Delta I_p(k)$ has a negative value. This means that $Sign(\Delta I_p(k)) = -1$; so the next reference voltage

$V_{MPP}^{ref}(k)$ will move to the left side of the point B . According to Figures 3.7, 3.8 and Table 3.4, to force the operating point B instantly move to an immediate point J in the green vicinity curve of the new global MPP C (the line 2 in Figure 3.27), the output factor f_2 should be chosen a pretty large value such as 1 as shown in Table 3.4 to ensure the step-size to be a sufficiently large value in this transient period. Then, the first FLC's input is switched to be $|A_p(k)|$ for forcing the operating point from the point J to reach speedily the new global MPP C (the line 3 in Figure 3.27). In summary, the proposed INC-MPPT algorithm in this chapter can overcome effects of the partial shadow on the relatively small-scale PV array as validated in previous subsections 3.5.2 and 3.5.3.

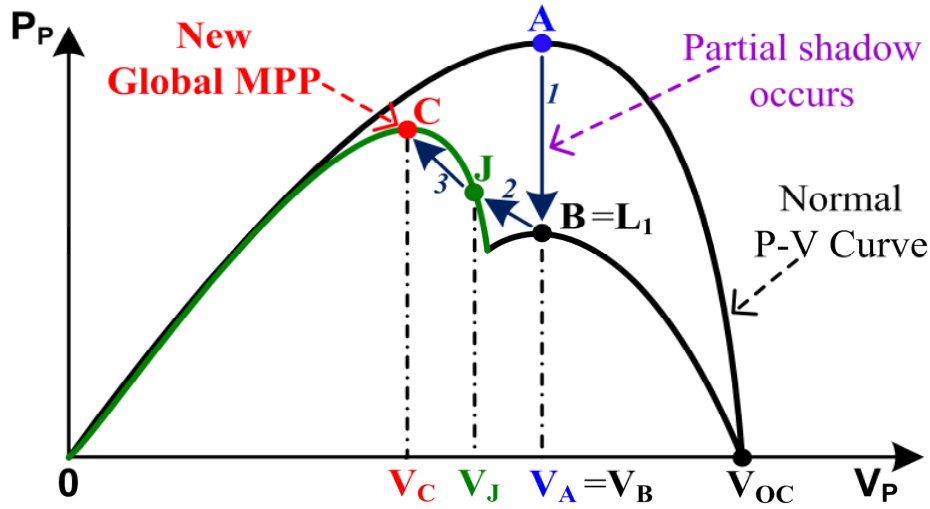


Figure 3.27: Partially shaded condition on small-scale PV array with the proposed INC-MPPT

3.6.2. In the case of large-scale PV array

In this case, the large-scale PV array consists of many PV panels, and complicated partial shadows occur as shown in Figure 3.28. As a result, the new P-V curve of PV array may have many local MPPs (points L_1 , L_2 , L_3 , and L_4) and one global MPP (point C) as illustrated in Figure 3.29. To seek accurately the new global MPP C , firstly, the operating point need be moved from the point B (L_1) to an immediate point J on the vicinity curve of the new global MPP C (the green curve as shown in Figure 3.29). According to [52], existing efficient algorithms utilized to overcome the complicatedly partially shaded condition on large-scale PV array are: *Power Curve Slope*, *Load-Line Maximum Power Point Tracking* (including Type I and Type II), *Diving Rectangles Technique*, *Power Increment Technique*, *Instantaneous Operating Power Optimization*, *Fibonacci Search*, *Artificial Neural Networks*, and *Particle Swarm Optimization*.

Wherein, as expressed in (3.8)-(3.10) and Figure 3.30, the *Load-Line Maximum Power Point Tracking* (Type II) technique introduced in [53],[52] can be employed appropriately to support for the proposed fuzzy-based INC-MPPT algorithm in this chapter to seek exactly and efficiently the

new global MPP under complicatedly partially shaded conditions. In detail, when the partially shaded condition is detected according to (3.8) and (3.9), the reference voltage $V_{MPP}^{ref}(k)$ is instantly set as the voltage V_J of the immediate point J on the vicinity curve of the new global MPP C (the green curve in Figure 3.29) according to (3.10). After that, the proposed fuzzy-based INC-MPPT algorithm in this chapter is utilized to reach rapidly and accurately the new global MPP C .

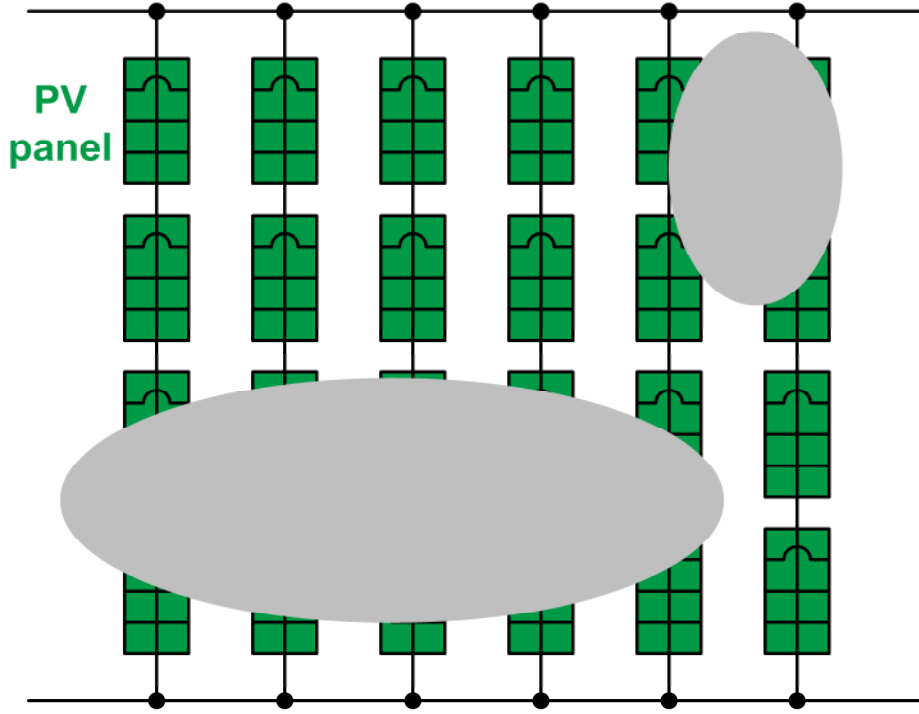


Figure 3.28: Complicatedly partially shaded condition within a large-scale PV array.

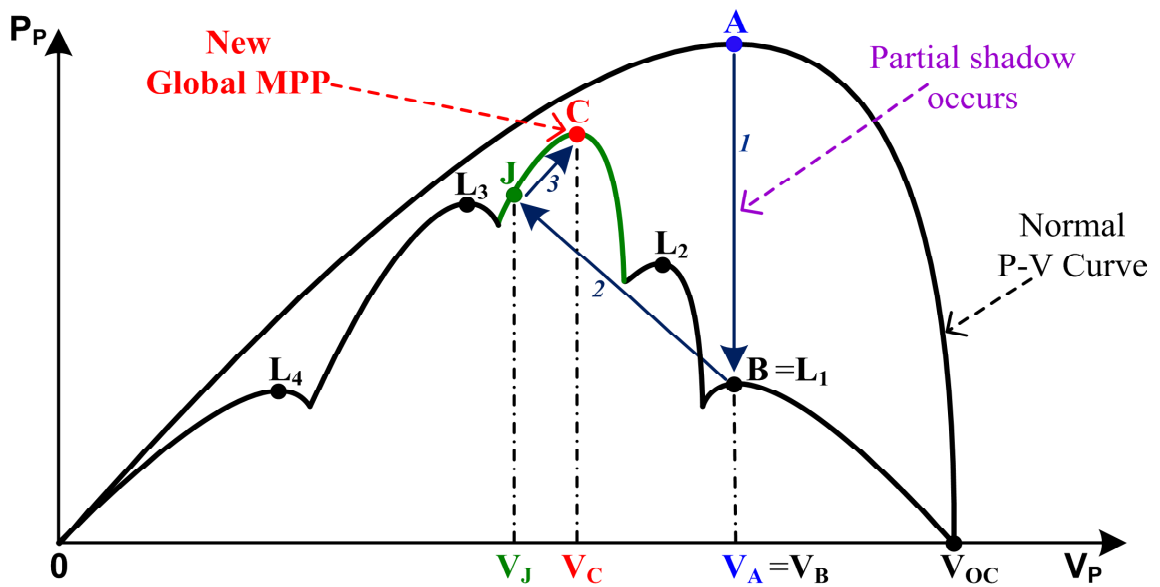


Figure 3.29: Multiple local and global MPPs on P-V curve under complicated partial shadow.

$$\Delta V_p(k) = V_p(k) - V_p(k-1) < \Delta V_{p,set} \quad (3.8)$$

$$\frac{\Delta I_p(k)}{I_p(k-1)} = \frac{I_p(k) - I_p(k-1)}{I_p(k-1)} < -\Delta I_{p,set} \approx -\frac{I_p(k)}{N_p} \quad (3.9)$$

Where $\Delta V_{p,set}$ is the threshold value, and is tuned manually by the user or set by manufacturer [53].

$$V_J = V_{MPP}^{ref}(k) = \frac{N_s V_{OC}}{N_p I_{SC}} I_p(k) \quad (3.10)$$

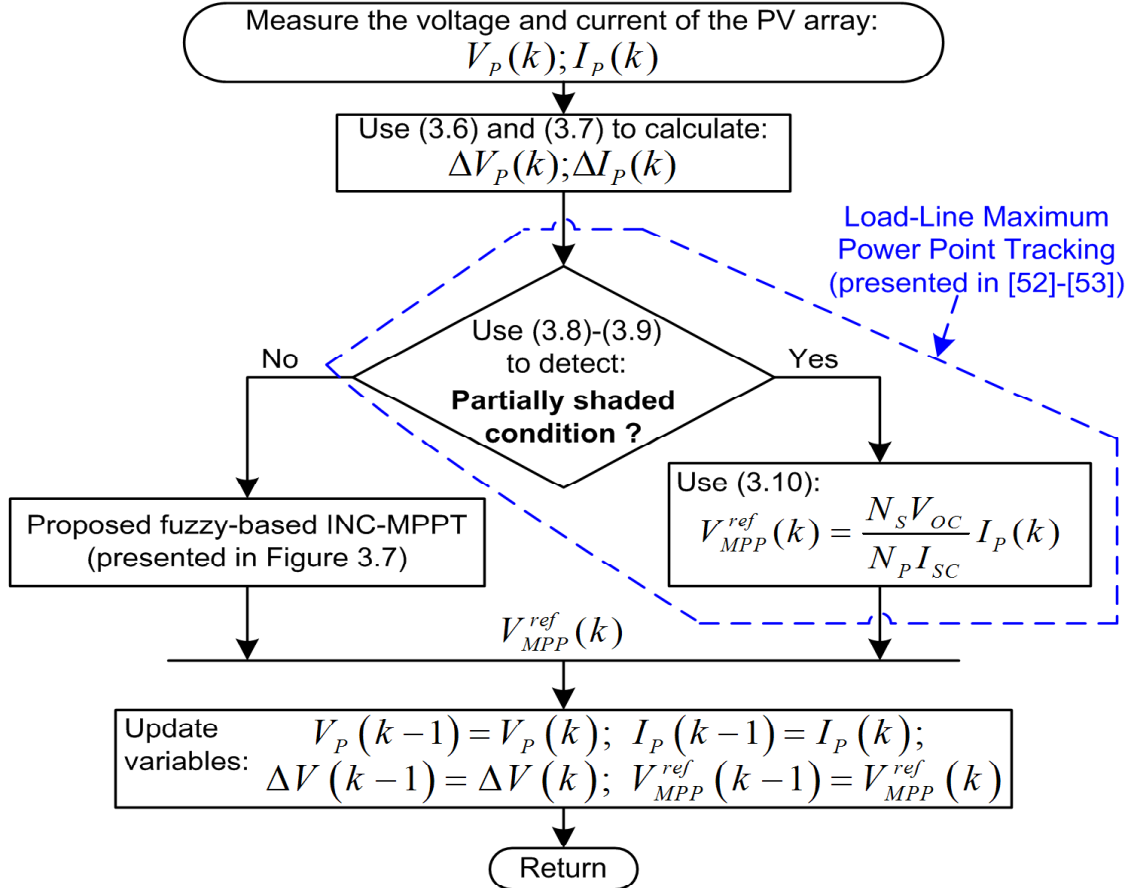
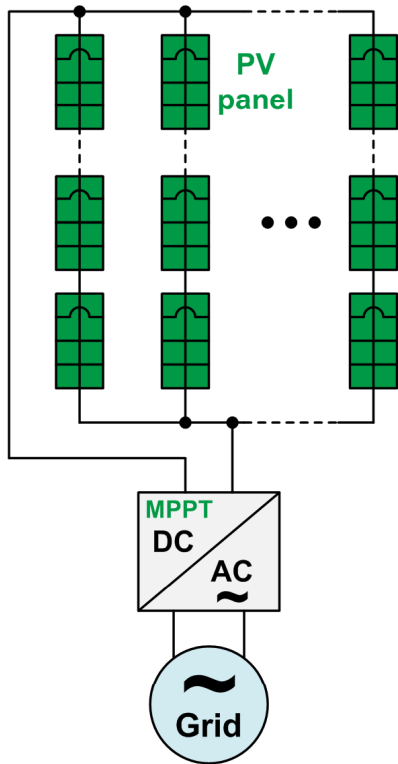
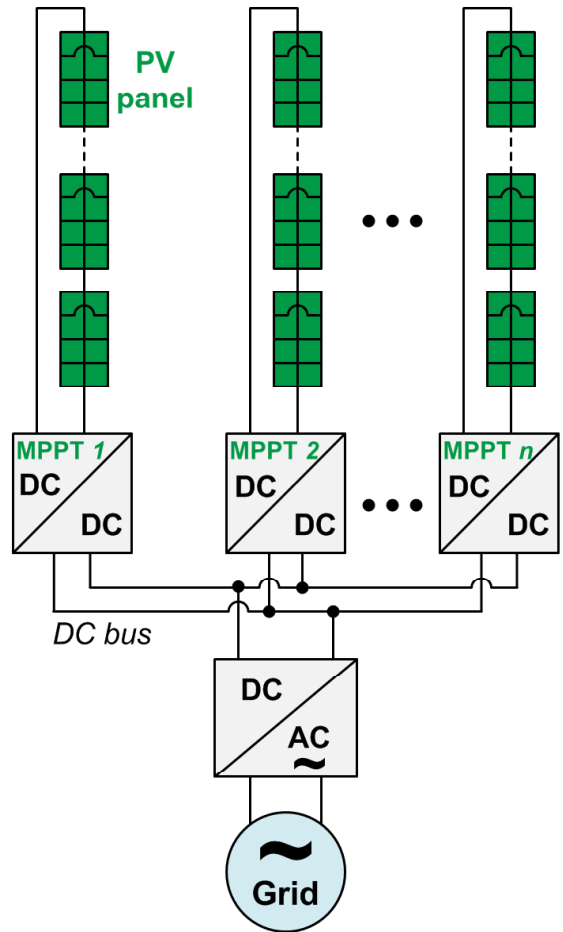


Figure 3.30: A demonstrative combination of the technique introduced in [53] to detect the partially shaded condition and the proposed INC-MPPT algorithm in this chapter.

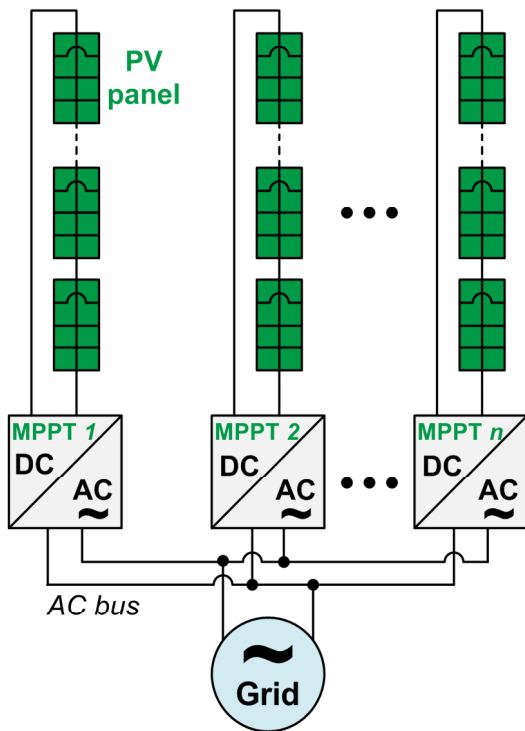
On the other hand, the connection structure of large-scale PV array also affects heavily the efficiency of MPPT algorithms under partially shaded condition [52]. As shown in Figure 3.31, there are four typical topologies of PV array as the centralized DC-AC inverter, multi-string DC-DC converter, multi-string DC-AC converter, and individually integrated DC-AC inverter. Wherein, the centralized inverter topology in Figure 3.31(a) utilizes only one DC-AC inverter implemented with a MPPT algorithm for all PV panels; obviously, this decreases noticeably the efficiency in obtaining the total output power of PV array in complicatedly partially shaded conditions. So this centralized inverter topology is not recommended to utilize in a large-scale high-power PV system.



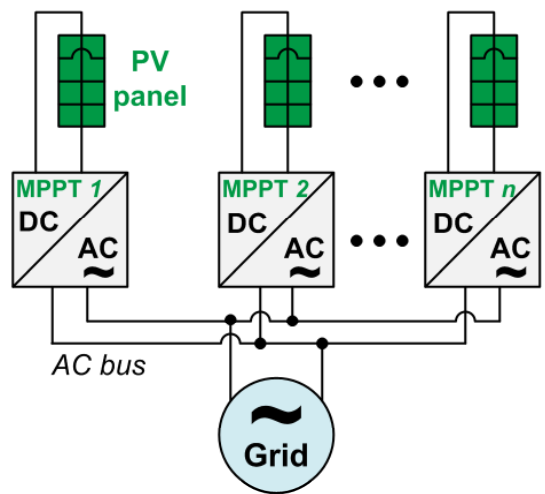
(a) Centralized DC-AC inverter topology



(b) Multi-string DC-DC converter topology



(c) Multi-string DC-AC converter topology



(d) Individual DC-AC inverter topology

Figure 3.31: Four typical topologies of the connection structure for large-scale PV array.

The three remaining topologies in Figure 3.31(b)-(c)-(d) use the separate MPPT for each DC-DC converter or DC-AC inverter, which can diminish significantly the negative effects of partially shaded condition on PV arrays and are convenient for upgrading. As a result, the efficiency in obtaining the total output power of PV array is boosted noticeably. With the topology of individual DC-AC inverter in Figure 3.31(d), the number of DC-AC inverters can become very large within a large-scale high-power PV system; and this may be relatively difficult for control and monitoring.

In conclusion, to achieve the best efficiency in obtaining the total output power of a real large-scale PV power system, the connection structure of PV panels should be utilized with the topology of multi-string DC-DC converter or multi-string DC-AC converter as shown in Figure 3.31(b)-(c) to reduce the occurrence of complicated partial shadows, and an efficient technique to detect partial shadows (such as the *Load-Line Maximum Power Point Tracking* technique in [53],[52]) should be combined suitably with a MPPT algorithm (such as the proposed INC-MPPT in this chapter). Besides, in Chapter 5 of this thesis, the topology of multi-string DC-DC converter in Figure 3.31(b) is used for the connection structure of PV panels in a large-scale grid-connected PV solar farm.

3.7. Sample program in C and evaluation of program capacity and computation time

3.7.1. Sample program in C language to implement the proposed FLC [54],[26]

A basic sample program in C language to implement the 25-rule FLC proposed in this chapter (described in Figures 3.9 and 3.10 and Table 3.5) have key parts such as: declaring global variables, functions of fuzzification for two FLC's inputs, function of fuzzy inference based on *Max-Min* operation, function of defuzzification for the FLC's output, and main function of the program. Programs in C to implement the other FLCs presented in this thesis can be programmed similarly.

- **Declare the global variables for the FLC used in the sample program:**

```
float INPUT_1st; // the first input of FLC in Figure 3.9
float INPUT_2nd; // the second input of FLC in Figure 3.9
float bnn_INPUT_1st[5] = {0,0,0,0,0}; // for Columns in Table 3.5
float bnn_INPUT_2nd[5] = {0,0,0,0,0}; // for Rows in Table 3.5
float u[5][5]; // for the output values of rules in Table 3.5
float degree_NL, degree_NM, degree_NS, degree_NZ, degree_ZE, degree_PZ,
      degree_PS, degree_PM, degree_PL; // degree values of the output fuzzy sets
float output_value; // final output value of the defuzzification process
```

- **Function of fuzzification for the first input of FLC:** The fuzzification processes for the first input in the two value ranges of [0 0.03] and [0.03 0.15] (in Figure 3.9) are illustrated

in the program as sample codes. The fuzzification processes for the first input in the other value ranges in Figure 3.9 can be programmed similarly.

```
void Fuzzification_INPUT_1st() // For the first input of FLC in Figure 3.9
{
    if (INPUT_1st <= 0.03) // 0 ~ 0.03
    {
        bnn_INPUT_1st[0] = 1; // variable "AZ"
        bnn_INPUT_1st[1] = 0; // variable "SM"
        bnn_INPUT_1st[2] = 0; // variable "ME"
        bnn_INPUT_1st[3] = 0; // variable "LA"
        bnn_INPUT_1st[4] = 0; // variable "VL"
    }

    else if (INPUT_1st <= 0.15 && INPUT_1st > 0.03) // 0.03 ~ 0.15
    {
        bnn_INPUT_1st[0] = 1 - (INPUT_1st - 0.03)/(0.15-0.03); // "AZ"
        bnn_INPUT_1st[1] = (INPUT_1st-0.03)/(0.15-0.03); // "SM"
        bnn_INPUT_1st[2] = 0; // variable "ME"
        bnn_INPUT_1st[3] = 0; // variable "LA"
        bnn_INPUT_1st[4] = 0; // variable "VL"
    }

    ...

} // end of the function "Fuzzification_INPUT_1st()"
```

- **Function of fuzzification for the second input of FLC:** The fuzzification processes for the second input in the value ranges of [0 0.03], [0.6 1] and larger than 1 (in Figure 3.9) are illustrated in the program as sample codes. The fuzzification processes for the second input in the other value ranges in Figure 3.9 can be programmed similarly.

```
void Fuzzification_INPUT_2nd() // For the second input of FLC in Figure 3.9
{
    if (INPUT_2nd <= 0.03) // 0 ~ 0.03
    {
        bnn_INPUT_2nd[0] = 1; // variable "AZ"
        bnn_INPUT_2nd[1] = 0; // variable "SM"
        bnn_INPUT_2nd[2] = 0; // variable "ME"
        bnn_INPUT_2nd[3] = 0; // variable "LA"
        bnn_INPUT_2nd[4] = 0; // variable "VL"
    }

    ...

    else if (INPUT_2nd <= 1 && INPUT_2nd > 0.6) // 0.6 ~ 1
```

```

    {
        bnn_INPUT_2nd[0] = 0;           // variable "AZ"
        bnn_INPUT_2nd[1] = 0;           // variable "SM"
        bnn_INPUT_2nd[2] = 0;           // variable "ME"
        bnn_INPUT_2nd[3] = 1 - (INPUT_2nd-0.6)/(1-0.6); // variable "LA"
        bnn_INPUT_2nd[4] = (INPUT_2nd-0.6)/(1-0.6);    // variable "VL"
    }

    else if (INPUT_2nd > 1) // INPUT_2nd > 1
    {
        bnn_INPUT_2nd[0] = 0;           // variable "AZ"
        bnn_INPUT_2nd[1] = 0;           // variable "SM"
        bnn_INPUT_2nd[2] = 0;           // variable "ME"
        bnn_INPUT_2nd[3] = 0;           // variable "LA"
        bnn_INPUT_2nd[4] = 1;           // variable "VL"
    }
} // end of the function "Fuzzification_INPUT_2nd()"

```

- **Function of fuzzy inference based on *Max-Min* composition operation:** This function is programmed according to (2.6) and *Example 2.4* presented in subsection 2.2.2.3. Wherein, firstly, inference processes with *Min* composition rule are performed completely. Then, inference processes in *Max* composition rule for the two output linguistic variables (NZ, ZE) in Table 3.5 are presented for sample. Inference processes according to *Max* composition rule for the other output linguistic variables in Table 3.5 can be programmed similarly.

```

void Inference_Max_Min() // firstly, perform Min rule; then, perform Max rule.
{
    unsigned char i,j;    // column and row indexes in Table 3.5
    for (i=0;i<5;i++)    // ('i' is Column index) x 5
    {
        for (j=0;j<5;j++) // ('j' is Row index) x 5
        {
            if (bnn_INPUT_1st[i] > bnn_INPUT_2nd [j])
            {
                u[i][j] = bnn_INPUT_2nd[j]; // Min composition rule
            }
            else u[i][j] = bnn_ INPUT_1st[i]; // Min composition rule
        }
    } // End of Min composition rule

    ...

    // Max composition rule for variable NZ in Table 3.5
    degree_NZ = max5(u[0][1],u[1][2],u[2][3],u[3][4],0);
}

```

```

// Max composition rule for variable ZE in Table 3.5
degree_ZE = max5(u[0][0],u[1][1],u[2][2],u[3][3],u[4][4]);

...

} // end of the function "Inference_Max_Min()"

```

- **Function for defuzzification process based on *center of sums* method:** This function is developed mainly according to (2.10)-(2.12) and *Example 2.6* presented in subsection 2.2.2.4. Wherein, firstly, the individual centroid position and acreage for the two output linguistic variables (NL, NM) in Figure 3.10 are presented for sample. As well, the similar processes for the other output linguistic variables in Figure 3.10 can be programmed additionally. After that, the program codes to compute the final output value of the FLC are shown.

```

void Defuzzification()
{
    float NL_c, NM_b, NM_c, NS_b, NS_c, NZ_b, NZ_c, ZE_b, ZE_c, PZ_b, PZ_c,
          PS_b, PS_c, PM_b, PM_c, PL_b; // peaks of trapezoidal shaded fuzzy sets
    float NL_cen, NM_cen, NS_cen, NZ_cen, ZE_cen, PZ_cen, PS_cen, PM_cen,
          PL_cen; // individual centroid positions of the shaded output fuzzy sets
    float NL_sh_area, NM_sh_area, NS_sh_area, NZ_sh_area, ZE_sh_area,
          PZ_sh_area, PS_sh_area, PM_sh_area, PL_sh_area; // shaded acreages
    float numerator, denominator;

    // For the output fuzzy set "NL" in Figure 3.10
    if (degree_NL > 0)
    {
        NL_b = -1; // peak position "NL"_b
        NL_c = -0.45 - degree_NL*(-0.45+1); // peak position "NL"_c
        NL_cen = centroid_cal(-1, NL_b, NL_c, -0.45); // use equation (2.11)
        // the shaded acreage of "NL"
        NL_sh_area = 0.5*degree_NL*((-0.45+1)+(NL_c-NL_b));
    }
    else
    {
        NL_cen = 0; NL_sh_area = 0;
    }

    // For the output fuzzy set "NM" in Figure 3.10
    if (degree_NM > 0)
    {
        NM_b = -1 + degree_NM*(-0.45+1); // peak position "NM"_b
        NM_c = -0.15 - degree_NM*(-0.15+0.45); // peak position "NM"_c
    }
}

```

```

        NM_cen = centroid_cal(-1,NM_b,NM_c,-0.15); // use equation (2.11)
        // the shaded acreage of “NM”
        NM_sh_area = 0.5* degree_NM*((-0.15+1)+(NM_c-NM_b));
    }
    else
    {
        NM_cen = 0; NM_sh_area = 0;
    }

    ...

    // “Center of Sums” defuzzification method in equation (2.10)
    numerator = NL_cen*NL_sh_area + NM_cen*NM_sh_area + NS_cen*NS_sh_area
        + NZ_cen*NZ_sh_area + ZE_cen*ZE_sh_area + PZ_cen*PZ_sh_area
        + PS_cen*PS_sh_area + PM_cen*PM_sh_area + PL_cen*PL_sh_area;

    denominator = NL_sh_area + NM_sh_area + NS_sh_area + NZ_sh_area +
        + ZE_sh_area + PZ_sh_area + PS_sh_area + PM_sh_area + PL_sh_area;

    if (denominator != 0)
    {
        output_value = numerator / denominator; // “Center of Sums” in equ. (2.10)
    }
} // end of the function “Defuzzification()”

```

- **Main function in the C program to call the functions presented above:**

```

void main() // main level of the program
{
    ...

    while(1) // always loop
    {
        ...

        Fuzzification_INPUT_1st(); // call the function of fuzzification for 1st input
        Fuzzification_INPUT_2nd(); // call the function of fuzzification for 2nd input
        Inference_Max_Min(); // call the function of Max-Min fuzzy inference
        Defuzzification(); // call the function of defuzzification for output
        ...
    } // end of the loop “while(1)”
} // end of the function “main()”

```

3.7.2. Evaluation of the used memory capacity and estimated computation time for FLC

For review and evaluation purposes, in this thesis, I develop separate programs in C language to implement sequentially five different FLCs as follows:

- The first FLC in which its first input has 3 linguistic variables (AZ, SM, ME in Figure 3.9), its second input also has 3 linguistic variables (AZ, SM, ME in Figure 3.9), its output has 5 linguistic variables (NS, NZ, ZE, PZ, PS in Figure 3.10), and it has $3 \times 3 = 9$ fuzzy rules (in Table 3.5).
- The second FLC in which its first input has 3 linguistic variables (AZ, SM, ME in Figure 3.9), its second input has 5 linguistic variables (AZ, SM, ME, LA, VL in Figure 3.9), its output has 7 linguistic variables (NL, NM, NS, NZ, ZE, PZ, PS in Figure 3.10), and it has 3 columns x 5 rows = 15 fuzzy association rules (in Table 3.5).
- The third FLC in which its first input has 5 linguistic variables (in Figure 3.9), its second input also has 5 linguistic variables (in Figure 3.9), its output has 9 linguistic variables (in Figure 3.10), and it has $5 \times 5 = 25$ fuzzy association rules (in Table 3.5). In fact, this FLC is utilized to study in this chapter and its basic sample program in C is presented in the previous subsection 3.7.1. Besides, the 25-rule FLC proposed in Chapter 4 (illustrated in Figures 4.11 and 4.12 and Table 4.1) can be programmed similarly with the 25-rule FLC proposed in Chapter 3.
- The fourth FLC in which its first input has 5 linguistic variables (NM, NS, ZE, PS, PM in Figure 5.8 in Chapter 5), its second input has 7 linguistic variables (in Figure 5.9), its output has 9 linguistic variables (in Figure 5.10), and it has 5 columns x 7 rows = 35 fuzzy rules (in Table 5.2).
- The fifth FLC in which its first input has 7 linguistic variables (in Figure 5.8), its second input also has 7 linguistic variables (in Figure 5.9), its output has 9 linguistic variables (in Figure 5.10), and it has $7 \times 7 = 49$ fuzzy rules (in Table 5.2). In fact, this FLC will be presented in Chapter 5.

The core clock speed of microcontroller (MCU) used for implementation of FLCs is $f_{clock_MCU} = 20 \text{ Mhz}$, so the computation time for an assembly command is given as: $T_{cycle_MCU} = 1 / f_{clock_MCU} = 0.05 \mu s$. The comparisons of the C programs for the five FLCs are shown in Table 3.8. Wherein, as listed in the fourth row of the table, C program for the “FLC with $5 \times 5 = 25$ rules” occupies 12926 bytes in read only memory (ROM), and uses 232 bytes in random access memory (RAM) of MCU with the normal case (and 420 bytes in RAM with the maximum case); besides, the program has 210 C commands, which are compiled by a compiler software to become around 4256 assembly commands, so the computation time is estimated approximately as $212.8 \mu s$ (in the case where each assembly command is executed completely within one cycle time $T_{cycle_MCU} = 0.05 \mu s$). In the last row of Table 3.8, the C program for the “FLC with $7 \times 7 = 49$ rules” occupies 15616 bytes in ROM, uses 344 bytes in RAM with the normal case (and 540 bytes in RAM with the maximum case), has the estimated computation time of $264.95 \mu s$ (in the case where each assembly command is executed completely within one cycle time $T_{cycle_MCU} = 0.05 \mu s$).

Table 3.8: Comparison of the C programs for the five FLCs

Fuzzy Logic Controller (FLC)	ROM (used)	RAM (used)	Estimated computation time (where: $T_{cycle_MCU} = 0.05 \mu s$)
FLC with 3x3 = 9 rules	8154 <i>bytes</i>	Normal case: 136 <i>bytes</i> ~ Max case: 268 <i>bytes</i>	$2448 \times T_{cycle_MCU} = 122.4 \mu s$ (2448 assembly commands, compiled from 124 C commands)
FLC with 3x5 = 15 rules	10486 <i>bytes</i>	Normal case: 176 <i>bytes</i> ~ Max case: 336 <i>bytes</i>	$3372 \times T_{cycle_MCU} = 168.6 \mu s$ (3372 assembly commands, compiled from 165 C commands)
FLC with 5x5 = 25 rules	12926 <i>bytes</i>	Normal case: 232 <i>bytes</i> ~ Max case: 420 <i>bytes</i>	$4256 \times T_{cycle_MCU} = 212.8 \mu s$ (4256 assembly commands, compiled from 210 C commands)
FLC with 5x7 = 35 rules	14342 <i>bytes</i>	Normal case: 280 <i>bytes</i> ~ Max case: 476 <i>bytes</i>	$4814 \times T_{cycle_MCU} = 240.7 \mu s$ (4814 assembly commands, compiled from 253 C commands)
FLC with 7x7 = 49 rules	15616 <i>bytes</i>	Normal case: 344 <i>bytes</i> ~ Max case: 540 <i>bytes</i>	$5299 \times T_{cycle_MCU} = 264.95 \mu s$ (5299 assembly commands, compiled from 289 C commands)

Whereas, in some MCUs, several special assembly commands may have to be executed within two cycle times ($2 \times T_{cycle_MCU} = 0.1 \mu s$), so the maximum computation time for the “FLC with 7x7 = 49 rules” is strictly limited at $2 \times 264.95 \mu s = 529.9 \mu s < 1 ms$. Of course, this is just the worst case where all assembly commands are supposed to be executed within two cycle times of MCU. Meanwhile, in real PV energy systems, including power-electronic converters, the sampling time for generating control signals is often larger than one millisecond (1 ms); in fact, dependent on each application, this sampling time is chosen from several milliseconds (such as 5 ms) to other larger values. As a result, in applying for real PV energy systems, all the five FLCs in Table 3.8 can be implemented fairly easily with an average-level MCU or digital signal processor (DSP), which should have at least 24 kilobytes ROM, 1 kilobytes RAM and 20 Mhz core clock speed. Moreover, nowadays, most of commercially modern MCU and DSP types have the really fast processing speed and very large internal ROM and RAM capacities; for example, the low-cost 32-bit MCU *TM4C123GH6PM* used in experiments in this chapter has 256 kilobytes ROM, 32 kilobytes RAM and maximum core clock speed of 80 Mhz [51]. Besides, the evaluations and discussions in this subsection also will be used for design process of two FLCs proposed in Chapter 4 and Chapter 5.

3.8. Summary of chapter

This chapter has presented a newly enhanced INC-MPPT algorithm based on fuzzy logic for stand-alone PV systems. Wherein, a novel 25-rule FLC has been developed to fine-tune appropriately the step-size $\Delta V(k)$ of the INC-MPPT algorithm to determine fast and exactly the optimal voltage where the PV array operates at the MPP. And this is to boost significantly the response speed in tracking the MPP as well as to diminish considerably the steady-state oscillations around the MPP in varying operating conditions. Within the 320W stand-alone PV system for demonstration, numerical simulations in MATLAB have shown that the suggested method has good performance in seeking the MPP even if the solar radiation and temperature abruptly vary. Moreover, experimental results have illustrated clearly the salient efficacy of this presented algorithm even within the partial shadow case. After that, the issue of partially shaded condition on large-scale PV arrays, which causes multiple (global and local) maximum power points on the P-V curve, and feasible efficient solutions for this issue are reviewed and discussed. Finally, a basic sample program in C language to implement the designed 25-rule FLC is shown for reference, and detailed evaluations of issues on the used memory capacity and the estimated computation time in implementing five different FLCs within MCU are performed and discussed.

Chapter 4

Fuzzy-based Control of Active and Reactive Powers with Feedback Linearization for Grid-Connected PV Inverters

This chapter is the second key study part of this thesis, which discusses about two control techniques based on the feedback linearization (FBL) method and fuzzy logic to regulate the active and reactive output AC powers of three-phase grid-connected PV inverters.

Nomenclatures used in this chapter

v_{ia}, v_{ib}, v_{ic}	Line-to-neutral output voltages of the PV inverter in the $a-b-c$ reference frame. (V)
i_{ia}, i_{ib}, i_{ic}	Line output currents of the PV inverter in the three-phase $a-b-c$ reference frame. (A)
v_{ga}, v_{gb}, v_{gc}	Line-to-neutral voltages of the utility grid. (V)
i_{ga}, i_{gb}, i_{gc}	Line currents of the utility grid. (A)
ω_g	Angular frequency of grid voltage. (rad/s)
v_{id}, v_{iq}	Output voltages of the PV inverter in the rotating $d-q$ reference frame. (V)
v_{gd}, v_{gq}	Grid voltages in the $d-q$ reference frame. (V)
i_{gd}, i_{gq}	Grid currents in the $d-q$ reference frame. (A)
P_g, Q_g	Three-phase apparent (VA), active (W), and reactive (Var) powers delivered to grid.
R_1, L_1	Per-phase resistance (Ω) and inductance (H) of transformer's low-voltage winding.
R_2, L_2	Per-phase resistance (Ω) and inductance (H) of transformer's high-voltage winding.
R_m, L_m	Per-phase resistance (Ω) and inductance (H) of transformer's magnetizing branch.

Superscripts used in this chapter

*	Reference value.
A^T	The transposed matrix of a matrix A.
(pu)	Value expressed in per-unit system.
(base)	Base value used in converting to per-unit system.

4.1. Introduction of chapter

In recent years, the three-phase grid-connected PV inverters are being broadly used in distributed generation systems to inject the energy into the grid [4],[6],[16]. And the key control goal in those PV inverters is clearly how to deliver effectively the active and reactive powers to the utility grid. According to [16], the output powers of grid-connected inverters can be indirectly controlled via regulating the relevant currents, hence the name *current-controlled* technique. Wherein, the most popular control method, the traditional PI control, is often utilized to regulate the currents. The main advantage of those PI controllers is the simplicity in implementation. However, traditional PI controllers suffer from the slow response and large overshoot especially when the reference values are changed suddenly. In addition, a modified PI control structure has been introduced in [6] to improve the response time of the traditional PI method. Nevertheless, this method produces fairly large fluctuations in output powers at steady-state.

Furthermore, as proposed in [17], the backstepping approach was adopted to control the active and reactive output powers. The approach can regulate independently the active and reactive output powers, and its response is better than the traditional PI control method. Nonetheless, this study did not propose any efficient method to reduce oscillations in the output powers. Additionally, in the previous study of mine [18], the author proposed a PID-Fuzzy hybrid controller for single-phase grid-connected PV inverters. In which, fuzzy logic controllers were designed to tune automatically three coefficients (K_P, K_I, K_D) of the PID controller. The suggested PID-Fuzzy controller actually has better performances than the traditional PID controller in both transient dynamics and steady state. Nevertheless, in this research, the proposed modeling technique might be optimized only for the single-phase grid-connected inverters.

Additionally, authors in [55] introduced the direct power control (DPC) based on lookup table (LUT) method. In detail, the method uses an optimal switching table to generate suitable control signals for the voltage source converter (VSC). The table is developed from the angular information of terminal voltage vector of the inverter and the instantaneous errors between the measured and desired values of active/reactive powers. Moreover, two modified LUT-DPC techniques based on the virtual flux vector and the constant-switching-frequency approach, respectively, have been proposed in [56] to lower the output-power ripple and current distortion of the ordinary LUT-DPC. Referring in [57], known as the major drawback, responses of the LUT-DPC techniques have an unexpectedly wide harmonic-distortion band which may cause difficulty to design output filters. Besides, an active and reactive power control scheme based on the sliding mode approach within the α - β reference frame was proposed in [57]. This technique has good responses in tracking the desired values in both transient and steady states. However, most state

variables used in this α - β -frame-based method are sinusoidal values instead of constant DC quantities in d - q -frame-based design approaches. So this issue may decrease the stability of the method, especially in the unbalanced condition of grid voltages.

On the other hand, the FBL approach is known as a common and powerful tool to design the controller for multi-variable nonlinear systems [21],[58]-[62]. The key idea of the FBL is to transform algebraically nonlinear systems into linear equivalent models while keeping exactly the original dynamics. After that, linear control methods can be applied to the equivalent models. This is also considered as a capable idea to overcome the enumerated drawbacks of the aforementioned techniques in controlling the output powers. In fact, authors in [21] adopted the FBL approach for the grid-interactive AC/DC converter; and as presented in [58], an efficient simplified FBL method is proposed to use for the grid-connected PV inverter. The two FBL-based schemes have fine performances in regulating the output currents of converters to the reference values; however, have not yet been considered within the parametric uncertainty and unbalanced grid voltage cases. Whereas, as described in [62], the FBL is really a model-based control method; so the undesired modeling errors and the unbalanced grid voltage sag may cause negative effects to its control quality. Consequently, this problem should be considered thoroughly, as reported in this chapter.

In this study, after completely checking the compatibility of the nonlinear state-model of three-phase grid-connected PV inverters with the principle of FBL approach, the authors present two FBL-based schemes to control active and reactive output powers of the PV inverter. They are the direct FBL approach and the proposed FBL-fuzzy logic (FBL-FL) hybrid technique. In the FBL-FL, a newly unique FLC is proposed to boost the effectiveness of the linear proportional-integral method applied in the direct FBL scheme. In detail, the designed FLC automatically tunes the gain coefficients of integral modules in the linear method to improve the response time and reduce the overshoot. Additionally, as the second function, the proposed FLC also complements suitably for the linear method to diminish oscillations in the output powers at the steady state. Besides, to simplify the modeling and design of controllers for the PV inverter, measured values of grid voltage and current are converted to per-unit values; and then are transformed to the rotating d - q reference frame. Simulation results, with the parametric variation and unbalance in grid voltages, are provided to evaluate the efficacy and the robustness of each FBL-based control structure.

The content in this chapter is developed from my 2nd published journal paper in List of Research Achievements at page 138 with newly added improvements, simulations and explanations in the subsections 4.3.2, 4.4, 4.5 and 4.6.

The remainder of this chapter is organized as follows. Section 4.2 shows the modeling of the demonstrative 100kW grid-connected PV inverter in per-unit. Design steps and theoretical stability

analysis of the two FBL-based structures are represented in the next section. Section 4.4 illustrates the implementation of PV inverter simulation in MATLAB, making use the Fuzzy-Logic and SimPowerSystems toolboxes. Simulation results, including verifications for parametric variation and unbalanced grid voltages, are shown in Section 4.5. Moreover, this section describes the comparison between the two FBL-based schemes and the traditional PI control in [16]. Finally, Section 4.6 is the conclusion of this chapter.

4.2. Modeling of the three-phase grid-connected PV inverter

4.2.1. Demonstrative PV inverter description

In this study, a three-phase grid-connected PV inverter with a rated power of 100kW is designed for demonstration. As seen in Figure 1, the energy obtained from PV array is transferred to the three-phase DC-AC three-level VSC, then synchronously delivered to the 10kV/60Hz utility grid via the 250V/10kV three-phase transformer. In addition, the R-L output filter is utilized to reduce high-frequency harmonics of the output current.

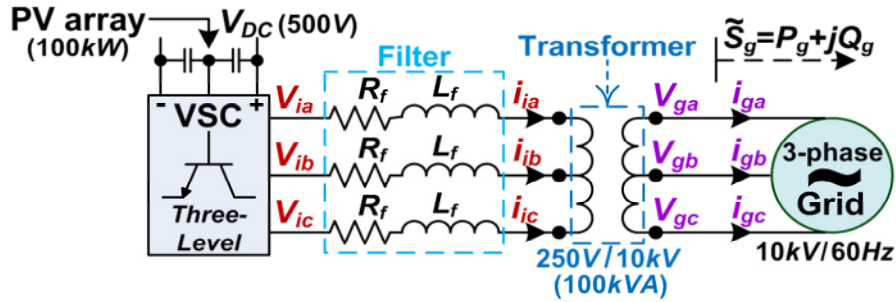


Figure 4.1: The demonstrative 100kW grid-connected PV inverter.

4.2.2. Demonstrative PV inverter modeling

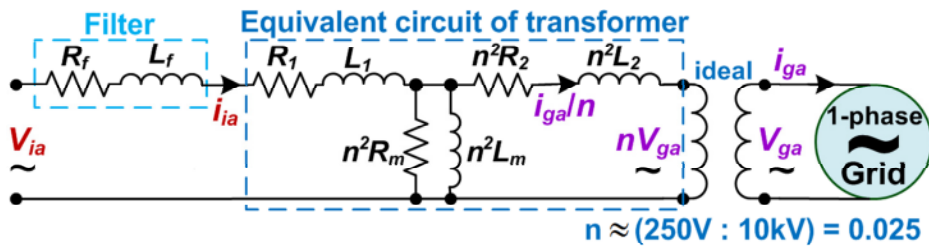


Figure 4.2: The single-phase equivalent circuit of the PV inverter.

From Figure 4.1, the single-phase equivalent circuit of the demonstrative grid-connected PV inverter, with the transformer's impedances referred to the low-voltage winding, is illustrated by Figure 4.2.

Besides, in the transformer, values of the magnetizing branch's resistance and inductance are generally extremely larger than values of the primary and secondary winding's resistance and inductance, respectively. In detail, this means that: $n^2 R_m \gg R_1$ and $n^2 L_m \gg L_1$. Thus, $n^2 R_m$ and $n^2 L_m$ can be disregarded in the modeling process, and the circuit shown in Figure 4.2 is now tantamount as below.

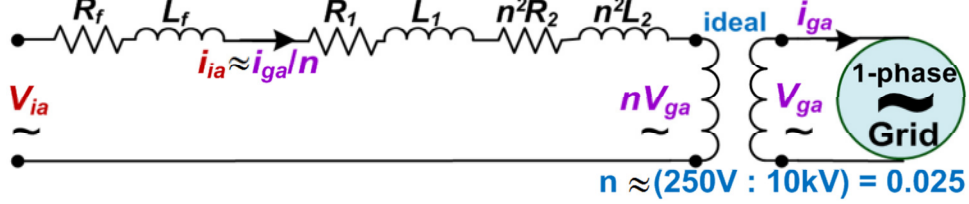


Figure 4.3: The single-phase equivalent circuit after $n^2 R_m$ and $n^2 L_m$ in Figure 4.2 were neglected.

According to the Kirchhoff's voltage law applied to the circuit represented in Figure 4.3, we have

$$v_{ia} = R_T \left(\frac{i_{ga}}{n} \right) + L_T \frac{d}{dt} \left(\frac{i_{ga}}{n} \right) + n v_{ga} \quad (4.1)$$

Where: $R_T = R_f + R_1 + n^2 R_2$, and $L_T = L_f + L_1 + n^2 L_2$.

According to [21],[43],[58],[63], most of the control structures for grid-connected PV inverters are often designed with the actual measured values of grid voltage, current and output powers. Consequently, the values of controllers' coefficients are normally very large. This may cause difficulties in determining and tuning those coefficients, especially in the grid-connected PV inverters within the high-power range.

Therefore, in this research, to simplify the design of control schemes for the PV inverter, a mathematic model of PV inverters based on the per-unit (pu) [64] is proposed as follows.

$$\begin{cases} V_{i, \text{line-to-line}}^{(base)} = 250 \text{ V} ; I_{i, \text{line}}^{(base)} = \frac{400}{\sqrt{3}} \text{ A} \\ V_{g, \text{line-to-line}}^{(base)} = 10 \text{ kV} ; I_{g, \text{line}}^{(base)} = \frac{10}{\sqrt{3}} \text{ A} \end{cases} \quad (4.2)$$

$$Z_i^{(base)} = \frac{V_{i, \text{line-to-line}}^{(base)}}{\sqrt{3} I_{i, \text{line}}^{(base)}} = 0.625 ; S_{g, 3-phase}^{(base)} = 100 \text{ kVA} \quad (4.3)$$

From (4.2) and (4.3), per-unit values for the voltages, currents, resistance, and inductance in (4.1) are computed by (4.4) and (4.5).

$$\begin{cases} v_{ia}^{(pu)} = \frac{v_{ia}}{V_{i,line-to-line}^{(base)}} ; v_{ga}^{(pu)} = \frac{v_{ga}}{V_{g,line-to-line}^{(base)}} = \frac{(nv_{ga})}{V_{i,line-to-line}^{(base)}} \\ i_{ia}^{(pu)} = \frac{i_{ia}}{I_{i,line}^{(base)}} = \left(\frac{i_{ga}}{n} \right) \frac{1}{I_{i,line}^{(base)}} = \frac{i_{ga}}{I_{g,line}^{(base)}} = i_{ga}^{(pu)} \end{cases} \quad (4.4)$$

$$R_T^{(pu)} = \frac{R_T}{Z_i^{(base)}} ; L_T^{(pu)} = \frac{2\pi f_{fuda} \times L_T}{Z_i^{(base)}} = \frac{120\pi \times L_T}{Z_i^{(base)}} \quad (4.5)$$

Using (4.4) and (4.5), equation (4.1) is now rewritten in the three-phase a - b - c reference frame with the per-unit values as below.

$$\begin{bmatrix} v_{ia}^{(pu)} \\ v_{ib}^{(pu)} \\ v_{ic}^{(pu)} \end{bmatrix} = R_T^{(pu)} \begin{bmatrix} i_{ga}^{(pu)} \\ i_{gb}^{(pu)} \\ i_{gc}^{(pu)} \end{bmatrix} + L_T^{(pu)} \frac{d}{dt} \begin{bmatrix} i_{ga}^{(pu)} \\ i_{gb}^{(pu)} \\ i_{gc}^{(pu)} \end{bmatrix} + \begin{bmatrix} v_{ga}^{(pu)} \\ v_{gb}^{(pu)} \\ v_{gc}^{(pu)} \end{bmatrix} \quad (4.6)$$

According to [6],[17], equation (4.6) can be expressed within the rotating d - q reference frame as follows.

$$\begin{cases} v_{id}^{(pu)} = R_T^{(pu)} i_{gd}^{(pu)} + L_T^{(pu)} \frac{di_{gd}^{(pu)}}{dt} - \omega_g L_T^{(pu)} i_{gq}^{(pu)} + v_{gd}^{(pu)} \\ v_{iq}^{(pu)} = R_T^{(pu)} i_{gq}^{(pu)} + L_T^{(pu)} \frac{di_{gq}^{(pu)}}{dt} + \omega_g L_T^{(pu)} i_{gd}^{(pu)} + v_{gq}^{(pu)} \end{cases} \quad (4.7)$$

Besides, the three-phase active and reactive output powers injected into the grid ($P_g^{(pu)}, Q_g^{(pu)}$) are computed by (4.8).

$$\begin{bmatrix} P_g^{(pu)} \\ Q_g^{(pu)} \end{bmatrix} = \frac{3}{2} \begin{bmatrix} v_{gd}^{(pu)} & v_{gq}^{(pu)} \\ v_{gq}^{(pu)} & -v_{gd}^{(pu)} \end{bmatrix} \begin{bmatrix} i_{gd}^{(pu)} \\ i_{gq}^{(pu)} \end{bmatrix} \quad (4.8)$$

where:

$$P_g^{(pu)} = \frac{P_g}{S_{g,3-phase}^{(base)}} = \frac{P_g}{10^5} ; Q_g^{(pu)} = \frac{Q_g}{S_{g,3-phase}^{(base)}} = \frac{Q_g}{10^5} \quad (4.9)$$

From (4.8), if the utility grid is in normal operation, this means that $\left[v_{gd}^{(pu)} \right]^2 + \left[v_{gq}^{(pu)} \right]^2 \neq 0$, $i_{g,dq}^{(pu)}$ and $i_{gq}^{(pu)}$ can be calculated by (4.10).

$$\begin{bmatrix} i_{gd}^{(pu)} \\ i_{gq}^{(pu)} \end{bmatrix} = \left(\frac{3}{2} \begin{bmatrix} v_{gd}^{(pu)} & v_{gq}^{(pu)} \\ v_{gq}^{(pu)} & -v_{gd}^{(pu)} \end{bmatrix} \right)^{-1} \begin{bmatrix} P_g^{(pu)} \\ Q_g^{(pu)} \end{bmatrix} \quad (4.10)$$

From (4.7), the differential equations of grid current are determined as described in (4.11).

$$\begin{cases} \frac{di_{gd}^{(pu)}}{dt} = -\frac{R_T^{(pu)}}{L_T^{(pu)}} i_{gd}^{(pu)} + \omega_g i_{gq}^{(pu)} - \frac{v_{gd}^{(pu)}}{L_T^{(pu)}} + \frac{1}{L_T^{(pu)}} v_{id}^{(pu)} \\ \frac{di_{gq}^{(pu)}}{dt} = -\frac{R_T^{(pu)}}{L_T^{(pu)}} i_{gq}^{(pu)} - \omega_g i_{gd}^{(pu)} - \frac{v_{gq}^{(pu)}}{L_T^{(pu)}} + \frac{1}{L_T^{(pu)}} v_{iq}^{(pu)} \end{cases} \quad (4.11)$$

Equation (4.11) can be expressed through the state model as

$$\begin{cases} \dot{x} = F(x) + G(x)u \\ y = H(x) \end{cases} \quad (4.12)$$

where:

- $x = \begin{bmatrix} i_{gd}^{(pu)} & i_{gq}^{(pu)} \end{bmatrix}^T$: are the state variables.
- $u = \begin{bmatrix} v_{id}^{(pu)} & v_{iq}^{(pu)} \end{bmatrix}^T$: are the input control signals.
- $F(x) = \begin{bmatrix} -\frac{R_T^{(pu)}}{L_T^{(pu)}} i_{gd}^{(pu)} + \omega_g i_{gq}^{(pu)} - \frac{v_{gd}^{(pu)}}{L_T^{(pu)}} \\ -\frac{R_T^{(pu)}}{L_T^{(pu)}} i_{gq}^{(pu)} - \omega_g i_{gd}^{(pu)} - \frac{v_{gq}^{(pu)}}{L_T^{(pu)}} \end{bmatrix}$
- $G(x) = \begin{bmatrix} 1/L_T^{(pu)} & 0 \\ 0 & 1/L_T^{(pu)} \end{bmatrix}$; $H(x) = \begin{bmatrix} i_{gd}^{(pu)} & i_{gq}^{(pu)} \end{bmatrix}^T$

4.3. The two FBL-based control schemes

The general structure of the two FBL-based control methods for the illustrative grid-connected PV inverter is described in Figure 4.4. In which, measured values of grid voltage and current are expressed in the rotating d - q reference frame to simplify the design of controllers. θ_g is the instantaneous phase angle of grid voltage, and detected by the Phase Lock Loop (PLL) module [6],[16]. To simplify the design of controller, the initial value of θ_g is often chosen as $\theta_g(t=0) = 0 \text{ rad}$. Besides, it should be noted that the two FBL-based control schemes are based on per-unit values of the relevant parameters. In detail,

- Then, from the values $i_{g,dq}^{*(pu)}$ calculated in (4.13) and the measured values of grid voltage-current ($v_{g,dq}^{(pu)}$, $i_{g,dq}^{(pu)}$), the Current Controller module defines the input control signals $v_{i,dq}^{*(pu)}$. Lastly, using the d - q to a - b - c transformation module, the actual reference signals for the PWM generator of VSC ($v_{i,abc}^{*(pu)}$) are determined. It is emphasized that the two control structures, namely, the direct FBL approach and the proposed FBL-FL hybrid technique, are implemented separately into the Current Controller module, as will be presented in the next two subsections 4.3.1 and 4.3.2, respectively.

4.3.1. The direct FBL control approach

From (4.12), the derivative of the system's outputs is given as

$$\dot{y} = \dot{x} = F(x) + G(x)u \quad (4.14)$$

As expressed in (4.14) and (4.12), relative degrees of each system's output are $r_1 = 1$ and $r_2 = 1$, respectively; with $r_1 + r_2 = 2$, is equal to the number of the system's state variables. In this case, the transformation to the linear equivalent model through FBL will be exact, without any unobservable state variables. Thus, the direct input-output FBL approach is fully compatible with the nonlinear system described in (4.12).

To force the actual grid currents $i_{g,dq}^{(pu)}$ to track closely their references $i_{g,dq}^{*(pu)}$, the virtual-control signals (β_d , β_q) can be chosen according to the linear proportional-integral technique as given by (4.15). Therein, the integrators are used to regulate the errors of grid current (e_d , e_q) to be zero and enhance robustness of the control system.

$$\begin{bmatrix} \beta_d \\ \beta_q \end{bmatrix} = \begin{bmatrix} \dot{y}_1 \\ \dot{y}_2 \end{bmatrix} = \begin{bmatrix} \dot{y}_1^* - K_{d1}e_d - K_{d2} \int e_d dt \\ \dot{y}_2^* - K_{q1}e_q - K_{q2} \int e_q dt \end{bmatrix} \quad (4.15)$$

where:

$$\begin{cases} e_d = y_1 - y_1^* = i_{gd}^{(pu)} - i_{gd}^{*(pu)} \\ e_q = y_2 - y_2^* = i_{gq}^{(pu)} - i_{gq}^{*(pu)} \end{cases} \quad (4.16)$$

and K_{d1} , K_{d2} , K_{q1} , K_{q2} are invariant positive values.

From (4.12), it is easy to prove that $G(x)$ is a nonsingular matrix. Hence, according to the FBL method presented in [60],[62], the input control signals are computed as

$$u^* = \begin{bmatrix} v_{id}^{*(pu)} \\ v_{iq}^{*(pu)} \end{bmatrix} = G^{-1}(x) \left(-F(x) + \begin{bmatrix} \beta_d \\ \beta_q \end{bmatrix} \right) \quad (4.17)$$

Substitute $G(x)$, $H(x)$ from (4.12), and β_d, β_q from (4.15) into (4.17), we have the input control signals as follows.

$$\begin{cases} v_{id}^{*(pu)} = R_T^{(pu)} i_{gd}^{(pu)} - \omega_g L_T^{(pu)} i_{gq}^{(pu)} + v_{gd}^{(pu)} + L_T^{(pu)} \beta_d \\ v_{iq}^{*(pu)} = R_T^{(pu)} i_{gq}^{(pu)} + \omega_g L_T^{(pu)} i_{gd}^{(pu)} + v_{gq}^{(pu)} + L_T^{(pu)} \beta_q \end{cases} \quad (4.18)$$

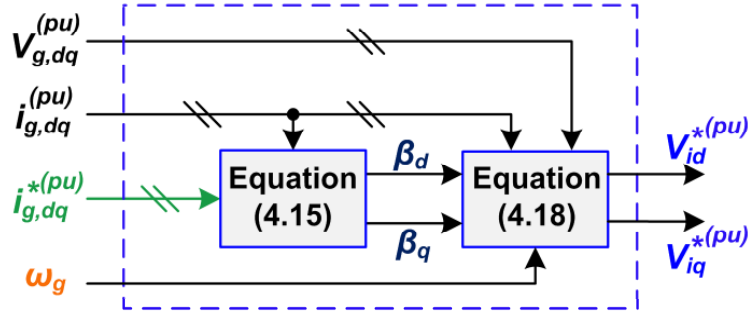


Figure 4.5: The detailed scheme of the direct FBL approach in the Current Controller module.

- **Assessment of stability of the direct FBL**

When the virtual-control signals (β_d, β_q) are chosen as (4.15), where the coefficients $(K_{d1}, K_{d2}, K_{q1}, K_{q2})$ are invariant positive values, the errors of grid current (e_d, e_q) will be governed according to the second-order functions in (4.19).

$$\begin{cases} \ddot{e}_d + K_{d1} \dot{e}_d + K_{d2} e_d = 0 \\ \ddot{e}_q + K_{q1} \dot{e}_q + K_{q2} e_q = 0 \end{cases} \quad (4.19)$$

4.3.2. The proposed FBL-FL hybrid control technique

As represented in Section 4.2, some physical parameters of the PV system, such as R_m, L_m , and internal resistors of semiconductor switches in the VSC, were disregarded in the modeling process. Moreover, in parametric uncertainties, design values of the parameters (R_T, L_T) in Figure 4.3 and (4.1) maybe not equal to their actual values. Furthermore, as shown in (4.15), since coefficients of the linear technique for making virtual-control signals, $K_{d1}, K_{d2}, K_{q1}, K_{q2}$, are fixed values; so modeling errors may cause the errors of grid current $(e_d$ and $e_q)$ to be significantly larger than zero. As an obvious consequence, those occurring errors (e_d, e_q) will produce large overshoots and steady-state fluctuations in the active and reactive output powers.

To solve the above problem, a unique FLC is proposed to enhance effectiveness of the linear technique applied in the direct FBL approach for generating the newly compatible final-virtual-control signals (β_d, β_q) as in Figure 4.6. Wherein, the proposed FLC is designed with two inputs and one output. In detail, the first FLC's input ($e_d(k)$ or $e_q(k)$) is the error between the measured value of grid current and its reference. And g_{d1} or g_{q1} is the scaling factor used for this input. Another input, $\beta_d^H(k-1)$ or $\beta_q^H(k-1)$, is the subtraction between the previous final-virtual-control signal ($\beta_d(k-1)$ or $\beta_q(k-1)$) and its mean value at the fundamental frequency of grid voltage ($\beta_d^M(k-1)$ or $\beta_q^M(k-1)$). The detailed characteristics of these values are illustrated by (4.20), (4.21) and Figure 4.7. Wherein, the fundamental frequency is $f_{fuda} = 60 \text{ Hz}$ with the electric grid utilized in this study.

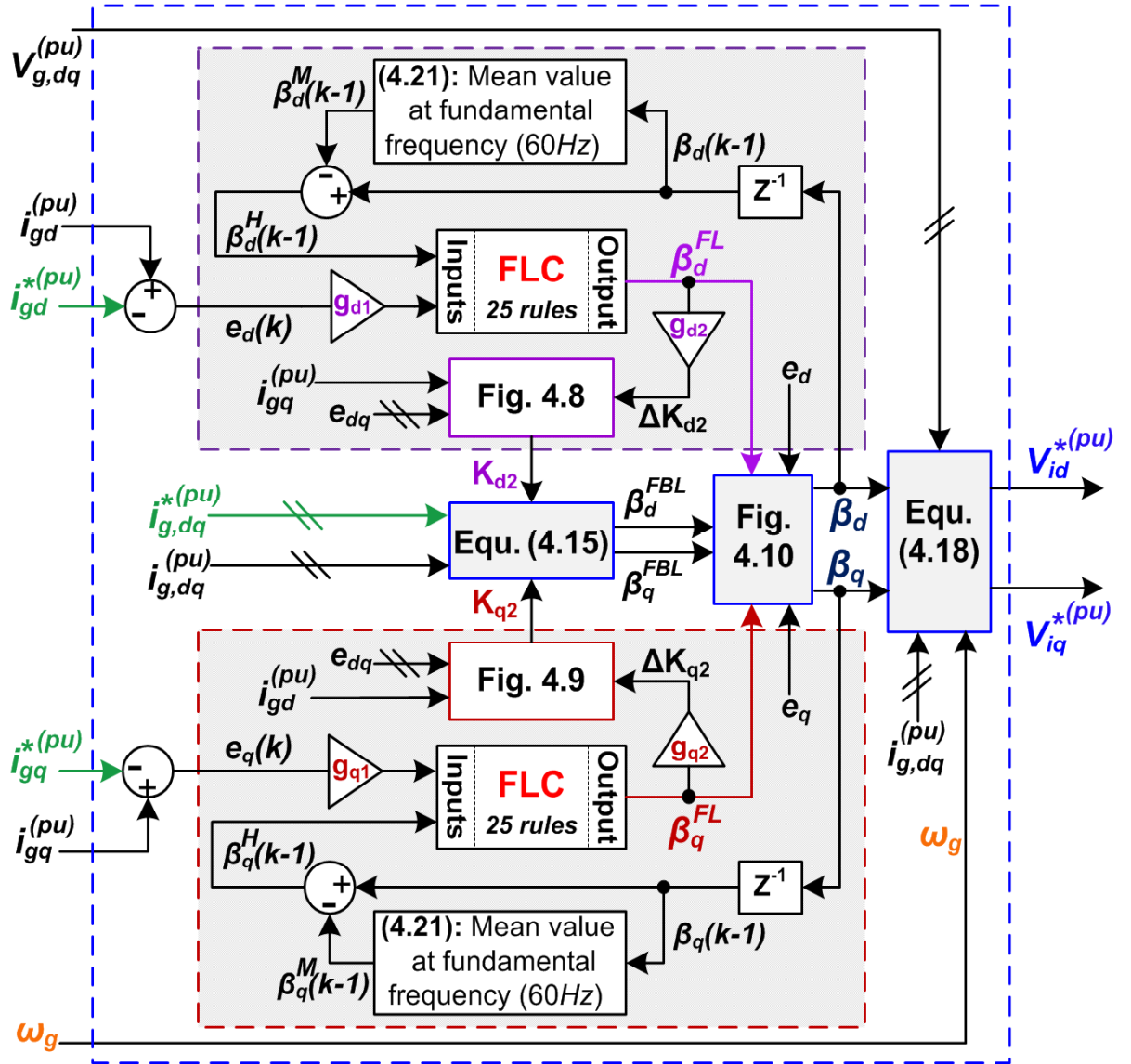


Figure 4.6: Particular structure of the proposed FBL-FL technique in the Current Controller module.

As presented in parts (c)-(d) of Figure 4.7, if $\beta_q^H(k-1)$ increases $e_q(k)$ will decrease, and vice versa. Similarly, impact of $\beta_d^H(k-1)$ on $e_d(k)$ is exactly the same as the effect of $\beta_q^H(k-1)$ on $e_q(k)$. And in this study, the above relationship between two FLC's inputs is the key idea to develop fuzzy membership functions and association rules shown in next subsections 4.3.2.1 and 4.3.2.2. Moreover, note that the first FLC used for $i_{gd}^{(pu)}$ (in the upper side of Figure 4.6) and the second FLC utilized for $i_{gq}^{(pu)}$ (in the lower side of Figure 4.6) are fully same in design structure. On the other hand, the two values (β_d^{FBL} and β_q^{FBL}) in Figure 4.6 currently denote for the two signals (β_d and β_q , respectively) in (4.15).

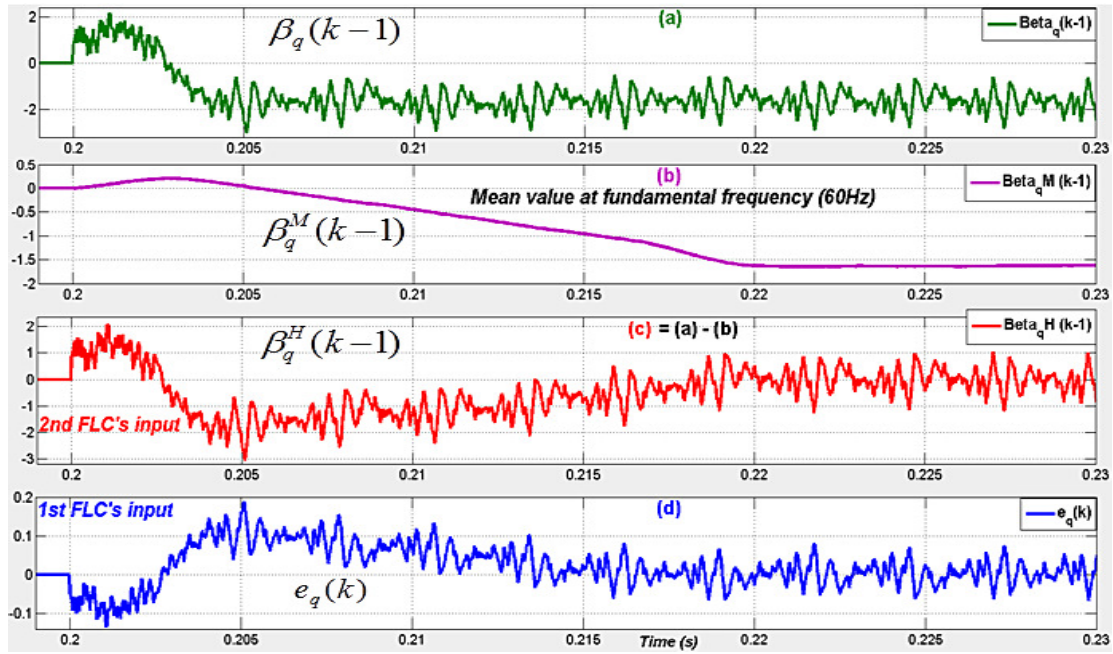


Figure 4.7: The characteristics of two inputs of the FLC.

$$\begin{cases} \beta_d^H(k-1) = \beta_d(k-1) - \beta_d^M(k-1) \\ \beta_q^H(k-1) = \beta_q(k-1) - \beta_q^M(k-1) \end{cases} \quad (4.20)$$

$$\text{where: } \begin{cases} \beta_d^M(k-1) = \frac{1}{T_{fuda}} \int_t^{t+T_{fuda}} \beta_d(k-1) dt \\ \beta_q^M(k-1) = \frac{1}{T_{fuda}} \int_t^{t+T_{fuda}} \beta_q(k-1) dt \end{cases} \quad (4.21)$$

and $T_{fuda} = 1/f_{fuda} = 1/60 \text{ s}$.

Besides, also shown in Figure 4.6, the FLC's output is an additional value, $\beta_d^{FL}(k)$ or $\beta_q^{FL}(k)$, utilized for two separate functions as follows.

- **The first function:**

That is to tune automatically the coefficients (K_{d2}, K_{q2}) of the integral modules in the linear method used in the direct FBL as shown in Figure 4.6. In detail, K_{d2} and K_{q2} in (4.15) are now the variable values and are adjusted suitably in the transient state by the designed FLC as expressed in Figures 4.8 and 4.9, respectively. Obviously, its objective is to boost the response speed and eliminate efficiently the overshoot of the output powers in the transient state, especially when the references ($P_g^{*(pu)}, Q_g^{*(pu)}$) are changed suddenly. Then, K_{d2} and K_{q2} will be maintained at the suitable fixed coefficients at the steady state to enhance stability of the proposed FBL-FL technique.

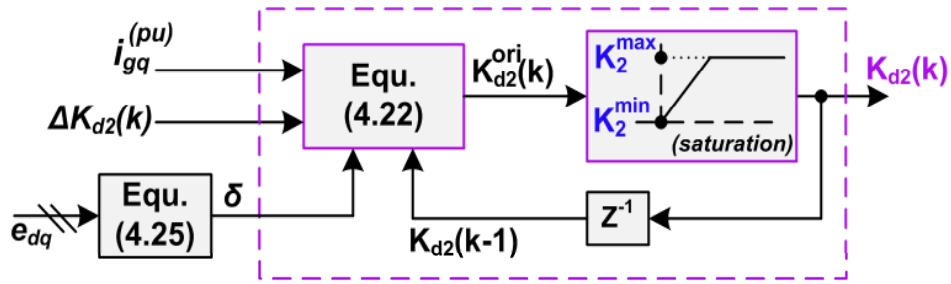


Figure 4.8: Tuning automatically the coefficient $K_{d2}(k)$ in the transient state.

$$K_{d2}^{ori}(k) = K_{d2}(k-1) + \left[1 - \delta(e_d^M, e_q^M)\right] \text{sgn}\left(-i_{sq}^{(pu)}\right) \Delta K_{d2}(k) \quad (4.22)$$

Where $\Delta K_{d2}(k) = g_{d2} \beta_d^{FL}(k)$ as described in Figure 4.6. The initial value of $K_{d2}(k)$ is $K_{d2}(0) = K_2^{min} > 0$.

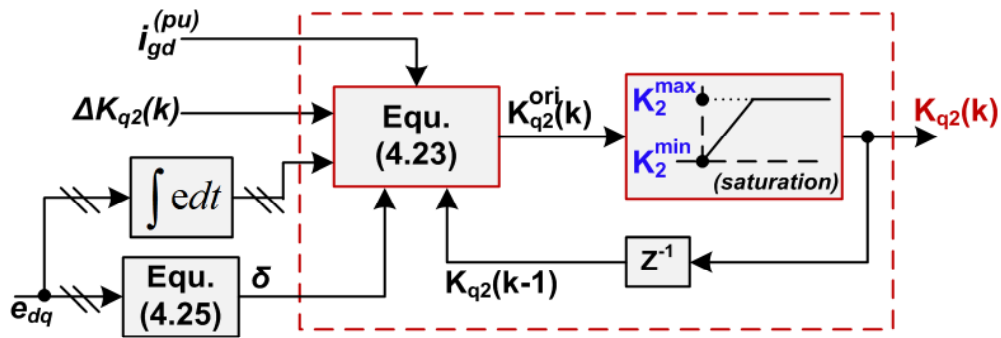


Figure 4.9: Tuning automatically the coefficient $K_{q2}(k)$ in the transient state.

$$K_{q2}^{ori}(k) = \begin{cases} K_{q2}(k-1) + \left[1 - \delta(e_d^M, e_q^M)\right] \text{sgn}\left(i_{gd}^{(pu)}\right) \Delta K_{q2}(k) & ; \text{if } \int e_q \geq 0. \\ K_{q2}(k-1) + \left[1 - \delta(e_d^M, e_q^M)\right] \text{sgn}\left(i_{gd}^{(pu)}\right) \Delta K_{q2}(k) \text{sgn}\left(-\int e_d\right) & ; \text{if else.} \end{cases} \quad (4.23)$$

Where $\Delta K_{q2}(k) = g_{q2}\beta_q^{FL}(k)$ as shown in Figure 4.6. And the initial value of $K_{q2}(k)$ is $K_{q2}(0) = K_2^{min} > 0$.

In (4.22) and (4.23), sgn is the sign function defined as expressed in (4.24); and $\delta(e_d^M, e_q^M)$ is the value to determine the current operation state of the controlled system, which is the transient or steady state, as described in (4.25).

$$\text{sgn}(z) = \begin{cases} 1 & ; \text{if } z > 0 \\ 0 & ; \text{if } z = 0 \\ -1 & ; \text{if } z < 0 \end{cases} \quad (4.24)$$

$$\delta(e_d^M, e_q^M) = \begin{cases} 1 & ; \text{if } \left\{ \begin{array}{l} |e_d^M(k)| \leq \varepsilon = 0.75\% \ll 1 \text{ pu} \\ \text{and } |e_q^M(k)| \leq \varepsilon = 0.75\% \ll 1 \text{ pu} \end{array} \right. \quad (\text{system is in steady state}). \\ 0 & ; \text{if else } (\text{system is in transient state}). \end{cases} \quad (4.25)$$

Where:

$$\begin{cases} e_d^M(k) = \frac{1}{T_{fuda}} \int_t^{t+T_{fuda}} e_d(k) dt \\ e_q^M(k) = \frac{1}{T_{fuda}} \int_t^{t+T_{fuda}} e_q(k) dt \end{cases} \quad (4.26)$$

In electric power systems, the measured value of grid current generally includes the component at the fundamental frequency and the harmonic values. Thus, in the steady state, when the output powers are regulated closely to the references, the mean values of the errors of grid current at the fundamental frequency (e_d^M, e_q^M) become tiny (nearly zero); this means that $|e_{d,q}^M| \rightarrow \varepsilon \ll 1 \text{ pu}$. Normally, in order to satisfy well control qualities, the steady-state error must be regulated to be smaller than 7.5% of the reference value. Besides, the operation value of reference signal is often used from 10% to 100% of its nominal value ($\pm 1 \text{ pu}$); this means that the absolute value of reference signal is usually in the interval $[0.1 \text{ pu} \ 1 \text{ pu}]$. So the limitation value ε can be chosen as $7.5\% \times 0.1 \text{ pu} = 0.75\% \text{ pu}$, which seems small enough to be used for almost operation cases.

In this study, as shown in (4.25) and (4.26), where ε is chosen as $0.75\% \text{ pu}$, the PV system will be in the transient state if $\delta(e_d^M, e_q^M) = 0$, or at the steady state if $\delta(e_d^M, e_q^M) = 1$. Thus, according to the value $[1 - (e_d^M, e_q^M)]$ as expressed in (4.22) and (4.23), the first function of FLC's output is activated only in the transient state when $\delta(e_d^M, e_q^M) = 0$. This means that the two coefficients

(K_{d2}, K_{q2}) are variable values in transient states to improve the transient dynamics, and then are fixed values at steady states to enhance stability of the proposed method.

As seen in Figures 4.8 and 4.9, the positive limitation values (K_2^{min}, K_2^{max}) of saturation modules and the output scaling factors (g_{d2}, g_{q2}) must be chosen suitably to ensure stability of the control system. In this chapter, the detailed process to determine these values will be presented in subsection 4.3.2.4.

Interpretation for parameter variables of sgn in (4.22) and (4.23):

In the first equation of (4.18), since the reactance $\omega_g L_T^{(pu)}$ is often very larger than the resistance $R_T^{(pu)}$, and $v_{gd}^{(pu)}$ is normally a DC fixed quantity [6],[65], so $v_{id}^{*(pu)}$ is mostly dependent on the changes of $-i_{gq}^{(pu)}$ and β_d . Therefore, to eliminate thoroughly the impact of $-i^{(pu)}$ on $v_{id}^{*(pu)}$, the change of β_d must be contra with the variation of $-i_{gq}^{(pu)}$. On the other hand, in the first equation of (4.15), the alteration of β_d is also in opposition to the variation of $K_{d2} \int e_d dt$. Furthermore, in this study, because the active power $P_g^{(pu)}$ is controlled only with non-negative value within the range of $[0 \text{ pu } 1 \text{ pu}]$, the grid current $i_{gd}^{(pu)}$ has value in the range $[0 \text{ pu } 1 \text{ pu}]$. As a consequence, the modification of K_{d2} should be driven in the same direction of the variation of $-i^{(pu)}$. After checking carefully with simulation results in this study, to tune K_{d2} appropriately, the parameter variable in the sgn function in (4.22) should be chosen as $-i_{gq}^{(pu)}$.

Similarly, from the second formulas in (4.18) and (4.15), the change of K_{q2} should be in the same direction of the variation of $i_{gd}^{(pu)}$. Hence, to adjust K_{q2} properly, the parameter variable in the sgn function in the upper part of (4.23) should be selected as $i_{gd}^{(pu)}$ in the case where $\int e_q \geq 0$. Besides, since the reactive power $Q_g^{(pu)}$ is controlled with both negative and positive values in the range of $[-1 \text{ pu } 1 \text{ pu}]$, the grid current $i_{gq}^{(pu)}$ has value in the range of $[-1 \text{ pu } 1 \text{ pu}]$; therefore, the integral value $\int e_q$ in (4.15) may change suddenly its sign (negative/positive) in some special circumstances. According to the opposite signs between the two values $\omega_g L_T^{(pu)} i_{gd}^{(pu)}$ and $-\omega_g L_T^{(pu)} i_{gq}^{(pu)}$ in (4.18) and checking on simulation results, the additional consideration of the integral value $-\int e_d$ in (4.15) is necessary in tuning K_{q2} where $\int e_q < 0$. As a result, to fine-tune

K_{q2} appropriately in the case where $\int e_q < 0$, parameter variables in the sgn functions should be chosen with $i_{gd}^{(pu)}$ and $-\int e_d$ as shown in the lower part of (4.23).

- **The second function:**

As shown in Figure 4.6 and Figure 4.10, the FLC's output ($\beta_d^{FL}, \beta_q^{FL}$) is also used to complement properly for the final-virtual-control signal (β_d, β_q) to reduce efficiently fluctuations in the output powers at the steady state. Additionally, to avoid unexpected bad impacts on transient responses of the output powers, this function is activated only when the PV inverter operates in the steady state.

Besides, as given by (4.25) and (4.26), the controlled PV system will be in the steady state if $\delta(e_d^M, e_q^M) = 1$. So, conversely with the first function that is only activated in the transient state when $\delta(e_d^M, e_q^M) = 0$, this second function of FLC's output is only activated at the steady state when $\delta(e_d^M, e_q^M) = 1$ as described in Figure 4.10 and (4.27).

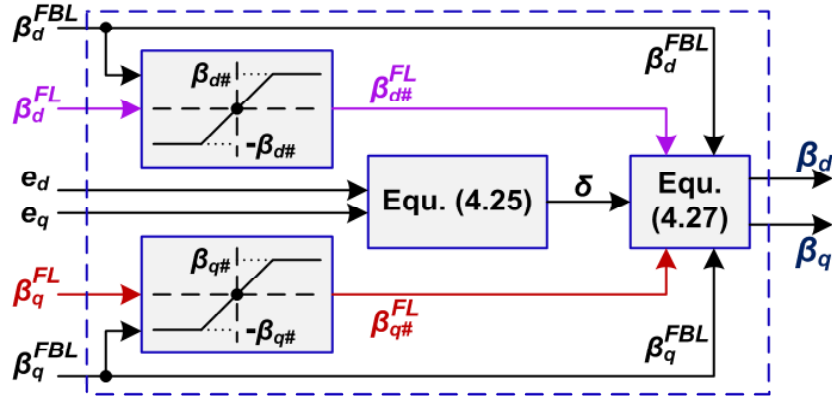


Figure 4.10: The detailed structure of the second function of the proposed FLC's output.

$$\begin{bmatrix} \beta_d(k) \\ \beta_q(k) \end{bmatrix} = \begin{bmatrix} \beta_d^{FBL}(k) \\ \beta_q^{FBL}(k) \end{bmatrix} + \delta(e_d^M, e_q^M) \begin{bmatrix} \beta_d^{FL}(k) \\ \beta_q^{FL}(k) \end{bmatrix} \quad (4.27)$$

As shown in Figure 4.10 and (4.27), $\beta_{d\#}^{FL}$ and $\beta_{q\#}^{FL}$ are the output signals of β_d^{FL} and β_q^{FL} respectively after the saturation modules. About making the final-virtual-control signals (β_d, β_q) in (4.27), notice that the values from (4.15) in Figure 4.6, β_d^{FBL} and β_q^{FBL} , are the major components; meanwhile, $\beta_{d\#}^{FL}$ and $\beta_{q\#}^{FL}$ are complementary quantities for β_d^{FBL} and β_q^{FBL} , respectively. Thus, as seen in Figure 4.10, the saturation modules should be used to limit the value ranges of $\beta_{d\#}^{FL}$ and $\beta_{q\#}^{FL}$ in order to maintain compatibility of the final-virtual-control signals (β_d, β_q) with (4.18).

In detail, if the limitation value of saturation module ($\beta_{d\#}$ or $\beta_{q\#}$) is big, such as larger than 40% of $|\beta_d^{FBL}|$ or $|\beta_q^{FBL}|$, $\beta_{d\#}^{FL}$ or $\beta_{q\#}^{FL}$ may affect negatively to β_d or β_q ; which leads to harm

stability of the system. Conversely, if the limitation value ($\beta_{d\#}$ or $\beta_{q\#}$) is tiny, such as smaller than 10% of $|\beta_d^{FBL}|$ or $|\beta_q^{FBL}|$, $\beta_{d\#}^{FL}$ or $\beta_{q\#}^{FL}$ cannot help reduce efficiently oscillating signals in β_d or β_q . So the range [10% 40%] could be used to examine in determining a suitable value for $\beta_{d\#}$ or $\beta_{q\#}$. In this study, after checking simulation results, those limitation values can be chosen as 25% of $|\beta_d^{FBL}|$ or $|\beta_q^{FBL}|$ as expressed in (4.28).

$$\begin{cases} \beta_{d\#}(k) = 0.25 \times |\beta_d^{FBL}(k)| \\ \beta_{q\#}(k) = 0.25 \times |\beta_q^{FBL}(k)| \end{cases} \quad (4.28)$$

As a result, the second function of FLC's output is used as an output filter for the virtual-control signals (β_d, β_q) in the steady state. In detail, its objective is to shape the signal forms of β_d and β_q to be smoother. And this will help diminish the harmonic distortions of grid current in order to lower efficiently oscillations in the output powers, especially in parametric uncertain conditions.

In summary, as described above, the proposed FBL-FL technique will have two main objectives. Those are to inherit advantages of the direct FBL approach (in quick response, robustness) and to reduce overshoot in transient responses and fluctuations of the output powers at steady states. For more detail, a sample operation of the two functions of the proposed FLC can be found in Figure 4.18 and Figure 4.19 in the subsection 4.5.1.

The fuzzification, fuzzy association rules and defuzzification of the proposed FLC are shown in the next three subsections 4.3.2.1, 4.3.2.2 and 4.3.2.3, respectively.

4.3.2.1. Fuzzification

In the study of this chapter, the two inputs of the proposed FLC ($e_d(k), \beta_d^H(k-1)$) have both negative and positive values; so the number of linguistic variables for each FLC's input ($N_{variable}$) should be an odd value to can divide into three groups as negative linguistic variables, 'zero' variable and positive linguistic variables. Obviously, the value of $N_{variable}$ cannot be 1 due to the very bad control quality. Moreover, if the value of $N_{variable}$ is 3, linguistic variables of each FLC's input will have one negative value, 'zero' value and one positive value; this clearly cannot perform a good control quality owing to the little number of control cases. Besides, as shown in Figure 4.6, the proposed FBL-FL technique utilizes two FLCs; thus, if the value of $N_{variable}$ is chosen as 7, according to the reviews in Table 3.8 and subsection 3.7.2, the total computation time of two FLCs may become pretty long. As a result, the value of $N_{variable}$ should be chosen as 5, which is the most suitable value on considering between the control quality and total computation time. On the

other hand, in the case where two inputs of the FLC have the same quantity of linguistic variables (such as 5), the table of fuzzy association rules (such as Tables 3.5 and 4.1) is often a symmetric fuzzy rule table. This can help the design of fuzzy association rules to become relatively simpler. Of course, the symmetric type of fuzzy rule table is just an optional priority in the design process. In summary, the proposed FLC in this chapter has two inputs, in which each input has 5 linguistic variables, and has $5 \times 5 = 25$ fuzzy association rules.

Two inputs: have five linguistic variables, membership function, and value in the interval of [-1 1].

- $e_d(k)$ or $e_q(k) = \{\text{Negative Large, Negative Small, Zero, Positive Small, Positive Large}\}$
 $= \{\text{NL, NS, ZE, PS, PL}\}$
- $\beta_d^H(k-1)$ or $\beta_q^H(k-1) = \{\text{Negative Large, Negative Small, Zero, Positive Small, Positive Large}\}$
 $= \{\text{NL, NS, ZE, PS, PL}\}$

The output: has seven linguistic variables and the value in [-1 1]

$$\beta_d^{FL}(k) \text{ or } \beta_q^{FL}(k) = \{\text{Negative Large, Negative Medium, Negative Small, Zero, Positive Small, Positive Medium, Positive Large}\}$$

$$= \{\text{NL, NM, NS, ZE, PS, PM, PL}\}$$

Membership functions:

The membership functions for the two inputs and output of the FLC are described in Figure 4.11 and Figure 4.12, respectively.

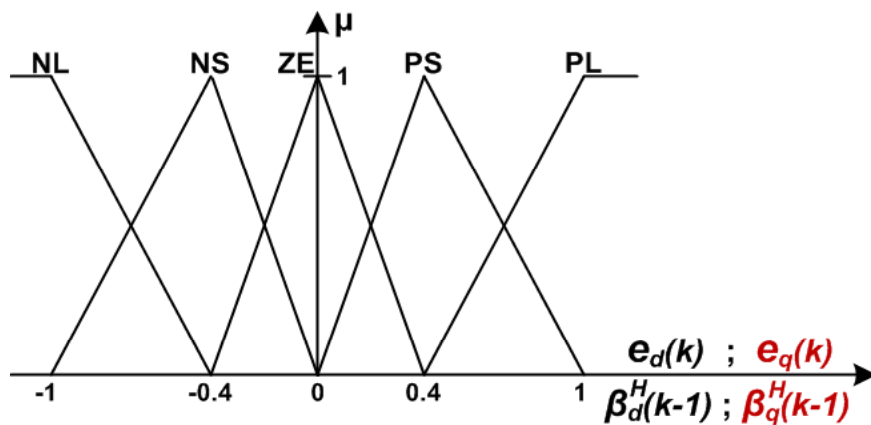


Figure 4.11: The membership function for the two FLC's inputs.

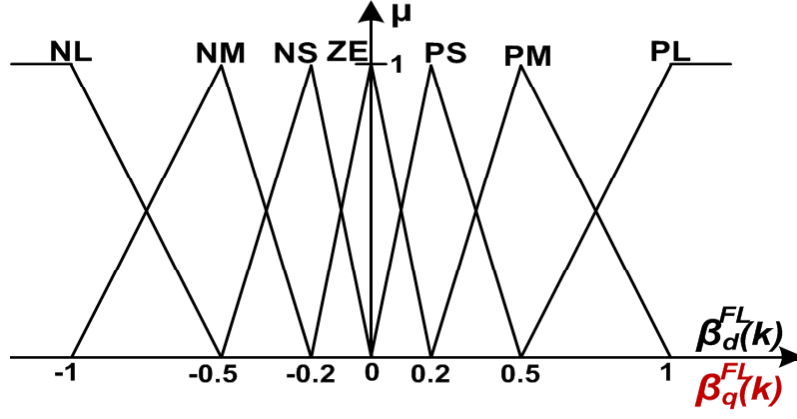


Figure 4.12: The membership function for the FLC's output.

On the other hand, it can be seen that the two FLC's inputs have the same linguistic variables, value interval in $[-1 \ 1]$, and membership functions as given by Figure 11. However, as shown in part (d) of Figure 4.7, the first FLC's input, $e_q(k)$, varies in the interval $[-0.1 \ 0.2]$, and is actually almost bounded in $[-0.1 \ 0.1]$ at the steady state. Thus, the scaling factor for this FLC's input (see Figure 4.6), g_{q1} , should be chosen in the value interval $[4 \ 10]$ to force $e_q(k)$ into the full scale of designed range $[-1 \ 1]$. Similar interpretation can be used to explain about the value range $[4 \ 10]$ for g_{d1} . And it means that every facultative value in the range $[4 \ 10]$ may be used for the scaling factors g_{d1}, g_{q1} . In this study, after checking simulation results, the suitable value for g_{d1} and g_{q1} is chosen as 4 (see Table 4.3). In the authors' idea, tuning manually values for the input scaling factors (g_{d1}, g_{q1}) seems simpler and more efficient than developing additionally linguistic-variables, value interval, and membership functions, which are specified only for the first FLC's input (e_d, e_q) . This will help simplify fairly much in the design process of the proposed FLC in simulation systems (and in experiments if any).

4.3.2.2. Fuzzy association rules

The fuzzy associative matrix is described in Table 4.1. It has totally $5 \times 5 = 25$ rules, and each rule is represented in the form “**if...then...**”. A sample rule is expressed as follows: “**if** $e_q(k)$ is NL and $\beta_q^H(k - 1)$ is PL **then** $\beta_q^{FL}(k)$ is NL”.

The fuzzy rules are developed according to the authors' logical deduction from observing impacts of the second FLC's input on the first FLC's input illustrated by parts (c)-(d) of Figure 4.7. Furthermore, in this research, the fuzzy association rules have been also optimized by the trial-and-error method.

Table 4.1: Fuzzy association rules of the proposed FLC.

$\beta_d^{FL}(k)$ or $\beta_q^{FL}(k)$		$\beta_d^H(k-1)$ or $\beta_q^H(k-1)$				
		NL	NS	ZE	PS	PL
$e_d(k)$ or $e_q(k)$	NL	ZE	NS	NM	NL	NL
	NS	PS	ZE	NS	NM	NL
	ZE	PM	PS	ZE	NS	NM
	PS	PL	PM	PS	ZE	NS
	PL	PL	PL	PM	PS	ZE

Interpretation for the fuzzy association rules:

As given by Table 4.1, the sample rule expressed as “**if** $e_q(k)$ is NL and $\beta_q^H(k-1)$ is PL **then** $\beta_q^{FL}(k)$ is NL”, is now used for analysis. In this case, because the error $e_q(k)$ is NL (negative large), it means that the grid current $i_{gq}^{(pu)}$ is now very smaller than its desired value $i_{gq}^{(pu)}$; meanwhile,

$\beta_q^H(k-1)$ is the PL (positive large) value. According to parts (c) and (d) of Figure 4.7, the error $e_q(k)$ may continue to decrease quickly; and this means that the decrement of $i_{gq}^{(pu)}$ will be sustained. To resolve this problem thoroughly, the final virtual-control signal β_q needs to be adjusted with a negative large quantity (β_q must be decreased significantly) to force $i_{gq}^{(pu)}$ to increase drastically and rapidly. Therefore, $\beta_q^{FL}(k)$ should be assigned as NL (negative large).

Whereas, in another case, $e_q(k)$ is still NL as same with the above condition, but $\beta_q^H(k-1)$ is now changed to NL (negative large). This means that the grid current $i_{gq}^{(pu)}$ has the tendency in increasing automatically to its reference $i_{gq}^{*(pu)}$. To avoid the large overshoot, the final virtual-control signal β_q should be kept invariant. So, in this situation, the complement value $\beta_q^{FL}(k)$ could be chosen as ZE (zero). In general, the similar deductive method can be utilized to interpret for other fuzzy rules shown in Table 4.1.

4.3.2.3. Fuzzy inference and defuzzification

In this study part, the *Max-Min* composition operation and the *centroid* (CoA: center of area) method, which are presented in Chapter 2 of this thesis and in [22],[23], are utilized for the fuzzy rule inference and the defuzzification, respectively.

4.3.2.4. Stability analysis for the proposed FBL-FL

- For the first function of proposed FLC's output

The first equation in (4.19) is rewritten as follows:

$$\begin{bmatrix} \dot{e}_d \\ \ddot{e}_d \end{bmatrix} = \begin{bmatrix} 0 & 1 \\ -K_{d2} & -K_{d1} \end{bmatrix} \begin{bmatrix} e_d \\ \dot{e}_d \end{bmatrix} \quad (4.29)$$

Set variables as

$$\gamma = [e_d \ \dot{e}_d]^T ; \ \phi = (\phi_1, \phi_2) = (K_{d1}, K_{d2})$$

Equation (4.29) can be expressed in an affine model [66]-[68]

$$\dot{\gamma}(t) = A(\phi)\gamma(t) \quad (4.30)$$

where:

$$A(\phi) := A_0 + \phi_1 A_1 + \phi_2 A_2 \quad (4.31)$$

$$A_0 = \begin{bmatrix} 0 & 1 \\ 0 & 0 \end{bmatrix}; \ A_1 = \begin{bmatrix} 0 & 0 \\ 0 & -1 \end{bmatrix}; \ A_2 = \begin{bmatrix} 0 & 0 \\ -1 & 0 \end{bmatrix}$$

In the proposed FBL-FL technique, the factor K_{d1} for proportional module in (4.15) is always a fixed positive value, and same with the one in the direct FBL. Meanwhile, according to Figure 4.8, the factor K_{d2} for integral module in (4.15) is a variant positive value in the transient state, and then is a fixed positive value at the steady state. So the following stability analysis is used for the transient state.

Ranges of value and rate-of-change of K_{d1}, K_{d2} can be defined in (4.32) and (4.33).

$$\begin{cases} \phi_1 = K_{d1} \in [K_1^{\min} \ K_1^{\max}] \\ \phi_2 = K_{d2} \in [K_2^{\min} \ K_2^{\max}] \end{cases} \quad (4.32)$$

$$\begin{cases} \left| \frac{d\phi_1}{dt} \right| = \left| \frac{dK_{d1}}{dt} \right| = 0 \\ \left| \frac{d\phi_2}{dt} \right| = \left| \frac{dK_{d2}}{dt} \right| = \left| \text{sgn}(-i_{gq}^{(pu)}) \times (g_{d2} \beta_d^{FL}) \right| \leq \Delta K_2^{\max} \end{cases} \quad (4.33)$$

$K_1^{\min}, K_1^{\max}, K_2^{\min}, K_2^{\max}, \Delta K_2^{\max}$ are positive constants.

Let ϕ_{mean} signify the average value of the parameter vector ϕ as follows:

$$\phi_{mean} = (\phi_{1,mean}, \phi_{2,mean}) = \left(\frac{K_1^{\min} + K_1^{\max}}{2}, \frac{K_2^{\min} + K_2^{\max}}{2} \right) \quad (4.34)$$

Since $\phi_{1,mean}$ and $\phi_{2,mean}$ are invariant positive values; thus, from (4.31), two eigenvalues of the matrix $A(\phi_{mean})$ have negative real-parts. As a result, $A(\phi_{mean})$ is stable.

Let \mathfrak{S} and \mathfrak{R} signify the sets of corners of the parameter box in (4.32) and the rate-of-change box in (4.33), respectively. According the *Theorem 3.2* in [66] and because $A(\phi_{mean})$ is stable, the system in (4.30) is affinely quadratically stable if there exist three symmetric matrices P_0, P_1, P_2 such that

$$P(\phi) := P_0 + \phi_1 P_1 + \phi_2 P_2 \quad (4.35)$$

where $P(\phi)$ must satisfy (4.36) and (4.37):

$$L(v, \xi) = A(v)^T P(v) + P(v) A(v) + P(\xi) - P_0 < 0 \quad (4.36)$$

for all $(v, \xi) \in \mathfrak{S} \times \mathfrak{R}$

$$A_j^T P_j + P_j A_j \geq 0 \quad \text{for } j=1, 2. \quad (4.37)$$

When the two constraints (4.36) and (4.37) are feasible, a Lyapunov function for stability of the system (4.30) will be given by

$$V(\gamma, \phi) := \gamma^T P(\phi) \gamma \quad (4.38)$$

From the above explanations, the main mission in this study is to find suitable values for the five positive parameters ($K_1^{\min}, K_1^{\max}, K_2^{\min}, K_2^{\max}, \Delta K_2^{\max}$) in order to ensure the two constraints (4.36) and (4.37) to be feasible.

Firstly, note that the sampling time used for generating control signal is $T_{s_control} = 100 \mu s = 10^{-4} s$, and the FLC's output β_d^{FL} is bounded in the interval $[-1 \ 1]$ as shown in Figure 4.12. Therefore, to avoid fast variation of the coefficient $K_{d2}(k)$ computed in Figure 4.8, the value of positive coefficient g_{d2} in (33) should be smaller than $T_{s_control}$. Besides, K_2^{\min} is the initial value for $K_{d2}(k)$, it means that $K_{d2}(0) = K_2^{\min}$; hence, K_2^{\min} is often chosen as a tiny positive value. In this study, to be simple, K_2^{\min} can be chosen as $K_2^{\min} = T_{s_control} = 10^{-4}$ as a sufficiently small value.

The process in analyzing stability of the system in (4.30) will be performed with *LMI Control Toolbox* of MATLAB [69]. Wherein, specified values for the five parameters manually chosen to test are shown in (4.39) and (4.40).

$$K_1^{\min} = 15 ; K_1^{\max} = 16 \quad (4.39)$$

$$\begin{cases} K_2^{\min} = T_{s_control} = 10^{-4} ; K_2^{\max} = 1 \\ \Delta K_2^{\max} = \left| g_{d2} \beta_d^{FL} \right|_{\max} = 0.2 \times T_{s_control} = 0.2 \times 10^{-4} \end{cases} \quad (4.40)$$

As expressed in (4.40), we have $\Delta K_2^{\max} = 0.2 \times 10^{-4}$; consequently, according to Figure 4.8 and (4.33), $K_{d2}(k)$ will be a slowly-varying positive parameter in the transient state. The MATLAB program used for stability analysis with the specified parameter box in (4.32)-(4.33) and (4.39)-(4.40) is shown as below:

```
A0 = ltisys([0 1; 0 0])           % A0
A1 = ltisys([0 0; 0 -1], 0)       % A1 (for K-d1)
A2 = ltisys([0 0; -1 0], 0)       % A2 (for K-d2)

pv = pvec('box', [15 16; 1e-4 1], [0 0; -0.2e-4 0.2e-4])
                                   % box: [K-d1; K-d2]; [d(K-d1); d(K-d2)]

ps = psys(pv,[A0 A1 A2])         % Affine parameter-dependent model

% CHECK STABILITY with the prescribed parameter box:

tmin = quadstab(ps)               % command "quadstab": Quadratic Stability

[tmin_2,P0,P1,P2] = pdlstab(ps)   % command "pdlstab": Parameter-Dependent-Lyapunov Stability
```

And results of the above analysis in MATLAB are obtained as follows:

```
This system is quadratically stable

tmin =
    -5.8116e-04           % Negative value shows the system is stable
    ...

This system is stable for the specified parameter trajectories

tmin_2 =
    -0.0012               % Negative value shows the system is stable

P0 =                      % The symmetric matrix P0
    1.0e+03 *
    4.0276   -0.0019
```

```

-0.0019  0.0301

P1 =                                % The symmetric matrix P1
330.4938  0.7575
0.7575   -12.4014

P2 =                                % The symmetric matrix P2
54.6665   -271.0764
-271.0764  21.6456

```

According to all the above results obtained with two stability analysis tools (*quadstab* and *pdlstab* commands) in *LMI Control Toolbox* [69], the system in (4.30) is stable (in both transient and steady states) with the specified parameter box in (4.39) and (4.40). Wherein, K_{d1} can be chosen as a facultative fixed value in the range of [15 16]; meanwhile, K_{d2} is a slowly-varying coefficient in the range of $[10^{-4} \ 1]$ in the transient state and then has the fixed value at the steady state. As well, the stability analysis for the second-order system defined by the second equation in (4.19) can be performed similarly. In summary, the specified parameter values in (4.39) and (4.40) will be used to simulate as shown in Table 4.3 to ensure stability of the proposed FBL-FL hybrid technique.

- **For the second function of proposed FLC's output**

In the second function of FLC's output, with two saturation blocks as described in Figure 4.10 and (4.28), $\beta_{d\#}^{FL}$ and $\beta_{q\#}^{FL}$ are bounded in $\pm 25\%$ of $|\beta_d^{FBL}|$ and $|\beta_q^{FBL}|$ respectively as expressed in (4.41). Then, from (4.27) and (4.41), the final-virtual-control signals (β_d, β_q) will be limited as given by (4.42).

$$\begin{cases} -0.25 \times |\beta_d^{FBL}(k)| \leq \beta_{d\#}^{FL}(k) \leq 0.25 \times |\beta_d^{FBL}(k)| \\ -0.25 \times |\beta_q^{FBL}(k)| \leq \beta_{q\#}^{FL}(k) \leq 0.25 \times |\beta_q^{FBL}(k)| \end{cases} \quad (4.41)$$

$$\begin{cases} 0.75 \times \beta_{d\#}^{FL}(k) \leq \beta_d(k) \leq 1.25 \times \beta_{d\#}^{FL}(k) \\ 0.75 \times \beta_{q\#}^{FL}(k) \leq \beta_q(k) \leq 1.25 \times \beta_{q\#}^{FL}(k) \end{cases} \quad (4.42)$$

According to (4.42), as a result, the second function of FLC's output (illustrated by Figure 4.10) will also not reduce considerably the stability of the controlled PV system.

4.4. Simulation settings in MATLAB

In MATLAB simulations, a detailed model of the illustrative 100kW grid-connected PV inverter is designed with the Fuzzy-Logic and SimPowerSystems toolboxes [70],[18]. In detail, the detailed simulation model is built according to Figures 4.4 to 4.6. Besides, to ensure the PV inverter can supply multi-level values of active and reactive powers, an unlimited DC voltage source with the output $V_{DC} = 500V$ is connected to the input of three-level dc-ac VSC [71]. From [70] and [57], the detailed model can be simulated in discrete time with two different sampling times. Namely, the first one utilized for the detailed simulation model and measurement is $T_{s_power} = 1 \mu s$; and the other used for generating control signals is $T_{s_control} = 100 \mu s$.

On the other hand, for comparison and assessment purpose, the traditional PI control method in [16] is also implemented into the Current Controller module shown in Figure 4.4(a) to regulate the grid currents as illustrated by Figure 4.13.

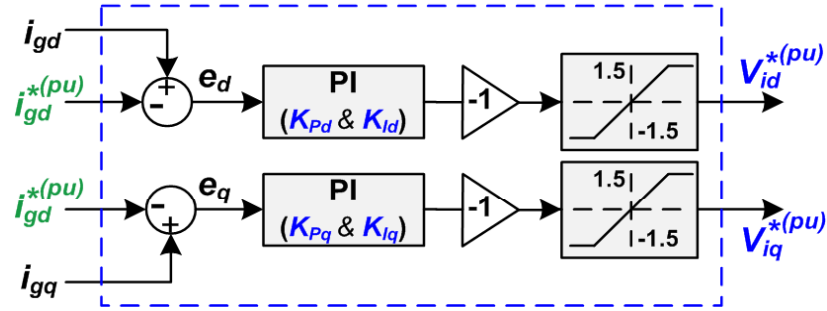


Figure 4.13: Traditional PI controllers from [16] implemented into the Current Controller module in Figure 4.4(a).

Table 4.2 shows the nominal design parameters of the switching PV inverter. Additionally, Table 4.3 gives the design coefficients of the PI controllers and the two FBL-based control schemes.

Table 4.2: Nominal parameters of the PV inverter

Module	Parameter and Value
DC link voltage	$V_{DC} = 500 \text{ V}$
R-L output filter [70]	$R_f = 2 \text{ m}\Omega$; $L_f = 250 \mu H$
Per-phase parameters of the transformer in per-unit value (Figure 4.2, [70])	$R_1^{(pu)} = 0.001 \text{ pu}$; $L_1^{(pu)} = 0.03 \text{ pu}$ $R_2^{(pu)} = 0.001 \text{ pu}$; $L_2^{(pu)} = 0.03 \text{ pu}$ $R_m^{(pu)} = 500 \text{ pu}$; $L_m^{(pu)} = 500 \text{ pu}$
Line-to-line grid voltage (RMS value)	$V_{g, \text{line-to-line}} = 10 \text{ kV}$
Initial phase angle of grid voltage (Figure 4.4)	$\theta_g(t=0) = 0 \text{ rad}$

Table 4.3: Design coefficients of the three control schemes.

Control scheme	Parameter and Value
The PI control (Figure 4.13)	$K_{pd} = K_{pq} = 0.5$; $K_{Id} = K_{Iq} = 20$
The direct FBL (Figure 4.5)	$K_{d1} = K_{q1} = 16$; $K_{d2} = K_{q2} = 0.2$
The proposed FBL-FL (Figure 4.6)	$K_{d1} = K_{q1} = 16$; $g_{d1} = g_{q1} = 4$; $g_{d2} = g_{q2} = 0.2 \times T_{s_control}$

The PV inverter starts to run at the time $t = 0.2$ s; and the desired values of active and reactive output powers (with *Case 1* to *Case 3* in next subsections 4.5.1 to 4.5.3, respectively) are changed according to step functions in four periods as follows.

- From the time $t = 0.2$ s to $t = 0.35$ s : $P_g^{*(pu)} = 0.8$ pu and $Q_g^{*(pu)} = 0$ pu
- From the time $t = 0.35$ s to $t = 0.5$ s : $P_g^{*(pu)} = 0.8$ pu and $Q_g^{*(pu)} = -0.6$ pu
- From the time $t = 0.5$ s to $t = 0.65$ s : $P_g^{*(pu)} = 0.2$ pu and $Q_g^{*(pu)} = -0.6$ pu
- From the time $t = 0.65$ s to $t = 0.8$ s : $P_g^{*(pu)} = 0.2$ pu and $Q_g^{*(pu)} = 0.6$ pu

where the actual values, P_g^* and Q_g^* , can be computed by (4.9).

On the other hand, with *Case 4* in subsection 4.5.4, the reference values of active and reactive output powers are altered according to ramp functions.

4.5. Simulation results and discussions

4.5.1. Case 1: Simulation without the parametric uncertainties and the unbalanced grid voltage sag

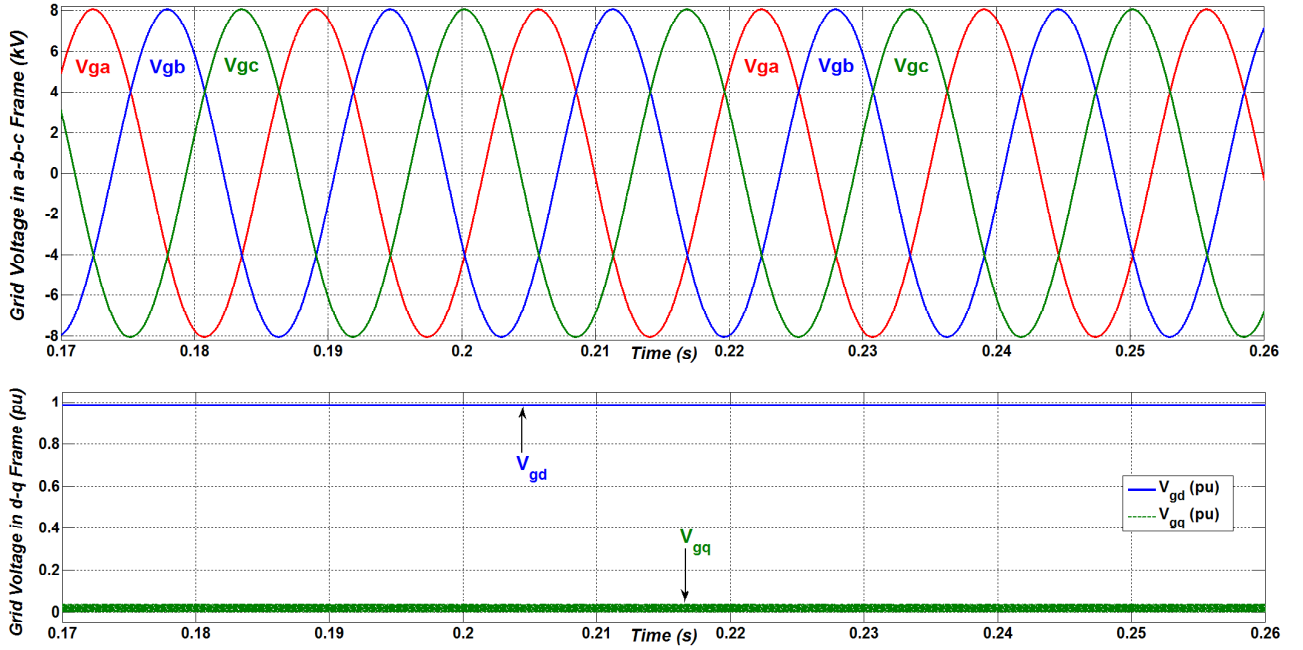


Figure 4.14: The balanced grid voltage expressed in the a - b - c and the rotating d - q reference frames.

In this case, the parameters of the designed PV inverter and the controllers are according to Table 4.2 and Table 4.3 respectively. As well, the three-phase grid voltage is balanced and kept at the nominal value during the operation time as shown in the upper part of Figure 4.14. The lower part of this figure illustrates the per-unit DC values of grid voltage ($v_{gd}^{(pu)}$, $v_{gq}^{(pu)}$) in the rotating d - q reference frame used in this case.

Performances of the illustrative PV inverter using the traditional PI control in Figure 4.13, the direct FBL approach and the proposed FBL-FL hybrid technique are shown in Figure 4.15, Figure 4.16 and Figure 4.17, respectively.

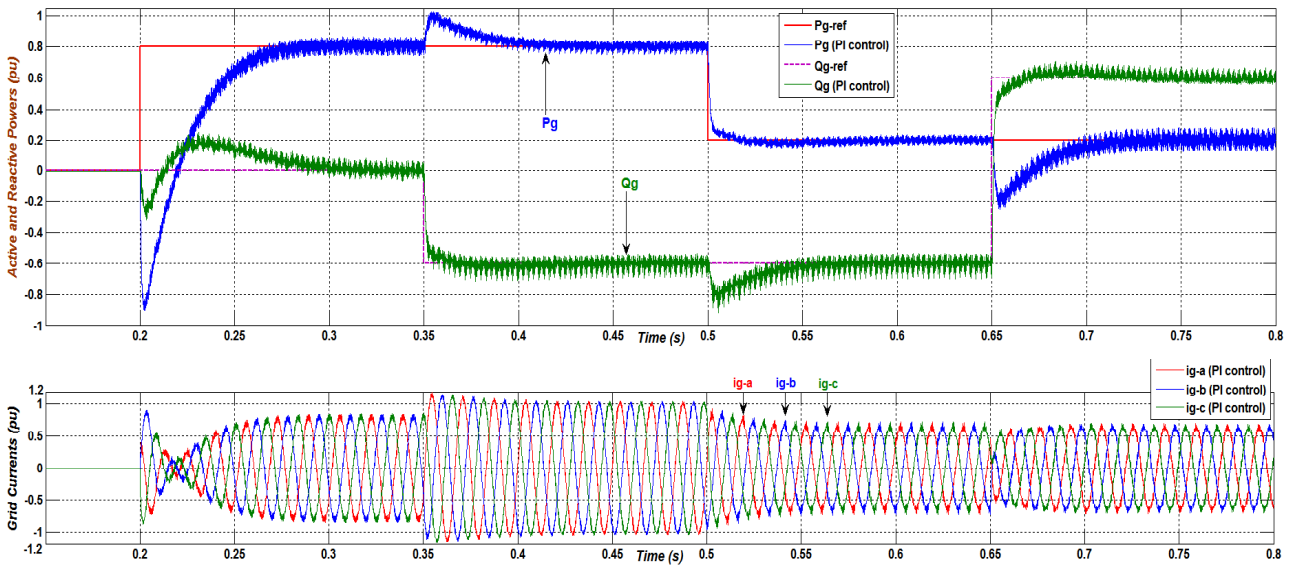


Figure 4.15: The performance with the traditional PI control in *Case 1*.

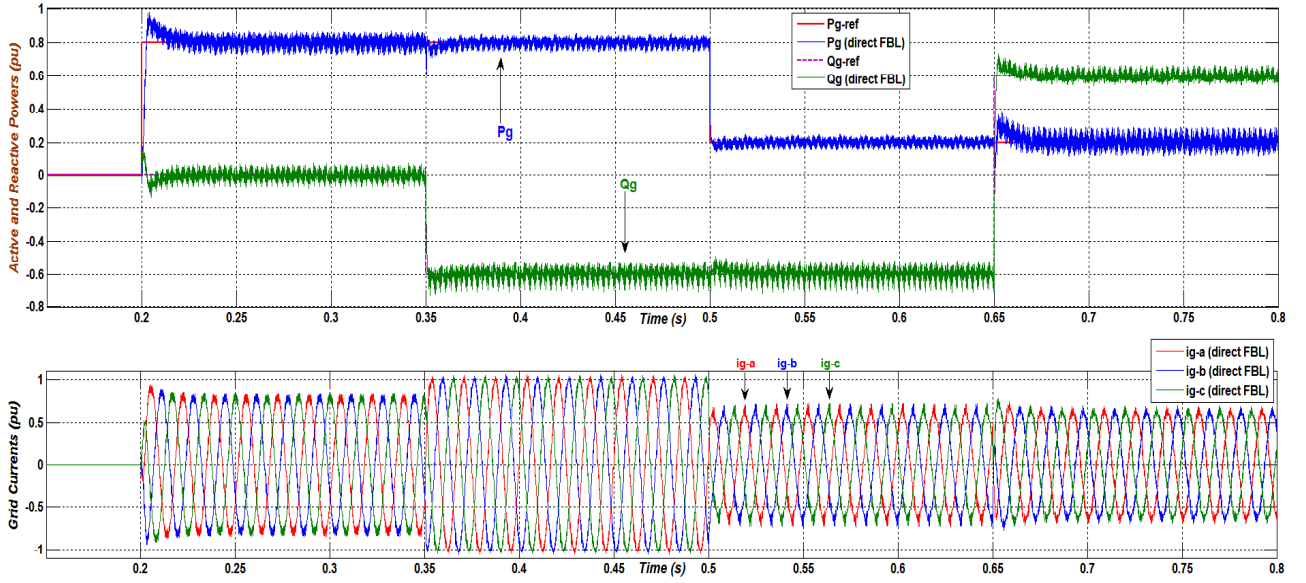


Figure 4.16: The performance with the direct FBL approach in *Case 1*.

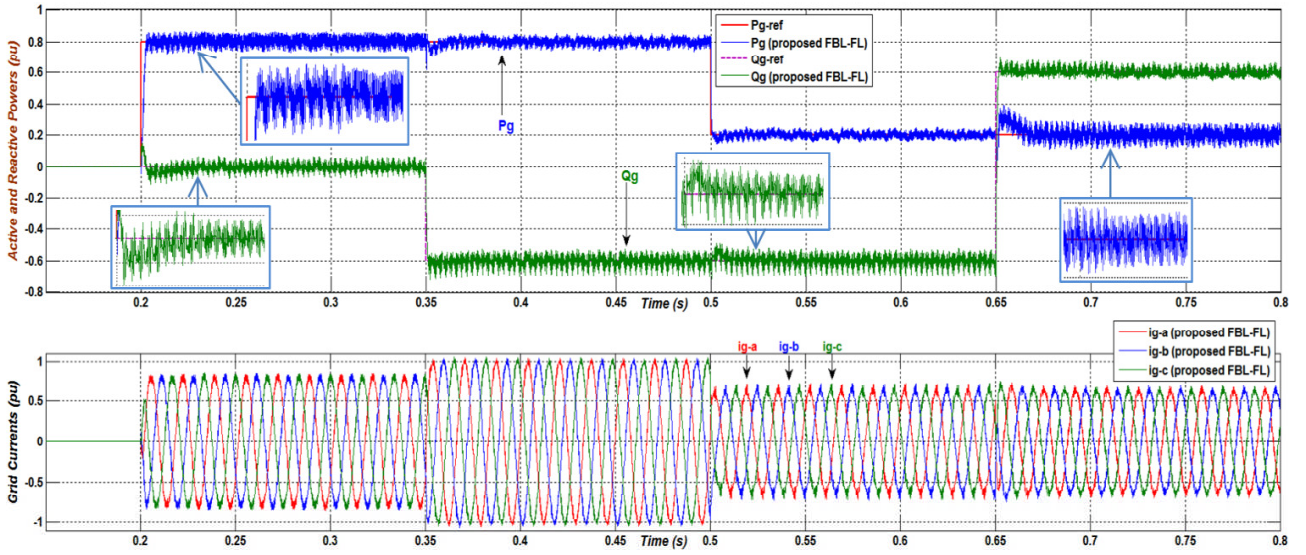


Figure 4.17: The performance with the proposed FBL-FL hybrid technique in *Case 1*.

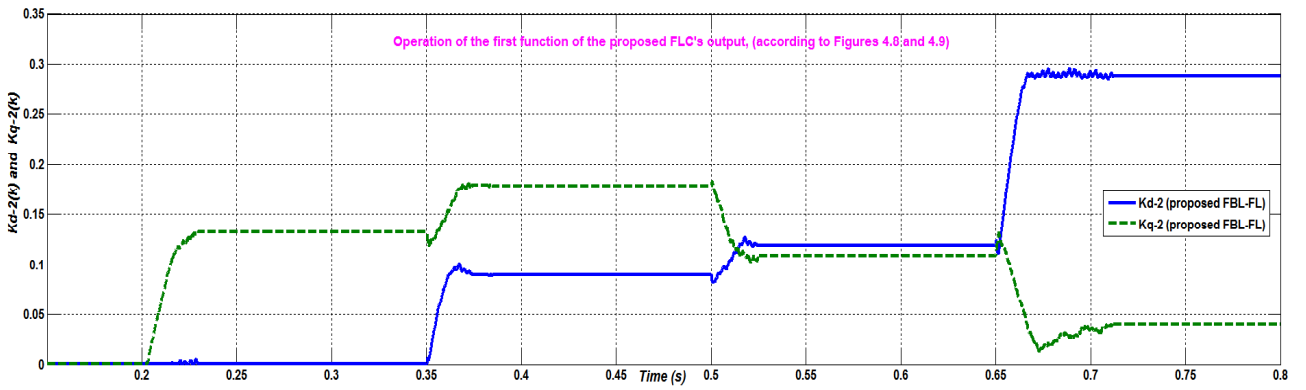


Figure 4.18: Variable values of K_{d2} , K_{q2} with the proposed FBL-FL hybrid technique in *Case 1*.

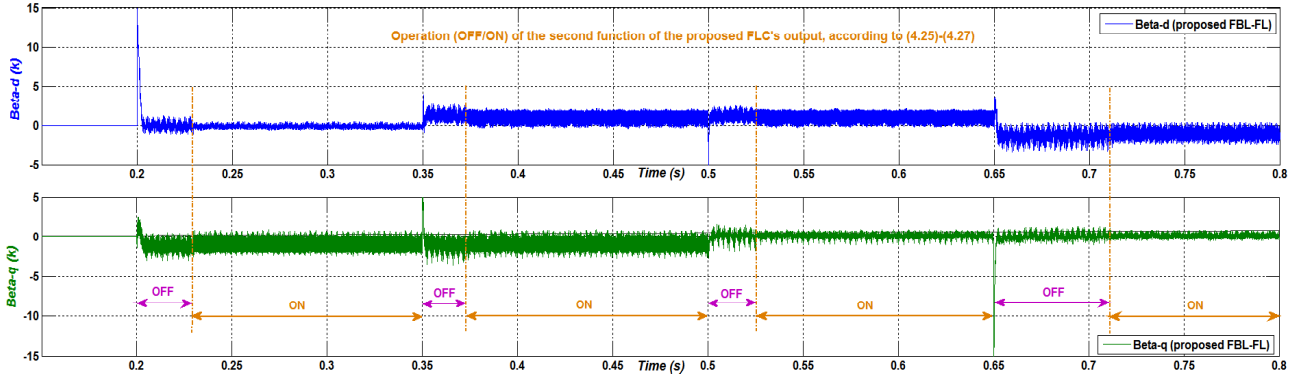


Figure 4.19: Values of β_d, β_q and operation of the second FLC's function of the FBL-FL in *Case 1*.

According to the results given by those figures, all the control methods can regulate independently active and reactive output powers to the reference values. In detail, firstly, as seen in Figure 4.15, the performance of the traditional PI control has the little fluctuations in the output powers; nevertheless, it includes the large overshoots and very slow response. Whereas, the direct FBL shows fast response and fairly small oscillations in output powers at steady states as described in Figure 4.16. However, it produces quite large overshoots at step changes of reference signals at $t = 0.2 \text{ s}$ and at $t = 0.65 \text{ s}$. Finally, Figure 4.17 represents that the proposed FBL-FL not only inherits the advantage of the direct FBL in terms of rapid response, but also eliminates significantly the overshoots in transient states (especially when the references are changed at $t = 0.2 \text{ s}$ and $t = 0.65 \text{ s}$) and decreases steady-state fluctuations in the output powers.

Operations of two functions of the proposed FLC in the FBL-FL hybrid technique are illustrated in Figure 4.18 and Figure 4.19 respectively. In detail, according to the first FLC's function presented in Figure 4.8 and Figure 4.9, the coefficients K_{d2}, K_{q2} are now tuned automatically and suitably in the transient states, and then are kept at the fixed values at the steady states, as described in Figure 4.18. In fact, this assists to eliminate the large overshoot in transients. Besides, the impact of the second FLC's function on the virtual-control signals β_d, β_q are represented in Figure 4.19. Wherein, the shapes of the signal forms of β_d and β_q become smoother when the second FLC's function is activated (to be ON) at the steady states. This helps reduce the harmonic distortion of grid current. And as a result, oscillations in the output powers with the proposed FBL-FL are kept nearly equal to those with the PI control.

Moreover, Table 4.4 shows the total harmonic distortion (THD) of grid current measured at the steady state in periods: from the time $t = 0.3 \text{ s}$ to $t = 0.35 \text{ s}$, and from $t = 0.45 \text{ s}$ to $t = 0.5 \text{ s}$. Therein, in the results attained with the proposed FBL-FL, compared to the direct FBL, the second FLC's function aided to lower THD from 4.85 % to 4.34 %, and from 3.85 % to 3.40 %, respectively. Besides, THD values with the proposed FBL-FL are equivalent to the ones obtained from the

traditional PI control. The statistics in this table are consistent with the responses as observed in Figures 4.15 to 4.17.

Table 4.4: THD of grid current in *Case 1*.

Control scheme	THD of grid current (%)	
	From $t = 0.3 \text{ s}$ to $t = 0.35 \text{ s}$	From $t = 0.45 \text{ s}$ to $t = 0.5 \text{ s}$
The PI control	4.33 %	3.31 %
The direct FBL	4.85 %	3.85 %
The proposed FBL-FL	4.34 %	3.40 %

4.5.2. Case 2: Simulation within parametric uncertainties and without unbalanced grid voltage sag

In this situation, the actual values of the parameters in Figure 4.3 and (4.1), R_T and L_T , are smaller of 30% as compared with the original values, and shown in Table 4.5. Notice that the parameters used in the detailed model of the demonstrative PV inverter are now based on Table 4.5; meanwhile, the design coefficients utilized in the PI controllers and the two FBL-based schemes are still according to Tables 4.2 and 4.3. Besides, the three-phase grid voltage is also balanced and kept at the rated value during the operation time as expressed in Figure 4.14 in *Case 1*.

Table 4.5: Parameters of the PV inverter in *Case 2*.

Module	Parameter and Value (70% of the original values)
R-L output filter	$R_f = 1.4 \text{ m}\Omega$; $L_f = 175 \text{ }\mu\text{H}$
Per-phase parameters of the transformer in per-unit value (where R_m and L_m are constant)	$R_1^{(pu)} = 0.0007 \text{ pu}$; $L_1^{(pu)} = 0.021 \text{ pu}$ $R_1^{(pu)} = 0.0007 \text{ pu}$; $L_2^{(pu)} = 0.021 \text{ pu}$ $R_m^{(pu)} = 500 \text{ pu}$; $L_m^{(pu)} = 500 \text{ pu}$

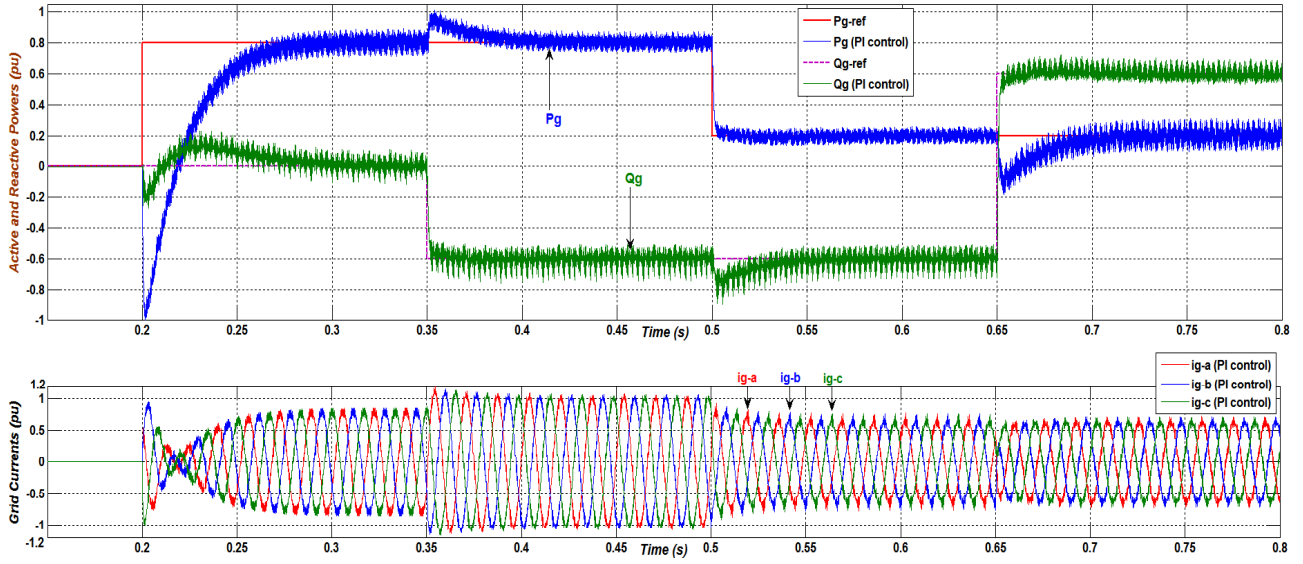


Figure 4.20: The performance with the traditional PI control in *Case 2*.

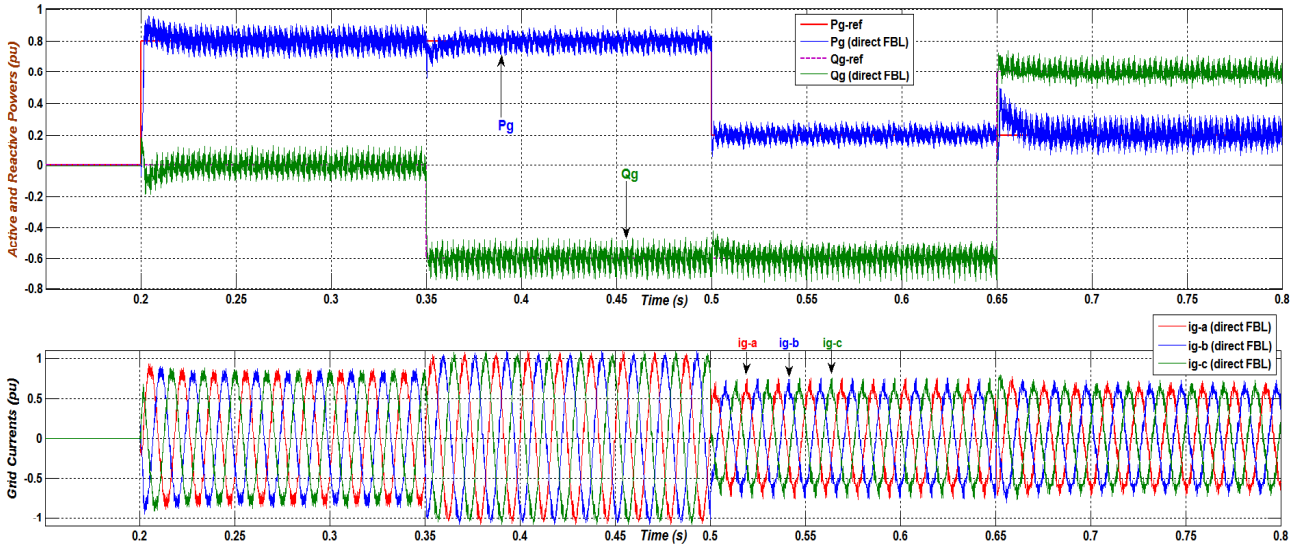


Figure 4.21: The performance with the direct FBL approach in *Case 2*.

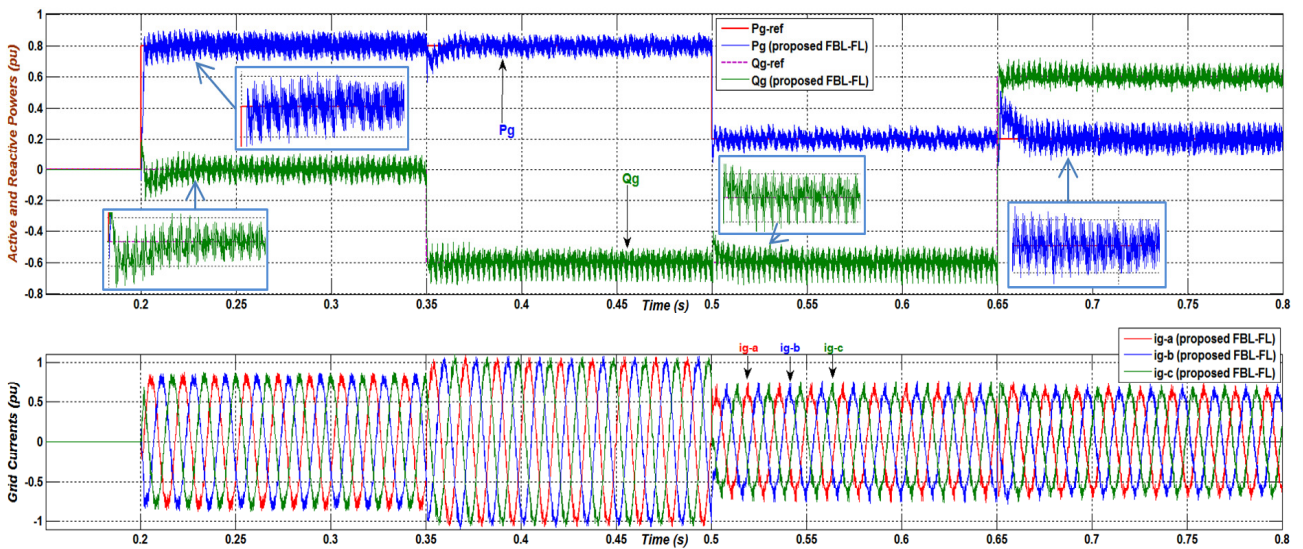


Figure 4.22: The performance with the proposed FBL-FL hybrid technique in *Case 2*.

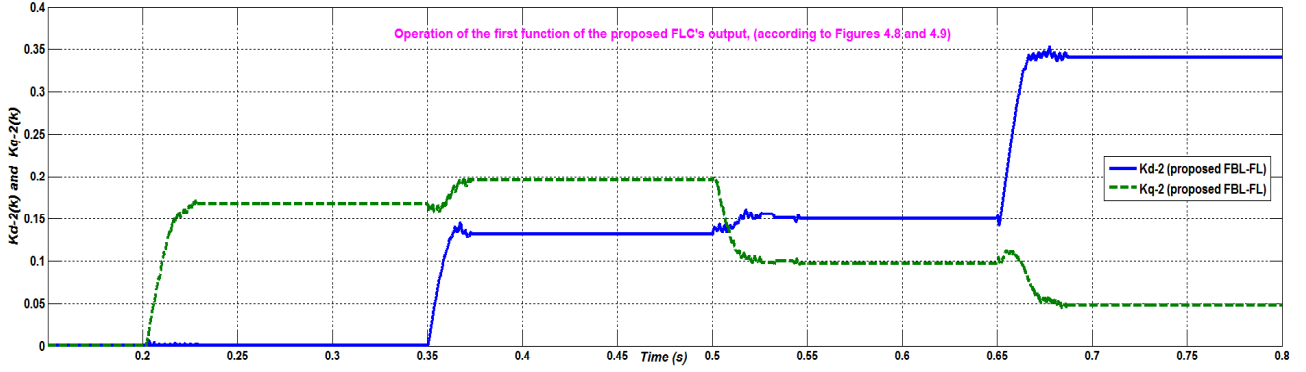


Figure 4.23: Variable values of K_{d2}, K_{q2} with the proposed FBL-FL hybrid technique in *Case 2*.

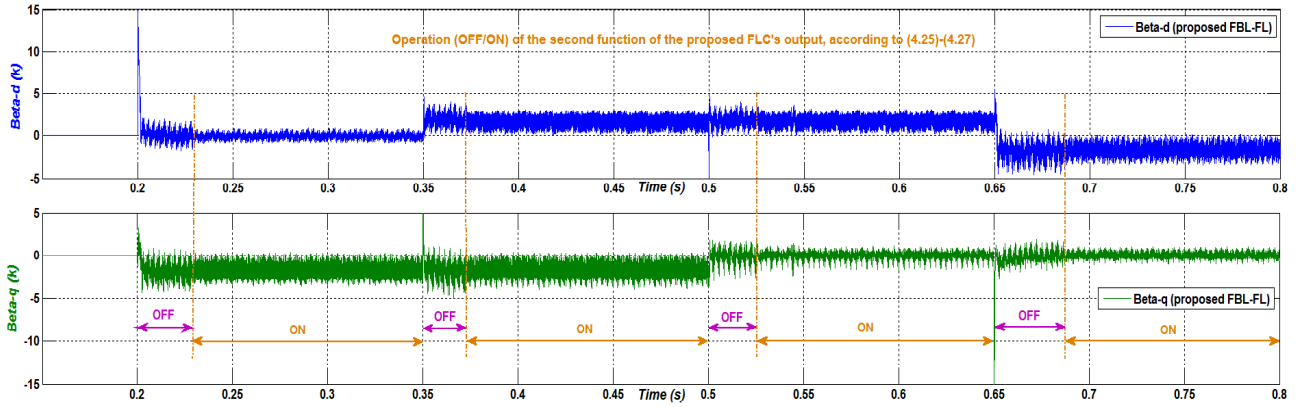


Figure 4.24: Values of β_d, β_q and operation of the second FLC's function of the FBL-FL in *Case 2*.

Performances of the demonstrative PV inverter using the traditional PI control in Figure 4.13, the direct FBL approach and the proposed FBL-FL hybrid technique are presented in Figure 4.20, Figure 4.21 and Figure 4.22, respectively.

As described in those figures, because of the parametric uncertainties, output-power ripples are currently rather much larger than the prior responses in *Case 1*. In detail, as seen in Figure 4.20, the performance of the traditional PI control continually includes the large overshoots and very slow response. Whereas, the direct FBL has the quick response and fairly big oscillations at the steady state in the output powers as described in Figure 4.21. Additionally, its performance still contains the pretty large overshoots especially when the desired values are changed significantly at $t = 0.2$ s and at $t = 0.65$ s. Lastly, Figure 4.22 represents that the proposed FBL-FL technique not only has the rapid response but also eliminates markedly the overshoots in transient states (especially when the references are varied considerably at $t = 0.2$ s and at $t = 0.65$ s), and maintains the steady-state oscillations be equivalent as in the PI control.

Operations of two functions of the proposed FLC in the FBL-FL hybrid technique are illustrated in Figure 4.23 and Figure 4.24 respectively. In detail, according to the first FLC's function described in Figure 4.8 and Figure 4.9, the coefficients K_{d2}, K_{q2} are adjusted automatically

and aptly in the transient states as shown in Figure 4.23. Actually, this helps remove efficiently the large overshoots in transient states. Besides, the effect of the second FLC's function on the virtual-control signals β_d, β_q are represented in Figure 4.24. Therein, the signal forms of β_d and β_q become smoother when the second FLC's function is activated (to be ON) at the steady states. Obviously, this assists to lower efficiently the harmonic distortion of grid current for decreasing significantly steady-state fluctuations in the output powers.

Furthermore, Table 4.6 shows the THD of grid current measured at the steady state in two periods: from the time $t = 0.3 \text{ s}$ to $t = 0.35 \text{ s}$, and from $t = 0.45 \text{ s}$ to $t = 0.5 \text{ s}$. Wherein, in the results achieved with the proposed FBL-FL, compared to the direct FBL, the second FLC's function helped reduce noticeably THD values from 7.54 % to 6.39 %, and from 6.07 % to 5.05 %, respectively. In addition, THD values with the proposed FBL-FL are clearly tantamount to the ones attained from the PI control. The data in this table highly corresponds to the performances as illustrated in Figure 4.20 to Figure 4.22.

Table 4.6: THD of grid current in *Case 2*.

Control scheme	THD of grid current (%)	
	From $t = 0.3 \text{ s}$ to $t = 0.35 \text{ s}$	From $t = 0.45 \text{ s}$ to $t = 0.5 \text{ s}$
The PI control	6.45 %	5.0 %
The direct FBL	7.54 %	6.07 %
The proposed FBL-FL	6.39 %	5.05 %

On the other hand, Figure 4.25 and Figure 4.26 illustrate the detailed harmonic orders of grid current with three the control structures from the time $t = 0.3 \text{ s}$ to $t = 0.35 \text{ s}$ in *Case 1* and *Case 2*, respectively. Wherein, compared to the direct FBL approach, we can see that the magnitudes of most of the harmonic orders (especially in the 5th, 7th, 11th and 13th orders) are noticeably decreased with the proposed FBL-FL technique. As well, notice that the 5th, 7th, 11th and 13th orders are generally the dominant harmonic orders in the electric grid which integrates the distributed renewable generators [71],[72]. In addition, the fine effectiveness of the proposed FBL-FL technique within diminishing magnitudes of harmonics in the grid current is confirmed more clearly as shown in Figure 4.26 when the parametric uncertainty case unexpectedly happens.

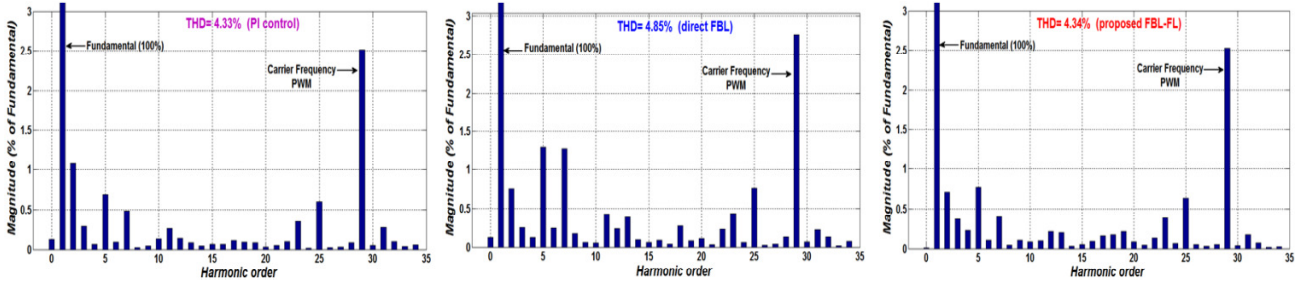


Figure 4.25: Harmonic orders of grid current with the three control structures in *Case 1* (from $t = 0.3$ s to $t = 0.35$ s).

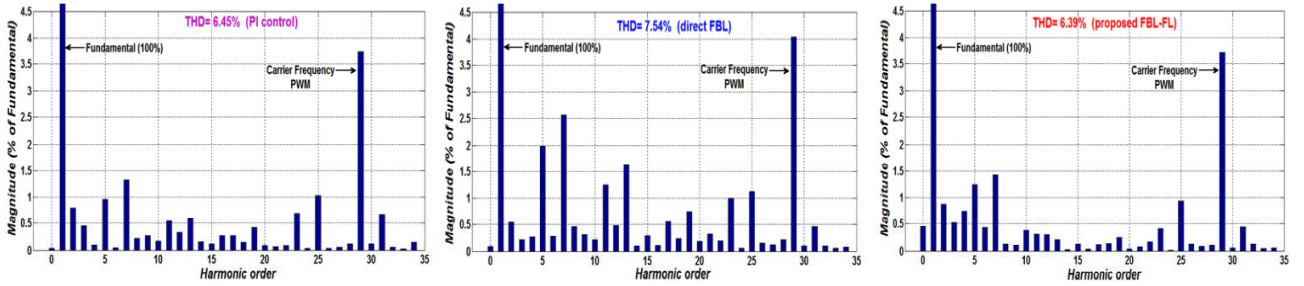


Figure 4.26: Harmonic orders of grid current with the three control structures in *Case 2* (from $t = 0.3$ s to $t = 0.35$ s).

4.5.3. Case 3: Simulation within parametric uncertainties and the unbalanced grid voltage sag

In this condition, the parameters used in the detailed model of the PV inverter are based on Table 4.5; meanwhile, the design coefficients utilized in the PI controllers and the two FBL-based control structures are still according to Table 4.2 and Table 4.3. However, note that the unbalanced grid voltage sag currently occurs from the time $t = 0.2$ s as represented in Figure 4.27. Wherein, the magnitude of v_{ga} is fixed at the nominal value; in the meantime, the magnitudes of v_{gb} and v_{gc} are now equal to 75% and 90% of the rated value, respectively.

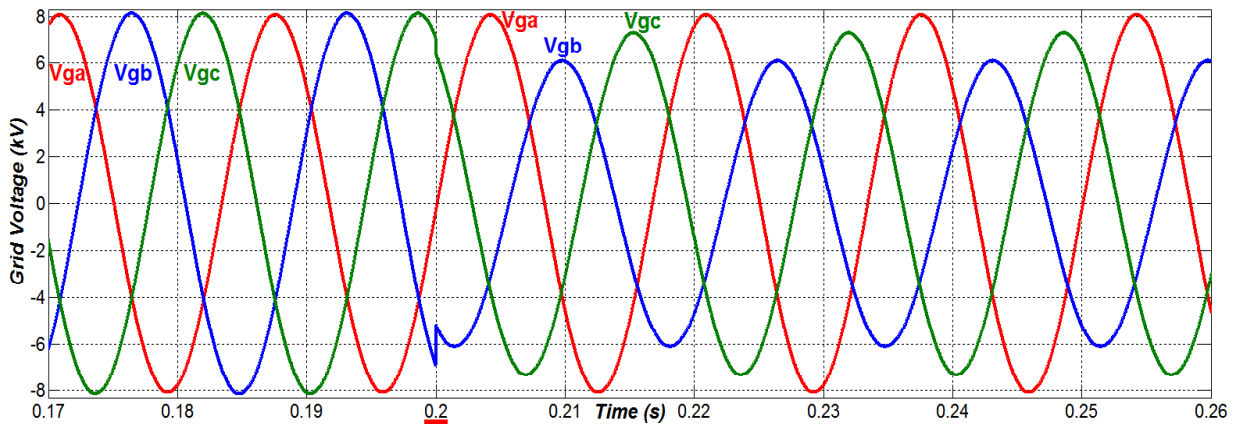


Figure 4.27: The unbalanced grid voltage occurs from $t = 0.2$ s.

Due to the unbalanced grid voltage sag in this case, measured voltages in the d - q reference frame ($v_{gd}^{(pu)}, v_{gq}^{(pu)}$) are currently not the DC quantities as in *Case 1* and *Case 2*. And from (4.13), as a consequence, the reference values of grid current are now the oscillating quantities (instead of the DC quantities as in *Case 1* and *Case 2*) as shown in Figure 4.28.

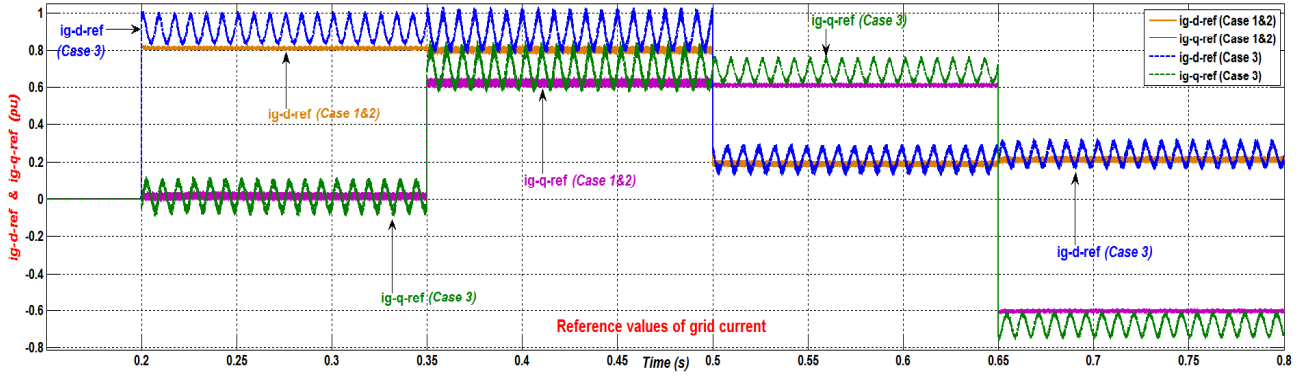


Figure 4.28: The oscillating reference values in *Case 3*, and the DC quantities in *Cases 1 & 2*.

Performances of the illustrative PV inverter using the traditional PI control in Figure 4.13, the direct FBL approach and the proposed FBL-FL hybrid technique are represented in Figure 4.29, Figure 4.30 and Figure 4.31, respectively.

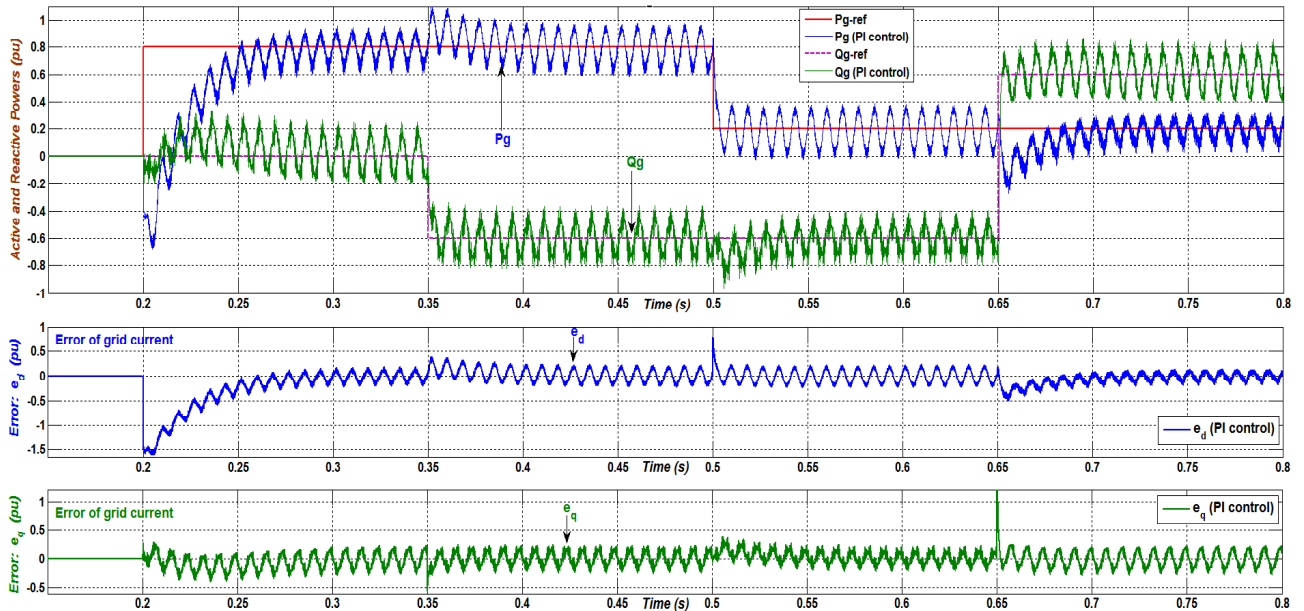


Figure 4.29: The performance with the traditional PI control in *Case 3*.

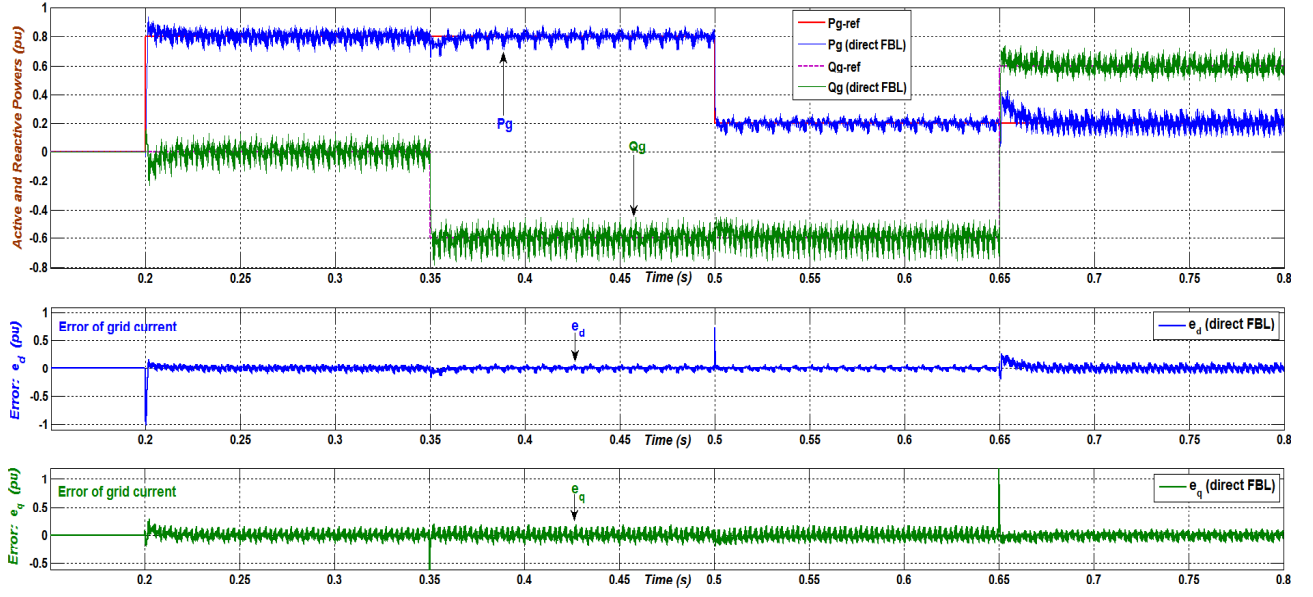


Figure 4.30: The performance with the direct FBL approach in *Case 3*.

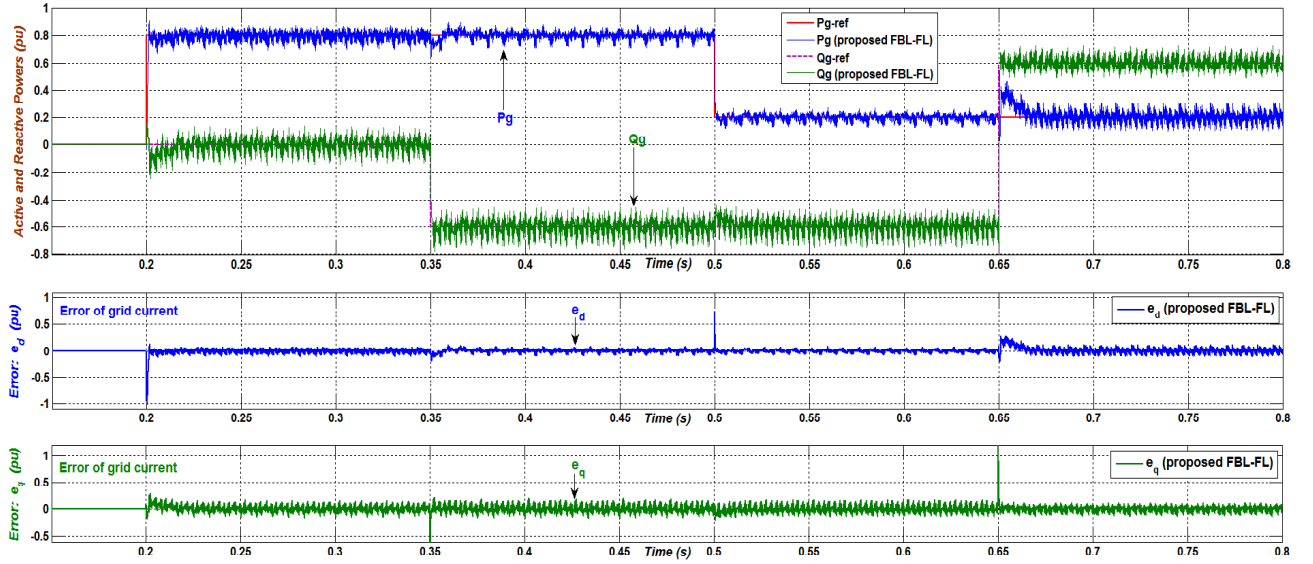


Figure 4.31: The performance with the proposed FBL-FL hybrid technique in *Case 3*.

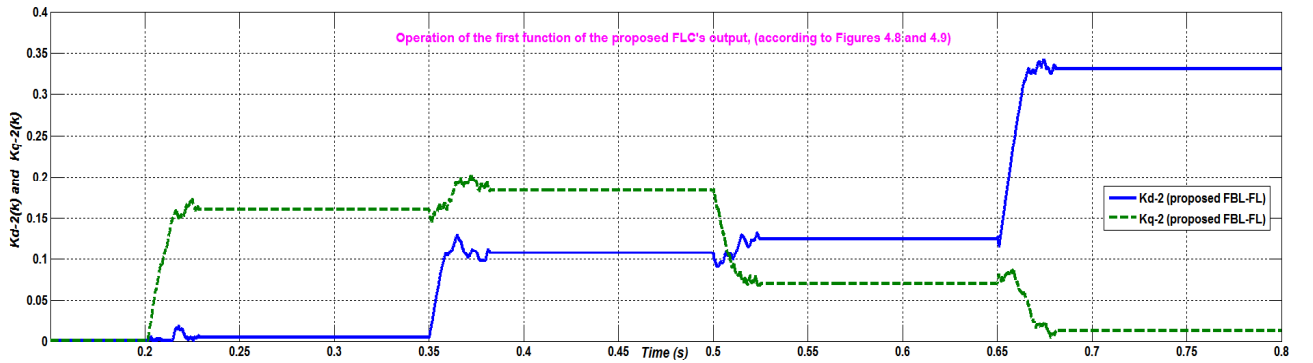


Figure 4.32: Variable values of K_{d2} , K_{q2} with the proposed FBL-FL hybrid technique in *Case 3*.

In detail, as described in the lower part of Figure 4.29, the errors of grid current with the traditional PI control are not equal to zero owing to the oscillating references in Figure 4.28. This causes the large overshoot, slow response and very big fluctuations in the performance with the traditional PI control as seen in the upper part of Figure 4.29. It clearly shows that the traditional PI controllers cannot regulate the output powers in this condition. Whereas, as illustrated in the lower parts of Figure 4.30 and Figure 4.31, the errors of grid current with the two FBL-based control methods are still maintained at nearly zero. As a result, the output powers are regulated well to the reference values as illustrated in the upper parts of Figure 4.30 and Figure 4.31. Nonetheless, the performance with the direct FBL approach includes the pretty large overshoots especially when the reference values are varied markedly at $t = 0.2 \text{ s}$ and at $t = 0.65 \text{ s}$. Meanwhile, the upper part of Figure 4.31 represents that the proposed FBL-FL has the quick response and decreases considerably the overshoots in transient states even when the desired values are changed suddenly.

In this case, according to (4.25)-(4.27) and to ensure the stability of the control system, the second FLC's function is not activated. Therefore, the designed FLC currently operates with only the first function of it as shown in Figures 4.8 and 4.9. In detail, as seen in Figure 4.32, the coefficients K_{d2}, K_{q2} are still altered automatically and appropriately in the transient times, and then are maintained at the suitable fixed values at the steady states. This obviously aids to diminish efficiently the large overshoot of the output powers in transient states.

4.5.4. Case 4: Simulation within parametric uncertainties and the reference values change in ramp functions

In this case, parameters of the switching PV inverter and the two FBL-based control structures are same with the ones in *Case 2*. Moreover, similar within *Case 1* and *Case 2*, the three-phase grid voltage is also balanced as expressed in Figure 4.14. However, as shown in Figures 4.33 and 4.34, the reference values of active and reactive powers, $P_g^{*(pu)}$ and $Q_g^{*(pu)}$, are now varied according to the ramp functions instead of the step functions in the previous three cases. Performances of the illustrative PV inverter using the two FBL-based methods are expressed in Figures 4.33 to 4.36.

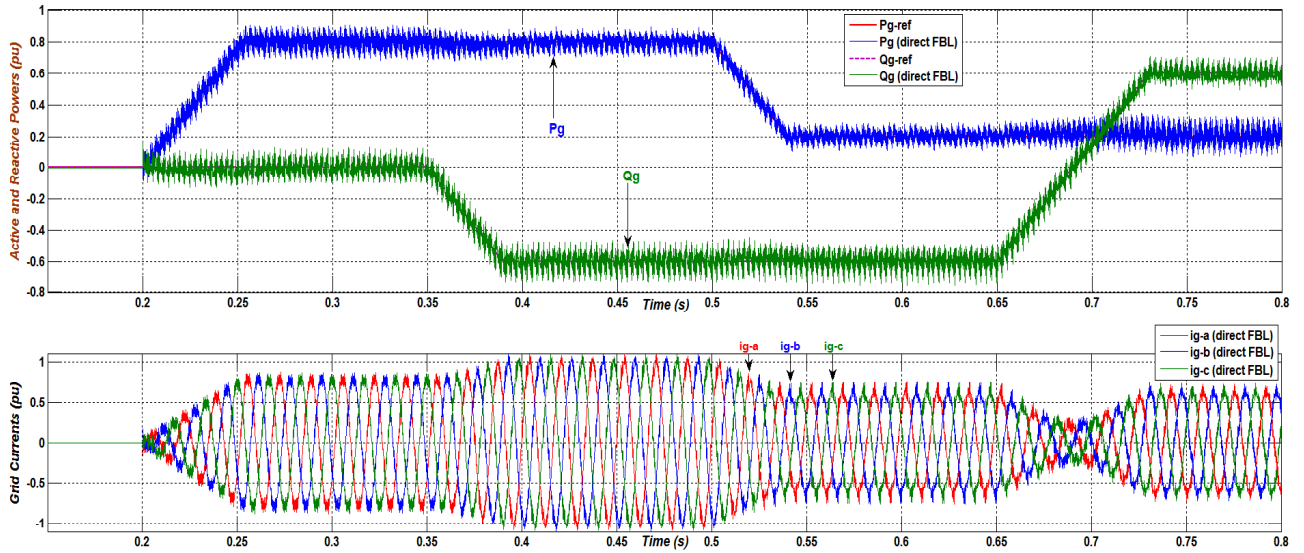


Figure 4.33: The performance with the direct FBL approach in *Case 4*.

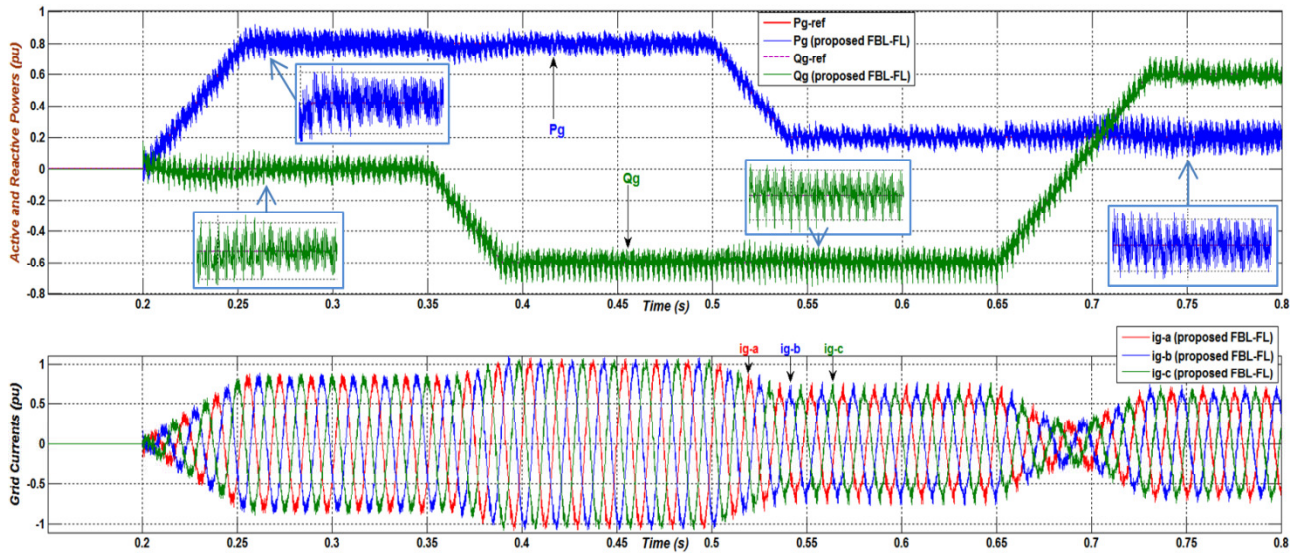


Figure 4.34: The performance with the proposed FBL-FL hybrid technique in *Case 4*.

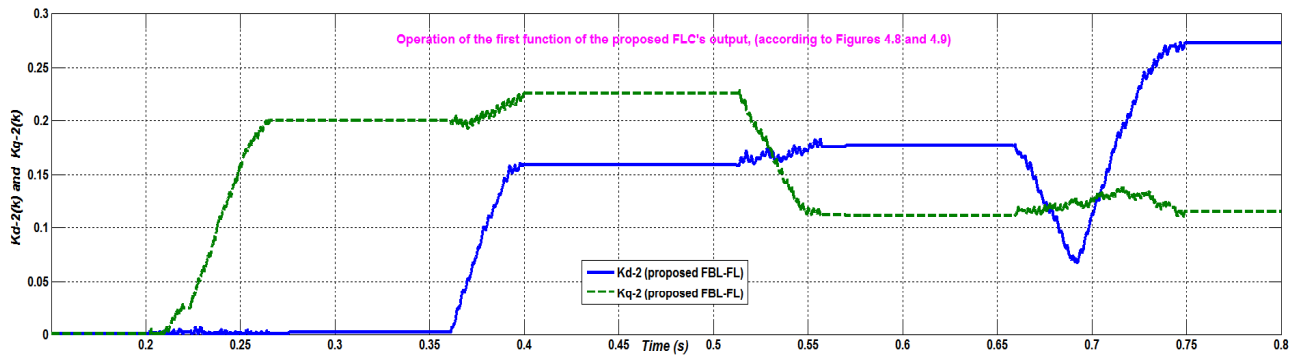


Figure 4.35: Variable values of K_{d2} , K_{q2} with the proposed FBL-FL hybrid technique in *Case 4*.

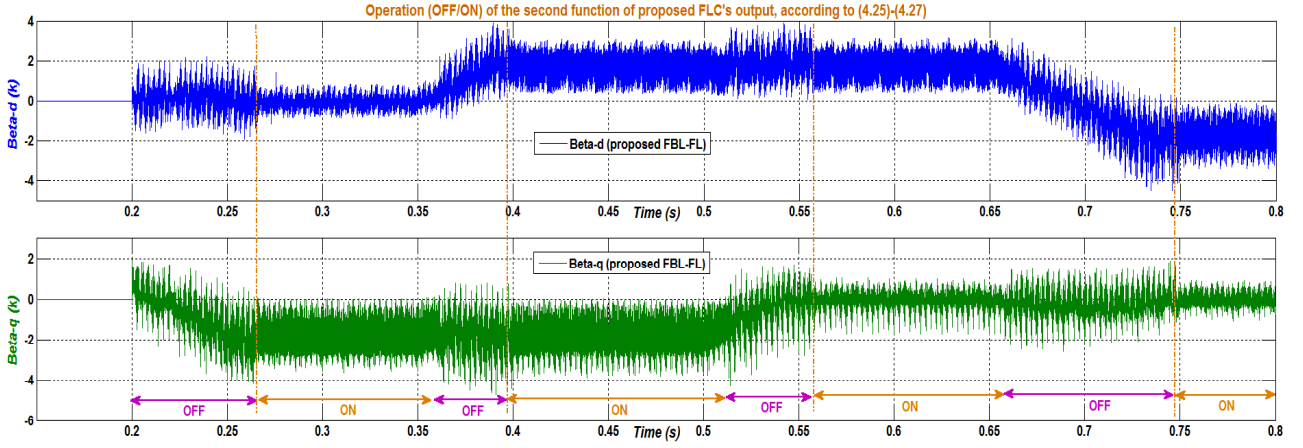


Figure 4.36: Values of β_d, β_q and operation of the second FLC's function of the FBL-FL in *Case 4*.

As shown in Figures 4.33 and 4.34, the two FBL-based structures still regulate very well the output powers to the reference values. In detail, because the desired values change slowly according to ramp functions, the output powers with the direct FBL method include small overshoot in transient responses as seen in Figure 4.33. However, as also presented in this figure, fluctuations in the output powers at steady states are still large. Meanwhile, the output powers with the proposed FBL-FL technique not only have the tiny overshoot in transient responses, but also reduce significantly oscillations at steady states as given by Figure 4.34.

Besides, the two functions of the proposed FLC's output operate properly as presented in Figures 4.35 and 4.36. Obviously, this helped the proposed FBL-FL technique still has good performances when the reference values vary in ramp functions. Wherein, as shown in Figure 4.35, since the desired values change gradually, the values of K_{d2}, K_{q2} alter slower than the ones seen in Figure 4.23 (with *Case 2*). Moreover, as illustrated in Figure 4.36, value ranges of the final virtual-control signals β_d, β_q are smaller than the ones expressed in Figure 4.24 (with *Case 2*).

Table 4.7: THD of grid current in *Case 4*.

Control scheme	THD of grid current (%)	
	From $t = 0.3 \text{ s}$ to $t = 0.35 \text{ s}$	From $t = 0.45 \text{ s}$ to $t = 0.5 \text{ s}$
The direct FBL	7.51 %	6.04 %
The proposed FBL-FL	6.28 %	5.06 %

Table 4.7 shows THD values of grid current measured at steady states in periods: from $t = 0.3 \text{ s}$ to $t = 0.35 \text{ s}$, and from $t = 0.45 \text{ s}$ to $t = 0.5 \text{ s}$. In the results obtained with the proposed FBL-FL, compared to the direct FBL, the second FLC's function helped lessen THD values from 7.51% to

6.28%, and from 6.04 % to 5.06 %, respectively. Obviously, these statistics correspond to the performances shown in Figures 4.33 and 4.34. Besides, the THD values in this table are also slightly lesser than the ones in Table 4.6 (with *Case 2*).

Additionally, as shown in Table 4.8, the main characteristics of the proposed FBL-FL hybrid technique are compared with the previously suggested PID-Fuzzy controller in [18] to demonstrate more clearly the salient improvements of the proposed FBL-FL.

Table 4.8: Comparison between the proposed FBL-FL and the previously suggested PID-Fuzzy

Control methods	The suggested PID-Fuzzy in [18]	Proposed FBL-FL in this study
a. <i>Complexity in design and computing</i>	<ul style="list-style-type: none"> - has three different FLCs for the coefficients K_P, K_I, K_D. - each FLC has 49 association rules. 	<ul style="list-style-type: none"> - has the two similar FLCs for $\beta_d^{FL}, \beta_q^{FL}$ as seen in Figure 4.6. - each FLC has 25 association rules.
b. <i>Field of applying</i>	<ul style="list-style-type: none"> - optimized only for the single-phase grid-connected PV inverters within the low-power range. 	<ul style="list-style-type: none"> - for the three-phase grid-connected PV inverters within all power levels.
c. <i>Electric system used for test</i>	<ul style="list-style-type: none"> - performed with an ideal controlled voltage source and a simple grid. - harmonic issues are fully disregarded. 	<ul style="list-style-type: none"> - performed with a switching VSC and a medium-voltage electric grid. - harmonic issues are considered carefully.
d. <i>Response and efficacy</i>	<ul style="list-style-type: none"> - can regulate well the active and reactive powers with the step change of reference values. - fast response, fairly small overshoot. - has not yet been checked with the parametric uncertainty of the system. 	<ul style="list-style-type: none"> - can regulate very well the active and reactive powers with both the step and ramp changes of reference values. - quick response, and tiny overshoot. - is robust against both the parametric uncertainty and the unbalanced grid voltage condition.

4.6. Summary of chapter

This study has presented the two FBL-based schemes to regulate the active and reactive output powers of three-phase grid-connected PV inverters, namely the direct FBL approach and the proposed FBL-FL technique. Wherein, a novel 25-rule FLC has been designed to improve the efficacy of the linear proportional-integral method used in the direct FBL approach, details:

- i. The FLC fine-tunes automatically and properly for the gain factors (K_{d2}, K_{q2}) of integral modules in the linear method in the transient state. This helped enhance considerably the transient response (response time, overshoot) of the output powers, especially when the reference values are varied noticeably and abruptly.
- ii. Additionally, the FLC also adjusts suitably for the final virtual-control signals (β_d, β_q) to reduce efficiently the steady-state fluctuations in the output powers, especially in the parametric uncertainty condition.

Within the demonstrative 100kW grid-connected PV inverter, simulations in MATLAB showed that the two FBL-based techniques can control the active and reactive output powers closely to the reference values. Furthermore, as compared to the traditional PI control and the direct FBL approach, the proposed FBL-FL technique has significantly better performances in boosting the response speed and lowering the overshoot of the output powers. As well, the oscillation in output powers with the proposed FBL-FL technique is maintained in a tolerable range that is nearly tantamount to the one with the traditional PI control. Besides, the suggested FBL-FL hybrid technique is also much robust against parametric variations and unbalanced grid voltage.

Additionally, the modeling technique based on per-unit quantities is also applied aptly. And this is really useful in determining and tuning exactly values for the controller's design coefficients in the medium-power and high-power grid-connected PV inverters with the transformer included.

Chapter 5

Fuzzy-based Control Strategy with Supporting the Regulation of Grid Frequency for Large-scale PV Farm

This chapter is the third key study part of the thesis, which introduces a novel coordinated-control strategy based on fuzzy logic to inject efficiently the total active power from a grid-connected large-scale PV farm, consisting of many local solar-energy agents and the battery bank at each agent, into an electric grid with supporting the regulation of grid frequency.

5.1. Introduction of chapter

Recently, the grid-connected large-scale PV solar farms have been broadly utilized to deliver the active power to the electric grid. Nevertheless, the large-scale solar farm, where many grid-connected PV power agents are integrated, is usually controlled to inject fully the total output active power of all agents into the grid; as a result, this may cause the frequency deviation of the electric grid to exceed much over the tolerable range of ± 0.2 Hz. Therefore, the grid-frequency regulation problem in an electric grid, containing grid-connected large-scale PV farms with battery banks for storing energy, should be examined and resolved thoroughly. To study and resolve this problem, some different control methods have been introduced in [7]-[9],[19],[20],[73]-[76].

In detail, according to [7],[8],[19],[73], a coordinated-control technique based on fuzzy logic for PV-diesel hybrid systems without battery banks has been presented to regulate grid frequency. This technique utilized two 49-rule fuzzy logic controllers (FLCs) to define the desired value for active power needed to supply to the grid. Nonetheless, in the case where the solar radiation decreases much and the system load is increased much, the PV system without using battery banks as an energy storage system (ESS) may not supply sufficiently power into grid to regulate well the grid frequency. Moreover, in [20],[74], grid-connected PV systems with battery banks for storing energy have been used to control grid frequency. Even so, the common disadvantage of most these studies is that state-of-charge (SOC) values of the battery banks have not yet been stabilized in the safe ratio range of [0.2 0.8] in order to ensure durability of the battery banks.

As introduced in [9], a double-layer capacitor and a proportional controller for grid-connected PV system have been utilized to regulate grid frequency. The control technique has not only the fairly simple structure but also good performances. Nevertheless, effects of AC-system loads in the grid have not yet been examined in this research. Besides, a grid-frequency control method based

on power curtailment, using the Newton quadratic interpolation (NQI) for PV grid-connected systems without energy storage, has been proposed in [75]. The key idea is to adjust regularly the operating point of PV arrays to obtain the desired power value. However, the method has not yet been considered within a large-scale solar farm which comprises many grid-connected PV power agents. On the other hand, regarding the issue of regulating both grid frequency and voltage for the distributed power generations, a model-free method based on the adaptive neuro-fuzzy inference system (ANFIS) has been introduced in [76]. This method can control well the grid frequency and voltage even under unpredicted changes of system load and line parameters of grid. Nonetheless, the efficacy of the proposed ANFIS is highly dependent on training to determine parameters in structure of the ANFIS, but this often requires pretty many calculation steps and suitable data information.

In this study, the proposed fuzzy-based control strategy with supporting the grid-frequency regulation for a grid-connected large-scale PV farm, including battery banks for storing energy at local agents, has three main goals as follows.

- a) The total output active power from the PV farm injected into the grid is tuned aptly to ensure the grid frequency in acceptable ranges. Two tolerable ranges for frequency deviation are $\pm 0.2 \text{ Hz}$ in transient state and $\pm 0.05 \text{ Hz}$ at steady state, where the nominal grid frequency is 60 Hz .
- b) At each local PV power agent, SOC of the battery bank is governed in the safe ratio range of $[0.2 \text{ } 0.8]$ to improve durability of the battery bank. Also, steady-state SOC of the battery bank is regulated closely to a desired ratio value of 0.5 if the frequency deviation is in range of $\pm 0.05 \text{ Hz}$.
- c) The two goals listed in a) and b) of the suggested strategy have to be validated well even if the AC-system load and solar irradiation abruptly change.

To achieve all the above objectives, the proposed strategy is designed according to the two-level control structure. Firstly, a central controller, comprising a frequency regulation module based on a newly designed fuzzy logic controller (FLC), is developed to define suitably the individual reference value of active power for the local controller at each PV power agent. Secondly, each local controller coordinates the DC-DC converters connected with PV arrays, bidirectional charger for the battery bank and three-phase DC-AC inverter installed at PV agent in order to supply the active power to the grid accurately according to the obtained reference signal. Furthermore, a method for controlling SOC of the battery bank in both transient and steady states to ensure durability of the battery bank is also implemented in each local controller.

The content in this chapter is developed from my 1st conference paper in List of Research Achievements at page 138 with newly added improvements, simulations and explanations in the subsections 5.1, 5.2.1, 5.3, 5.4.2 and 5.5.

The remainder of this chapter is organized as follows. Section 5.2 shows the description of the demonstrative grid-connected large-scale PV solar farm. Then, design steps of the proposed fuzzy-based coordinated-control strategy are presented in the next section. Simulation results, including considerations on effects of solar radiation, air temperature and load, are illustrated in Section 5.4. Besides, this section expresses comparisons between the proposed strategy and the conventional control strategy using full MPPT. Lastly, Section 5.5 shows conclusion of the study in this chapter.

5.2. Design grid-connected large-scale PV farm with multi-string PV array topology

5.2.1. Description of the grid-connected large-scale solar farm

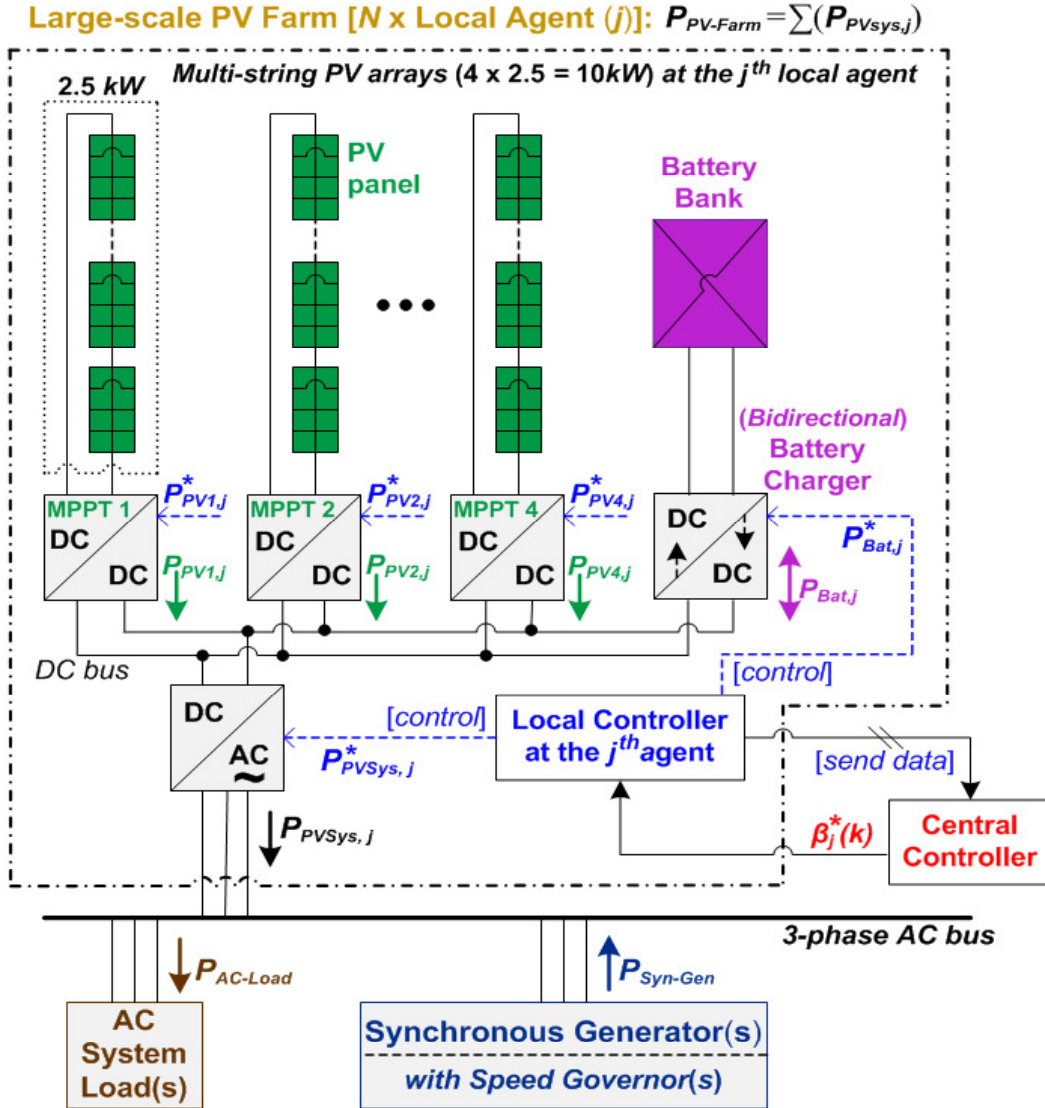


Figure 5.1: The demonstrative grid-connected large-scale PV solar farm.

The illustrative grid-connected large-scale PV farm is presented in Figure 5.1. Wherein, the farm consists of N local PV power agents and a central coordinating controller. Each local PV agent includes a local controller, four strings of PV panels with the total nominal power of $10kW$ (where each string has the nominal power of $2.5kW$), and a battery bank. The DC-DC converter utilized for each $2.5kW$ PV string can be chosen as the non-inverting buck-boost converter as introduced in [5],[60]. The battery bank can supply or absorb power via the bidirectional charger based on a half-bridge buck-boost converter [20],[74]. Then, output active power of each local PV agent is injected into the three-phase AC bus via a DC-AC inverter. All the six power-electronics converters are governed by the local controller. As well, the local controllers of all agents and the central controller can communicate and transfer data together via a Common Industrial Protocol (CIP) such as EtherNet/IP [7],[8],[73] or DeviceNet [77]. Wherein, the central controller receives data from all local controllers; and after calculating, it sends the individual reference value $\beta_j^*(k)$ to each local controller.

Besides, to study about the grid-frequency deviation, the electric grid can be modeled as one or some synchronous generator(s), including the speed governor(s) as given in Figure 5.2 and [78], [7]-[9]; and the AC-system load(s) is connected to the three-phase AC bus.

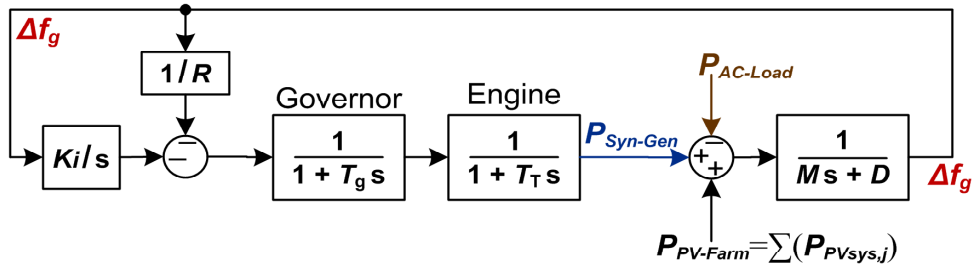


Figure 5.2: The diagram of speed governor for synchronous generator.

Referring in [79],[80] and presented in subsection 3.6 of Chapter 3, the multi-string DC-DC power converter topology inherits salient advantages combined from the central PV converter and string PV converter topologies as: save of installment cost, high efficacy in obtaining PV power due to separate MPPT algorithm, optimal monitoring of PV system and much compatibility for large-scale PV solar farms. Furthermore, commercial merchandises, which utilize the multi-string converter topology for PV system, have been introduced pretty popular. In this research, the multi-string converter topology is implemented in each local PV power agent as presented in Figure 5.1.

5.2.2. PV panel model

From Figure 3.2 and (3.1)-(3.3) in Chapter 3, the one-diode equivalent model of a PV panel (where the number of cells in parallel of the PV panel in use is $N_p = 1$) is expressed again in Figure 5.3 and (5.1)-(5.3), respectively. In this chapter, the 250W PV panel from [81], which has manufacturing parameters as shown in Table 5.1, is utilized for the demonstrative grid-connected large-scale solar farm in Figure 5.1.

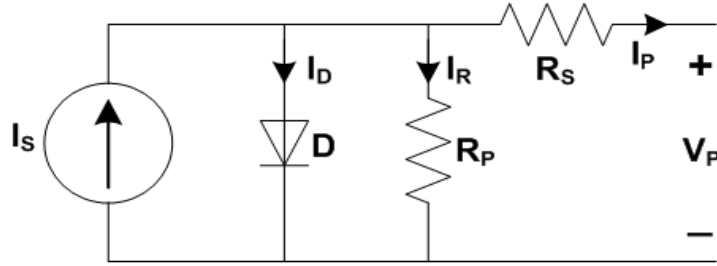


Figure 5.3: The equivalent circuit for a PV panel (re-shown from Figure 3.2).

$$I_p = I_s - I_o \left[\exp \left\{ \frac{q(V_p + R_s I_p)}{N_s a k T_{cell}} \right\} - 1 \right] - \left(\frac{V_p + R_s I_p}{R_p} \right) \quad (5.1)$$

$$I_s(T_{cell}, G_{so}) = \left[I_{sc,n} + k_T (T_{cell} - T_n) \right] \frac{G_{so}}{G_n} \quad (5.2)$$

$$I_o(T_{cell}) = \left[\frac{I_{sc,n}}{\exp \left\{ \frac{q V_{oc,n}}{N_s a k T_{cell}} \right\} - 1} \right] \left(\frac{T_{cell}}{T_n} \right)^3 \exp \left\{ \frac{q E_g}{a k} \left(\frac{1}{T_n} - \frac{1}{T_{cell}} \right) \right\} \quad (5.3)$$

Table 5.1: Manufacturing parameter values of the 250W PV panel.

Parameter	Symbol	Value
Maximum output power (nominal)	P_p^{\max}	250 W
Voltage at the MPP	V_{MPP}	30.4 V
Current at the MPP	I_{MPP}	8.23 A
Open-circuit voltage	V_{OC}	38.1 V
Short-circuit current	I_{SC}	8.91 A
Number of cells in series, parallel	N_s, N_p	60, 1
Number of PV panels of each PV array (each string) in Figure 5.1	$N_{PV-panels}$	10 (10 x 250W = 2.5 kW/array)

5.3. The proposed Fuzzy-based control strategy

The detailed scheme of the proposed fuzzy-based strategy is presented in Figure 5.4. In which, each local controller uses the predicted maximum power value from PV arrays simulated by the prediction module, $\beta_{PV,j}^{pre}(k)$, and the measured SOC of the battery bank, $SOC_{Bat,j}^{mes}(k)$, to compute the maximum power capacity of the local agent. Then, the predicted maximum power capacity $\beta_{PV+Bat,j}^{pre,max}(k)$ and previous actual power delivered to the grid $\beta_{PVsys,j}^{mes}(k-1)$ of each PV agent are sent to the central controller for processing.

Meanwhile, from the desired value and measured value of grid frequency, the proposed FLC integrated in the central controller defines the adjustable value $\Delta \beta^{pre}(k)$ for updating the reference value of total active power needed to inject into the grid $\beta_{\Sigma}^*(k)$. According to (5.10)-(5.12), the total active-power reference value $\beta_{\Sigma}^*(k)$ is computed from the values received from all local PV agents and $\Delta \beta^{pre}(k)$. After that, the individual desired active-power value for each agent $\beta_j^*(k)$ is determined as expressed in (5.13), and sent to each local controller.

Finally, each local controller coordinates suitably the four DC-DC converters connected with PV strings, bidirectional DC-DC battery charger and three-phase DC-AC inverter, which are shown in Figure 5.1, in order to supply the output active power of local agent to the grid according to the desired value $\beta_j^*(k)$ received from the central controller.

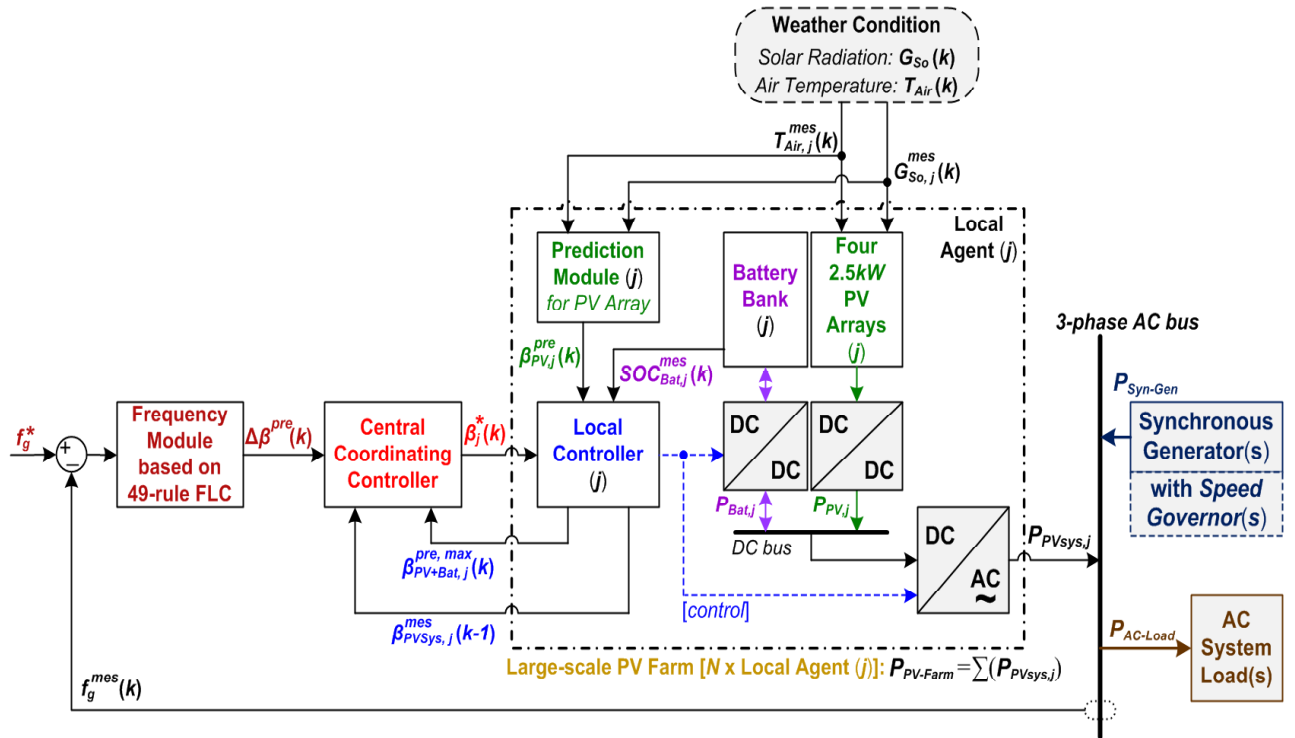


Figure 5.4: The detailed scheme of the proposed fuzzy-based coordinated-control strategy.

5.3.1. The Prediction Module in each Local Controller

The detailed structure of the prediction module installed at each local controller is shown in Figure 5.5. Wherein, the mathematical model of each PV panel is based on (5.1)-(5.3), and the manufacturing parameter values of PV panel are according to Table 5.1. It is noted that the design parameter values of a PV panel can be easily found in its user guide and technical catalogue provided from the manufacturer.

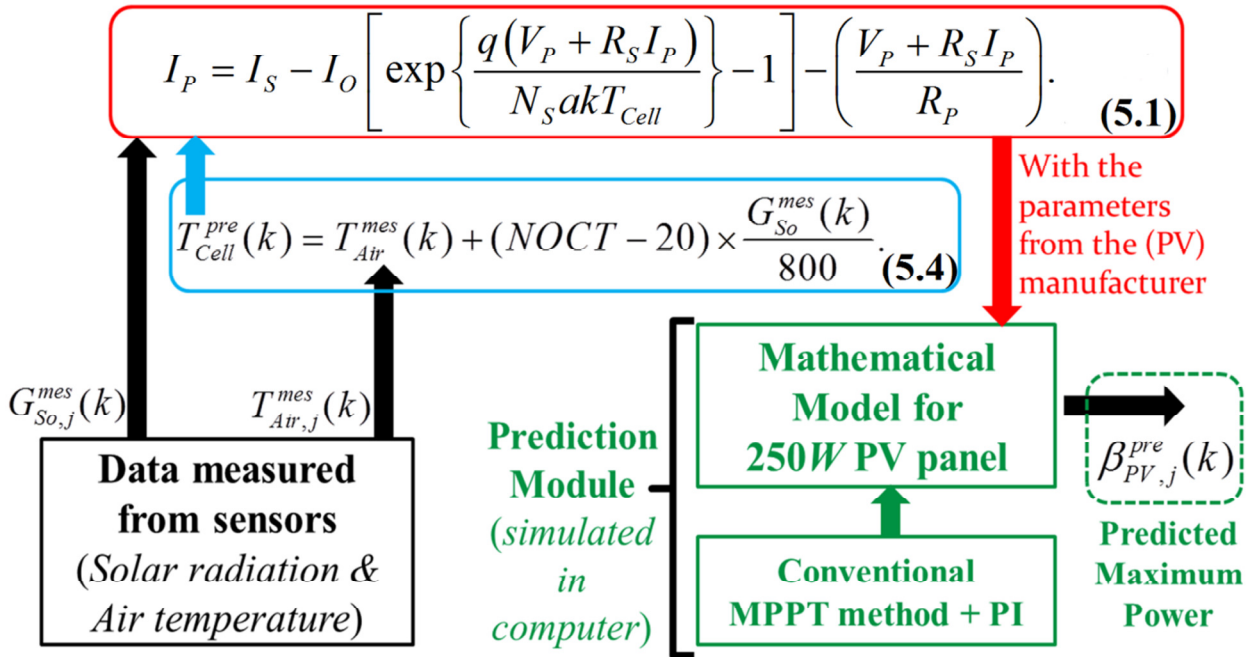


Figure 5.5: The detailed scheme of the prediction module.

Step A.1: According to [82],[83], using the Nominal Operating Cell Temperature (NOCT) coefficient, the temperature of PV cell (inside PV panel) at each local PV agent can be estimated from the measured value of air temperature as follows:

$$T_{Cell,j}^{pre}(k) = T_{Air,j}^{mes}(k) + (NOCT - 20) \times \frac{G_{So,j}^{mes}(k)}{800} \quad (5.4)$$

From the measured value of solar radiation using sensor and the PV cell temperature estimated in (5.4), the output current of each PV panel can be computed by (5.1). Then, Figure 5.6 is modeled and implemented in computer simulation to predict the maximum power of a PV panel. Wherein, the mathematical model of non-inverting buck-boost converter and the conventional MPPT method with PI controller can be found in [12],[5]. Lastly, the predicted maximum power of all PV arrays $\beta_{PV.i}^{pre}(k)$ will be computed as given in Figures 5.4 and 5.5.

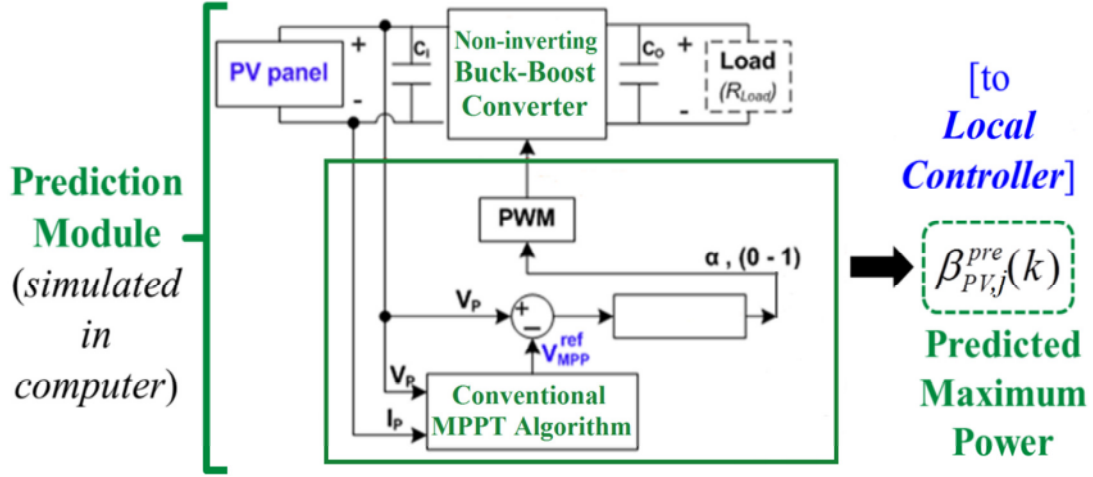


Figure 5.6: Structure for implementing MPPT algorithm for PV panel.

Step A.2: In this study, all parameters are converted to per-unit (pu) values to simply the design process of the proposed control strategy [64]. Some typical per-unit values labeled as β at each local PV power agent are shown in (5.5).

$$\begin{cases} P_{PV,j}^{rated} = 10kW; \beta_{Bat,j}^{rated} = \frac{P_{Bat,j}^{rated}}{P_{PV,j}^{rated}} = 80\% = 0.8 \\ \beta_{PV,j}^{pre}(k) = \frac{P_{PV,j}^{pre}(k)}{P_{PV,j}^{rated}}; \beta_j^*(k) = \frac{P_{PVsys,j}^*(k)}{P_{PV,j}^{rated}} \end{cases} \quad (5.5)$$

Step A.3: At each local PV power agent, the power supply and absorption capacity of the battery bank are computed by (5.6) and (5.7), respectively.

$$\beta_{Bat,j}^{pre, supply}(k) = \begin{cases} 0, & \text{if } SOC_{Bat,j}^{mes}(k) < SOC_{Bat}^{min} = 20\% = 0.2 \\ [SOC_{Bat,j}^{mes}(k) - SOC_{Bat}^{min}] \times \beta_{Bat}^{rated}, & \text{if else} \end{cases} \quad (5.6)$$

$$\beta_{Bat,j}^{pre, absorb}(k) = \begin{cases} 0, & \text{if } SOC_{Bat,j}^{mes}(k) > SOC_{Bat}^{max} = 80\% = 0.8 \\ [SOC_{Bat,j}^{mes}(k) - SOC_{Bat}^{max}] \times \beta_{Bat}^{rated}, & \text{if else} \end{cases} \quad (5.7)$$

Step A.4: The predicted maximum power capacity from all the PV arrays and battery bank of each local PV agent is expressed as (5.8). Meanwhile, the previous actual active power injected into the grid of each PV agent is given by (5.9).

$$\beta_{PV+Bat,j}^{pre,max}(k) = \beta_{PV,j}^{pre}(k) + \beta_{Bat,j}^{pre, supply}(k) \quad (5.8)$$

$$\beta_{PVsys,j}^{mes}(k-1) = \beta_{PV,j}^{mes}(k-1) + \beta_{Bat,j}^{mes}(k-1) \quad (5.9)$$

From the local controller at each PV power agent, the two values $\beta_{PV+Bat,j}^{pre,max}(k)$, $\beta_{PVsys,j}^{mes}(k-1)$ will be sent to the central controller for processing as illustrated in Figure 5.4.

5.3.2. Process steps in the Central Coordinating Controller

Step B.1: The predicted maximum total power capacity $\beta_{PV+Bat,\Sigma}^{pre,max}(k)$ and the previous actual total power injected into the grid $\beta_{PVsys,\Sigma}^{mes}(k-1)$ of the PV solar farm are calculated in (5.10) and (5.11), respectively.

$$\beta_{PV+Bat,\Sigma}^{pre,max}(k) = \sum_{j=1}^N \beta_{PV+Bat,j}^{pre,max}(k) \quad (5.10)$$

$$\beta_{PVsys,\Sigma}^{mes}(k-1) = \sum_{j=1}^N \beta_{PVsys,j}^{mes}(k-1) \quad (5.11)$$

Step B.2: With the adjustable value $\Delta^{pre}(k)$ determined from Figures 5.4 and 5.7, the k th reference value of total output power for the solar farm, comprising all N local PV agents, is updated by

$$\beta_{\Sigma}^*(k) = \beta_{PVsys,\Sigma}^{mes}(k-1) + \left[N \times \Delta^{pre}(k) \right] \quad (5.12)$$

where its limitation is $0 \leq \beta_{\Sigma}^*(k) \leq \beta_{PV+Bat,\Sigma}^{pre,max}(k)$.

The above limitation formula is utilized to ensure that the reference value of total active power $\beta_{\Sigma}^*(k)$ must be not larger than the total power capacity of the PV farm $\beta_{PV+Bat,\Sigma}^{pre,max}(k)$ predicted in advance. This ensures stability of the proposed coordinated-control strategy.

Step B.3: According to [7],[73], individual reference value of power for each local PV agent can be computed as follows:

$$\beta_j^*(k) = \left[\frac{\beta_{\Sigma}^*(k)}{\beta_{PV+Bat,\Sigma}^{pre,max}(k)} \right] \times \beta_{PV+Bat,j}^{pre,max}(k) \quad (5.13)$$

where its limitation is $0 \leq \beta_j^*(k) \leq \beta_{PV+Bat,j}^{pre,max}(k)$.

This limitation formula is utilized to ensure that the individual reference value of active power for each local PV agent $\beta_j^*(k)$ must be not larger than the predicted power capacity (including PV arrays and battery bank) of the local agent $\beta_{PV+Bat,j}^{pre,max}(k)$. This ensures feasibility and efficacy of the

proposed control strategy in each local PV agent. Then, the individual reference value $\beta_j^*(k)$ will be sent to the corresponding local controller of each PV power agent.

For more clearly and easier to understand, the above three processing steps (B.1, B.2 and B.3) in the central coordinating controller are re-expressed graphically in Figure 5.7(a).

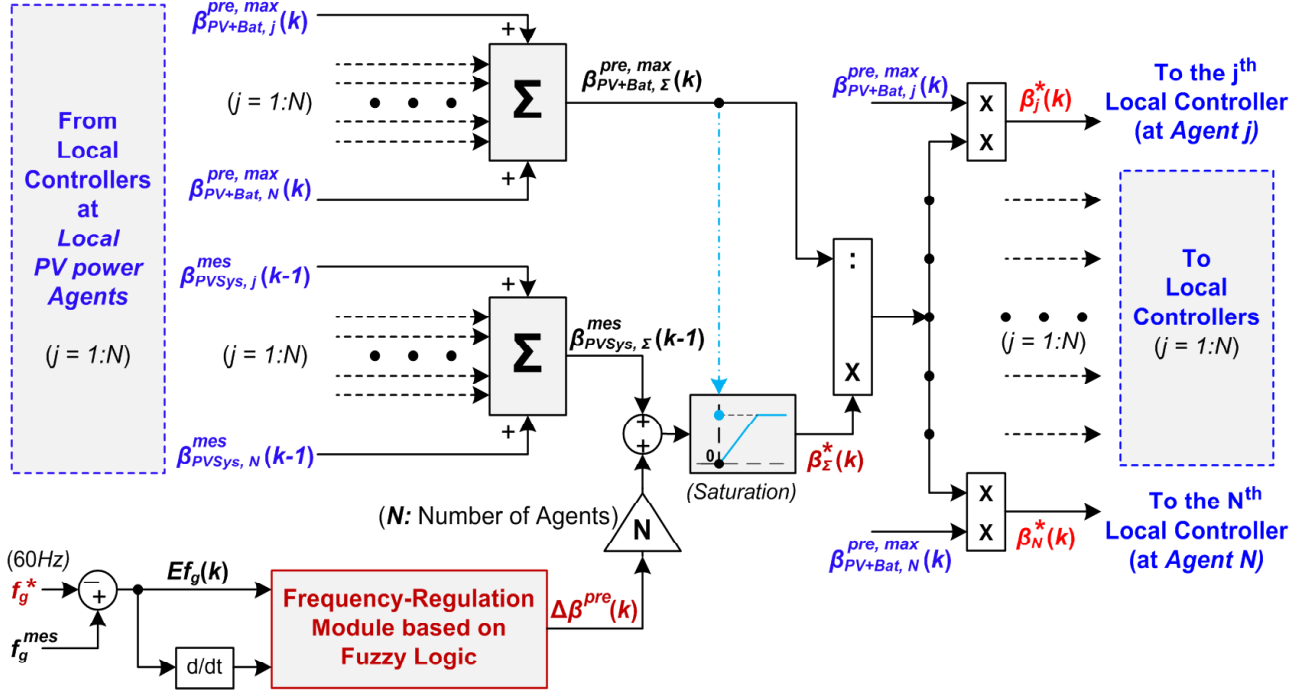


Figure 5.7(a): The processing diagram in the central controller (including Steps B.1, B.2 and B.3)

5.3.3. Determine the operations for PV arrays and battery bank in each Local Controller

Step C.1: To determine the operation mode for each DC-DC converter, a ratio value $\delta_j(k)$ is defined as follows:

$$\delta_j(k) = \left[\frac{\beta_j^*(k)}{\beta_{PV,j}^{pre}(k)} \right] \times 100\% \quad (5.14)$$

In this study, it is noted that PV strings are installed in a not too-large area, so the predicted maximum power of each PV string can be assumed to be equivalent together.

- a. If $\delta_j(k) \geq 100\%$: all the DC-DC converters for PV arrays will be controlled to operate with MPPT mode.
- b. If $75\% \leq \delta_j(k) < 100\%$, we check two sub-cases:
 - If $SOC_{Bat,j}^{mes}(k) < SOC_{Bat}^{\max}$: all the four DC-DC converters for PV arrays will be controlled to operate with MPPT mode; meanwhile, the battery bank will be predicted to absorb power.

- If $SOC_{Bat,j}^{mes}(k) \geq SOC_{Bat}^{max}$: the three DC-DC converters for the 1st, 2nd and 3rd PV arrays will be controlled to operate with MPPT mode; meanwhile, the 4th DC-DC converter will be deactivated, and the battery bank will be predicted to supply power.
- c. If $50\% \leq \delta_j(k) < 75\%$, we check two sub-cases:
 - If $SOC_{Bat,j}^{mes}(k) < SOC_{Bat}^{max}$: the three DC-DC converters for the 1st, 2nd and 3rd PV arrays will be controlled to operate with MPPT mode; meanwhile, the 4th DC-DC converter will be deactivated, and the battery bank will be predicted to absorb power.
 - If $SOC_{Bat,j}^{mes}(k) \geq SOC_{Bat}^{max}$: the two DC-DC converters for the 1st and 2nd PV arrays will be controlled to operate with MPPT mode; meanwhile, the 3rd and 4th DC-DC converters will be deactivated, and the battery bank will be predicted to supply power.
- d. If $25\% \leq \delta_j(k) < 50\%$, we check two sub-cases:
 - If $SOC_{Bat,j}^{mes}(k) < SOC_{Bat}^{max}$: the two DC-DC converters for the 1st and 2nd PV arrays will be controlled to operate with MPPT mode; meanwhile, the 3rd and 4th DC-DC converters will be deactivated, and the battery bank will be predicted to absorb power.
 - If $SOC_{Bat,j}^{mes}(k) \geq SOC_{Bat}^{max}$: the DC-DC converter for the 1st PV array will be controlled to operate with MPPT mode; meanwhile, the 2nd, 3rd and 4th DC-DC converters will be deactivated, and the battery bank will be predicted to supply power.
- e. Else ($0\% \leq \delta_j(k) < 25\%$), we check two sub-cases:
 - If $SOC_{Bat,j}^{mes}(k) < SOC_{Bat}^{max}$: the DC-DC converter for the 1st PV array will be controlled to operate with MPPT mode; meanwhile, the 2nd, 3rd and 4th DC-DC converters will be deactivated, and the battery bank will be predicted to absorb power.
 - If $SOC_{Bat,j}^{mes}(k) \geq SOC_{Bat}^{max}$: All the four DC-DC converters for PV arrays will be deactivated, and the battery bank will be predicted to supply power.

Step C.2: Use sensors to measure the k th actual total operating power of all PV arrays $\beta_{PV,j}^{mes}(k)$, and then compute the differential value $\beta_j^{SUB}(k)$.

$$\beta_j^{SUB}(k) = \beta_j^*(k) - \beta_{PV,j}^{mes}(k) \quad (5.15)$$

Step C.3: Determine the amount of active power should be supplied or absorbed from battery bank and the operation mode (supplying or absorbing) for the battery bank. The detailed algorithm is given as below.

a. If $\beta_j^*(k) < \beta_{PV,j}^{mes}(k)$, we check two sub-cases:

- If $SOC_{Bat,j}^{mes}(k) < SOC_{Bat}^{max} = 0.8$: the battery bank can continue to absorb power; therefore, it will be controlled to absorb power according to the reference value for battery bank as follows.

$$\beta_{Bat,j}^*(k) = \beta_j^{SUB}(k) < 0 \quad (5.16)$$

However, if $\beta_j^{SUB}(k) < \beta_{Bat}^{pre, absorb}(k)$, we reset as

$$\beta_{Bat,j}^*(k) = \beta_{Bat,j}^{pre, absorb}(k) \quad (5.17)$$

- Else ($SOC_{Bat,j}^{mes}(k) \geq SOC_{Bat}^{max}$): The battery bank cannot absorb any further power. So, in this case, the battery bank will be controlled to operate in the neutral mode: $\beta_{Bat,j}^*(k) = 0$.

b. If $\beta_j^*(k) \geq \beta_{PV,j}^{mes}(k)$, we check two sub-cases:

- If $SOC_{Bat,j}^{mes}(k) \leq SOC_{Bat}^{min} = 0.2$, the battery bank cannot supply power any more. Thus, in this condition, the battery bank will be controlled to operate in the neutral mode: $\beta_{Bat,j}^*(k) = 0$.
- Else ($SOC_{Bat,j}^{mes}(k) > SOC_{Bat}^{min}$): the battery bank will be controlled to supply power.

$$\beta_{Bat,j}^*(k) = \beta_j^{SUB}(k) > 0 \quad (5.18)$$

However, if $\beta_j^{SUB}(k) > \beta_{Bat,j}^{pre, supply}(k)$, we reset as

$$\beta_{Bat,j}^*(k) = \beta_{Bat,j}^{pre, supply}(k) \quad (5.19)$$

Step C.4: At the steady state, if the frequency deviation is in the range of $[-0.05Hz \ 0.05Hz]$, the battery bank will be controlled to regulate its SOC to the desired ratio value of 0.5 (equivalent with 50% expressed in percentage value). The purpose of this step is to ensure the battery bank can absorb/supply sufficiently energy as needed for next operation time. The detailed algorithm for regulating SOC of the battery bank is presented as below.

- If $|Ef_g(k)| \leq 0.05$, we check three sub-cases:

- If $SOC_{Bat,j}^{mes}(k) < 0.5$: The battery DC-DC charger will be controlled to absorb power from PV arrays to force SOC of the battery bank reach the desired ratio value of 0.5.
- If $SOC_{Bat,j}^{mes}(k) > 0.5$: The battery DC-DC charger will be controlled to inject power into the grid via the DC-AC inverter to decrease SOC of the battery bank to the desired ratio value of 0.5.
- Else ($SOC_{Bat,j}^{mes}(k) = 0.5$) : The battery bank will be kept to operate in the neutral (rest) mode.

5.3.4. Design of the proposed FLC for Frequency Regulation Module in Central Controller

As illustrated in Figures 5.7(a) at page 119 and 5.7(b) below, the proposed FLC uses the grid-frequency error $Ef_g(k)$ (this value is also the frequency deviation Δf_g indicated in Figure 5.2) and its derivative $dEf_g(k)$ as two inputs to define the adjustable value $\Delta \beta^{pre}(k)$. Then, $\Delta \beta^{pre}(k)$ will be used to update suitably the desired value for total active power $\Sigma^*(k)$ as expressed in (5.12).

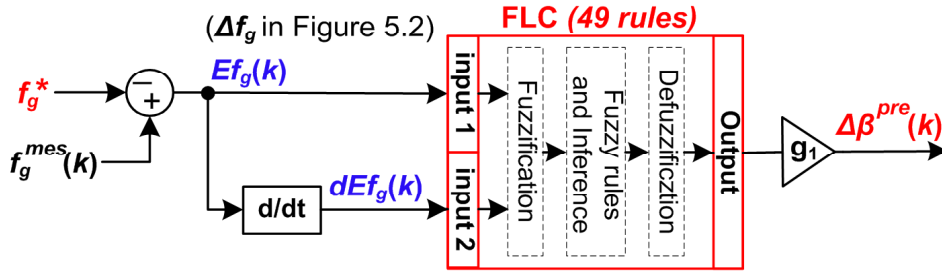


Figure 5.7(b): Detailed design structure of the proposed FLC in the central coordinating controller.

In the study of this chapter, the two inputs of the proposed FLC ($Ef_g(k)$, $dEf_g(k)$) have both negative and positive values; so the number of linguistic variables for each FLC's input () should be an odd value to can divide into three groups as negative linguistic variables, 'zero' variable and positive linguistic variables. Obviously, the value of cannot be 1 due to the very bad control quality. Furthermore, if the value of is 3, linguistic variables of each FLC's input will have one negative value, 'zero' value and one positive value; this clearly cannot achieve a good control quality because of the little number of control cases. As a result, the value of

should be chosen as 5 or 7 as the most suitable values on considering between the control quality and the computation time. Besides, as illustrated in Figures 5.4 and 5.7(a), the proposed coordinated-control strategy uses only one FLC; additionally, the central controller for a realistic large-scale PV farm is usually performed with an industrial computer or a high-speed modern MCU (or DSP), which can implement easily and efficiently a 49-rule FLC in experiments according to the reviews in Table 3.8 and subsection 3.7.2. So, to achieve the best control quality, the value of

should be chosen as 7. In summary, the proposed FLC in this chapter has two inputs, in which each input has 7 linguistic variables, and has totally $7 \times 7 = 49$ fuzzy association rules.

Two inputs: The two inputs have seven linguistic variables and values in the interval of [-0.3 0.3].

$$\begin{aligned} Ef_g(k), dEf_g(k) &= \{\text{Negative Large, Negative Medium, Negative Small, Zero, Positive Small,} \\ &\quad \text{Positive Medium, Positive Large}\} \\ &= \{NL, NM, NS, ZE, PS, PM, PL\} \end{aligned}$$

The output: has nine linguistic variables and value in the interval of [-0.4 0.4]

$$\begin{aligned} \Delta\beta^{pre}(k) &= \{\text{Negative Ultimate, Negative Large, Negative Medium, Negative Small, Zero,} \\ &\quad \text{Positive Small, Positive Medium, Positive Large, Positive Ultimate}\} \\ &= \{NU, NL, NM, NS, ZE, PS, PM, PL, PU\} \end{aligned}$$

Membership functions:

The membership functions for the two inputs and the output of the proposed 49-rule FLC are described in Figure 5.8, Figure 5.9 and Figure 5.10, respectively. Wherein, the shapes of membership functions are fine-tuned manually by the author with the highest priority as follows: $\Delta\beta^{pre}(k)$ has the very big value in the case where the frequency deviation is currently outside far away the limitation value range of $\pm 0.2 \text{ Hz}$ in order to force the frequency deviation to move quickly into the range of $\pm 0.2 \text{ Hz}$, and then $\Delta\beta^{pre}(k)$ has to be set as the so small value in the steady state to reduce thoroughly the oscillations of frequency.

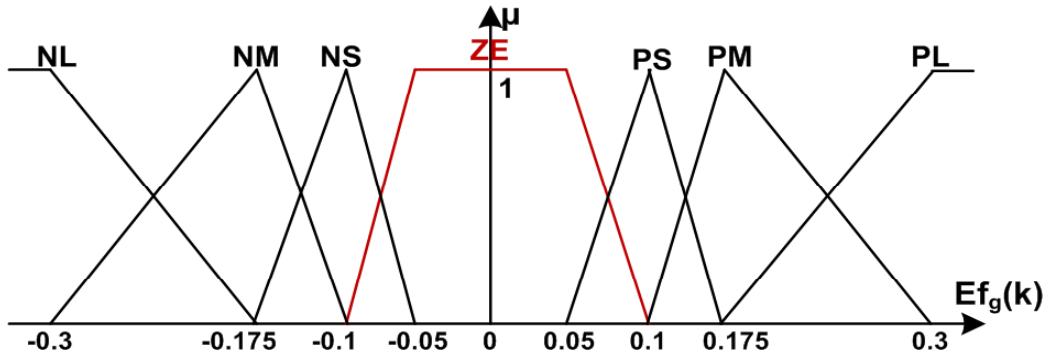


Figure 5.8: The membership functions for the first FLC's input.

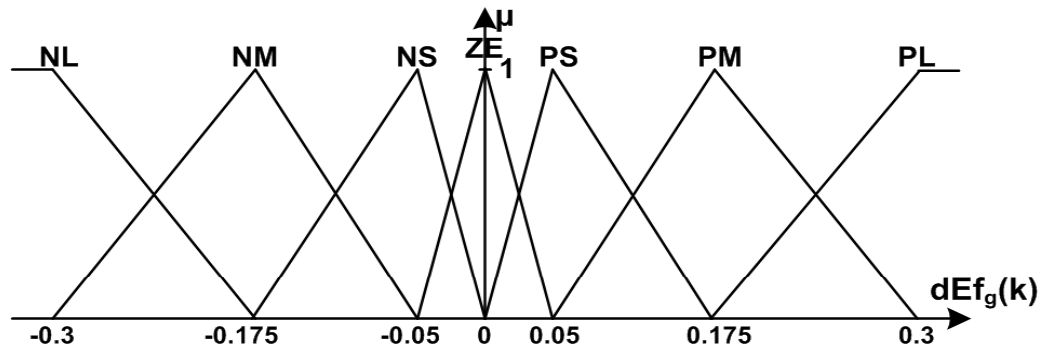


Figure 5.9: The membership functions for the second FLC's input.

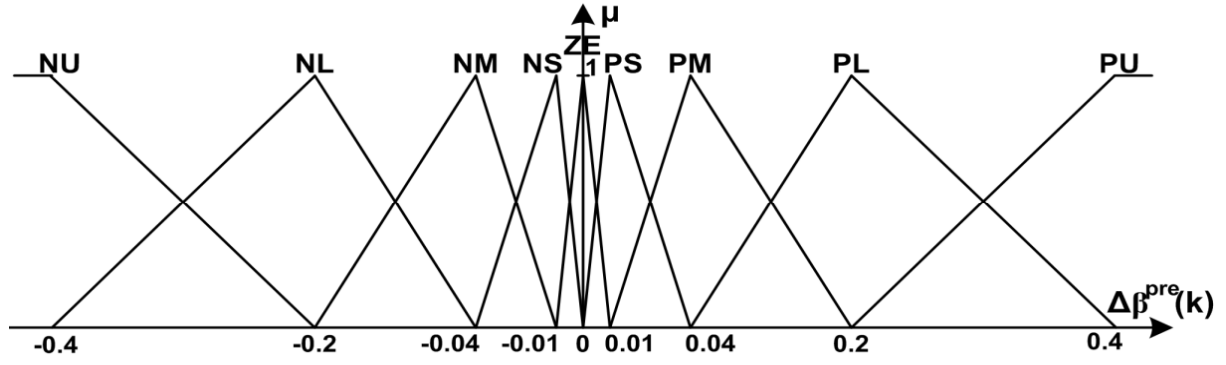


Figure 5.10: The membership functions for the first FLC's output.

The fuzzy associative matrix is illustrated in Table 5.2. It has totally $7 \times 7 = 49$ rules, and each rule is represented in the form “**if...then...**”. In detail, a sample rule can be expressed as “**if** $Ef_g(k)$ is NL and $dEf_g(k)$ is ZE **then** $\Delta\beta^{pre}(k)$ is PL”.

Table 5.2: Fuzzy association rules of the proposed FLC.

$\Delta\beta^{pre}(k)$		$Ef_g(k)$						
		NL	NM	NS	ZE	PS	PM	PL
$dEf_g(k)$	NL	PU	PU	PL	PM	PM	PS	ZE
	NM	PU	PL	PL	PM	PS	ZE	NS
	NS	PL	PL	PM	PS	ZE	NS	NM
	ZE	PL	PM	PS	ZE	NS	NM	NL
	PS	PM	PS	ZE	ZE	NM	NL	NL
	PM	PS	ZE	NS	ZE	NL	NL	NU
	PL	ZE	NS	NM	NS	NL	NU	NU

As shown in Table 5.2, the sample rule expressed as “**if** $Ef_g(k)$ is NL and $dEf_g(k)$ is NL **then** $\Delta\beta^{pre}(k)$ is PU”, is now used for analysis. In this case, because the error $Ef_g(k)$ is NL (negative large), it means that the grid frequency is now much smaller than its desired value $f_g^* = 60Hz$; meanwhile, the change of error (change of frequency deviation) $dEf_g(k)$ is also NL (negative large) value. This means the error $Ef_g(k)$ may continue to decrease rapidly, and the grid frequency has the tendency to become very much smaller than its nominal value $f_g^* = 60Hz$. To resolve this issue thoroughly, the reference value of total power $\beta_\Sigma^*(k)$ has to be adjusted with a very large quantity ($\beta_\Sigma^*(k)$ must be increased significantly) as compared with the previously actual total power injected into the grid $\beta_\Sigma^*(k-1)$, to force the grid frequency to increase drastically and quickly. So the k th adjustable value $\Delta\beta^{pre}(k)$ should be chosen as PU (positive ultimate).

Otherwise, in another case, the error $Ef_g(k)$ is still NL (negative large) as same with the above situation, but the change of error $dEf_g(k)$ is now varied to PL (positive large). This means that the grid frequency has the tendency in increasing automatically to its reference value $f_g^* = 60 \text{ Hz}$. To avoid the large overshoot, the the reference value of total power $\beta_\Sigma^*(k)$ should be kept unchanged. Thus, in this condition, the the k th adjustable value $\Delta^{pre}(k)$ should be as ZE (zero). In general, the similar deductive method can be utilized to interpret for other fuzzy rules shown in Table 5.2.

In this study part, the *Max-Min* composition operation and the *centroid* (CoA: center of area) method, which are presented in Chapter 2 of this thesis and in [22],[23], are utilized for the fuzzy rule inference and the defuzzification, respectively.

5.4. Simulation results and discussion

Detailed values for parameters of the demonstrative PV farm and the suggested fuzzy-based control strategy in MATLAB simulation [84] are given by Table 5.3. As well, the conventional strategy based on full MPPT mode for the PV farm will be also simulated to assess effectiveness of the proposed strategy. It is noted that, in the conventional strategy based on full MPPT mode, the power obtained from all PV arrays installed at the solar farm is fully delivered to the grid.

Table 5.3: Parameter values used in MATLAB simulation.

Parameter values of the speed governor (in Figure 5.2):
$K_i = 8$; $R = 0.1$; $T_g = 0.2$; $T_T = 0.5$; $M = 3.5$; $D = 0.7$
Parameter values of the proposed FLC (in Figure 5.7(b)):
$g_I = 0.6$; Fuzzy inference method: <i>Max-Min</i> ; Defuzzification method: <i>centroid</i>
Number of local PV agents: $N = 3$; Nominal AC-system load: 4.92 pu
Sampling time: $T_{s_control} = 0.05s$

5.4.1. Case 1: Effects of solar radiation and AC-system load

In this simulation case, the temperature is fixed at 25°C during the operation time; meanwhile, the AC-system load and solar radiations at three local PV agents are shown in Figure 5.11. In detail, they respectively have nominal values of 4.92 pu and 1 kW/m^2 in the 1st operational period $t = [0\text{ s } 20\text{ s})$. Then, the AC-system load is decreased of 35% in the 2nd operational period $t = [20\text{ s } 35\text{ s})$; meanwhile, solar radiation at the 2nd local PV agent reduces to 0.6 kW/m^2 , and solar radiation at the 3rd local PV agent increases to 1.2 kW/m^2 . Finally, in the 3rd period $t = [35\text{ s } 50\text{ s}]$, the AC-system load is increased of 30%; meanwhile, solar radiation at the 2nd local PV agent rises to 1 kW/m^2 , and solar radiations at both the 1st and 3rd local PV agents alter to 0.85 kW/m^2 .

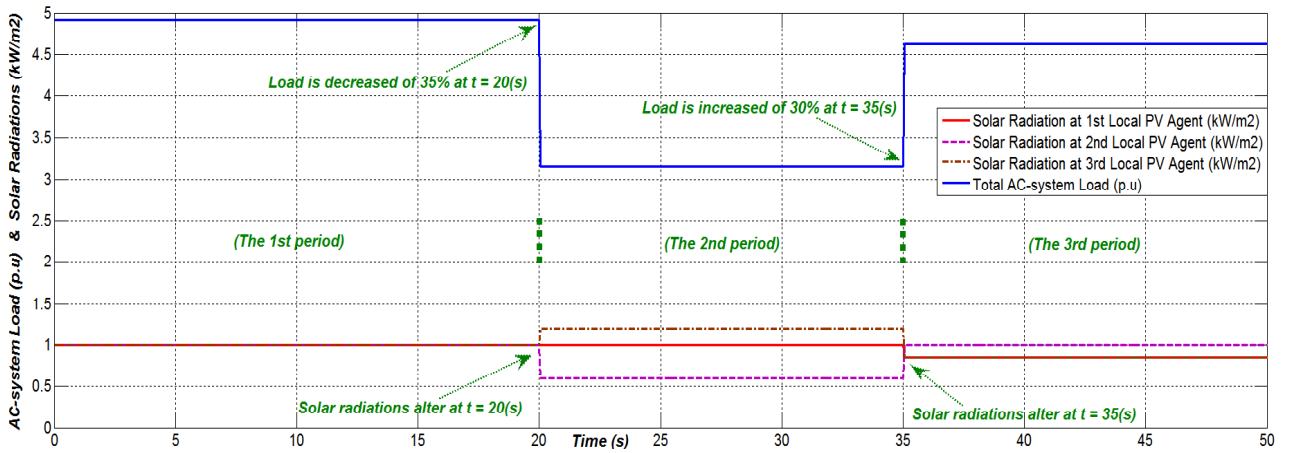
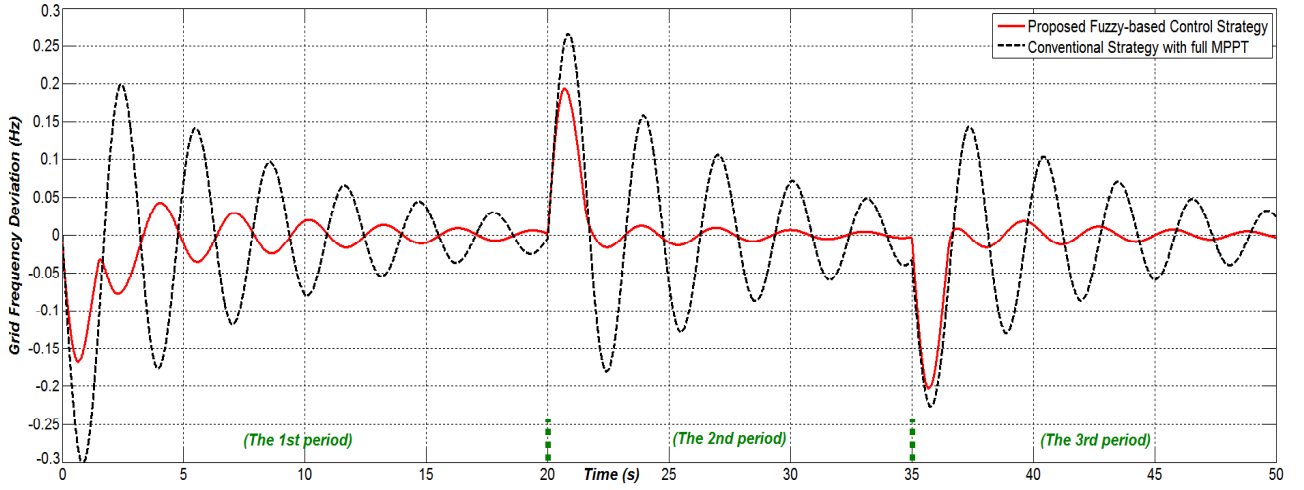
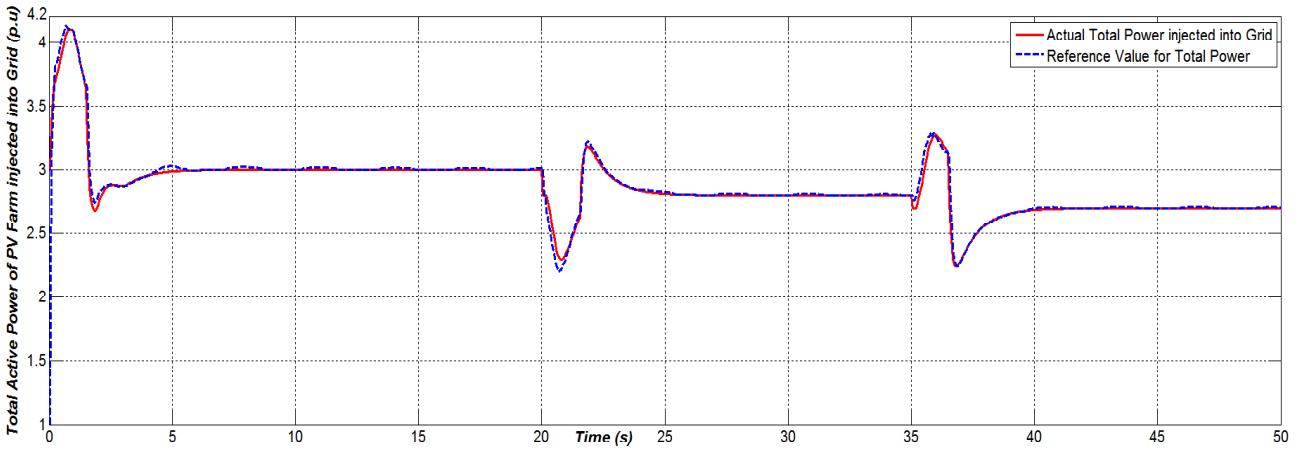


Figure 5.11: AC-system load and solar radiations at three local PV agents in three periods in *Case 1*.

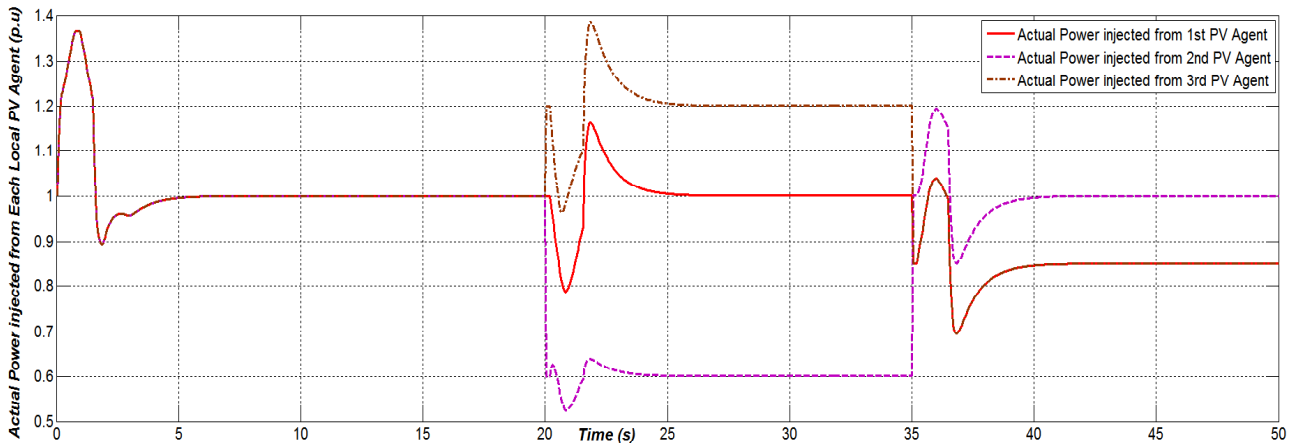
Simulation results are described in Figures 5.12 and 5.13. Wherein, according to Figure 5.12(a), the frequency fluctuation with the proposed fuzzy-based control strategy (the red solid line) is really much smaller than the other (the black dash line). In detail, it is regulated in the range of $\pm 0.2\text{ Hz}$ in transient states and also in the range of $\pm 0.05\text{ Hz}$ at steady states. Meanwhile, the frequency deviation with the conventional strategy using full MPPT mode exceeds the limitation values of $\pm 0.2\text{ Hz}$ in three periods $t = [0.4\text{ s } 1.3\text{ s}]$, $t = [20.5\text{ s } 21.2\text{ s}]$ and $t = [35.5\text{ s } 36\text{ s}]$. As well, the response speed for reaching steady states (where the frequency deviation is in the range of $\pm 0.05\text{ Hz}$) of the presented fuzzy-based strategy is remarkably faster than the conventional technique. For example, in the first operation period of this simulation, the proposed strategy needs only time of 3 s (from $t = 0\text{ s}$ to $t = 3\text{ s}$) to reach the steady state; meanwhile, the conventional strategy using full MPPT mode needs time of 12 s (from $t = 0\text{ s}$ to $t = 12\text{ s}$) to reach the steady state.



(a) Grid frequency deviation in three different operational periods in *Case 1*.

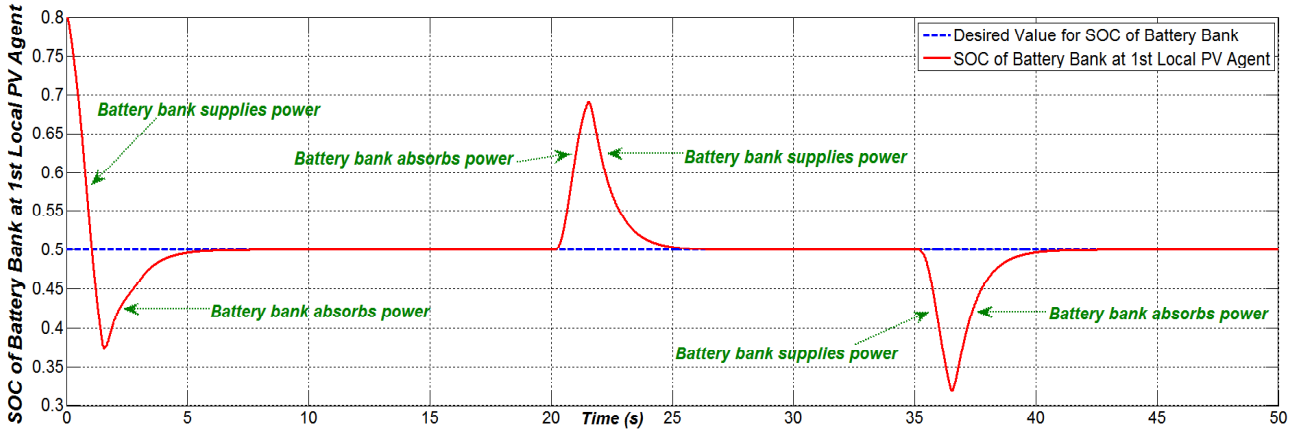


(b) Total power injected from PV farm into grid with the proposed fuzzy-based strategy in *Case 1*.

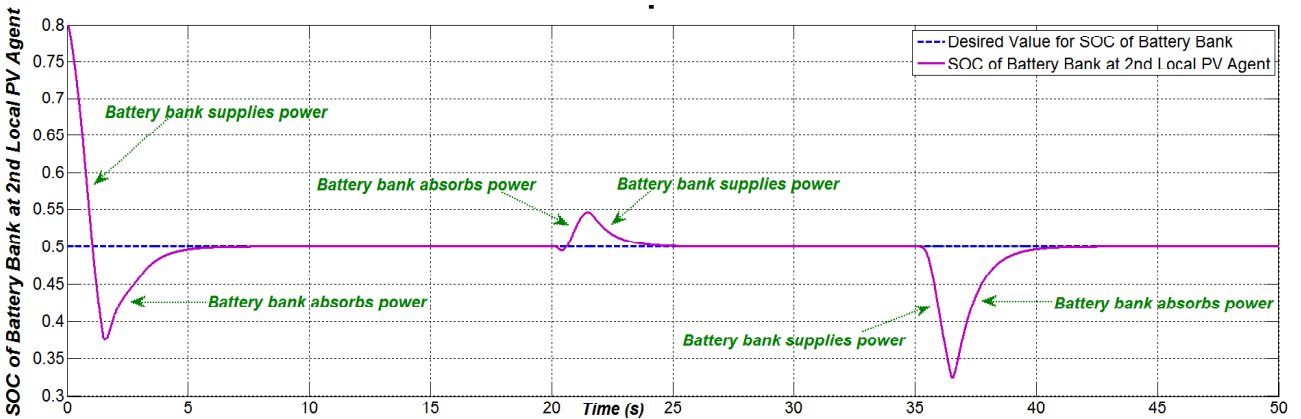


(c) Power injected from each local PV agent into grid with the proposed strategy in *Case 1*.

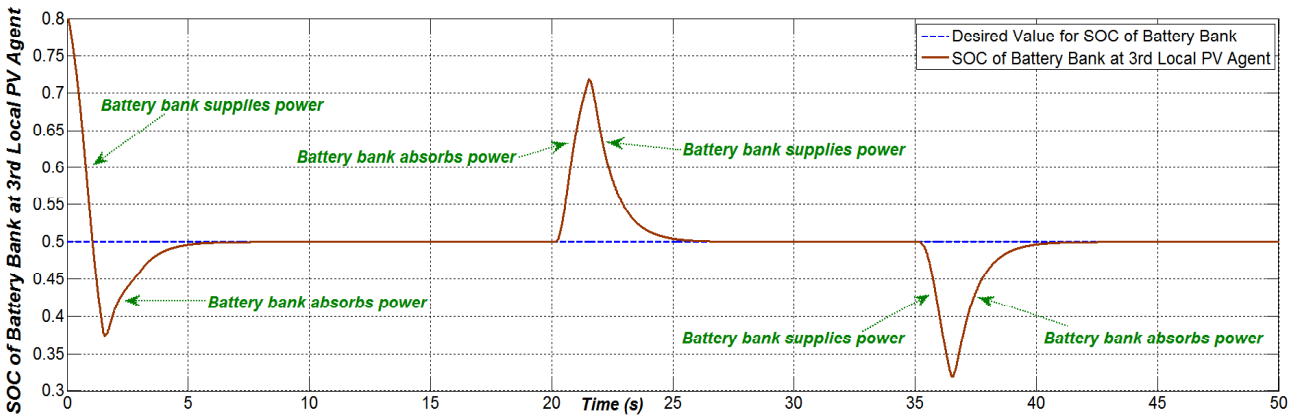
Figure 5.12: Simulation results of the control system in three different operation periods in *Case 1*.



(a) At the 1st local PV power agent in *Case 1*.



(b) At the 2nd local PV power agent in *Case 1*.



(c) At the 3rd local PV power agent in *Case 1*.

Figure 5.13: SOC of battery banks at local PV agents in three different operation periods in *Case 1*.

Indeed, the actual total power delivered (the red solid line) from the PV solar farm to grid is controlled accurately according to the reference value (the blue dash line) calculated beforehand by the central controller as illustrated in Figure 5.12(b). In detail, the actual active power injected from each local PV agent is adjusted suitably within three different operational conditions as given in Figure 5.12(c).

Also, as shown in Figure 5.13, battery banks installed in three local PV agents are governed to supply energy in about the three periods $t = [0s \ 1.6s]$, $t = [21.6s \ 26.2s]$ and $t = [35.2s \ 36.5s]$, and to absorb power in about the three periods $t = [1.6s \ 6s]$, $t = [20.1s \ 21.5s]$ and $t = [36.5s \ 41.1s]$. With the suggested control strategy, the appropriate operations of battery banks clearly help diminish significantly the grid-frequency deviation, especially when the changes of AC-system load and solar radiations suddenly occur at the times $t = 20s$ and $t = 35s$.

5.4.2. Case 2: Effects of air temperature and AC-system load

In the real weather condition, the change of air temperature is commonly not very fast, so the effect of air temperature on the output power of PV array is not as much as the effect of the solar radiation. However, in this simulation situation, to check and evaluate clearly the efficacy of the proposed fuzzy-based control strategy, the value of air temperature is assumed to alter abruptly and significantly.

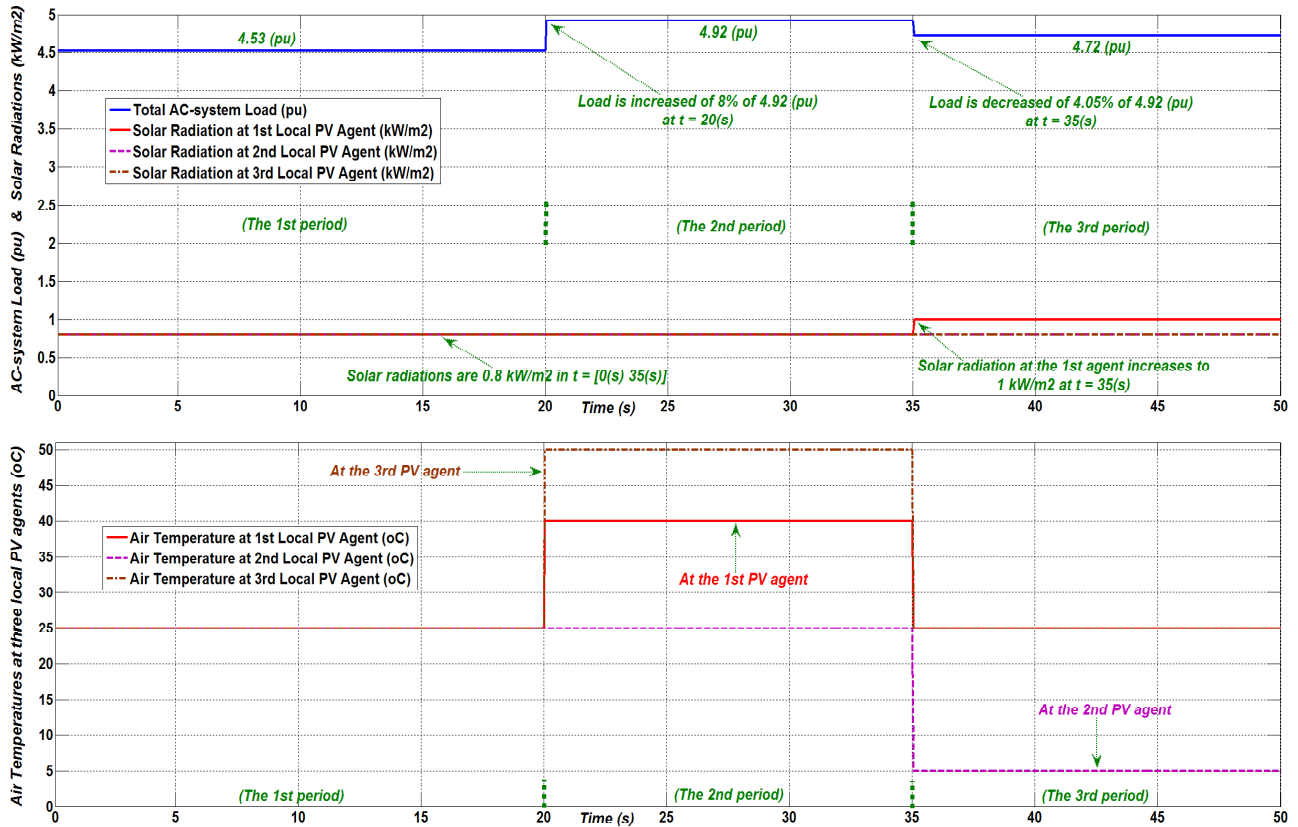


Figure 5.14: AC-system load, solar radiations and air temperatures at local PV agents in three periods in Case 2.

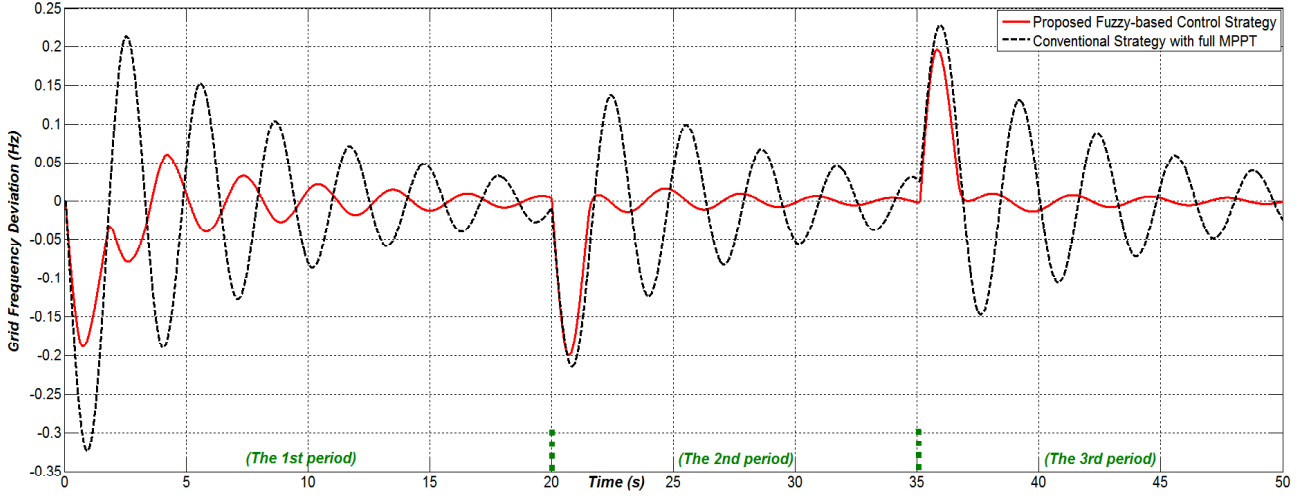
As shown in Figure 5.14, the temperatures at three local PV agents have the nominal value of 25 °C in the 1st operational period $t = [0s \ 20s]$; meanwhile, the AC-system load and solar radiation

are 4.53 *pu* (is 92% of the nominal value of 4.92 *pu*) and 0.8 kW/m^2 , respectively. Then, in the 2nd operational period $t = [20\text{s } 35\text{s}]$, the temperature at the 1st local PV agent increases to 40 °C, and the temperature at the 3rd local PV agent increases to 50 °C; meanwhile, the temperature at the 2nd local PV agent is still 25 °C. Besides, the AC-system load is increased of 8% to the nominal value of 4.92 *pu*, and the solar radiations at three local PV agents are still unchanged at 0.8 kW/m^2 . Finally, in the 3rd operational period $t = [35\text{s } 50\text{s}]$, the temperatures at the 1st, 2nd, and 3rd local PV agents reduce to 25 °C, 5 °C and 25 °C, respectively. The AC-system load is reduced of 4.05% to the new value of 4.72 *pu*; meanwhile, solar radiation at the 1st PV agent rises to 1 kW/m^2 , and solar radiations at both the 2nd and 3rd local PV agents are still invariant at 0.8 kW/m^2 .

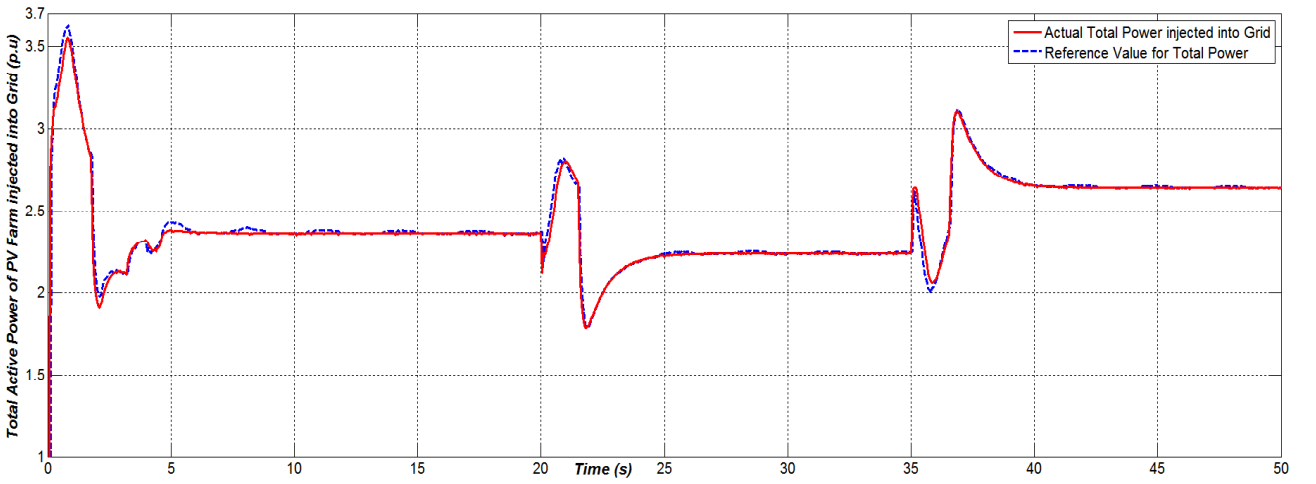
Simulation results are described in Figures 5.15 and 5.16. Wherein, according to Figure 5.15(a), the grid frequency fluctuation with the proposed control strategy (the red solid line) is really much smaller than the other (the black dash line). In detail, it is regulated in the range of $\pm 0.2 \text{ Hz}$ in transient states and also in the range of $\pm 0.05 \text{ Hz}$ at steady states. Meanwhile, the frequency deviation with the conventional control strategy using full MPPT mode exceeds the limitation values of $\pm 0.2 \text{ Hz}$ in four periods $t = [0.4\text{s } 1.42\text{s}]$, $t = [2.27\text{s } 2.7\text{s}]$, $t = [20.65\text{s } 21.03\text{s}]$ and $t = [35.52\text{s } 36.1\text{s}]$. As well, the response speed for reaching steady states (where the frequency deviation is in the range of $\pm 0.05 \text{ Hz}$) of the suggested fuzzy-based strategy is remarkably faster than the conventional technique. For example, in the second operation period of this simulation, the proposed strategy needs time of about 2 s (from $t = 20\text{s}$ to $t = 22\text{s}$) to reach the steady state; meanwhile, the conventional strategy using full MPPT mode needs time of 8.5 s (from $t = 20\text{s}$ to $t = 28.5\text{s}$) to reach the steady state.

As illustrated in Figure 5.15(b), the actual total power (the red solid line) delivered from the PV solar farm to grid is controlled accurately according to the reference value (the blue dash line) calculated beforehand by the central controller. In detail, the actual active power injected from each local PV agent is adjusted suitably within three different operational conditions as given in Figure 5.15(c).

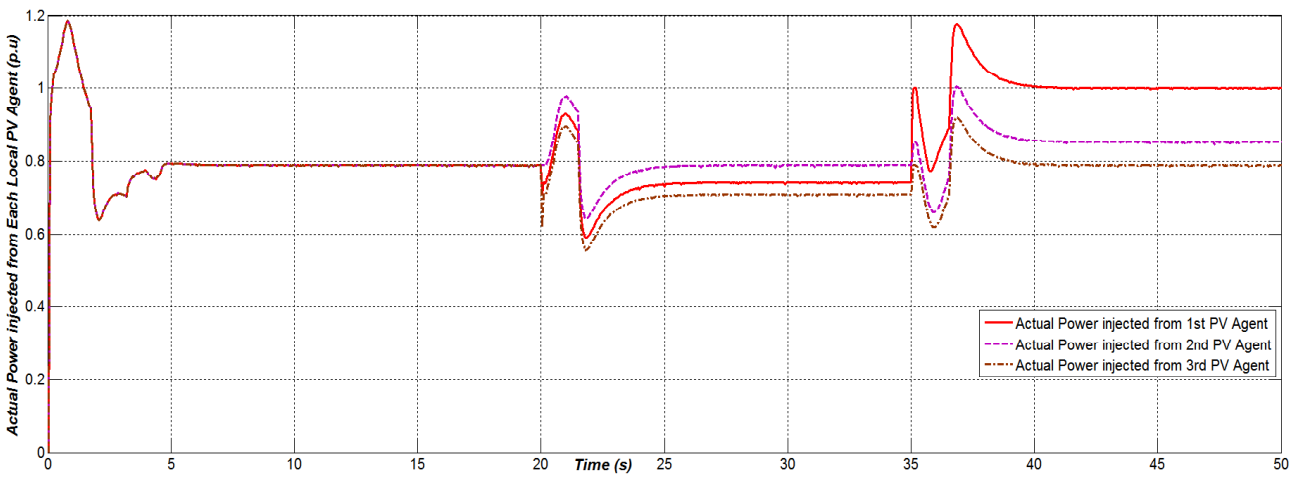
Also, as shown in Figure 5.16, battery banks installed in the three local PV agents are governed to supply energy in about the three periods $t = [0\text{s } 1.6\text{s}]$, $t = [20.1\text{s } 21.5\text{s}]$ and $t = [36.5\text{s } 41.1\text{s}]$, and to absorb power in about the three periods $t = [1.6\text{s } 6\text{s}]$, $t = [21.6\text{s } 26.2\text{s}]$ and $t = [35.2\text{s } 36.5\text{s}]$. With the suggested control strategy, the appropriate operations of battery banks clearly help diminish significantly the grid-frequency deviation, especially when the changes of AC-system load and temperature suddenly occur at the times $t = 20\text{s}$ and $t = 35\text{s}$.



(a) Grid frequency deviation in three different operational periods in *Case 2*.

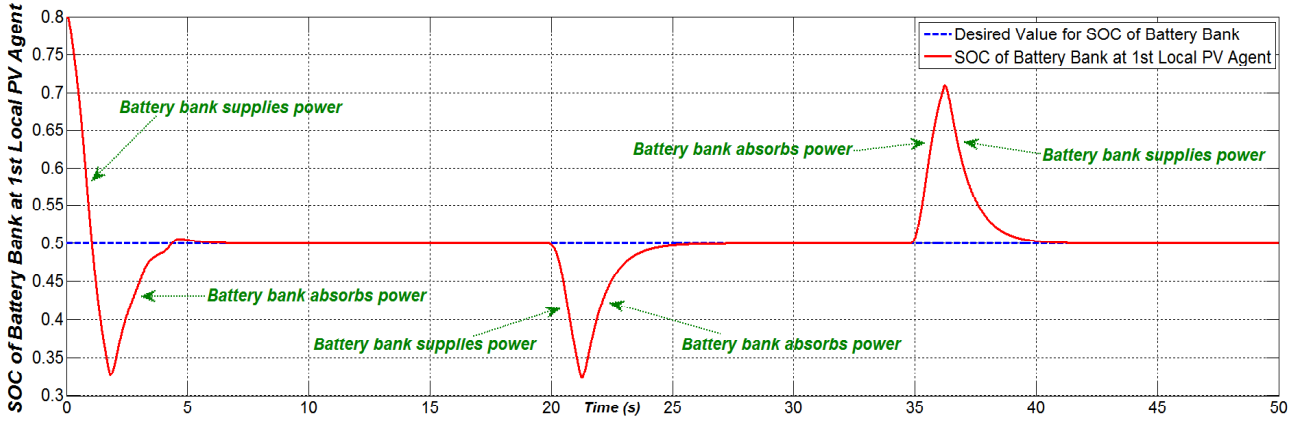


(b) Total power injected from PV farm into grid with the proposed fuzzy-based strategy in *Case 2*.

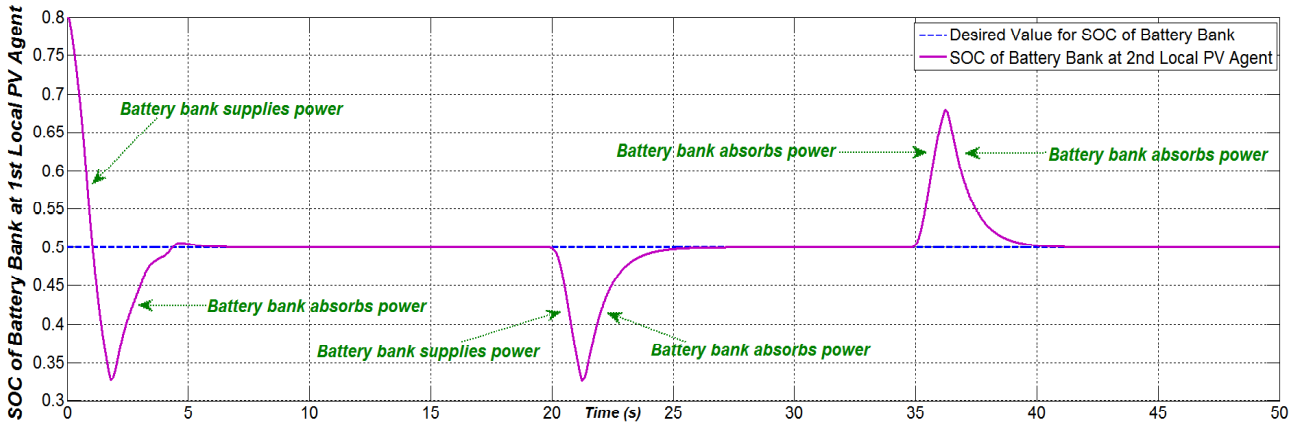


(c) Power injected from each local PV agent into grid with the proposed strategy in *Case 2*.

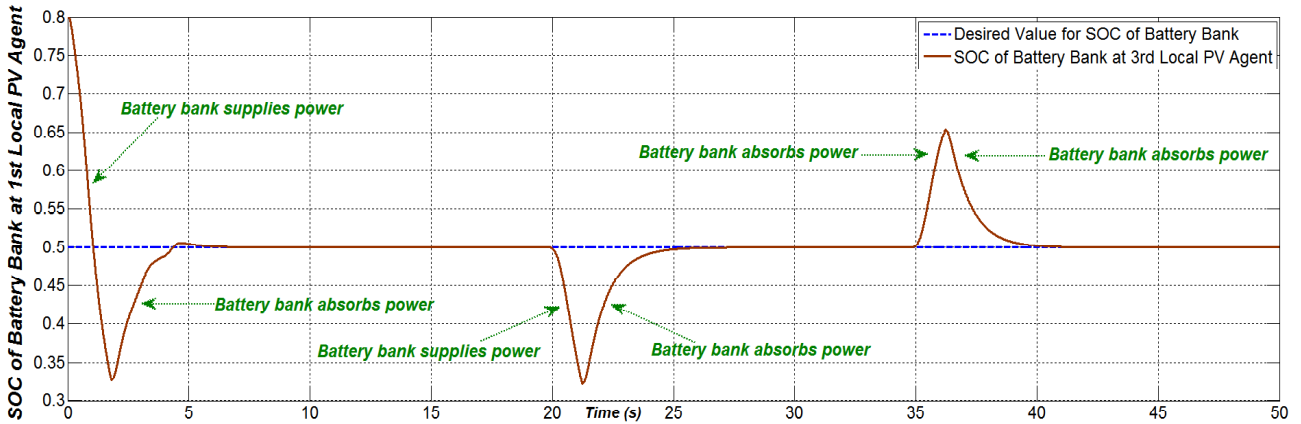
Figure 5.15: Simulation results of the control system in three different operation periods in *Case 2*.



(a) At the 1st local PV power agent in *Case 2*.



(b) At the 2nd local PV power agent in *Case 2*.



(c) At the 3rd local PV power agent in *Case 2*.

Figure 5.16: SOC of battery banks at local PV agents in three different operation periods in *Case 2*.

5.5. Summary of chapter

This chapter has presented a unique coordinated-control strategy based on fuzzy logic with supporting the grid-frequency regulation for a grid-connected large-scale PV solar farm, containing battery banks at local PV power agents. Wherein, the control strategy consists of a central

coordinating controller, including a frequency-regulation module using the newly developed 49-rule FLC to define the reference value of total active power needed to inject into grid; and then coordinates the individual reference value for the local controller installed at each PV power agent. Besides, at each local PV agent of the illustrative solar farm, all the power-electronics converters in use are driven by the local controller to deliver properly the output active power to grid for governing the grid frequency in the acceptable range of $\pm 0.2 \text{ Hz}$ in transient states and especially in the range of $\pm 0.05 \text{ Hz}$ at steady states. Simulation results have demonstrated advantages of the suggested control strategy not only in supplying the total active power from the solar farm to the grid but also in regulating the grid frequency, as well as keeping SOC of the battery banks at local PV power agents to be in the safe ratio range of $[0.2 \ 0.8]$ during operation time and close to the desired ratio value of 0.5 at the steady state.

Moreover, simulation results obtained with the proposed control strategy and the conventional strategy based on full MPPT mode have also shown salient efficacy of the presented fuzzy-based coordinated-control strategy, even when the AC-system load, solar radiation and air temperature alter abruptly and markedly.

Chapter 6

Conclusion

6.1. Completed contents and results in thesis

This Doctoral dissertation has presented a fairly comprehensive study in developing the efficient hybrid controllers based on fuzzy logic for PV energy systems. Wherein, the first two proposed control methods, that are the fuzzy-based INC-MPPT algorithm and the FBL-FL hybrid technique, are applied for a solar power agent; and the third proposed method is the fuzzy-based coordinated-control strategy which is applied for a grid-connected large-scale solar farm, consisting of many local PV power agents and the battery bank to store energy at each agent. As a main point should be noted, in the three above proposed methods, the three corresponding FLCs are developed newly and suitably for the PV system used in each the study part. In detail:

1) In Chapter 3, the fuzzy-based INC-MPPT algorithm has been proposed to apply for the DC-DC converter connected with PV array to obtain optimally the maximum power of PV array in varying weather conditions. Wherein, a unique 25-rule FLC is designed to alter appropriately the step-size $\Delta V(k)$ of the INC-MPPT algorithm to become a variable non-negative value, instead of a constant positive value in the conventional INC-MPPT method. With the 320W stand-alone PV system, simulations in MATLAB have shown that the proposed method can track speedily and efficiently the MPP of PV array even if the solar radiation and temperature suddenly vary. Besides, experimental results have illustrated the noticeable efficacy of the proposed algorithm even within the partial shadow case. In addition, both simulations and experiments have demonstrated the suggested method has better performance as compared with the conventional INC-MPPT and the conventional fuzzy-based INC-MPPT introduced in [37].

2) In Chapter 4, the FBL-FL hybrid technique has been introduced to regulate the active and reactive output AC powers of three-phase grid-connected PV inverters. Wherein, a novel 25-rule FLC has been developed to enhance effectiveness of the linear PI method used in the direct FBL approach as follows: [i] To fine-tune automatically the gain factors (K_{d2}, K_{q2}) of integral modules in the linear method to help improve significantly the transient dynamics (response time, overshoot) of the output powers, [ii] To adjust suitably for the final virtual-control signals (β_d, β_q) to reduce efficiently the steady-state oscillations in the output powers. With the 100kW grid-connected PV

inverter, simulations in MATLAB have demonstrated that the proposed FBL-FL can regulate well the active and reactive output powers closely to the desired values. Moreover, as compared to the traditional PI control and the direct FBL approach, the proposed FBL-FL technique has noticeably better performance in increasing the response speed and reducing the overshoot of the output powers. Also, the steady-state oscillation in output powers with the proposed FBL-FL is kept in an acceptable range. Finally, the robustness and efficacy of proposed FBL-FL technique have been validated within conditions of the parametric uncertainties and unbalanced grid voltage.

3) In Chapter 5, the fuzzy-based coordinated-control strategy has been proposed to control the total output active power of a grid-connected large-scale PV farm, containing battery banks at local PV power agents, to help regulate the grid frequency. Wherein, the control strategy has been developed with two-level structure as follows. The central coordinating controller, including a frequency-regulation module using the newly designed 49-rule FLC, determines accurately the desired value of total active power needed to deliver to grid; and then sends the individual desired value for the local controller located at each PV power agent. Simulations in MATLAB have shown that the suggested fuzzy-based strategy can inject efficiently the total active power into the grid, and also support to regulate the grid frequency in the tolerable range of $\pm 0.2 \text{ Hz}$ in transient states and in the very small range of $\pm 0.05 \text{ Hz}$ at steady states; as well as it can control SOC of battery banks at local PV power agents to be in the safe ratio range of $[0.2 \ 0.8]$ during operation time and especially close to the desired ratio value of 0.5 at steady states. Besides, the proposed fuzzy-based strategy has been verified well even when the AC-system load, solar radiation and temperature change unpredictably and markedly; and its performance is also better than the conventional control strategy which uses the full MPPT mode.

6.2. Several optionally complementary suggestions for the three study parts of thesis

This section presents several optionally complementary suggestions for the three study parts of the thesis for customizing and/or improving them to can have the better performance and more functions. In detail:

Regarding the first study part in Chapter 3, the designed FLC in the proposed INC-MPPT algorithm adjusts suitably the step-size in voltage $\Delta V(k)$ for making it to become a variable non-negative value in order to determine rapidly and accurately the optimal voltage $V_{MPP}^{ref}(k)$, where the PV array operates at the MPP. This is called the *voltage-based* INC-MPPT algorithm. On the other aspect, we can customize the above proposed algorithm to use the PV current as follows. The designed FLC will now fine-tune the step-size in current $\Delta I(k)$ for making it to become a variable

non-negative value in order to seek quickly and exactly the optimal current $I_{MPP}^{ref}(k)$, where the PV array also operates at the MPP. This customized method is called the *current-based* INC-MPPT algorithm. Then, we compare performances of the two *voltage-based* and *current-based* algorithms in terms of speed and accuracy in tracking MPP and steady-state fluctuations around MPP to choose the most suitable algorithm for each individual-type of DC-DC converters used for PV systems in different applications. Besides, the issue of partially shaded condition on large-scale PV solar systems and efficient solutions for it (as already reviewed in subsection 3.6.2 of Chapter 3) should be continually verified within simulations and experiments in the future.

Regarding the second study part in Chapter 4, the proposed FBL-FL hybrid technique can regulate well the active and reactive output powers (P_g, Q_g) of three-phase grid-connected PV inverters by indirectly controlling the corresponding currents (i_{gd}, i_{gq}). This is called the *current-control* technique. On the other aspect, we can customize the proposed FBL-FL technique to regulate directly the active and reactive output powers (P_g, Q_g) without controlling the currents (i_{gd}, i_{gq}). This means that there is no need the Current Controller module as shown in Figure 4.4(a), and is called the *direct-power-control* technique. After that, we compare performances of the two current-control and direct-power-control FBL-FL techniques in terms of transient dynamics (response speed, overshoot), steady-state oscillation, robustness and also the complexity in design.

Regarding the third study part in Chapter 5, the suggested fuzzy-based coordinated-control strategy just adjusts the total output active power of a grid-connected large-scale PV farm to help regulate the grid frequency. Besides, the regulation of grid voltage at the point of common coupling (PCC) of the solar farm by controlling the total reactive power of PV farm is also important issue and is currently an interesting research theme. So, an additionally new coordinated-control strategy for the PV farm with supporting the regulation of grid voltage at PCC should be studied to can combine suitably with the already proposed strategy (with supporting the regulation of grid frequency) in this thesis.

6.3. Direction of future development for thesis

In the direction of future development for this thesis, remarkable problems about coordinated-control strategy, balance of supply and demand of power and power quality in the large-scale electric network, where many distributed PV and wind energy farms are installed, will be examined and researched. Wherein, the newly proposed coordinated-control strategy will be designed with the three-level control structure. In detail, according to the real-time consumption demand, the

highest-level central coordinating host, which regularly collects and monitors the detailed status of all the PV and wind energy farms installed in the network, determines the individual reference values of active and reactive powers for each PV farm and wind farm. Then, the *secondary-level* central controller of each (PV, wind) farm suitably coordinates all the *lowest-level* controllers of local energy agents installed in the farm to deliver the active and reactive powers to the grid accurately according to the desired values obtained from the *highest-level* central host, as well as to ensure well balance of the consumption demand and the total supplying power capacity of all farms. Obviously, the ultimate objective of the coordinated control strategy is to help regulate real-time not only the grid frequency but also the grid voltage in acceptable ranges. Besides, an efficient automatically-tuning controller based on fuzzy logic for power active filter to eliminate thoroughly the harmonic resonances on the common bus of renewable farms will be studied and developed./.

List of Research Achievements

Journal Papers

- 1. Nguyen Gia Minh Thao, Kenko Uchida, and Nam Nguyen-Quang, “An Improved Incremental Conductance-Maximum Power Point Tracking Algorithm based on Fuzzy Logic for Photovoltaic Systems”, *SICE Journal of Control, Measurement, and System Integration*, Vol. 7, No. 2, pp. 122-131, 20th March 2014, DOI: 10.9746/jcmsi.7.122.
- 2. Nguyen Gia Minh Thao and Kenko Uchida, “Active and Reactive Power Control Techniques based on Feedback Linearization and Fuzzy Logic for Three-Phase Grid-Connected Photovoltaic Inverters”, *Asian Journal of Control*, Vol. 17, No. 5, pp. 1-25, September 2015, published online early view on 10th September 2014, DOI: 10.1002/asjc.998.

International Conference Papers

- 1. Nguyen Gia Minh Thao and Kenko Uchida, “A Novel Fuzzy-based Control Strategy for Grid-connected Large-scale Solar Farm with Supporting The Grid-Frequency Regulation”, *Proceeding of Asian Control Conference 2015 (ASCC 2015)*, pp. 224-231, Kota Kinabalu, Malaysia, 31st May - 3rd June 2015.
- 2. Nguyen Gia Minh Thao and Kenko Uchida, “A Control Strategy based on Fuzzy Logic for Three-phase Grid-connected Photovoltaic System with Supporting Grid-Frequency Regulation”, *Proceeding of International Conference on Intelligent and Automation Systems 2015 (ICIAS 2015)*, paper ID: S0009, Ho Chi Minh City, Vietnam, 6th-7th February 2015.
- 3. Nguyen Gia Minh Thao and Kenko Uchida, “Control The Active and Reactive Powers of Three-phase Grid-Connected Photovoltaic Inverters Using Feedback Linearization and Fuzzy Logic”, *Proceeding of Australian Control Conference 2013 (AUCC 2013)*, pp. 133-140, Perth, Australia, 4th-5th November 2013, DOI: 10.1109/AUCC.2013.6697261.
- 4. Nguyen Gia Minh Thao and Kenko Uchida, “Control The Photovoltaic Grid-Connected System Using Fuzzy Logic and Backstepping Approach”, *Proceeding of Asian Control Conference 2013 (ASCC 2013)*, pp. 1-8, Istanbul, Turkey, 23rd-26th June 2013, DOI: 10.1109/ASCC.2013.6606123.

5. Nguyen Gia Minh Thao, Kenko Uchida, Kentaro Kofuji, Toru Jintsugawa, and Chikashi Nakazawa, “A Comprehensive Analysis Study about Harmonic Resonances in Megawatt Grid-Connected Wind Farms”, *Proceeding of International Conference on Renewable Energy Research and Applications 2014 (ICRERA 2014)*, pp. 387-394, Milwaukee, The United States, 19th-22nd October 2014, DOI: 10.1109/ICRERA.2014.7016415.
6. Truc Pham-Dinh, Hai Nguyen-Thanh, Kenko Uchida, and Nguyen Gia Minh Thao, “Modified Controls for Grid-Connected Wind-Turbine Doubly Fed Induction Generator under Unbalanced Voltage Dip for Torque Stability and Reduction of Current Harmonic”, *Proceeding of SICE Annual Conference 2014 (SICE 2014)*, pp. 1493-1500, Sapporo, Japan, 9th-12th September 2014, DOI: 10.1109/SICE.2014.6935281.
7. Truc Pham-Dinh, Hai Nguyen-Thanh, Kenko Uchida, and Nguyen Gia Minh Thao, “Comparison between Modifications of SFOC and DPC in Control of Grid-Connected Doubly Fed Induction Generator under Unbalanced Voltage Dip”, *Proceeding of SICE Annual Conference 2013 (SICE 2013)*, pp. 2581-2588, Nagoya, Japan, 14th-17th September 2013.

Bibliography

- [1] O. Edenhofer, R. Pichs-Madruga, Y. Sokona, K. Seyboth, P. Eickemeier, P. Matschoss, G. Hansen, S. Kadner, S. Schlömer, T. Zwickel, and C. V. Stechow, “Special Report on Renewable Energy Sources and Climate Change Mitigation,” *Intergovernmental Panel on Climate Change*, 2012, available online at: www.ipcc.ch/pdf/special-reports/srren/SRREN_FD_SPM_final.pdf
- [2] B. N. Alajmi, K. H. Ahmed, S. J. Finney, and B. W. Williams, “Fuzzy-Logic Control Approach of a Modified Hill-Climbing Method for Maximum Power Point in Microgrid Standalone Photovoltaic System,” *IEEE Transactions on Power Electronics*, Vol. 26, No. 4, pp. 1022–1030, 2011.
- [3] L. Fangrui, D. Shanxu, L. Fei, L. Bangyin, and K. Yong, “A variable step-size INC MPPT method for PV systems,” *IEEE Transactions on Industrial Electronics*, Vol. 55, No. 7, pp. 2622–2628, 2008.
- [4] B. Yang, W. Li, Y. Zhao, and X. He, “Design and Analysis of a Grid-Connected Photovoltaic Power System,” *IEEE Transactions on Power Electronics*, Vol. 25, No. 4, pp. 992-1000, 2010.
- [5] N. G. M. Thao, and K. Uchida, “Control The Photovoltaic Grid-connected System using Fuzzy Logic and Backstepping Approach,” *Proceedings of Asian Control Conference 2013 (ASCC 2013)*, pp. 1-8, Turkey, June 2013.
- [6] G. A. Raducu, “Control of Grid Side Inverter in a B2B Configuration for WT Applications,” *Master Thesis*, Aalborg University, 2008.
- [7] M. Datta, T. Senjyu, A. Yona, T. Funabashi, and C. H. Kim, “A Coordinated Control Method for Leveling PV Output Power Fluctuations of PV–Diesel Hybrid Systems Connected to Isolated Power Utility,” *IEEE Transactions on Energy Conversion*, Vol. 24, No. 1, pp. 153-162, March 2009.
- [8] M. Datta, H. Ishikawa, H. Naitoh, and T. Senjyu, “LFC by Coordinated Virtual Inertia Mimicking and PEVs in Power Utility with MW-class Distributed PV Generation”, *Proceedings of IEEE COMPEL 2012*, Kyoto, Japan, June 2012.
- [9] N. Kakimoto, S. Takayama, H. Satoh, and K. Nakamura, “Power Modulation of Photovoltaic Generator for Frequency Control of Power System,” *IEEE Transactions on Energy Conversion*, Vol. 24, No. 4, pp. 943-949, December 2009.

- [10] I. J. Pérez-Arriaga, "Managing large scale penetration of intermittent renewables," *Energy Initiative Symposium 2011*, Massachusetts Institute of Technology, 20th April 2011.
- [11] News release: "World's First Large-Scale Power Storage System Made From Reused EV Batteries Completed in Japan," *Sumitomo Corporation*, February 2014, available online at: www.sumitomocorp.co.jp/english/news/detail/id=27673
- [12] T. Esum and P. L. Chapman, "Comparison of Photovoltaic Array Maximum Power Point Tracking Techniques," *IEEE Transactions on Energy Conversion*, Vol. 22, No. 2, pp. 439–449, 2007.
- [13] K. H. Hussein and G. Zhao, "Maximum photovoltaic power tracking: an algorithm for rapidly changing atmospheric conditions," *IEE Proceedings of Generation, Transmission, and Distribution*, Vol. 142, No. 1, pp. 59–64, 1995.
- [14] D. Menniti, A. Pinnarelli, and G. Brusco. "Implementation of a novel fuzzy-logic based MPPT for grid-connected photovoltaic generation system," *Proceedings of 2011 IEEE Trondheim PowerTech*, pp. 1–7, 2011.
- [15] J. Li, and H. Wang, "Maximum Power Point Tracking of Photovoltaic Generation Based on the Fuzzy Control Method," *Proceedings of SUPERGEN 2009*, pp. 1–6, 2009.
- [16] M. P. Kazmierkowski, and L. Malesani, "Current Control Techniques for Three-Phase Voltage-Source PWM Converters: a Survey," *IEEE Transactions on Industrial Electronics*, Vol. 45, No. 5, pp. 691-703, 1998.
- [17] M. Benchagra, M. Hilal, Y. Errami, M. Maaroufi, and M. Ouassaid, "Nonlinear Control of DC-bus Voltage and Power for Voltage Source Inverter," *Proceedings of ICMCS 2012*, pp. 1049-1054, 2012.
- [18] N. G. M. Thao, M. T. Dat, T. C. Binh, and N. H. Phuc, "PID-Fuzzy Logic Hybrid Controller for Grid-Connected Photovoltaic Inverters," *Proceedings of 5th IFOST*, pp. 140-144, South Korea, 2010.
- [19] M. Datta, T. Senjyu, A. Yona, H. Sekine, and T. Funabashi, "Smoothing Output Power Variations of Isolated Utility Connected Multiple PV Systems by Coordinated Control," *Journal of Power Electronics*, Vol. 9, No. 2, pp. 320-333, March 2009.
- [20] M. Datta, T. Senjyu, A. Yona, T. Funabashi, and C. H. Kim, "Fuzzy Control of Distributed PV Inverters/ Energy Storage Systems/ Electric Vehicles for Frequency Regulation in a Large Power System," *IEEE Transactions on Smart Grid*, Vol. 4, No. 1, pp. 479-488, March 2013.
- [21] D. E. Kim, and D. C. Lee, "Feedback Linearization Control of Grid-Interactive PWM Converters with LCL Filters," *Journal of Power Electronics*, Vol. 9, No. 2, pp. 288-299, 2009.

- [22] T. J. Ross, *Fuzzy Logic with Engineering Applications*, 3rd edition, Wiley, 2010.
- [23] O. Wolkenhauer, "Fuzzy Inference Engines," *Control Systems Centre*, University of Manchester Institute of Science and Technology, available online at: www.sbi.uni-rostock.de/uploads/tx_templavoila/SBI_Materials_Fuzzy-Inference_Engines.pdf
- [24] "Fuzzy Logic Toolbox: Why Use Fuzzy Logic?," MATLAB User's Guide, Version R2015a, *The MathWorks, Inc.*, March 2015.
- [25] "Intelligent Control Techniques in Mechatronics - Fuzzy logic," online available at: www.ro.feri.uni-mb.si/predmeti/int_reg/Predavanja/Eng/4.Fuzzy%20logic/_33.html
- [26] H.-M. Lee, T.-Ye. Lee, and S.-Y. Lee, "A Note on 'Evaluating the Rate of Aggregative Risk in Software Development using Fuzzy Set Theory'," *Proceedings of The 6th Asia-Pacific Decision Sciences Institute Conference*, Singapore, 18th-21st July 2001, online available at: <http://iceb.nccu.edu.tw/proceedings/APDSI/2001/PAPERS/Lee,%20Huey-Ming.doc>
- [27] R. Fuller, *Neural Fuzzy Systems*, Abo Akademi University, Åbo, Finland, 1995.
- [28] A. Mellit, S.A. Kalogirou, L. Hontoriac, S. Shaari, "Artificial Intelligence Techniques for Sizing Photovoltaic Systems: A Review," *Renewable and Sustainable Energy Reviews*, Vol. 13, Issue 2, pp. 406–419, February 2009.
- [29] Y. Wu, B. Zhang, J. Lu, and K. -L. Du, "Fuzzy Logic and Neuro-fuzzy Systems: A Systematic Introduction," *International Journal of Artificial Intelligence and Expert Systems*, Vol. 2, Issue 2, pp. 47-80, May 2011.
- [30] J. Vieira, F. M. Dias, and A. Mota, "Neuro-Fuzzy Systems: A Survey," *Proceedings of 5th WSEAS International Conferences on: Neural Networks and Applications (NNA 2004)*, Udine, Italy, 25th-27th March 2004.
- [31] E. M. Natsheh and A. Albarbar, "Hybrid Power Systems Energy Controller Based on Neural Network and Fuzzy Logic," *Smart Grid and Renewable Energy*, Vol. 4, pp. 187-197, 2013.
- [32] B. Akdemira and N. Çetinkaya, "Long-term load forecasting based on adaptive neural fuzzy inference system using real energy data," *Energy Procedia*, Vol. 14, pp. 794-799, 2012.
- [33] A. Abraham and B. Nath, "Connectionist Models for Intelligent Reactive Power Control," *Proceedings of The Australasian Matlab Users Conference*, Melbourne, Australia, 9th-10th November 2000.
- [34] A. G. Abro and J. M.-Saleh, "Control of Power System Stability – Reviewed Solutions Based on Intelligent Systems," *International Journal of Innovative Computing, Information and Control*, Volume 8, Number 10(A), pp. 6643–6666, October 2012.

- [35] “Fuzzy Logic Toolbox,” MATLAB User’s Guide, Version R2015a, *The MathWorks, Inc.*, March 2015.
- [36] Q. Mei, M. Shan, L. Liu, and J. M. Guerrero, “A Novel Improved Variable Step-Size Incremental- Resistance MPPT Method for PV Systems,” *IEEE Transaction on Industrial Electronics*, Vol. 58, No. 6, pp. 2427–2434, 2011.
- [37] N. Patcharaprakiti, and S. Premrudeepreechacharn, “Maximum Power Point Tracking using Adaptive Fuzzy Logic Control for Grid-Connected Photovoltaic System,” *Power Engineering Society Winter Meeting*, Vol. 1, pp. 372–377, The United States, 27-31 January 2002.
- [38] N. Khaehintung, and P. Sirisuk, “Application of Maximum Power Point Tracker with Self-organizing Fuzzy Logic Controller for Solar-powered Traffic Lights,” *Proceedings of 7th PEDS*, pp. 642–646, 2007.
- [39] T. L. Kottas, Y. S. Boutalis, and A. D. Karlis, “New maximum power point tracker for PV arrays using fuzzy controller in close cooperation with fuzzy cognitive networks,” *IEEE Transaction on Energy Conversion*, Vol. 21, No. 3, pp. 793–803, 2006.
- [40] A. A. Ovalle, H. R. Chamorro, and G. Ramos, “Step-size Fuzzy Control to Maximum Power Point Tracking Algorithms for PV Microgrid Arrays,” *Proceedings of Robotics Symposium – LARC 2011*, pp. 1–6, 2011.
- [41] N. Shah and R. Chudamani, “Grid Interactive PV System with Harmonic and Reactive Power Compensation Features using a Novel Fuzzy Logic Based MPPT,” *Proceedings of 7th ICIIIS*, pp. 1–6, 2012.
- [42] T.-F. Wu, C.-H. Yang, Y.-K. Chen and Z.-R. Liu, “Photovoltaic Inverter Systems with Self-Tuning Fuzzy Control Based on an Experimental Planning Method,” *Proceedings of IEEE Industry Application Conference*, Vol.3, pp.1887-1894, 1999.
- [43] S. Haibin and B. Jingjing, “Maximum Power Point Tracking Algorithm Based on Fuzzy Neural Networks for Photovoltaic Generation System,” *Proceedings of ICCASM 2010*, Vol. 1, pp. 353–357, 2010.
- [44] R. F. Coelho, F. Concer, C. Martins, “A Study of the Basic DC-DC Converters Applied in Maximum Power Point Tracking,” *Proceedings of COBEP 2009*, pp. 673–678, 2009.
- [45] L. Zhao and J. Qian, “DC-DC Power Conversions and System Design Considerations for Battery Operated System,” *Texas Instruments*, 2006.
- [46] H. Sira-Ramírez and R. Silva-Ortigoza, *Control Design Techniques in Power Electronics Devices*, Springer, 2010 edition, 2010.

- [47] M. G. Villalva, J. R.I Gazoli, and E. R. Filho, "Comprehensive Approach to Modeling and Simulation of Photovoltaic Arrays," *IEEE Transactions on Power Electronics*, Vol. 24, No. 5, pp. 1198–1208, 2009.
- [48] BP-380J 80W PV module, *BP Solar Co.*, 2004.
- [49] X. L. Li, J. G. Park, and H. B. Shin, "Comparison and Evaluation of Anti-Windup PI Controllers," *Journal of Power Electronics*, Vol. 11, No.1, pp. 45-50, 2011.
- [50] K. Åström, T. Hägglund, *Advanced PID Control*, The International Society of Automation, North California, The U.S., August 2005.
- [51] Tiva C Series LaunchPad Evaluation Kit, *Texas Instruments*, available online at: www.ti.com/tool/ek-tm4c123gxl
- [52] A. Bidram, A. Davoudi, and R. S. Balog, "Control and Circuit Techniques to Mitigate Partial Shading Effects in Photovoltaic Arrays," *IEEE Journal of Photovoltaics*, Vol. 2, No. 4, pp. 532-546, October 2012.
- [53] Y.-H. Ji, D.-Y. Jung, J.-G. Kim, J.-H. Kim, T.-W. Lee, and C.-Y. Won, "A Real Maximum Power Point Tracking Method for Mismatching Compensation in PV Array under Partially Shaded Conditions," *IEEE Trans. on Power Electronics*, Vol. 26, No. 4, pp. 1001-1009, 2011.
- [54] G. Viot, "Fuzzy Logic in C," *Dr. Dobb's Journal*, pp. 40-56, February 1993, online available at: www.drdoobbs.com/cpp/fuzzy-logic-in-c/184408940
- [55] T. Noguchi, H. Tomiki, S. Kondo, and I. Takahashi, "Direct Power Control of PWM Converter without Power Source Voltage Sensors," *IEEE Transactions on Industry Applications*, Vol. 34, No. 3, pp. 473-479, 1998.
- [56] D. Zhi, L. Xu, and B. W. Williams, "Improved Direct Power Control of Grid-Connected DC/AC Converters," *IEEE Transactions on Power Electronics*, Vol. 24, No. 5, pp. 1280-1292, 2009.
- [57] J. Hu, L. Shang, Y. He, and Z. Q. Zhu, "Direct Active and Reactive Power Regulation of Grid-Connected DC/AC Converters Using Sliding Mode Control Approach," *IEEE Transactions on Power Electronics*, Vol. 26, No. 1, pp. 210-222, 2011.
- [58] X. Bao, F. Zhuo, Y. Tian, and P. Tan, "Simplified Feedback Linearization Control of Three-Phase Photovoltaic Inverter With an LCL Filter," *IEEE Transactions on Power Electronics*, Vol. 28, No. 6, pp. 2739-2752, 2013.
- [59] X. Zhou, Y. B. Guo, M. Zhang, X. Zhang, and H. Chen, "Dual Feedback Linearization Control of Three-Phase Pulse-Width-Modulation Voltage Source Rectifier based on Direct Power Control," *Proceedings of 7th IPEDMC*, pp.1859-1865, 2012.

- [60] T. L. Chien, C. C. Chen, Y. C. Chen, and S. L. Wu, "Improved Fuzzy Feedback linearization and Sinswat-transformation Control of Inverted Pendulum," *Control and Cybernetics*, Vol. 39, No. 4, pp. 1069-1093, 2010.
- [61] M. C. Tanaka, J. M. M. Fernandes, A. W. MacKenzie, and W. M. Bessa, "Feedback Linearization with Fuzzy Compensation for Electro-Hydraulic Actuated Systems," *Proceedings of ABCM Symposium Series in Mechatronics*, Vol. 5, pp. 438-446, 2012.
- [62] R. Marino, and P. Tomei, *Nonlinear Control Design: Geometric, Adaptive, and Robust*, 1st edition, Prentice Hall, 1995.
- [63] P. Cortés, J. Rodríguez, P. Antoniewicz, and M. Kazmierkowski, "Direct Power Control of an AFE Using Predictive Control," *IEEE Transactions on Power Electronics*, Vol. 23, No. 5, pp. 2516-2523, 2008.
- [64] P. Jirutitijaroen, "Transformer and Per-unit Analysis," *EE2022 Electrical Energy Systems - lecture 11*, National University of Singapore, 2012.
- [65] K. Meah, and S. Ula, "Investigation on Fuzzy logic-based Self-tuning Current Controller Applications in HVDC Links," *Proceedings of IEEE Region 5 Technical Conference*, pp. 226-272, 2007.
- [66] P. Gahinet, P. Apkarian, and M. Chilali, "Affine Parameter-Dependent Lyapunov Functions and Real Parametric Uncertainty," *IEEE Transactions on Automatic Control*, Vol. 41, No. 3, pp. 436-442, 1996.
- [67] C. Scherer, "Robust Stability," *Course of Linear Matrix Inequalities in Control – lecture 4*, Delft University of Technology, 2009.
- [68] F. H. Dupont, V. F. Montagner, J. R. Pinheiro, H. Pinheiro, S. V. G. Oliveira, and A. Péres, "Comparison of Linear Quadratic Controllers with Stability Analysis for DC-DC Boost Converters Under Large Load Range," *Asian Journal of Control*, Vol. 15, Issue 3, pp. 861–871, 2013.
- [69] P. Gahinet, A. Nemirovski, A. J. Laub, and M. Chilali, "LMI Control Toolbox for Use with MATLAB," User's Guide, Version 1, *The MathWorks, Inc.*, 1995.
- [70] P. Giroux, G. Sybille, C. Osorio, and S. Chandrachood, "Two Demonstrations of a Grid-connected PV Array using SimPowerSystems," File Exchange - MATLAB Central, *The MathWorks, Inc.*, 2012.
- [71] R. M. Strzelecki, and G. Benysek, *Power Electronics in Smart Electrical Energy Networks*, Springer, 2008.

- [72] IEEE SM 519-1992, "IEEE Recommended Practices and Requirements for Harmonic Control in Electrical Power Systems," *IEEE Industry Applications Society/ Power Engineering Society*, 1993.
- [73] M. Datta, T. Senjyu, A. Yona, T. Funabashi, and C. H. Kim, "A Frequency-control Approach by Photovoltaic Generator in a PV–Diesel Hybrid Power System," *IEEE Transactions on Energy Conversion*, Vol. 26, No. 2, pp. 559-571, June 2011.
- [74] K. Sun, L. Zhang, Y. Xing, and J. M. Guerrero, "A Distributed Control Strategy Based on DC Bus Signaling for Modular Photovoltaic Generation Systems with Battery Energy Storage," *IEEE Transactions on Power Electronics*, Vol. 26, No. 10, pp. 3032-3045, October 2011.
- [75] H. Xin, Y. Liu, Z. Wang, D. Gan, and T. Yang, "A New Frequency Regulation Strategy for Photovoltaic Systems Without Energy Storage," *IEEE Transactions on Sustainable Energy*, Vol. 4, No. 4, pp. 985-993, October 2013.
- [76] H. Bevrani, and S. Shokoohi, "An Intelligent Droop Control for Simultaneous Voltage and Frequency Regulation in Islanded Microgrids," *IEEE Transactions on Smart Grid*, Vol. 4, No. 3, pp. 1505-1513, September 2013.
- [77] S. Biegacki and D. VanGompel, "The application of DeviceNet in process control," *ISA Transactions*, Vol. 35, Issue 2, pp. 169–176, 1996.
- [78] P. Kundur, N. J. Balu, and M. G. Lauby, *Power System Stability and Control*, 1st edition, McGraw-Hill Professional, January 1994.
- [79] D. C. Martins, "Analysis of a Three-Phase Grid-Connected PV Power System using a Modified Dual-State Inverter," *ISRN Renewable Energy*, Vol. 2013, ID: 406312, 18 pages.
- [80] M. Meinhardt, G. Cramer, B. Burger, and P. Zacharias, "Multi-String-Converter with Reduced Specific Costs and Enhanced Functionality," *Solar Energy*, Vol. 69, Supplement 6, pp. 217–227, July–Dec 2001.
- [81] KWT-250M60A 250W K-Solar PV panel, *KyungWon Co. Ltd.*, 2012.
- [82] E. Skoplaki and J. A. Palyvos, "On the Temperature Dependence of Photovoltaic Module Electrical Performance: A Review of Efficiency /Power Correlations," *Solar Energy*, Vol. 83, pp. 614–624, 2009.
- [83] M. C. Garcia and J. L. Balenzategui, "Estimation of Photovoltaic Module Yearly Temperature and Performance Based on Nominal Operation Cell Temperature Calculations," *Renewable Energy*, Vol. 29, pp. 1997–2010, 2004.
- [84] A. Notholt, D. Coll-Mayor, and A. Engler, "Setting Up a Grid Simulator," *Proceedings of International Conference on Power Quality and Renewable Energies (ICREPQ'06)*, Palma de Mallorca, Spain, 5-7 April 2006.